Diss. ETH Nr. 25826

EDM Drilling and Milling of Aerospace Materials

A thesis submitted to attain the degree of
DOCTOR OF SCIENCES of ETH ZURICH
(Dr. sc. ETH Zurich)

presented by
Mikhail Kliuev

M. tech.

born on 6th December 1988
citizen of Russian Federation

accepted on the recommendation of
Prof. Dr. Ing. Konrad Wegener, examiner
Dipl. El. Ing. Marco Boccadoro, co-examiner
Dr. Ing. Roberto Perez, co-examiner
Prof. Dr. Ing. Andrey Kutin, co-examiner

2019

Abstract

The present work analyses new strategies and methods to combine drilling and milling of hard to cut materials on one machine in order to increase productivity and precision. The aim of this work is in the enlargement of EDM drilling machine abilities to erode the aerospace materials such as Inconel 718, SiC based CMCs and electrically non-conducting zirconia dioxide. The tendencies found in the experimental part are further analysed by simulations in order to prove the proposed hypothesis. Furthermore, the new method to machine electrically non-conducting materials in water, which was not possible before, is setup during this work. Also, the new method to machine slots in the turbine blades faster and better than the state-of-art method is shown.

The increase of productivity of electro discharge machining (EDM) is crucial for industrial applications such as drilling holes in turbine blades for aerospace or drilling in the fuel injection systems for automotive. Therefore machining abilities of modern EDM drilling machines for drilling cooling holes and shaping diffusors in turbine blades are described. For improving the process capability and machining efficiency of aerospace alloys, drilling of cooling holes and formation of diffusors can be combined into a single process by using the same electrode for both processes. Furthermore, shaping can be used for the seal slot machining. Complex sealing arrangement in turbomachinery can increase turbine efficiency by reducing leakage of high-pressure cooling flows into the hot gas path. Die-sinking EDM is widely used to machine straight seal slots, but electrode preparation makes it less efficient for complex shapes. This work presents research on the optimisation of a variant of EDM milling using process control and fluid dynamics simulation to exploit optimal machining conditions. The analysis demonstrates a stable process to machine complex shaped slots by focusing on the critical requirements for large-scale turbomachinery component manufacture, namely productivity, surface integrity and process monitoring.

Ceramics machining is another promising application for EDM drilling. A growing interest in the machining of Silicon carbide (SiC) is caused by its excellent mechanical properties, thermal conductivity, resistance to corrosion and oxidation. Furthermore, the new generation of turbine blades is made out of SiC/SiC CMCs, therefore machining of this material is analysed.

Ceramics often have high electrical resistivity, which causes difficulties during electric erosion. For instance zirconia dioxide is an electrically non-conducting material. It is typically used for the thermal barrier coating (TBC) of turbine blades. For EDM drilling process it is crucial to have an ability to erode electrically non-conducting TBC in deionized water. EDM of electrically non-conducting materials currently is only possible with the help of an auxiliary conductive layer, known as assisting electrode. Therefore, an assisting conductive layer is applied to the surface of the workpiece to initiate the discharge process. In order to continue erosion, the eroded surface regions must have a new conductive layer in contact with the original assisting conductive layer, which is typically achieved by depositing

carbonaceous material through dielectric oil decomposition. In this work, the renewal of such conductive layer is proposed to be done by material deposition from the tool electrode. This alternative solution enables machining of electrically non-conductive materials in deionized water instead of dielectric oil. The deposition of material from the tool electrode is achieved through erosion in very narrow interelectrode gaps and controlled short-circuiting. It is shown that machining of zirconium dioxide ceramics (ZrO_2) is possible in deionised water using a sacrificial electrode.

In order to better understand the experimental results, single crater simulations are performed. However, the discharge energy distribution of the EDM process is not fully understood. The present work provides modelling, simulation and verification by experiments of the EDM discharge in water, to understand the material removal mechanism of the single discharge better. In the present work, finite element analysis (FEA) of a single discharge is performed to calculate the energy fraction distributed into the workpiece (anode). Computational fluid dynamics (CFD) simulations with Marangoni effect and considering the temperature dependent material properties are accomplished. It is shown that the influence of the temperature dependent material properties compared to temperature independent properties on the crater depth is up to 24%. The temperature in the simulation varies from 293K to 2450K for temperature dependent material properties.

Another aspect, which is crucial for EDM, is flushing conditions. Insufficient flushing reduces the material removal efficiency, since the material, which remains in the gap, is remolten in the subsequent pulse and some is reattached to the bulk material. This work presents an analysis of the flushing flow through high-speed observation and simulation. The behaviour of debris, bubbles development, movement and evacuation is observed by high-speed imaging. Flushing characteristics and flow velocity vectors were following calculated with particle tracking velocimetry (PTV). Data from the measurements is used to compare and validate the CFD simulations. Simulation of the dielectric flow inside and outside of the eroded cavity is shown. CFD simulations are used to investigate analytically the influence of drilling conditions on the pressure drop and dielectric flow during EDM drilling. The influence of flushing on MRR and electrode wear is also analysed. This work describes a setup for high-speed imaging in the micrometre scale of a common EDM drilling process using electrode with multi-hole flushing. The analysis of the erosion process is performed within two conditions: first, the initial contact of the electrode with the material surface and second, erosion inside a predrilled hole. It is concluded that the flushing has a significant influence in those two conditions and therefore to the MRR, whereas the flushing efficiency drops by an increase of the drilling depth.

Zusammenfassung

In der vorliegenden Arbeit wird der neuartige Ansatz, den EDM-Bohr- und EDM-Fräs-Prozess von schwer zerspanbaren Materialien auf einer Maschine durchzuführen, beschrieben. Dies führt zu einer signifikanten Steigerung von Produktivität und Präzision in der Fertigung. Durch diese Kombination können die Anwendungsgebiete von EDM-Bohr-Maschinen massgeblich erweitert werden. Somit können für die Luftfahrtindustrie Materialien, wie z. B. Inconel 718, CMC (basierend auf SiC), und auch nicht elektrisch leitfähige Materialien, wie z. B. Zirkondioxid, effizient bearbeitet werden. Die Resultate aus Experimenten können durch Simulationen bestätigt werden. Während der Arbeit konnte das Erodieren nichtleitfähiger Materialien in Wasser erstmals erfolgreich durchgeführt werden, was dem Stand der Technik zufolge bisher als unmöglich galt. Im Rahmen dieser Arbeit werden innovative Möglichkeiten zur Fertigung von Nuten aufgezeigt, welche in Turbinenschaufeln zur Aufnahme von verbindenden Dichtungselementen zum Einsatz kommen .

Die Erhöhung der Produktivität der Funkenerosion (EDM) ist ein wichtiger Faktor für Industrieanwendungen, wie z. B. EDM-Bohren von Kühlungsbohrungen in Tubinenschaufeln oder Bohrungen von Einspritzdüsen. Deshalb werden die Prozesse zum EDM-Bohren von Kühlungsbohrungen und das EDM-Fräsen von Diffusoren für Turbinenschaufeln als Schwerpunkte beschrieben. Die Bearbeitung von Legierungen, welche in der Luftfahrt angewandt werden, kann wirtschaftlicher gestaltet werden, indem die zwei Operationen mit derselben Elektrodenform durchgeführt werden. Die Herstellung von Verbindungsnuten wird ebenfalls mittels EDM hergestellt. Eine komplexe Anordnung von Verbindungsnuten erhöht die Leistungsfähigkeit, da Leckage des Hochdruck-Kühlungsstroms vermindert wird. Häufig wird Senk-EDM zur Herstellung der Nuten angewandt, wobei jedoch die Elektrodenpräparation zur Bearbeitung komplexer Formen sehr aufwendig ist. In dieser Arbeit werden Prozesskontrolle und Fluiddynamik-Simulationen diskutiert, wodurch der EDM-Fräsprozess optimiert werden kann. Somit können eine hohe Produktivität, exzellente Oberflächenqualität und sichere Prozessüberwachung gewährleistet werden.

Die Bearbeitung von Keramiken durch EDM-Bohren ermöglicht eine kostengünstige Alternative zu konventionellen Fertigungstechniken. Wegen der aussergewöhnlichen mechanischen Eigenschaften, z. B. thermische Leitfähigkeit sowie Korrosions- und Oxidationsverhalten, steigt der Bedarf an Silikonkarbid (SiC) an. Deswegen werden zukünftig Turbinenschaufeln häufig aus SiC/SiC hergestellt.

Aufgrund des elektrischen Widerstands ist die EDM-Bearbeitung von Keramiken stark eingeschränkt. Zirkonoxid ist ein elektrisch nicht leitfähiges Material, welches als Wärmedämmschicht für Turbinenblätter eingesetzt wird. Zur Herstellung von Kühlungsbohrungen muss der EDM-Bohrprozess angewandt werden, welches nur durch den Einsatz von Opferelektroden möglich ist. Diese ermöglicht es, eine elektrisch leitfähige Schicht auf einer Keramik abzusetzen, auf der eine Entladung initialisiert werden kann. Um

den EDM-Prozess aufrecht zu erhalten, muss die leitfähige Schicht erneuert werden. Durch Ablagerungen von Kohlenstoff aus dem Dielektrikum auf der zu bearbeitenden Oberfläche, wird der EDM-Prozess nicht unterbrochen. Materialablagerungen durch die Opferelektrode kann durch kontrollierte Kurzschlüsse erzielt werden.

Um die experimentellen Ergebnisse besser zu verstehen, werden Einzelkratersimulationen durchgeführt. Die Entladungsenergieverteilung des Erodierprozesses ist jedoch nicht vollständig verstanden. Die vorliegende Arbeit beschreibt die Modellierung, Simulation und Verifikation durch Experimente der EDM-Funken in Wasser, um den Abtragmechanismus des materials der der einzelnen Einleitungen besser zu verstehen. In der vorliegenden Arbeit wird mit der Finite-Elemente-Analyse (FEA) eine Entladung simuliert, um den in das Werkstück (Anode) eingebrachten Energieanteil zu berechnen. Die CFD-Simulationen (Computational Fluid Dynamics) berücksichtigen den Marangoni-Effekt und temperaturabhängige Materialeigenschaften. Es wird gezeigt, dass der Einfluss der temperaturabhängigen Materialeigenschaften im Vergleich zu den temperaturunabhängigen Eigenschaften auf die Kratertiefe bis zu 24% beträgt. Die Temperatur in der Simulation variiert zwischen 293K und 2450K für temperaturabhängige Materialeigenschaften.

Ein weiterer Aspekt, der für die Funkenerosion entscheidend ist, sind die Spülbedingungen. Eine unzureichende Spülung reduziert den Materialabtrag, da das im Spalt verbliebene Material im nachfolgenden Impuls wieder aufgeschmolzen und sich teilweise wieder am Werkstück ablagert. Diese Arbeit zeigt eine Analyse der Spülströmung durch Hochgeschwindigkeitsbeobachtung und Simulation. Das Verhalten von Ablagerungen, Blasenbildung, Bewegung und Evakuierung wird durch Hochgeschwindigkeitsaufnahmen beobachtet. Spüleigenschaften und Strömungsgeschwindigkeitsvektoren wurden anschließend mit der Partikelverfolgungsgeschwindigkeitsmessung (PTV) berechnet. Die Daten aus den Messungen werden verwendet, um die CFD-Simulationen zu vergleichen und zu validieren. CFD-Simulationen werden verwendet, um den Einfluss des Druckabfalls und der Strömung auf die Bohrbedingungen analytisch zu untersuchen. Der Einfluss der Spülung auf die MRR und den Elektrodenverschleiß wird ebenfalls analysiert. Diese Arbeit beschreibt einen Aufbau für die Hochgeschwindigkeitskamera eines gängigen Bohrerodierprozesses im Mikrometerbereich mit einer Elektrode mit Mehrlochspülung. Zwei Zustände des Erosionsprozesses werden analysiert: erstens des ersten Kontakts der Elektrode mit der Materialoberfläche und zweitens die Erosion in einem vorgebohrten Loch. Es wird der Schluss gezogen, dass die Spülung unter diesen beiden Bedingungen und auf die MRR einen signifikanten Einfluss hat, die Spülleistung sinkt mit zunehmender Bohrtiefe.

Аннотация

В настоящей работе анализируются новые методы и стратегии комбинирования процессов сверления и фрезерования труднообрабатываемых материалов, используя один станок, с целью повышения точности и производительности. Целью данной работы является расширение возможностей сверлильного станка EDM для обработки аэрокосмических материалов, таких как Inconel 718, композитов с керамической матрицей на основе SiC и токонепроводящих керамик на основе диоксида циркония. Тенденции, обнаруженные в экспериментальной части, анализируются с помощью моделирования, для проверки предложенных гипотез. Кроме того, во время этой работы был открыт новый метод обработки диэлектрических материалов в деионизированной воде, что считалось ранее невозможным. Помимо этого, показан новый способ обработки уплотнительных слотов в лопатках турбины быстрее и лучше, чем ранее известные методы.

Увеличение производительности электроэрозионной обработки имеет решающее значение для такого промышленного применения, как сверление отверстий в лопатках турбин для аэрокосмической промышленности или сверление отверстий для систем впрыска топлива для автомобилей. В этой работе описаны возможности современных сверлильных станков EDM для сверления охлаждающих отверстий и формирования диффузоров в лопатках турбин. Для расширения возможностей процесса и увеличения эффективности обработки аэрокосмических сплавов сверление охлаждающих отверстий и электроэрозионное фрезерование диффузоров могут быть объединены в один процесс с использованием одного и того же электрода для обоих процессов. Кроме того, электроэрозионное фрезерование может быть использовано для обработки уплотнительных слотов в лопатках турбины. Сложные слоты уплотнения в турбине повышают эффективность за счет уменьшения утечки охлаждающих потоков высокого давления в канал горячего газа. Электроэрозионная обработка широко используется для обработки прямых пазов уплотнения, но подготовка электрода делает его менее эффективным для сложных форм. В данной работе представлены исследования по оптимизации метода электроэрозионного фрезерования путем анализа параметров процесса и моделирования гидродинамики промывки для определения оптимальных условий обработки. Анализ демонстрирует стабильность процесса обработки слотов сложной формы, уделяя особое внимание требованиям при производстве компонентов реактивных двигателей, а именно производительности, целостности поверхности и мониторингу процесса.

Обработка керамики - еще одно перспективное применение для электроэрозионного метода обработки. Растущий интерес к обработке карбида кремния (SiC) обусловлен его превосходными механическими свойствами, теплопроводностью, устойчивостью к коррозии и окислению. Кроме того, лопатки

турбин нового поколения изготовлены из SiC / SiC композитов с керамической матрицей, все это обуславливает актуальность обработки этого материала.

Керамика часто имеет высокое удельное электрическое сопротивление, что вызывает трудности при электрической эрозии. Например, диоксид циркония не является токопроводящим материалом. Однако именно этот вид керамики используется как покрытие лопаток турбины. Для процесса электроэрозионного сверления крайне важно иметь возможность обрабатывать электрически непроводящие покрытие лопаток турбин в деионизированной воде. Электроэрозия непроводящих материалов в настоящее время возможна только с помощью вспомогательного проводящего слоя, известного как вспомогательный электрод. Вспомогательный проводящий слой наносится на поверхность заготовки, чтобы инициировать разряды. Для продолжения эрозии области обработанной поверхности должны иметь новый проводящий слой в контакте с исходным вспомогательным проводящим слоем, что обычно достигается путем осаждения углерода путем разложения диэлектрического масла. В этой работе обновление такого проводящего слоя предлагается осуществлять путем осаждения материала электрода инструмента. Это альтернативное решение позволяет обрабатывать диэлектрические материалы в деионизированной воде, а не в масле. Осаждение материала из электрода инстумента достигается за счет эрозии в узких межэлектродных зазорах и контролируемых коротких замыканий. Показано, что обработка керамики из диоксида циркония (ZrO_2) возможна в деионизированной воде с использованием вышеописанного метода.

Для того чтобы объяснить полученные эмпирическим путем результаты, разработана модель единиченого кратера. Эта модель необходима, так как распределение энергии разряда в процессе электроэрозии до конца не изучено. Чтобы лучше понять механизм удаления материала проводится моделирование и верификация экспериментом единичного разряда в воде. В этой работе анализ методом конечных элементов одиночного разряда выполняется для расчета доли энергии, распределенной в заготовке (анод). Выполнено моделирование гидродинамики, включая эффект Марангони и с учетом терм-зависимых свойств материала. Показано, что влияние на глубину кратера термозависимых свойств материала по сравнению с постоянными свойствами составляет до 24%. Температура в моделировании варьируется от 293K до 2450K.

Другим важным аспектом являются условия промывки. Недостаточная промывка снижает эффективность обработки, поскольку материал, который остается в зазоре между электродами, повторно расплавляется при последующем разряде, и часть снова осаждается на исходном материале. В данной работе представлен анализ потока промывки с помощью высокоскоростного наблюдения и моделирования. Поведение продуктов эрозии, образование пузырей, и их движение изучается с помощью высокоскоростной камеры. Характеристики промывки и векторы скорости потока в последующем рассчитывали с помощью велосиметрии частиц. Данные измерений

используются для сравнения и проверки моделирования. Показано моделирование диэлектрического потока внутри и снаружи эродированной полости. Моделирование CFD используется для аналитического исследования влияния условий сверления на перепад давления и диэлектрический поток во время электроэрозионного сверления. Влияние промывки на скорость удаления материала и износ электрода также анализируется. В этой работе описана установка для высокоскоростного визуального анализа в микрометровом масштабе процесса электроэрозионного сверления с использованием электрода, который имеет внутренние каналы для промывки. Анализ процесса эрозии выполняется в двух положениях: во-первых, первоначальный контакт электрода с поверхностью материала и, во-вторых, эрозия внутри предварительно просверленного отверстия. Таким образом, доказано, что промывка оказывает значительное влияние в обоих положениях, и следовательно, влияет на скорость удаления материала, а эффективность промывки падает с увеличением глубины сверления.

Acknowledgements

„The centuries-long reign of the mechanical method of metal machining comes to an end. Its place is being taken by a higher organized process when a metal is treated by electrical forces. There can be no reasons that would have stopped the development of this revolutionary process breaking the present day conceptions of the machining of materials. It will govern in the future; moreover, in the nearest future". -B.A. Lazarenko, 1947 [1]

I would like to express my deep gratitude to Prof. Dr. Konrad Wegener for his patient guidance and useful critiques of this research work. Prof. Wegener showed an example of a splendid combination of scientific advisor and the head of IWF and in both guises his help has been indispensable.

I wish to acknowledge the help provided by Mr. J. Stirnimann from the first day of mine in IWF till my defense day. His willingness to give so much of his time so generously at the beginning of my work has been very much appreciated. I would also like to thank Dr. F. Kuster for valuable advice and support in my research.

This work would be impossible without GF Machining Solutions as an industrial partner and all the people who helped me in this work. I must particularly thank Mr. M. Boccadoro, Dr. R. Perez, Dr. S. Shurov, Mr. W. Dal Bò, Dr. U. Maradia and others who helped me in handling Drill 300.

I want to thank all my colleagues at IWF who have become an important part of my life for these long six years. I want especially thank the first generation of EDM group for a warm welcome, I want to thank again Dr. U. Maradia now as a colleague for his continuing help during my work, I will always remember our philosophical roof discussions. Dr. E. Weingärtner and Dr. R. Roth were both extremely kind to me and from now on will remain in my heart. The new generation of EDM group is keeping high standards and I'm looking forward to see the great achievements whey will have. The personal help of Dr. F. Barata is absolutely appreciated. I wish to acknowledge the help of my office colleagues Mr. H. Büttner and Mr. M. Wiessner, I cannot imagine my life in IWF without scientific and non-scientific discussions with them. I appreciate all the help given by Mr. C. Baumgart for our join publications and who became an unofficial part of our group. I want to acknowledge the help provided by Dr. M. Akbari and all the others with whom I'm proud to share the authorship of various publications we have made.

Assistance provided by my students has greatly appreciated especially the help of the students, whom I was directly supervising Mr. Y. Isler, Mr. K. Florio and Mr. P. Wiedenmann.

I wish to acknowledge the help provided by the workshop, namely to Mr. S. Wigger and Mr. A. Webere.

Finally, I wish to thank my family for their support and encouragement throughout my study. I want to thank my Mother for keeping me on the right track despite of my intolerable character; her efforts made me believe that everything is possible. I really appreciate the selfless decision of my wife to take a part in all the challenges I'm constantly having.

„Wo ein Wille ist, ist auch ein Weg" - Albert Einstein, 1922

Mikhail Kliuev

Zürich, 2019

Acronyms

Abbreviation	Unit	Full name
EDM		Electric Discharge Machining
ECM		Electro Chemical Machining
PFE		Plasma Flush Efficiency
CMC		Ceramic matrix composite
MRR		Material Removal Rate
RLT		Recast Layer Thickness
FEA		Finite Element Analysis
CFD		Computational Fluid Dynamics
PTV		Particle Tracking Velocimetry
PIV		Particle Image Velocimetry
TBC		Thermal Barrier Coating
CVI		Chemical Vapour Infiltration

Nomenclature

Abbreviation	Unit	Full name
f_a		the fraction of energy in the anode
f_c		the fraction of energy in the cathode
Q_p	$\mathrm{W/m^2}$	heat sources on the upper boundary
V_p	$\mathrm{m/s}$	velocity of plasma radius expansion
r_p	$\mu\mathrm{m}$	the radius of plasma (radius within which heat flux occur)
A_p	$\mu\mathrm{m^2}$	the area of the plasma (where the heat source is incident)
r_0	$\mu\mathrm{m}$	initial radius of plasma (at time t=0 of the simulation)
t_{ON}	$\mu\mathrm{s}$	discharge time
t_{off}	$\mu\mathrm{s}$	pulse interval time
I_d	A	current discharge intensity
U_d	V	discharge voltage
U_{open}	V	open voltage
Pol	$+/-$	polarity
ρ	$\mathrm{kg/m^3}$	density
C_p	$\mathrm{J/(kg \cdot K)}$	specific heat capacity at constant pressure
σ	$\mathrm{N/m^2}$	surface tension
μ	$\mathrm{Pa \cdot s}$	dynamic viscosity coefficient of the fluid
T	K	temperature
K	$\mathrm{W/(m \cdot K)}$	thermal conductivity
A	$\mathrm{m^2/s}$	thermal diffusivity

$\underline{q}$	$\mathrm{W/m^2}$	heat flux by conduction
$\underline{\dot{q}}$	$\mathrm{W/(m^3 \cdot s)}$	the rate of energy generation per unit volume
$\underline{u}$	$\mathrm{m/s}$	velocity field
x, y, z		coordinates in the Cartesian coordinate system
P	$\mathrm{kr/m^3}$	density
G	$\mathrm{m/s^2}$	gravitational constant
Γ	$\mathrm{N/(K \cdot m)}$	temperature derivative of the surface tension
$\nabla_t T$	K	tangential temperature gradient
P	Pa	pressure
T	Pa	viscous stress
$\underline{F}$	N	volume force vector (includes gravity force)
$\underline{\underline{S}}$		strain rate tensor
$\underline{\underline{I}}$		identity matrix
V	$\mathrm{m/s}$	the velocity of the fluid concerning the object
L	m	linear dimension
L	m	characteristic length
Q	$\mathrm{m^3/s}$	volumetric flow rate
R	m	radius
Δp	Pa	pressure difference
ε	μm	sand-grain roughness
H	mm	Feed of the electrode, which is set as the parameter on the EDM machine and the electrode wear is not compensated
R	$\Omega \cdot \mathrm{cm}$	volume resistivity

Contents

1. Introduction

The current chapter is starting with the history of EDM and pointing out the trends of manufacturing in EDM drilling and milling processes as well as it is introducing to the overall content of the thesis.

Eighty years ago in 1938 young research assistant of All-Union Electro-Technical Institute (Moscow) Boris Lazarenko and his wife Natalia Lazarenko discovered a new method of metals machining. They were analyzing the destruction of the collector fire of electric motors in order to mitigate it. They thought, that cooling of this thermal effect with the oil would be a right approach, but had to learn, that the destruction increased by a factor of 100. Then Lazarenkos came up with the idea to exploit this discovery for material removal processes. The inventor certificate no. 70010 was received five years later on the third of April 1943 on „A method of metals and other electro-conductive materials machining" [2]. Thus began the history of EDM. Laboratory work of B.A. Lazarenko and N. I. Lazarenko is shown in Fig. 1-1, the first electrical discharge device (it was used for removal of broken tools by EDM drilling) and the first commercial EDM machine are inFig. 1-2.

Fig. 1-1: Boris Lazarenko and Natalia Lazarenko during their work in TsNIL Elektrom, 1960 [2].

New machining technology was patented worldwide in 1946, and the first commercial EDM machine was shown by Charmilles Technologies in 1952 (Fig. 1-2). The first EDM machine with numerical control was presented by AGIE in 1969.

Fig. 1-2: From left to right: the first known electrical discharge device for removal of broken tools (early 40-ies) [2], De Eleroda D1 of Charmilles Technologies- the first commercial EDM machine (photo by Reinold Tomberg).

EDM is a non-conventional method of contactless material removal by a series of electrical discharges. Each electrical discharge creates a crater on both the anode and the cathode side. The phases of the electrical discharge are shown in Fig. 1-3. They can be presented in three main groups: preparation ignition phase; discharge phase; collapse and interval phase between discharges [3].

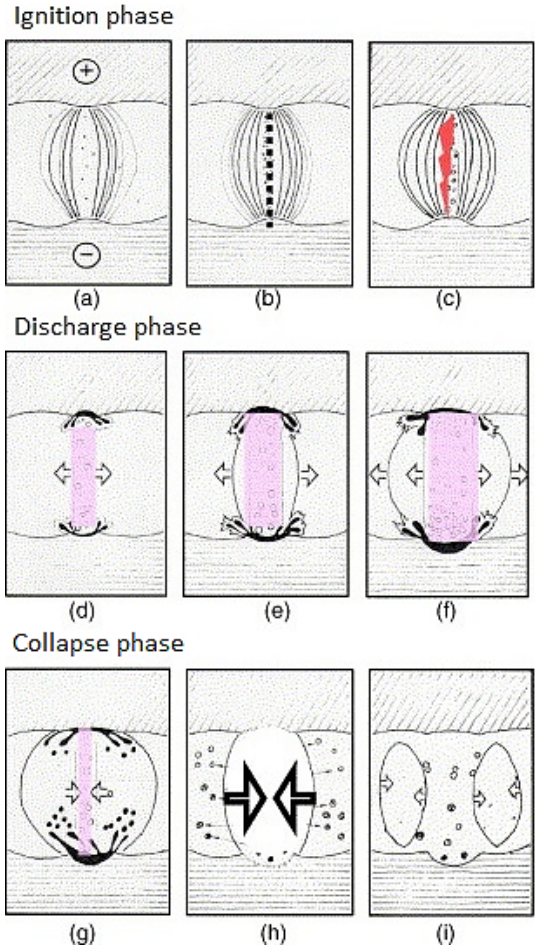

Fig. 1-3: The electrical discharge phases: ignition (a, b, c), discharge (d, e, f) and collapse (g, h, i) [3].

The discharge takes place between two electrodes: anode and cathode. When the sparks generator is switched on, the electric field is established. The breakthrough of dielectric will happen in the place with the strongest electrical field, and it is influenced by the dielectric characteristics, surfaces of the electrodes and the place of the previous discharge. The influence of one discharge location to another is shown in Fig. 1-4.

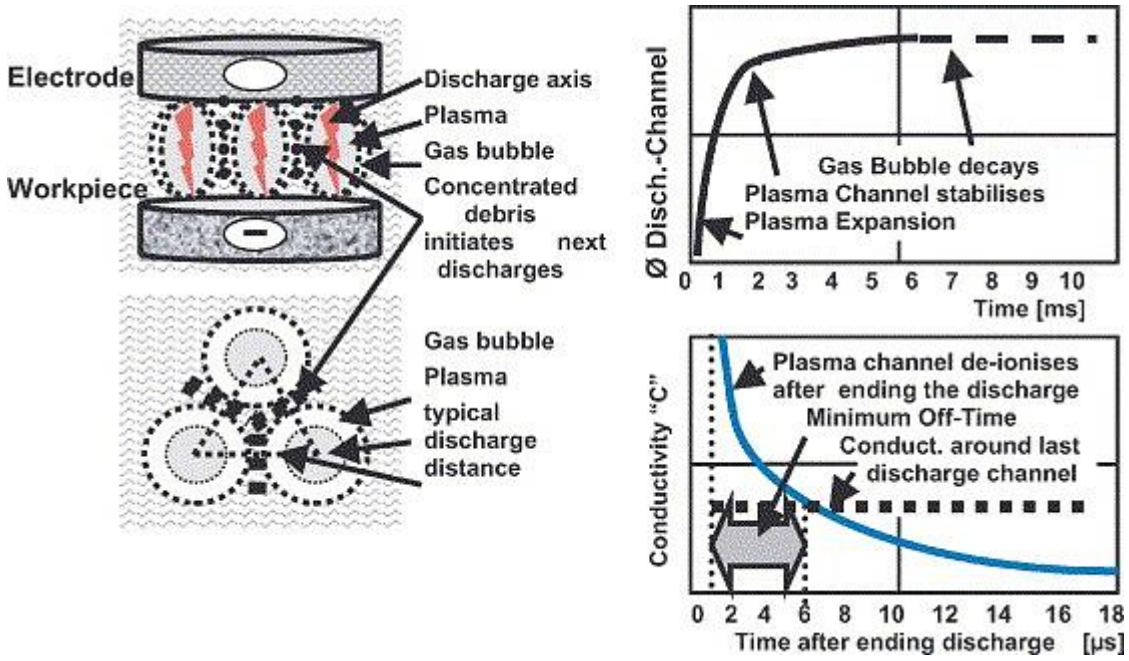

Fig. 1-4: Ignition conditions in the EDM gap are on the left, the growth of the discharge channel after ignition and deionisation after the end of the discharge are on the right .The gas bubble moves the dielectric around the discharge channel; the discharge channel is rapidly growing in the first microseconds of the discharge and then stabilizes. Several microseconds are needed to de-ionize after the end of the discharge [3].

As it is indicated [3] and as it is shown in Fig. 1-4 (left), the areas with high concentration of the debris particles are located in between the discharges since the liquid together with the debris is moved by the gas bubble.

The discharge phase starts when the ignition phase is over, and the plasma channel is created. The hot plasma vaporizes the surrounding dielectric, and the created gas bubble distributes the shock wave to the liquid. The flow of ions and electrons establishes a high-temperature region on the anode and cathode side. The discharge channel grows faster at the beginning of the discharge as it is shown in Fig. 1-4. The optimum discharge time depends on the other process parameters, the optimisation of the process is discussed in more details in Section 5.5.

The collapse phase starts when the discharge time is over. Without the pressure of discharge, the molten material ejects from both anode and cathode side creating craters on the surfaces. The interval time is also needed for deionisation of the gap as it is shown in Fig. 1-4.

Nowadays three main classes of EDM machine tools are present on the market, distinguished by their application field namely for die-sinking, drilling and wire cutting. Die-sinking machines are also often used for small hole drilling. A sharp distinction between die-sinking and drilling machines is in the flushing method. In die-sinking EDM flushing is performed by repetitive, alternating motion of electrode, whereas in drilling EDM flushing is mainly organized through internal flushing channels within the electrode. The internal flushing of the dielectric fluid is widely used in deep-hole drilling, where it is nearly the only method capable of evacuating the removed material from the hole during erosion.

At present, EDM is one of the most widely used non-conventional machining processes. Material removal in EDM is based on the thermoelectric effect caused by spark discharge in a gap between electrode and workpiece. The material is removed by melting and vaporization [4]. In EDM the electrode does not exert mechanical forces onto the workpiece, allowing the machining of thin and fragile materials. Another significant advantage is the scalability of the chip volume since the energy of spark depends on process parameters and influences chips.

A significant consideration in EDM is given to the improvement of surface quality, maximization of MRR and minimization of electrode wear. Ho and Newman [5] found these three process outputs as one of the significant areas of EDM research. Electrode coating is often used for the improvement of major process outputs.

EDM in general and EDM drilling particularly have a high potential for a turbine blade production due to its precision and its ability to machine hard-to-cut materials. The high burning temperature inside jet engines has made material selection complicated. Such materials required high strength and temperature resistance. A gas turbine engine is shown in Fig. 1-5. According to [6] the Rolls-Royce Trend 800 and General Electric GE90, which were used in Boeing 777 required to resist temperature beyond 800 °C. Presently superalloys, high creep resistant nickel-based superalloys, according to [7], are the most widely used materials for turbine blades. However, also these superalloys materials need additional internal and external cooling to survive sufficiently long under these severe conditions.

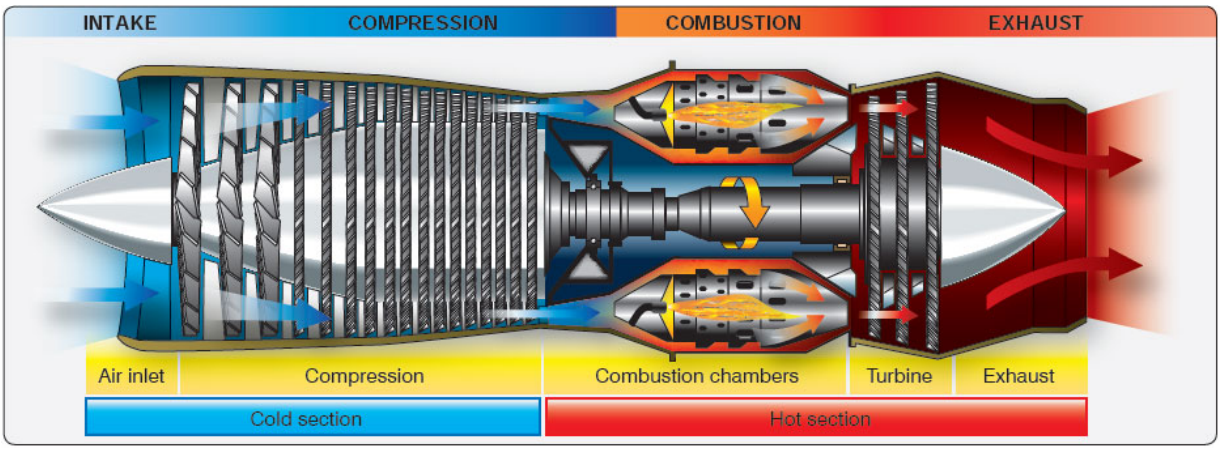

Fig. 1-5: Schematic representation of the gas turbine blade engine [8].

For internal cooling, gas or liquid passes through channels inside the blade. One of the widely used methods for external cooling is a film cooling. The turbine blade is cooled down by the air which is flowing through the cooling holes inside the blade and exits through diffusor openings in the blade wall to the outer surface of the blade as it is shown in Fig. 1-6. Each blade requires a large number of holes to cover the blade with a cooling air film evenly. Thereby the drilling of cooling holes and shaping of diffusors became one of the primary processes in turbine blade manufacturing.

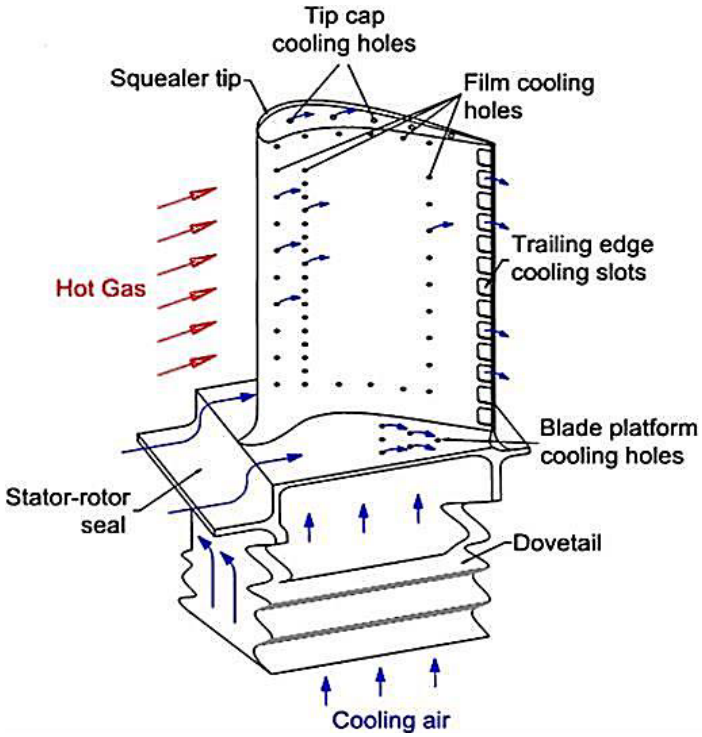

Fig. 1-6: Gas turbine blade with film cooling schematic [9].

Another method, which is often used in combination with a film cooling, is the thermal barrier coating. This coating is also used to protect a turbine blade. The coating is often made from electrically non-conducting ceramics, such as Zirconium dioxide. Therefore the erosion of these coatings and materials become crucial. The composition of the blade coating is shown in Fig. 1-7. Unfortunately for ceramics processing, the material has to be sufficiently conductive. Material resistivity higher than 100 Ω·cm is seen by [10] as a limitation for EDM processing. Nevertheless, sinking EDM and WEDM are already today widely used for ceramics [11, 12]. This work provides a new method to erode electrically non-conducting materials in deionised water in order to study the EDM drilling machining abilities in solving the complex problem of film cooling machining including diffusor shaping and the thermal barrier coating machining.

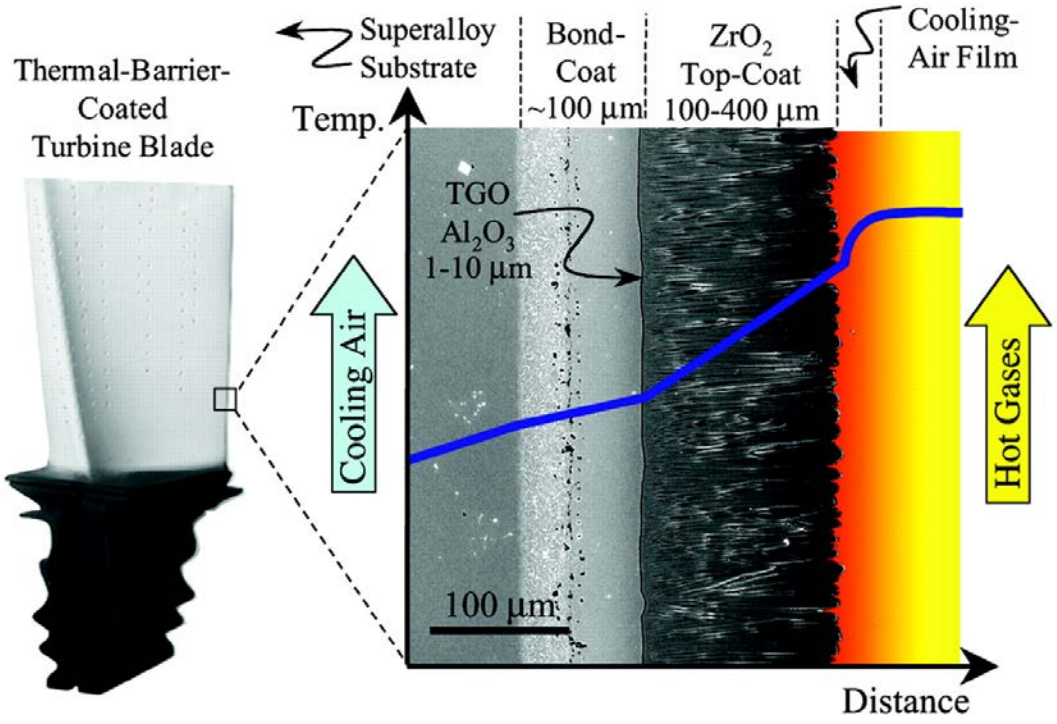

Fig. 1-7: Composition of Thermal-Barrier coated turbine blade [13].

A different application, where EDM is typically used is the machining of the seal slots. In turbomachinery, leakage of high-pressure cooling flows between adjacent turbine components (such as stator shrouds, nozzles, and diaphragms, inner shell casing components, and rotor components) into the hot gas path, also known as parasitic leakage leads to reduced efficiency or requires an increase in burning temperature [14]. Thus, turbine efficiency can be improved by reducing or eliminating leakage between the turbine components. Traditionally, leakage between turbine component junctions is treated with metallic seals positioned in the seal slots formed between the turbine components. Seal slots are deep narrow grooves made to accommodate a seal used to block or otherwise inhibit leakage through the junctions.

Most significant limitations in the EDM process are insufficient flushing and ineffective discharge energy distribution. The evacuation of the removed material is a crucial limiting factor in EDM drilling, as debris particles remaining in the gap between the tool electrode and the workpiece could reattach to the workpiece or cause ineffective discharges. In order to increase the particle evacuation rate, electrodes with internal flushing channels are used.

The maximization of the heat on the tool-electrode and minimisation on the workpiece-electrode are the optimisation goals in the EDM process. The energy of the discharge is partially used for conducting channel creation and the sustentation this energy cannot be used for material removal. Another significant part of the energy is divided the tool electrode and the workpiece; these fractions are influenced by EDM process parameters, the dielectric in the gap, materials of the anode and cathode etc.

This thesis mainly aims to develop EDM to fulfil open requirements of the aero-engine industry. One of the main goals is to be able to machine the holes, the diffusors and the seal slots on one machine, without removing the turbine blade from it. Several types of materials such as Inconel superalloys, ceramic matrix composites (CMCs), electrically conducting and non-conducting ceramics are analysed.

EDM in general and particular EDM drilling is mostly used for difficult-to-cut materials, due to another physical material removal principle in comparison to the conventional machining processes. EDM can remove materials independently of their hardness or strength. The biggest consumer of such difficult-to-cut materials and advanced alloys is the aerospace industry in which EDM is used for decades to machine aerospace components such as turbine blades and shafts, but some difficulties have still remained, which is the answer to the question, why EDM and especially EDM drilling and milling is not used predominantly or more frequently. In order to enhance manufacturing of aerospace components and for this promote EDM technology, this thesis follows the task to remove and overcome those remaining difficulties.

As it was mentioned in before EDM is used to machine film cooling holes diffusors and seal slots and wire cut EDM is used to machine dovetails of turbine blades. With the exception of the latter manufacturing task, all these applications of EDM are made by die-sinking machines and have a high potential to be manufactured by EDM drilling machine, where the standard tubular electrodes are used instead of complex and expensive die-sinking electrodes.

Intersegment sealing is used to connect turbine segments in order to prevent leakage of high-pressure cooling flows in gaps between components. Parasitic leakage of gas leads to a reduction of efficiency, which is naturally unwanted by the turbine manufacturer. Seal slots are machined on the lateral side of the blade. They hold a metal sheet/strip seal which is used to prevent the leakage through the assembly's junctions. The multiple spline seals can be positioned in intersecting slots in axial and radial directions, as it is indicated in Fig. 1-8. EDM drilling is not yet used for machining of the seal slots, but some strategies to machine slots and cavities by EDM drilling are found in the literature, more details are given in section 4.4.

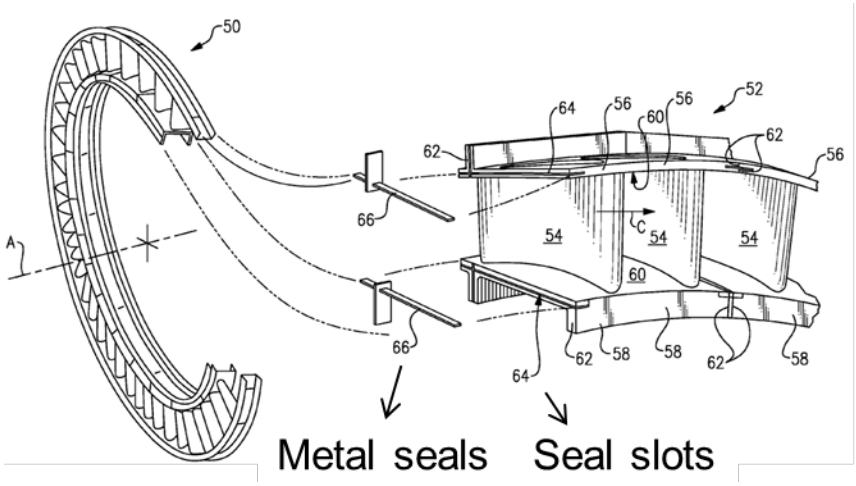

Fig. 1-8: A typical nozzle–shroud intersegment sealing arrangement [15].

Surface integrity is another important aspect, it is one of the most critical restrictions for aerospace components, for EDM such a restriction is mostly defined by the thickness of the recast layer after machining and the appearance of micro-cracks. The same limitation is usually applied for components machined by laser, when in machines diffusors in the turbine blade. The ability to use the EDM machine for diffusor milling and film cooling drilling of the blade is barely investigated, and more details about drilling and milling of aerospace components are in section 2.1.

In order to resist high temperatures, turbine blades are often coated with ceramics which produces a thermal-barrier (as it is shown in Fig. 1-7) and protects the turbine. Such a barrier is often made out zirconia dioxide ceramics which according to [10] is not possible to machine by EDM.

Fig. 1-9 shows the specific electric conductivity of different materials. Even so, the electrical resistivity of this type of ceramics is high, specific methods to machine it by EDM are found in literature, more details are in section 2.3.

All mentioned above applications to machine difficult-to-cut materials are not well analysed yet to reach the goal of EDM drilling application where it is feasible and economically beneficial.

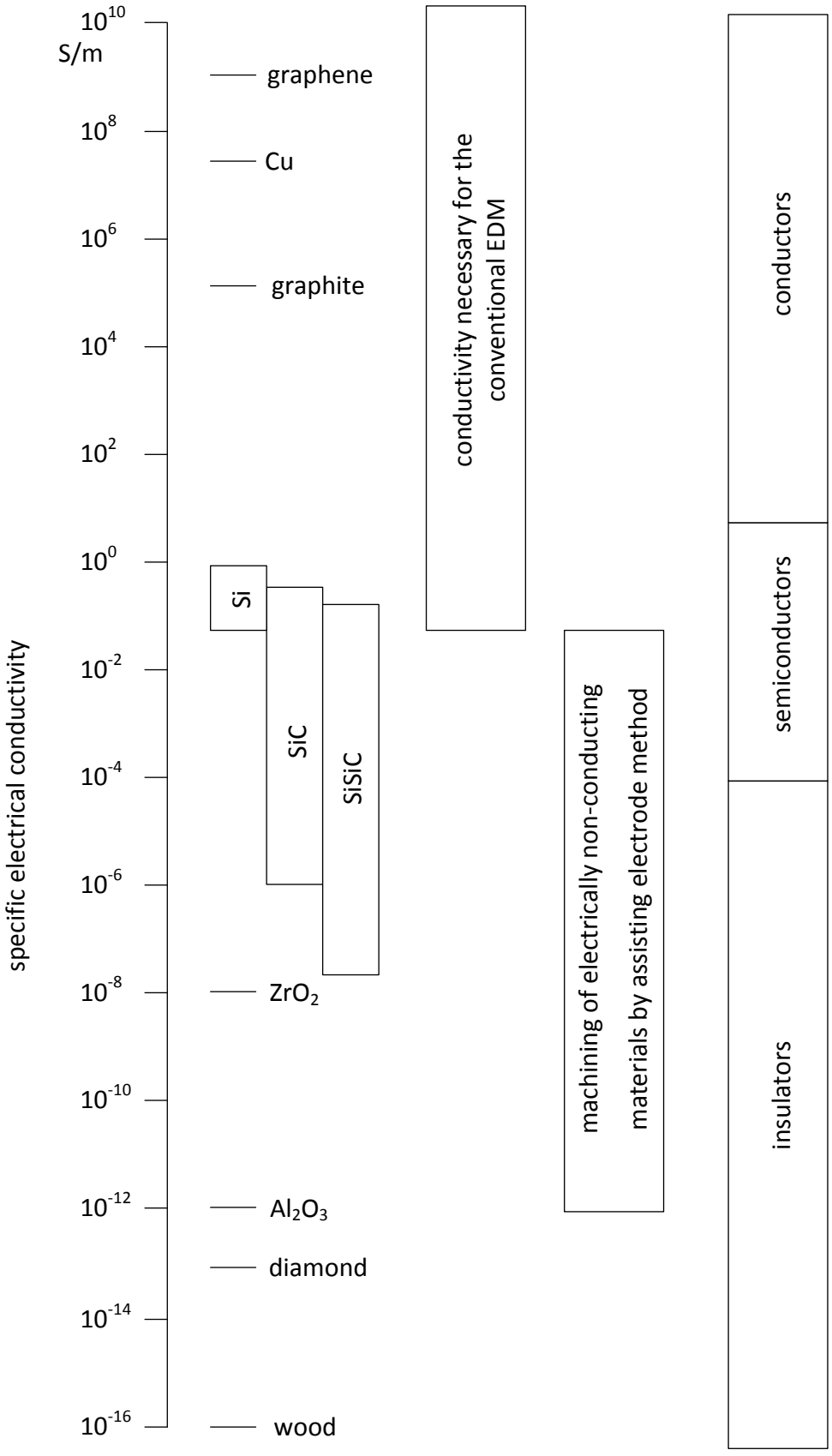

Fig. 1-9: Specific electrical conductivity of various materials and their ability to be machined by EDM, based on [10].

2. State-of-art EDM Drilling and Milling

This chapter starts with an introduction into the EDM process and includes the review of the most recent or/and most important publications about EDM drilling and milling of jet engine materials. The overview of the signal crater simulations and fluid dynamics in EDM drilling process is also given. The outcome of this chapter is the research gap of this thesis.

2.1 EDM drilling of Inconel 718

As it is described in chapter 1, the film cooling is currently the most used method to protect the turbine blade from overheating. The production of a large number of cooling holes in superalloys is a complex production task. Holes of small diameter must be drilled with an inclination angle to the turbine blade surface to provide a correct cooling flow and protect the blade from overheating. For some applications, conventional drilling and milling operations could be used. The application requires acute angles which would load the drill tip with high lateral forces leads to inaccurate machining and causes tool breakage due to bending according to [16]. Moreover, nickel-based alloys are difficult to cut with conventional processes.

Presently in aerospace industry ECM, laser and EDM drilling are used to produce microscale cooling holes in superalloy materials by [17-19]. Difficulties of conventional processes could be overcome by laser drilling, but this method had a high thermal effect on the machining surface and in the range of deep hole drilling the recast layer thickness varies between 80 µm and 100 µm according to [18] or 40 µm with different drilling conditions according to [20], also laser drilling has worse geometric accuracy the deeper the hole becomes. On the one hand, it is possible to avoid any thermal effect to the surface by ECM but cutting rate is relatively low 0.025 mm/s according to [21], which is equal to 1.2 mm^3/min. On the other hand, ECM is an environmentally unfriendly process.

The material removal rate of Inconel 718 in EDM depends on the following process parameters: electrode polarity, pulse duration, discharge current and dielectric properties. In [19, 22] it was in the range from 1.2 mg/s to 1.8 mg/s, which is equal to 9 mm^3/min to 13 mm^3/min. In [23] was shown that relative tool wear in EDM was varying between 6% and 44% and according to [24, 25] the recast layer thickness was between 2 µm and 40 µm and could be reduced by additional finishing process. The summary of the described information is presented in Table 2-1.

Table 2-1: Drilling of holes in Inconel 718, technology comparison.

Drilling technology	advantages	disadvantages
Laser drilling	- Relatively fast (85 mm3/min)	-geometric inaccuracy in deep hole drilling -relatively high recast layer (from 40 µm to 100 µm)
Electrochemical machining (ECM)	- No thermal effects	-relatively slow (1.2 mm3/min) -environmentally unfriendly
Electric discharge machining(EDM)	- Relatively fast (13 mm3/min) - Deep hole drilling is possible -environmentally friendly	-In some cases slower than laser -the surface is thermally affected

The reviewed literature indicates the high potential of EDM in comparison to other manufacturing technologies, but further investigations have to be done in order to guarantee the integrity of the machined surface (limit the heat affected zone) and at the same time increase the productivity.

2.2 Erosion of ceramics and ceramic matrix composites

Drilling of semiconductors is another potential application of EDM, especially interesting is drilling of silicon based ceramics and particularly silicon carbide, since it is not only widely used in electronics, but also became a based material of fibres and matrix of a new generation of CMC materials. SiC is hard to machine engineering ceramic material due to its excellent mechanical and physical properties, such as high thermal conductivity (360 - 490 $Wm^{-1}K^{-1}$), high melting point (3100 K) and the Vickers Hardness is between 20 and 27 GPa. Ceramic materials have good wear and corrosion resistance. The conventional processing method of SiC and SiSiC is grinding, but it is expensive and complex geometric features are difficult to produce according to [26]. Therefore WEDM and sinking EDM were proposed to process SiC by [11, 12], while EDM-drilling is not particularly analyzed in the literature.

The material removal mechanism demands detailed investigations. There are several descriptions of it. The first one is pointed out by [11] where typical material removal based on vaporization and spalling can be supplemented by oxidation and decomposition of the base material. The second one describes that material removal can also be based on cracking and fracturing besides melting or vaporization [12, 27].

The development of more fuel efficient, low emission turbine engines requires lighter and higher temperature resistant components in the hot section of an aircraft engine.

Nickel-based alloys are reaching their upper limits [28] as it is shown in Fig. 2-1. The new CMC SiC/SiC materials are coming as new, alternative materials for the further development of the turbine engines [29-31].

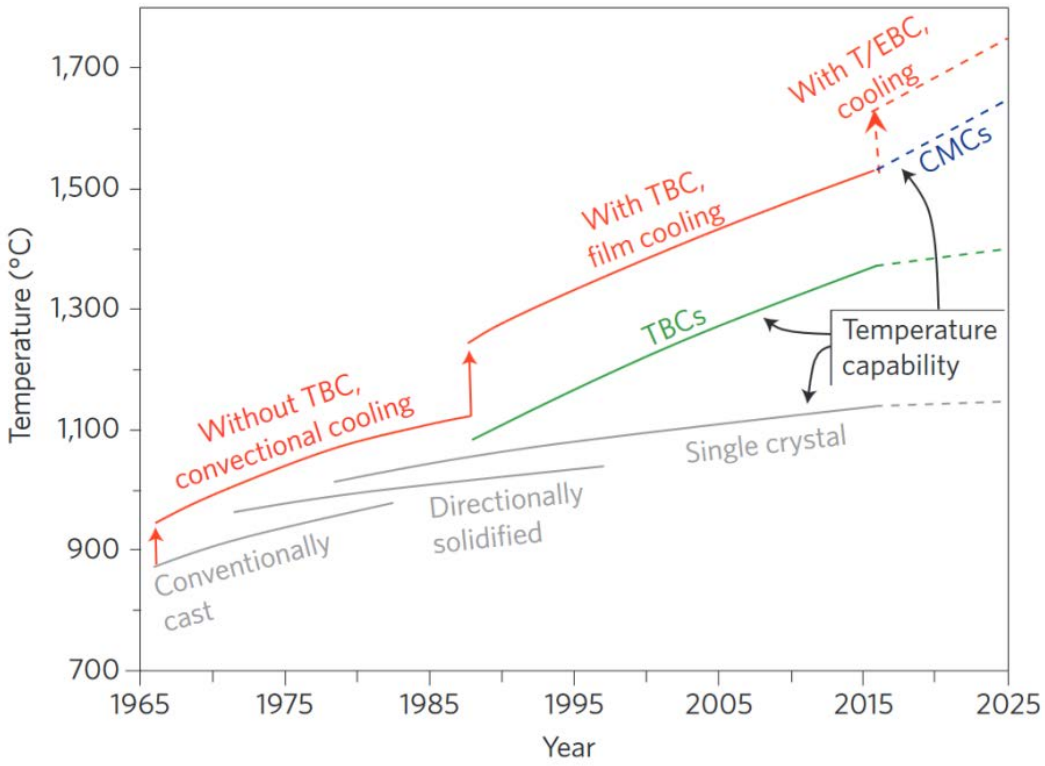

Fig. 2-1: Temperature capabilities of turbine blade materials progression and projection [30].

From all industrially used ceramics, SiC becoming the most exciting materials to analyse due to its relatively low electrical resistivity (from 100 Ω · cm) and a significant number of industrial applications, as it was mentioned above, including CMC SiC/SiC materials.

2.3 Electrically non-conductive material erosion

As it was already mentioned in the sections above, the machining of ceramics and ceramic composites has become essential for various industrial applications due to their high strength, thermal resistance, corrosion- and wear-resistance. However, these materials such as ZrO_2, Al_2O_3, Si_3N_4 typically have high electrical resistivity. Zirconia dioxide is widely used for various applications, e.g. mould protections in casting [32, 33], turbine blade protection for aerospace and energy industry [34] or medical applications [35]. However other electrically non-conducting ceramics, e.g. Al_2O_3 can also be used for thermal coating formation of turbine blades [36].

The broad application range of highly resistant ceramics is an essential reason to enhance the abilities of EDM of electrically non-conducting ceramics such as ZrO_2. Due to the fact, that ceramics and ceramic composites are extremely difficult to cut materials, EDM is a promising alternative. In fact, EDM drilling is used to machine cooling holes in turbine

blades. However, ceramic coated turbine blades often necessitate alternative methods such as laser drilling or a combination of Laser and EDM drilling. Furthermore, by nearly forceless influence to the workpiece EDM is a well-known method for machining of brittle and hard materials, although very low electrical resistivity can be a limiting factor for EDM, such as for machining of Al_2O_3.

EDM can be applied for machining of electrically non-conducting materials using assisting or sacrificial electrodes as described by Mohri [37] and tested in sinking EDM and WEDM. In such method, while an initial conductive layer is needed to initiate discharges between a conductive and the coated electrically non-conducting electrode, the conductive layer is worn away in the discharge region, as it is shown in Fig. 2-2. In order to continue the erosion process, such a conductive layer must be regenerated continuously. Typically, it is generated on the workpiece surface based on carbonaceous material decomposed from the surrounding hydrocarbon-based dielectric fluid. Furthermore, electrode polarity and electrical pulse shape play a crucial role to generate such layer on the workpiece surface. The assisting electrode method that was used for EDM milling of electrically non-conductive zirconia ceramics was investigated by Schubert [38], micro-drilling was shown by Schubert and Zeidler [39]. They found that the tool electrode rotation positively influences machining speed and leads to reduced electrode wear. The machining of grooves was shown by Schubert and Zeidler [38]. Gotoh [40] showed wire EDM milling of ZrO_2 using the assisting electrode method, while Guo [41] investigated in wire-EDM of Si_3N_4. He found that the conductive layer can be adjusted by the electrical discharge waveform control. Sabur [42] and Chen [43] made a parameter study of ZrO_2. Ojha [44] studied the process parameters of electrically non-conductive SiC machining.

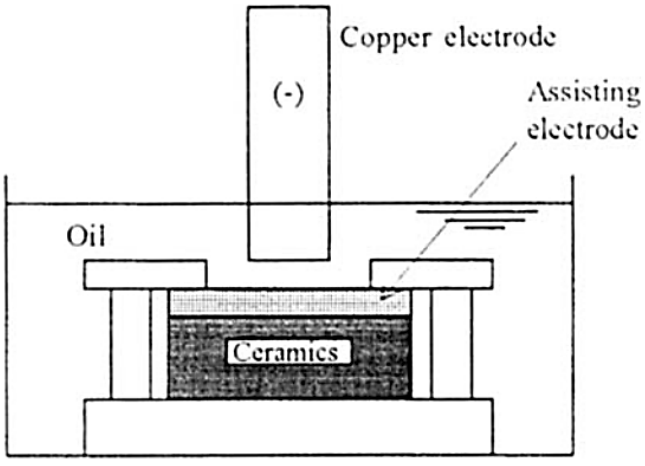

Fig. 2-2: Schematic illustration of EDM for insulating ceramics machining with assisting electrode [37].

Machining of ceramic composites based on ZrO_2 (ZrO2–TiN grade 66/34 vol.% composition) and Al_2O_3 (Al3O2–TiC0.7N0.3 grade 60/40 vol.% composition) were shown by Ferraris [45]. These ceramic composites were conductive, and the process behaviour was

similar to the EDM of steel. However, electrode wear was four times lower compared to steel. Melk [46] investigated the material removal mechanism of zirconia-based nanocomposites and found that additions of CNTs in the zirconia matrix significantly increases the specific electric conductivity and thus made the composite suitable for EDM.

Electrochemical aspects of electrically non-conductive and conductive ceramics were investigated by Wüthrich et al. [47] and by Lauwers et al. [11] respectively. Electrochemical discharges take place with both electrically conductive and non-conductive ceramics. Removal mechanism combines thermal and chemical components, but the thermal components were dominating.

Some material properties of ZrO_2 are presented in Table 2-2 in comparison to silicon carbide SiC, where the latter is machined by the author [48] using assisting electrode method. It is seen that ZrO_2 has a high specific resistivity, which makes it difficult to machine by EDM. Also, Zirconia has a much lower thermal conductivity which creates thermal energy localization, and on the other hand, the coefficient of thermal expansion is higher than that of SiC which results in the spalling effect as shown [48].

Brittle and hard materials with very low electrical conductivity such as SiC or ZrO_2 have different material removal mechanism compared to metals. Cracking and spalling along with melting and evaporation were reported as the origin of material removal by Lauwers et al. [11] for ZrO_2 and for SiC and SiSiC by Kliuev et al. [48]. Other mechanisms such as oxidation and dissolution were investigated by Lauwers et al. [11] and Wüthrich et al. [47].

Table 2-2 Relevant material properties of ZrO_2 and SiC.

Property	Unit	SiC	ZrO_2
k	$W/(m \cdot K)$	360-490	1.7-2.7
Melting point	K	3103	2823-2988
R	$\Omega \cdot cm$	10^2-10^6	10^9-10^{14}
ρ	$g \cdot cm^3$	3.21	4.3-5.6
Hardness	Kg/mm^2	2800	1600
Thermal exp.	$10^{-6}K^{-1}$	2.77-4.0	2.3-12.2

For SiC and SiSiC machining, the optimum technology for both quality and speed erosion was found [48] with the negative polarity of tool electrode, low pulse duration (1µs) and high ignition voltage (250V). Here, the high ignition voltage facilitates electric breakdown between highly electrically resistant materials, while low pulse duration enhances the spalling effect.

Summarising all mentioned above, the absence of the method to machine electrically non-conducting materials in deionised water is one of the most significant limitations of

EDM. Overcoming this limitation is a key to increase EDM abilities in machining electrically non-conducting coatings of the turbine blades.

2.4 Layer-by-layer milling, diffusor shaping and Seal slots machining

EDM milling is a method to machine complex cavities by using rotary standard shape cylindrical electrode. The method was first shown by Yu [49]. The uniform wear strategy is realised by using layer-by-layer machining on the micrometre scale. The method was further developed [50, 51] and schematically is shown in Fig. 2-3.

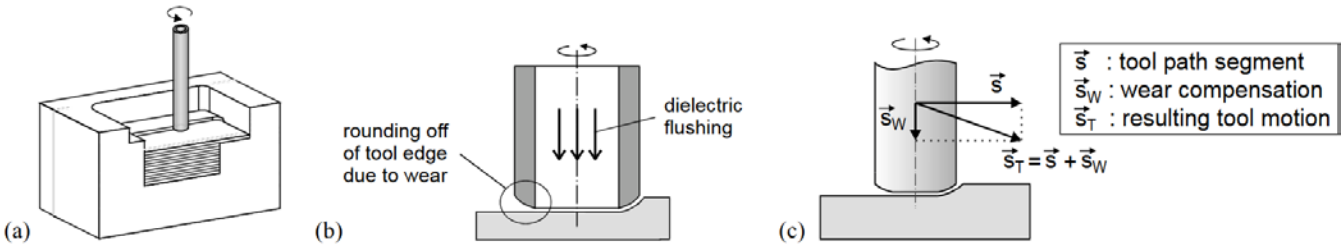

Fig. 2-3: Layer-by-layer milling, (a) schematic representation of the method, (b) rounding of the tool edge, (c) tool path direction and wear compensation vector [50].

Multiple spline seals are often positioned in axial and radial directions, in intersecting slots to reduce leakage. An example of a complexly shaped seal slot in nozzle guide vanes is presented in Fig. 2-4.

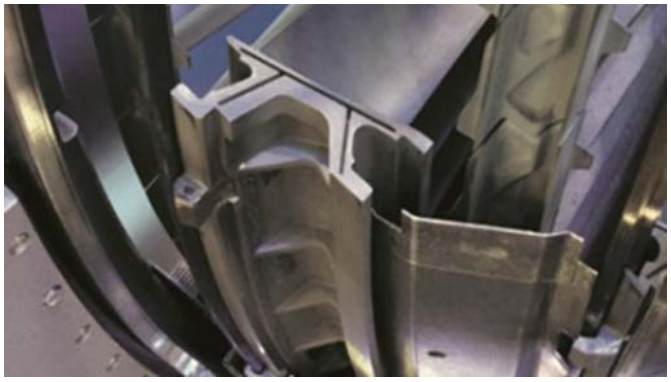

Fig. 2-4: Seal slot with a complex shape in nozzle guide vanes [52].

Machining of seal slots, pockets and grooves apart from the drilling of cooling holes are the main areas for application of Electrical discharge machining (EDM) in turbine manufacture [53], due to the apparent advantages of EDM over other more conventional processes. In EDM productivity is not limited by the hardness or strength of the workpiece and complex features, or high aspect ratio holes and cavities can be readily machined.

Due to the required narrow, deep geometry in difficult-to-cut materials, research in seal slot machining using die-sinking EDM mainly focuses on machining efficiency, tooling and surface integrity for different alloys such as Ti–6Al–4V [54], nickel-based superalloys [55] and

γ-TiAl [56]. Regarding machining efficiency, poor flushing or debris evacuation from high aspect ratio grooves deteriorate the machining efficiency. Some methods have been analysed for better debris evacuation such as ultrasonic assisted process [57] or special electrode designs [58]. For tooling, mainly graphite rib electrodes are used, where the type of graphite for high productivity is analysed [59] and due to electrode wear, automated dressing of electrodes is analysed [60].

In practice, some common requirements from most engine manufacturers regarding seal slot machining are high productivity, surface integrity, automation and quality traceability. These are often achieved by modern die-sinking machines, where using dedicated fixtures and process control, seal slots are machined simultaneously in multiple workpieces to overcomes the lower material removal rate (MRR) of the EDM process. While surface integrity protocols for EDM of aerospace components are confidential from engine manufacturers, generally, surface cracks extending beyond the re-solidified layer are unacceptable, whereas re-solidified layer thickness acceptance may vary from 10 µm to 50 µm and the typical geometric accuracy is ±50 µm. In terms of tooling, for complexly shaped slots, rib electrodes are arranged using fixtures or electrodes can be machined, requiring additional setup time and costs.

EDM milling is usually considered to be the domain of die-sinking machines, but modern CNC EDM drilling machines can fulfil all requirements of EDM milling process. Moreover, the internal flushing in EDM drilling can have high applicability in EDM milling. Furthermore, combining EDM drilling and milling opens a way to machine a film cooling and seal slots on one EDM machine without reclamping.

2.5 Electrode protection

Electrode protection is often used in wire cutting EDM. According to [61], electrode coating is applied to the electrode, for instance, Cu-ZrB2 composite coating is able to improve the electrode wear resistance. Diamond coating in micro-EDM is analyzed by Uhlmann et al. [62], where it was found that smaller discharge craters on the tool occur with a nanocrystalline coating as compared to microcrystalline coating. Mohri et al. [37] used graphite deposition on the workpiece to increase the electrical conductivity and machine highly insulating ceramics. According to [63], with polycrystalline diamond composite electrode material for EDM, it is possible to achieve from 20 to 50 times lower wear in comparison with Cu-W electrode and in case of tungsten carbide workpiece (WP) material. Zero wear can be realized in the case of SKD11 steel WP at short and long pulse duration. Therefore electrode coating is used in EDM in order to improve some of the major process outputs.

Graphene with its superior properties shows potential for a number of application fields. graphene is a single layer thickness pure carbon; atoms of carbon are bonded in a hexagonal honeycomb lattice. According to [64], graphene is the lightest and thinnest known material;

it is also the strongest discovered compound. Graphene also has very high electrical and thermal conductivity.

Due to some similarities of EDM drilling and wire cutting EDM, for instance, similar discharge pulses, ability to have refined electrode geometry without its changing and so on, the electrode protection can have a big potential for EDM drilling, and it has to be analysed.

2.6 Single crater simulations

Understanding of EDM drilling or EDM milling process is impossible without an understanding of single discharge. Creation and movements of ions and electrons inside the plasma channel allows the current to pass through the electrode and through the workpiece. The bombardment of ions, together with the highly concentrated the electricity flow and the conduction of heat from plasma to the electrodes, heats the material on both the anode and cathode side. During the discharge time, a bubble of vapour is created around the plasma due to the high temperature. Moreover, the plasma is enlarging during the discharge. In the EDM drilling configuration, where the tool is the cathode, and the workpiece is the anode, the discharge duration is relatively short, and water is used as a dielectric. The heat flux on the anode is generally higher than on the cathode. Therefore MRR is maximized, and wear of the electrode is minimized. Finally, the discharge is interrupted in order to keep the optimum process conditions, when the discharge ends the plasma collapses, and the material is then ejected. The rapid cooling leads to the formation of spherical debris, a typical shape that is obtained when a liquid is rapidly solidified.

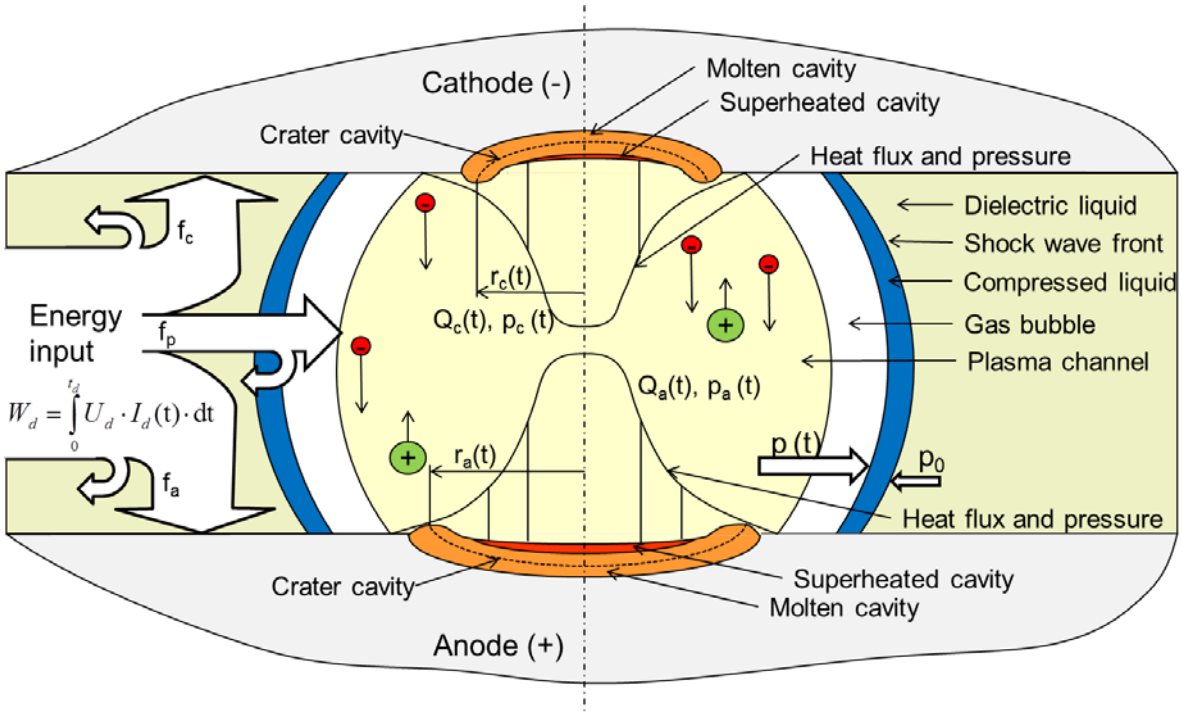

Fig. 2-5: Energy balance, crater formation, heat flux and pressure distribution during single discharge in EDM

Fig. 2-5 shows the main phenomena involved in the single discharge and crater formation, as well as the growing of a rim around the crater during the discharge, due to the high pressure applied by the plasma on the melt pool, in some cases, the rims can be generated during the plasma collapse itself.

Several heat models and simulations of EDM have been proposed in the literature. The earliest known analytically solved heat model is presented by Van Dijck et al. in 1971 [65-67], while the most recent models used CFD analysis. On the one hand for the discharges longer than 5 µs, which is the case in the current work, the heating of material is considered as the most significant effect for material removal. On the other hand, for the discharges shorter than 5 µs, the electro-mechanical principle of material removal is considered to be most significant by Singh et al. [68]. The electro-mechanical material removal principle was also found [69], to be one of the crucial factors for the machining of brittle materials.

Jilani et al. [70-72], have first implemented a growing heat source to take into account the expansion of the plasma during the discharge. One of the most influential heat models are made by Dibitonto et al. [73-75]: they laid the basis for the assumption that material removed mainly due to the heating and super-heating effect and showed a complete experimental validation. Dibitonto assumed that during the discharge material is heated above the melting temperature and even above the vaporization point, but the change of phase between liquid and gas does not happen because of the high pressure applied by plasma (superheating of the melt pool). Vaporization is considered to account for less than 1-2% of the total material removal. Dibitonto [73] points out that the result of f_c (fraction of energy on the cathode side) obtained for 12.8 A of the discharge current. Dibitonto pointed out that f_c can be extended without significant errors to the rest of the range considered for discharge current. This lays the foundation for assuming f_c constant in different discharge conditions and at the same time proves the relevance of f_c value estimation for simulation.

The expansion of the heat source represents the experimentally observed plasma expansion. Most of the works considered a Gaussian heat flux distribution with a constant heat source. Yeo et al. [76] proved that the results of the heating models could be significantly improved by taking into account the fitted cathode fraction f_c of energy and considering an expanding disk heat source according to

$$r_p = 0.788\, t_{ON}^{3/4} \tag{2-1}$$

which is already proposed in work by Patel et al. [74] and where r_p is a plasma radius and t_{ON} is a pulse duration.

The estimation of energy absorbed by cathode (f_c) and anode (f_a) is the key factor for model validation, but these values can change depending on several parameters, including electrode and workpiece material, dielectric fluid, type of discharge, discharge time

duration, voltage, current etc. The estimation is usually performed through heat modelling and f_c fitting in order to find an agreement between model and experiment.

Dibitonto performed the first estimation [73]: his results are f_c=0.18 and f_a=0.08. Yeo et al. [77] estimated f_a=0.39 and f_c=0.14. The difference between the models can be explained by very short pulse time (micro-EDM, capacity discharges are shorter than 1 µs) [77], while Dibitonto considers longer EDM pulses type provided by a commercially available die sinking EDM machine (a minimum discharge duration of 5.6 µs was considered). Finally, Rajendran et al. [78] conducted a similar investigation and found a value of f_c=0.06 (f_a was not calculated).

The only found attempts to measure more directly the values of these fractions are given by Kunieda et al. [79] and Xia et al. [80], where temperature measurements are used to define the fraction of energy. Their results are f_c=0.34 and f_a=0.48.

One of the first FEA of EDM single discharge is given by Das [81], who performed a thermo-mechanical analysis. The main outcomes were residual stresses, deformation and final microstructure. The authors neglected the fluid flow influence on the heat distribution, and the material is considered solid, which, above the melting temperature, has extremely low yield stress and the Young's Modulus (10% of the original value or less). f_c is considered constant, and it is assumed equal to the result of Dibitonto [73] (f_c=0.18). Following the same work of Dibitonto Das also defined the velocity of the plasma expansion (i.e. of the heat source) and a Gaussian distribution of the heat source. However, they removed all material which has the temperature above the melting point, assuming a plasma flush efficiency (PFE) of 100%.

More recently numerical modelling was extended by Weingarten [82], who tackled the numerical difficulties of using non-constant material properties in Finite Difference Method (FDM). The result shows that temperature-dependent material properties have a relevant impact on the accuracy of the simulation.

Tao et al. [83] simulate the effect of a plasma collapse; their assumption was that material removal occurs during the plasma collapse. The method of Tao tracks the interface between workpiece and dielectric. The melt pool, in this case, is previously calculated with a transient heat analysis. In the same work, the authors supposed that the inaccuracy in the simulation is mainly due to the simplification of the plasma-heating phase. Tao et al. also measured the recast layer and concluded that the plasma heating simulation, including only the thermal effects and using a specific value of f_a=0.39, is not able to accurately define the shape of the melt pool, especially regarding the depth, which is in that work always larger than the experimental values.

Mujumdar et al. [84] presented a plasma model, which receives as input the material properties of the anode, cathode and dielectric, inter-electrode gap distance and electrical

field. With these inputs, the model is able to estimate the composition, pressure, temperature and radius of the plasma and the heat fluxes to the electrodes. The outputs of the plasma model are the inputs for the subsequent plasma heating simulation, reported [85]. In this paper, the simulation included the Marangoni effect and fluid flow, which are shown to have a relevant influence on the crater shape. The maximum velocity of the fluid flow in the melt pool was estimated to be 130 m/s. The result is then validated with a single crater experiment. Mujumdar also considers the material removal during the plasma collapse. However, constant material properties were used for each phase, which have been already proven by Weingaertner [82] to be only a rough approximation.

The comparison of the most valuable crater simulation models is given in Table 2-3.

Summary of the observed single crater models:

- Heat boundary conditions: all the models assume a two-dimensional disk heat source on the upper surface, except for Dibitonto's model. Most of the works considered Gaussian heat distribution.
- The fraction of discharge energy f_c: considered constant during the discharge and depends on discharge conditions.
- The radius of the heat source is constant, or it is expanding with time which is similar to the experimentally observed plasma expansion.
- The importance of fluid flow analysis was investigated by Mujumdar et al. [85], who identified the Marangoni effect as an important factor for convective heat transfer in the molten pool, being able to modify the crater shape consistently.

Although EDM simulations were stated more than 50 years ago, some open questions remained. The amount of energy fraction depends on the process parameters, but this dependency is not clearly explained in the observed literature. Moreover, numerical complexity has not allowed in the past to combine temperature dependent material properties with growing heat source, phase transformation and Marangoni effect. Finally, PFE is almost all the time considered 100 % without taking into account the recast layer. All mentioned here is required to have a better understanding of the EDM process.

Table 2-3: Comparison of different single crater numerical models from 1971 to 2015

	Van Dijck's model [65]	DiBitonto's model [73, 74]	Das's model [81]	Yeo's model [77]	Weingaertner's model [82]	Tao's model [83]	Mujumdar's model [85]
Thermophysical properties of the material	Constant	Average (whole temperature range)	Temp. dependent	Average (whole temperature range)	Temp. dependent	Constant for the liquid and solid phase	Constant for each phase
Plasma flush efficiency (PFE)	100%	<100%, recast layer considered	2%-96%	Included in the fraction of energy	PFE not considered	<100%, recast layer considered	100%
Latent heat	melting	neglected	Melting, vaporization	neglected	Melting, vaporization	Melting, vaporization	melting
Fraction of energy	$F = 0.5$	$F_c = 0.18$	$F_c = 0.18$ [73]	$\mathrm{F_a} = 0.39$ $\mathrm{F_c} = 0.14$	$\mathrm{F_c} = 0.35$ [86]	$\mathrm{F_a} = 0.39$	Calculated from plasma
Heat flux distribution	Uniform heat flux	Point heat source	Gaussian heat flux	Uniform heat flux equivalent to Gaussian	Uniform heat flux	Gaussian heat flux	Gaussian heat flux
Dimension of the heat source	disk heat source	Point	disk heat source	disk heat source	disk heat source	disk heat source	disk heat source
Expansion of the heat flux	Constant heat flux	The plasma radius remains small during the discharge	Constant heat flux	Experimentally defined expanding heat source	Heat source expands from 5 µm to 80 µm	$\mathrm{r_c} = 0.788\ \mathrm{t_d^{3/4}}$	Time-dependent heat source radius (from plasma model)
CFD for liquid phase	Not considered	Not considered	Not considered	Not considered	Not considered	heat conduction and fluid dynamics separately calc.	Calculated simultaneously

PFE (plasma flush efficiency) is the percentage of molten material is ejected at the end of the discharge or during the plasma collapse

2.7 Fluid dynamics in electrode flushing channel

Nearly all electrodes used for EDM drilling have internal flushing channels. Especially in deep hole drilling flushing of dielectric fluid through those channels is practically the only one effective method to evacuate removed material.

One of the most significant limitations during deep hole drilling is caused by side electrode wear induced by lateral sparks, which is also promoting electrode vibration. Vibrations and therefore wear increase with the aspect ratio between hole depth and electrode diameter.

Insufficient flushing increases the probability of lateral sparks and slows down the removed material evacuation. The flushing efficiency depends on electrode length and geometry, hole depth and initial pressure.

Multi-channel electrodes are mainly used for blind-hole drilling, whereas single-channel electrodes cannot be used because of spike creation in the centre of the hole. Various internal channel configurations of multi-channel electrodes exist depending on the diameter and electrode manufacturer.

Depending on the application dielectric could be streamed through single or multi-channel electrodes. Comparison between single-channel and multi-channel electrodes was made by Yilmaz [22] and by Bozdana [87]. In these works, different channel configurations were used. This fact leads Yilmaz and Bozdana to contradictory results. Bozdana showed higher material removal rate (MRR) with a multi-channel electrode, while Yilmaz considered higher MRR with the single-channel electrode. Yilmaz and Bozdana were using different channel configurations this fact influence there MRR results. This is the confirmation of the significance of multi-channel configuration analysis and its influence on the process outputs. Different multi-channel electrode configurations are shown in Fig. 2-6. The design of the cross section highly influences the flow conditions as the flow regime, and the pressure drop can rise and these factors the influence flushing.

Fig. 2-6: The multi-channel electrodes configuration comparison [22, 87, 88]. Type 1 is used for flow simulation, this type is recommended by GF Machining Solutions, Agie Charmilles SA machine tool manufacturer for Drill 300.

Cylindrical electrodes (without flushing channels) are widely used in die-sinking, where flushing originates in periodic electrode movement. Special electrode types, e.g. helical electrodes can be used. Plasa [89] showed that the use of helical electrodes is reasonable for deep hole machining in Ti6Al4V. However helical electrodes are expensive in production.

The largest number of CFD simulations in EDM is performed for die-sinking processes in oil dielectric. Eroded particle and bubble distribution were studied by Pontelandolfo [90], where he was assuming a homogeneous distribution of the eroded material in a dielectric. He found that bubbles are increasing the evacuation rate of the removed material. Wang and Han [91] were researching bubbles and debris movement. They found out that electrode jump height (double amplitude of electrode movement) is influencing the amount of clean oil in the electrode-workpiece gap. Therefore the electrode jump speed is influencing removed material distribution.

Maradia [92] high-speed camera observation of bubbles. He investigated bubble dynamics in micro-/meso-/macro scale. In micro-scale, the discharge forces the gas bubble to move, while in meso-/macro scale the bubble remains in the discharge region.

The two-phase (liquid-solid) flow in the gap was investigated by Wang [93] for drilling EDM. Deionized water was used as a dielectric. Wang showed the drop of dielectric pressure of 15% along the depth of 25 mm and proved the influence of the hole depth to the pressure drop. Wang also showed higher concentrations of eroded material in the corner of the machined hole.

Hass [94] used CFD simulations of the dielectric flow from the nozzle in wire cut EDM in order to improve debris evacuation rate and therefore increase the machining speed. By better flushing conditions Hass also increased the cooling effect of the wire by 20% and therefore, the probability of wire breakage was reduced. Okada [95] used CFD simulations for the flow analysis in wire cutting machining and verified the simulation results with Particle Image Velocimetry (PIV) of high-speed camera images.

A better understanding of flushing flow in EDM can help to increase the MRR of EDM drilling process significantly, especially in deep and narrow cavities, such as deep holes in EDM drilling. However, the flushing through the internal electrode channels, which are often used for this purpose, is barely investigated.

One of the most significant advantages of EDM drilling process to die-sinking is dielectric flushing through the electrodes internal channels, but the efficiency of flushing and the pressure drop into those channels are barely investigated in the observed literature.

2.8 Research gap

The aim of this work is to enlarge the potential of EDM drilling/milling to machine aerospace materials and investigate new applications of EDM in this field. As it is indicated in section 2.1, nickel-based alloys are the most widely applied materials in the hot section of gas turbines. The biggest limitations of EDM application are the surface integrity after machining and low MRR of the EDM process. The recast layer thickness is one of the main criteria for surface integrity. Therefore the minimization of the recast layer thickness and at the same time maximizing also the material removal rate (MRR) is required for EDM to become the primary technology of Inconel machining. Furthermore, the ability to combine

EDM drilling and EDM milling for diffusors shaping and film cooling holes drilling using one machine and without re-clamping of WP is essential, but not investigated in the observed literature.

A new generation of turbine blade and vane materials are CMCs, as it is shown in section 2.2; the most widely used combination consists of silicon-based fibres embedded in the silicon matrix. In order to understand EDM drilling capabilities of the new generation of SiC/SiC CMC materials, the material removal mechanism of SiC and SiSiC ceramics need to be analyzed. For further development of EDM machines the research must be aimed at investigation how to increase the material removal rate (MRR), reduce relative tool wear as well as enhancing surface integrity through the reduction of the recast layer.

In order to protect the blade of a gas turbine from overheating thermal protection coatings of the blade are used. As reported in section 2.3 this coating is often made out of electrically non-conductive ceramics. It is evident that most of the research on electrically non-conductive material erosion relies on hydrocarbon oil as a dielectric to regenerate the assisting electrode layer. However, the achievable MRR in deionised water is higher, as reported by [96]. In addition, water is much cheaper than oil and more environmentally friendly. In terms of particular industrial application, turbine blades with thermal barrier coating (TBC) often employ ZrO_2 based coating, which limits the use of EDM drilling. Overcoming the limitation of EDM drilling of electrically non-conductive materials in deionised water is a key to increase EDM abilities in machining the coatings of the turbine blades.

Another potential application of EDM machines is seal slot machining, as it is indicated in chapter 1. In order to support the trend of increasing turbine efficiency through better sealing by the inclusion of complexly shaped seals and ecological machining an alternative method for seal slot machining in high-temperature alloys by combining EDM drilling for roughing and EDM milling for finishing operation must be investigated. The new method must be focused on productivity and surface integrity, which are of primary interest for turbomachinery component manufacturing.

Further development of EDM machines is likely impossible without a deeper understanding of electrical discharge phenomena, energy fraction between anode and cathode and process parameters influence on it. The further research must be focused on the development of a single crater simulation which takes into account temperature-dependent material properties, growing heat source, phase transformation and Marangoni effect, as it is described in section 2.6. The same simulation is used for fitting the value of energy fraction going into the cathode, plasma radius, velocity and plasma initial radius. In fact, fitting of these values can be interesting in order to tackle the difficulties in plasma modelling and the high approximations of its results. Finally, the simulation must be verified with experiments with different process parameters, in order to estimate their influence on the energy fraction f_c.

Finally, as it is shown in section 2.7, the flushing efficiency through internal electrode channels in EDM drilling is also barely investigated. Flushing is especially important for deep holes and for complex geometries of electrode flushing channels. Existing CFD simulations in EDM drilling are not verified by PIV or PTV calculation. PIV or PTV calculation is nearly the only way to confirm the distribution of the dielectric, but existing CFD simulations in EDM drilling are not verified by these methods. Therefore the simulations must be verified by the experiment setup in order to track the eroded particle movement in around 50 µm gap between electrode and WP.

Fig. 2-7 indicates the development of high-temperature resistant aerospace materials and shows methods used to protect parts in the hot section of jet engine from overheating. Machining of indicated materials in required conditions of aerospace industry is crucial for further development of EDM drilling and milling technologies.

Chapter 3 focuses on the EDM drilling of hard to machine materials. A part of this chapter is given to the analysis of EDM process parameters for Inconel 718 machining. MRR, electrode wear and RLT are analyzed, and regression models are given to describe process parameter influence. Another part of this chapter is drilling of semi-conductive and nonconductive ceramics. The process mechanism of ceramic machining is described, and a new method of non-conducting materials erosion is proposed.

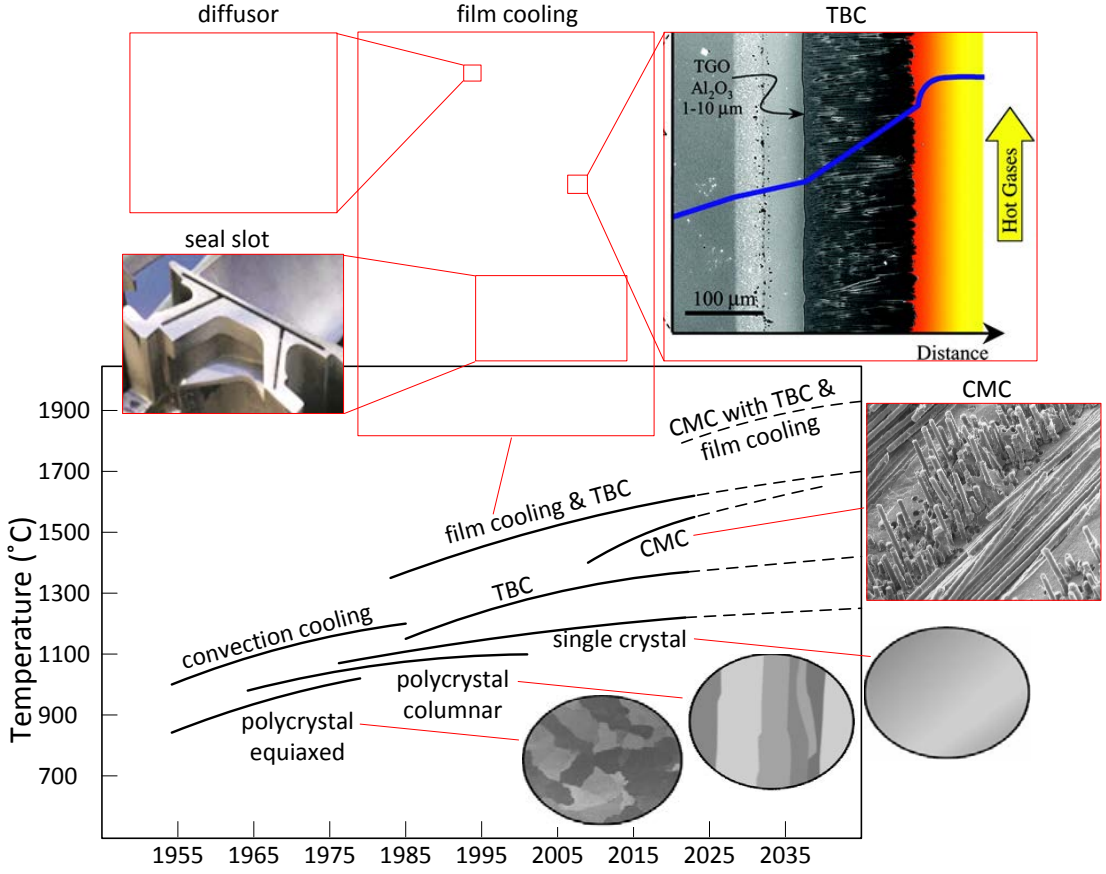

Fig. 2-7: Turbine blade material development, their temperature capability growth over decades and relevant improvements [9, 13, 15, 30, 52, 97-99].

In chapter 4 the new methods of EDM milling are proposed using an EDM drilling machine. Milling of diffusors in Inconel 718 is described, the integrity of the machined surface is investigated. Another part of this chapter describes the new method of turbine blade seal slot machining in aerospace materials, such as Inconel 718, Titanium alloy (γ-TiAl) and CMC (SiC-SiC).

Chapter 5 deals with simulations, which are relevant for this work, and includes single crater simulation and dielectric flushing simulation. Single crater simulations are aimed to explain the energy balance during the electrical discharge and influence of process parameters. Flushing simulations explain the dielectric flow in different EDM conditions, simulations are verified by PTV.

Chapter 6 describes flushing during EDM drilling processes. The influence of the electrode length and flushing channel configuration is investigated. Flushing conditions during slot machining are investigated and finally, flushing during the drilling process is measured by particle tracking velocimetry (PTV) and particle image velocimetry (PIV).

Chapter 7 summarizes the information, which is presented in this thesis. This chapter provides the results of EDM process analysis, comparison of the experiments with the simulations, taking into account the specificity of internal electrode flushing. Finally, it gives recommendations for further research to be performed.

3. EDM drilling

This chapter covers EDM drilling of electrically conductive, semi-conductive and non-conductive materials, with the focus on the materials used by turbine blade manufactures. A new method to machine electrically non-conductive materials in deionized water is shown.

Parts of this chapter have been published [48, 88, 100].

3.1 Description of the machined materials

In order to address challenges indicated in section 2.8 three groups of materials are investigated. The most widely used material of turbine is represented by superalloy Inconel 718. New generation CMC SiC/SiC material (almost not accessible for the research needs) is replaced by SiC, SiSiC separately. Milling testes of C/SiC and also SiC/SiC are shown in the next chapter. The third material is ZrO_2 since it is used as TBC of the turbines.

Table 3-1 shows differences in the physical properties of Si and SiC and SiSiC. EDX of Inconel 718 is presented in Fig. 3-1, EDX of SiSiC in Fig. 3-2, EDX of SiC in Fig. 3-3, and a BSD mapping of SiC is addressed in Fig. 3-4 to indicate the content of precipitations. EDX of ZrO_2 shows Fig. 3-5.

Table 3-1: Physical properties of SiSiC, SiC and Si.

Property	Unit	Si	SiC	SiSiC
Thermal conductivity	$W/(m \cdot K)$	130	360-490	120- 200
Melting point	K	1412	3103	1350*
Electrical resistivity	$\Omega \cdot cm$	0.1-60	0.1-100 [101]	10^2-10^8
Density	$g \cdot cm^3$	2.33	3.21	3.07-3.15
Thermal expansion	$10^{-6}K^{-1}$	2.56	2.77	3.6- 4.3

*maximum operating temperature

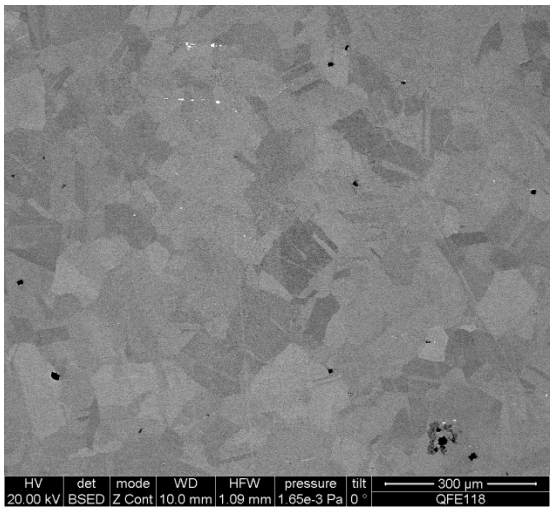

Fig. 3-1: Energy dispersive X-Ray analysis (EDX) of Inconel 718 material by backscattered (BSE) detector.

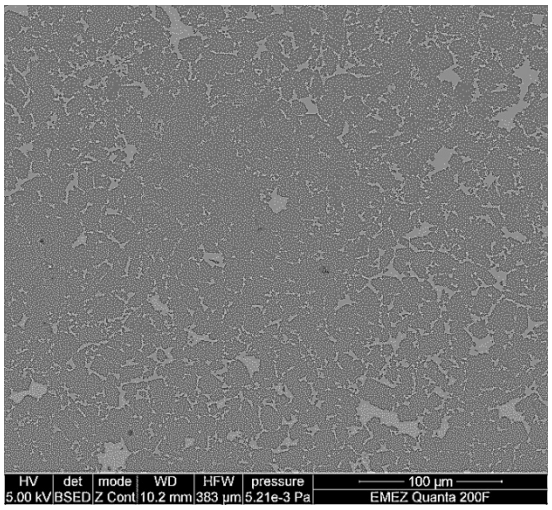

Fig. 3-2: Energy dispersive X-Ray analysis (EDX) of SiSiC material by backscattered (BSE) detector. Grey SiC grains can be seen; bright grey indicates silicon.

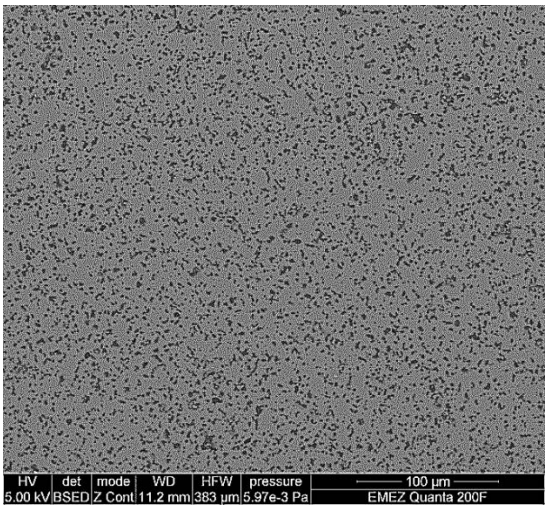

Fig. 3-3: Energy dispersive X-Ray analysis (EDX) of SiC material by backscattered (BSE) detector. Darker areas are precipitation of carbon due to a sintering process.

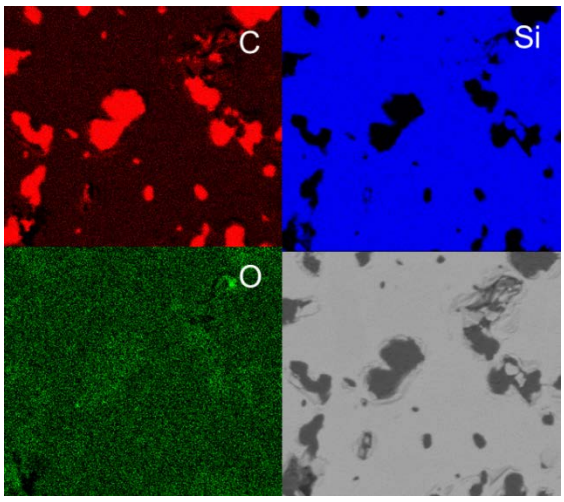

Fig. 3-4: BSE mapping of SiC, it is seen that Si is a dominating element; darker areas in BSE image are the precipitation of carbon.

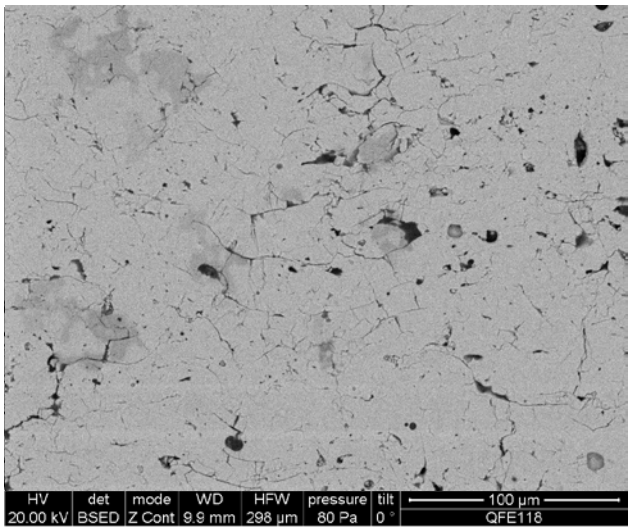

Fig. 3-5: Energy dispersive X-Ray analysis (EDX) of ZrO_2 material by backscattered (BSE) detector.

Ceramic matrix composite (CMC) materials consist of two components, coated ceramic fibres and the ceramic matrix. The most common materials, which are used as the fibres for CMCs are carbon (C), silicon carbide (SiC), alumina (Al2O3) and mullite (Al2O3–SiO2). The matrix is usually consist of the same (or similar) material as the fibre, these materials are usually C, SiC, alumina and mullite [102, 103].

CMCs used for jet engine parts production are typically made of silicon carbide (SiC) ceramic fibres coated with a boron nitride (about 1 µm coating). The coated fibres are embedded in SiC, the CMC material can contain 10–15 percent silicon [102]. SiC/SiC CMC is shown in Fig. 3-6.

SiC/SiC is produced by Chemical Vapour Infiltration Process (CVI) as it is shown in Fig. 3-7. CVP production process starts with textile-forming into preform, then conventional CVI methods are used to deposit interfacial coatings on the surface of the fibre [104].

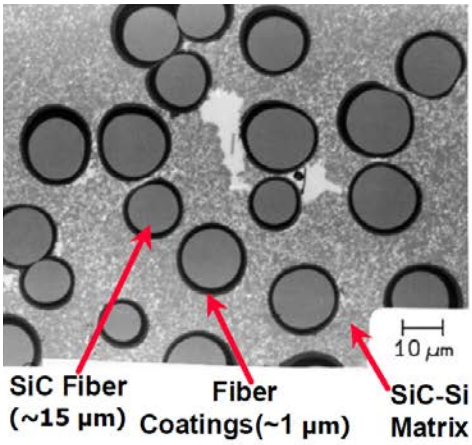

Fig. 3-6: SiC/SiC CMC material [97].

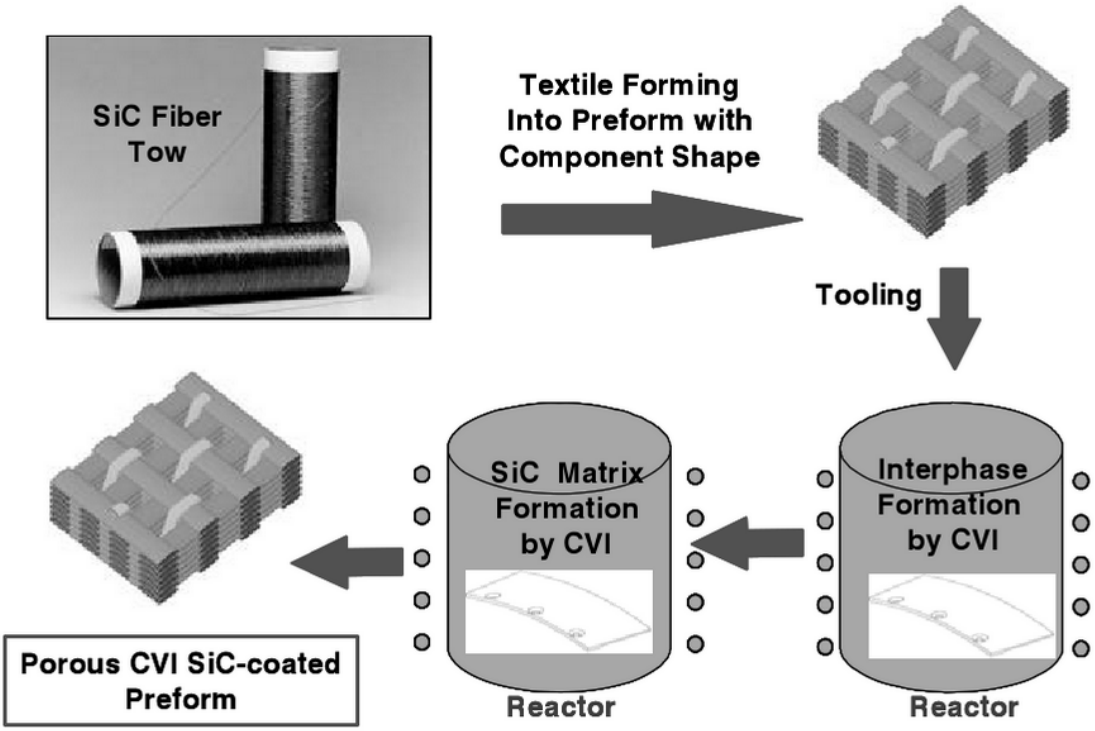

Fig. 3-7: Baseline processing route for the NASA CMC systems [104].

Fiber to matrix interface has a significant influence on the lifetime and on the mechanical behaviour of the final CMC composite. A lot of investigations have been done on the optimization of interface properties. CVI SiC/SiC composites with relatively strong interfaces properties (fibre/coating bond) are obtained by using fibres that have been treated to increase it [105, 106].

The crack initiated in the matrix my cause the deboning of the fibre (Fig. 3-8), The role of coating is in prevention of the cracks propagation [107].

Fig. 3-8: Schematic diagram showing crack deflection when the fibre coating/interface is (a) strong or (b) weak [107].

3.2 Electrode dressing

Electrode dressing is a preparation step for the drilling process in order to achieve stable and reliable results and mitigate any influence of the previous test. Electrode dressing is also required in many drilling applications for finishing strategy, where the cylindrical shape of the electrode is essential and conicity has to be avoided.

Several materials and parameters were used to dress the multi-hole 1 mm brass electrodes. The visualisation of the tests is in Fig. 3-9 and the details of the experimental conditions are summarized in Table 3-2.

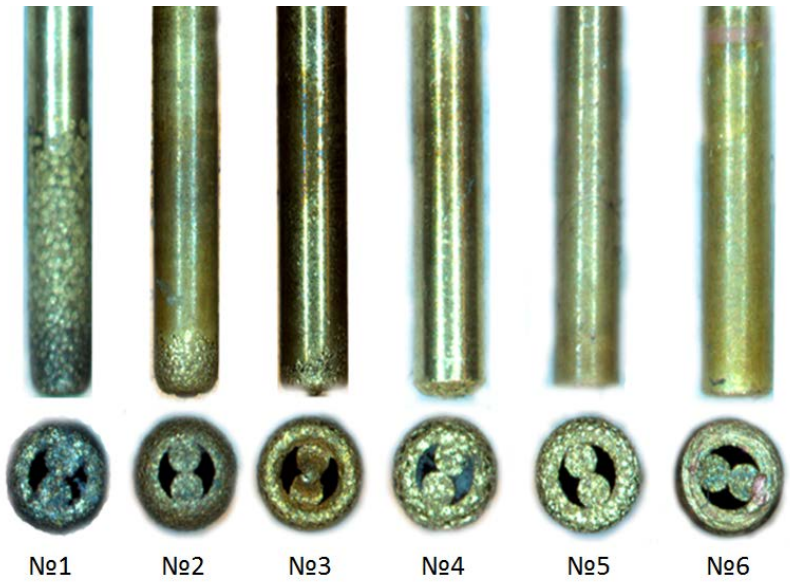

Fig. 3-9: Dressing experiments, electrode 1 is without dressing. The best shape after dressing is achieved in the last test, the best results concerning time and quality were achieved by № 4 set of parameters.

Table 3-2: Dressing strategies and their parameters.

№ 1	№ 2	№ 3	№ 4	№ 5	№ 6
The materials used for dressing					
No dressing	Graphite	Steel W300	Copper	Copper	Copper
Depth of dressing					
0mm	10mm	10mm	10mm	1mm (after № 4)	10mm
Time					
0sek	12sec	12sec	12sec	18sec	180sec
Technology					
No dressing technology	t_{on} = 3.2 µs; P=10 µs; I_d=6 A; U_{open} =250 U; Pol +	t_{on} = 3.2 µs; P=10 µs; I_d=6 A; U_{open}=250 U; Pol +	t_{on} = 3.2 µs; P=10 µs; I_d=6 A; U_{open} =250 U; Pol +	t_{on}= 3.2 µs; P=10 µs; I_d=2 A; U_{open} =250 U; Pol +	t_{on} =3.2 µs; P=10 µs; I_d=2 A; U_{open} =250 U; Pol +

The influence of the material used for dressing to the shape of the electrode is shown in Fig. 3-9, after the use of graphite, electrode remained significantly conical, which is unwanted in dressing. The use of Steel W300 has the opposite effect when dressing creates a cavity in the middle part. Dressing with copper showed the best shape of the electrode.

Final dressing parameters were found as a trade-off between the shape and machining time in combining the strategies 4 and 6. The results are presented in the strategy 5. The dressing is used to prepare the electrode before drilling for all experiments in this chapter.

3.3 Process parameter analysis by regression modelling

EDM of superalloys such as Inconel 718 are researched in the literature, but the details about recast layer measurements after EDM drilling are rarely investigated. These investigations are present in this section in order to guarantee the integrity of the machined surface in order to meet the requirements of turbine manufacturing. At the same time machining has to be done at reasonably high rates.

3.3.1 Experimental Method and Procedure

A full factorial design of experiments is selected for exploring the parameter space. Independent variables are discharge current and pulse duration, which are specified in Table 3-3, as seven different levels. The dependent variables are relative tool wear, material removal rate MRR and recast layer thickness. Experiments are performed on a Drill 300 from GF Machining Solutions, Agie Charmilles SA Switzerland (Fig. 3-10).

Fig. 3-10: Drill 300 GF Machining Solutions, Agie Charmilles SA. Source: GFMS.

Table 3-3: Input parameters and selected levels.

Variable	Unit	Level						
		1	2	3	4	5	6	7
Pulse duration (T_{on})	µs	16	20	24	28	32	37	42
Discharge current (I_d)	A	8.5	12	16	20	24	28	32

Inconel 718 as workpiece material and copper multi-hole electrodes are used for all drilling tests. The electrode diameter is 1 mm. Further EDM drilling machine parameters, are not changed during the experiment and are presented in Table 3-4.

Table 3-4: EDM conditions.

	EDM Condition
Workpiece material	Inconel 718
Electrode material	Copper
Dielectric	Deionized water
Holes type	Blind
Pause duration	15µs
Ignition voltage	130V
Feed of the electrode (H)*	10 mm
Electrode polarity	negative

* Feed of the electrode is set on EDM machine and the wear is not compensated.

3.3.2 Recast layer analysis

The recast layer thickness (RLT) is one of the most significant process parameters for the determination of quality limits for the aerospace industry. In [25] it was found that a thick recast layer has a higher tendency to emit cracks. Therefore on recast layer thickness depends surface integrity and strength characteristics of turbine blades. The RTL of all drilled holes is measured. Specimen preparation including grinding, polishing and etching is performed. Polishing is performed with Al_2O_3 abrasive with grain size 3 µm. Etching solution V2A is used and the etching time is 30 s. The V2A etching solution consists of a mixture of 100 ml water, 100 ml hydrochloric acid and 10 ml nitric acid. Etching temperature is 50° C.

The RTL measurements and imaging are made by Alicona infinite focus microscope, Austria. Thereafter the images are transferred into a binary format as shown in Fig. 3-11, to make the recast layer clearly visible and measurable.

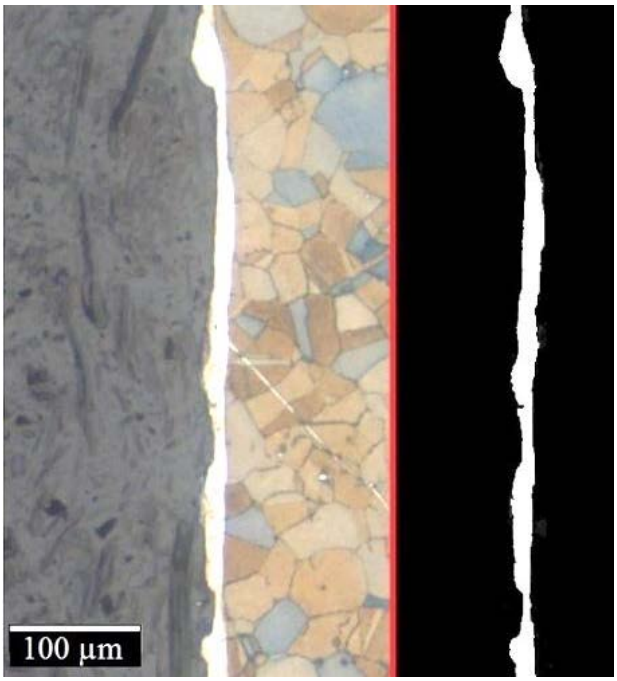

Fig. 3-11: Recast layer image transformation, the original image on the left and binary image on the right.

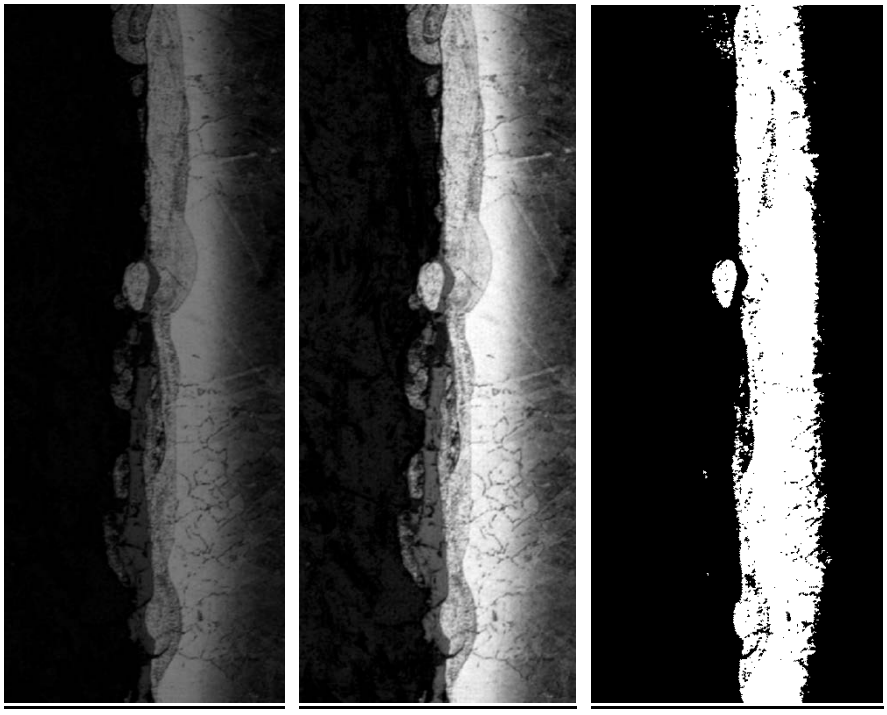

Fig. 3-12: Image transformation, from left to right: measurements (grey scale), colour balance, binary format.

The RLT measurement is based on the line-by-line counting of the white pixels along horizontal lines after adjustment of the white layer vertically. The maximum thickness of the recast layer is usually not higher than twice the average thickness R_L, which is then, calculated from.

$$R_L = \frac{\sum_{i=1}^{k} N_i \cdot K_t}{k} \tag{3-1}$$

Here N_i is the number of white pixels in measured horizontal line *i*, while *k* is the total number of lines in the picture and K_t is the transformation coefficient which represents the microscope resolution times the pixel width.

3.3.3 Recast layer measurements correction

The measurements of the recast layer are susceptible to the longitudinal-section cut, if it is not made exactly in the middle of the hole, the values of the recast layer are incorrect. The uncertainty usually comes from the grinding and polishing of the specimens, where the thickness of the removed material may vary significantly. In order to determine the actual recast layer (the recast layer measured precisely in the middle of the hole) based on a deviated measurement, two calculations are necessary.

The deviation Δ of which the original measurements deviate to the actual values has to be determined. Therefore the radiuses of the deviated measurements have to be compared to the non-deviated measurements. The derivation is shown in Fig. 3-13.

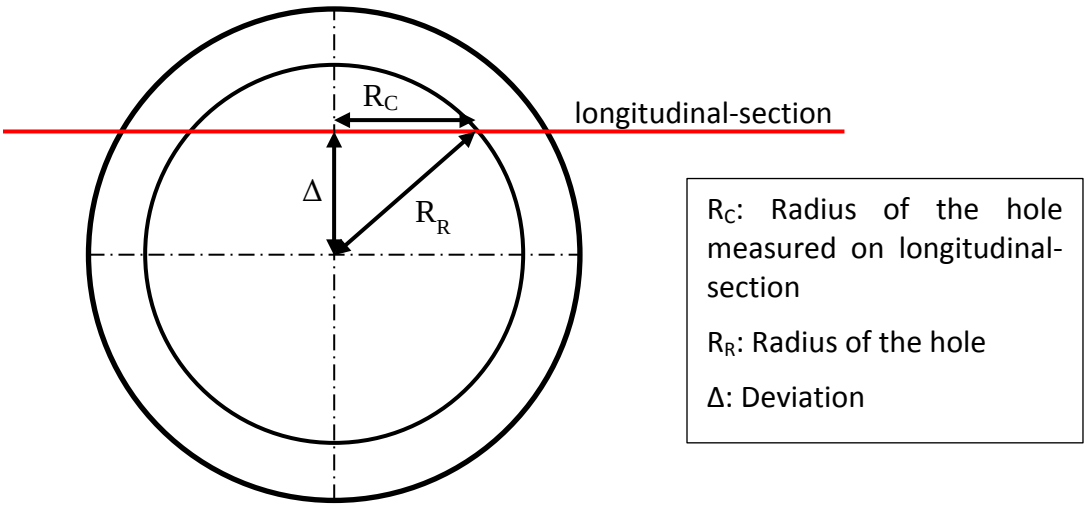

Fig. 3-13: Deviation of the longitudinal-section deviation from the centre of the hole.

Following the deviation which is shown in Fig. 3-13, the equation to calculate it from the longitudinal-section is:

$$\Delta = \sqrt{R_R^2 - R_C^2} \tag{3-2}$$

Using this deviation, the actual recast layer can be calculated from the measurements. This procedure can be used for both the average recast layer and maximum recast layer. The calculations are explained in the following Fig. 3-14:

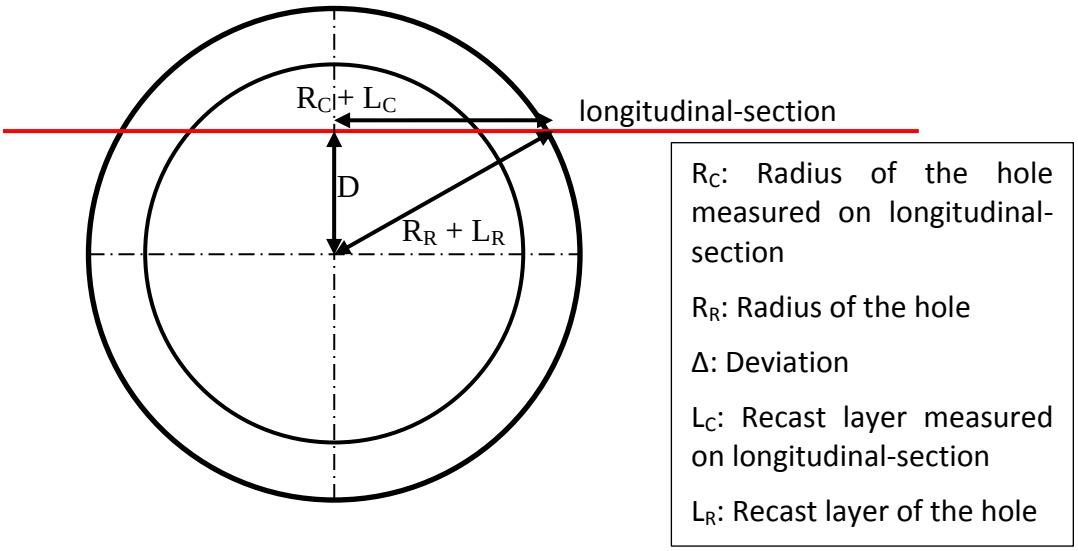

Fig. 3-14: Deviation of actual recast layer.

$$R_R + L_R = \sqrt{D^2 + (R_C + L_C)^2} \tag{3-3}$$

The formulas (1) and (2) can then be combined to calculate the non-deviated recast layer:

$$L_R = \sqrt{(R_R^2 - R_C^2) + (R_C + L_C)^2} - R_R \tag{3-4}$$

In combination with the recast layer compensation method the image analysis method, presented in section 3.3.2, is only limited by the resolution of the microscope (size of a pixel) and in the case of this work a pixel size is 0.88 µm

3.3.4 Electrode wear and material removal calculation

Electrode wear measurements E_{Wt} are performed after every erosion as a reduction of the length of the electrode. From those measurements the relative tool wear

$$E_W = \frac{E_{Wt}}{H - E_{Wt}} \cdot 100\% \tag{3-5}$$

is calculated as wear related to the eroded workpiece volume, where E_{Wt} is the total reduction of electrode length, as graphically explained in Fig. 3-15.

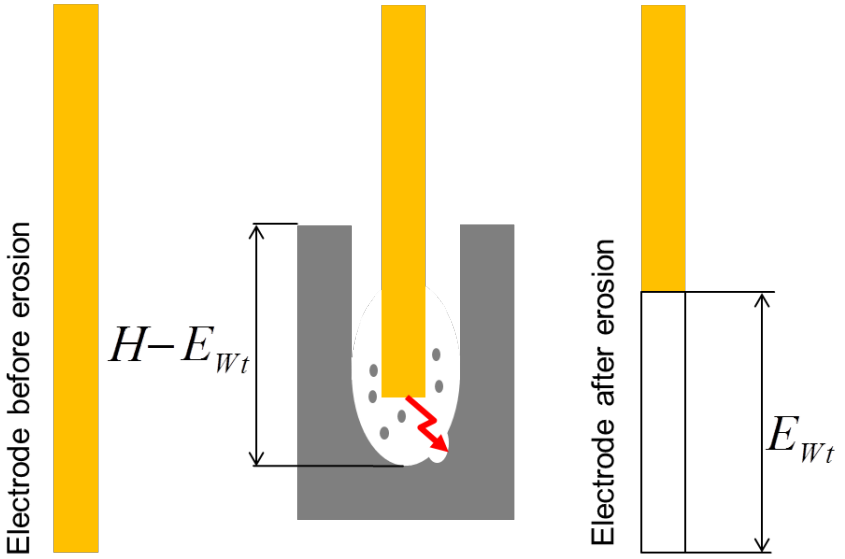

Fig. 3-15: Electrode wear is calculated as a ratio between the total reduction of the electrode length and depth of the hole.

Material removal rate MRR is calculated as

$$\dot{V}_{MRR} = \frac{(H - E_{Wt}) \cdot \mathrm{A}}{t} \tag{3-6}$$

where *t* is the machining time, and A is the cross section of the hole.

3.3.5 EDM drilling statistical model

A second order polynomial regression is used as a mathematical model for MRR and RLT; and a third order polynomial regression for the relative tool wear. The variables pulse duration T_{on} and discharge current I_d are taken into account by the regressions.

Analysis of Variance (ANOVA) is used to investigate significance and highest effect of and the highest effect of a variable, independent parameters: pulse duration T_{on} and discharge current I_d to dependent process parameters: relative electrode wear, MMR and RLT.

The p-value for statistical testing of experimental results in the model is 5 % that evaluates the significance of the parameters. More information about p-value and F-value can be found [108].

Table 3-5 shows that the effect from individual variable T_{on} is higher than the effect from I_d and effects from higher order variables and an interaction term. T_{on}, T_{on}^2, and T_{on}^3 have a significant contribution to the relative tool wear regression model since p-values are less than 0.05. F-value is used in ANOVA to determine the tests statistical significance. P-value or probability value evaluates the null hypothesis of the statistical model true.

Table 3-5: Results from the analysis of variance for electrode wear eq. (3-7).

Source	F-value	p-value
Regression	687.81	0.000
T_{on}	46.13	0.000
I_d	1.55	0.214
T_{on}^2	46.97	0.000
I_d^2	0.1	0.752
$T_{on}\times I_d$	0.52	0.471
T_{on}^3	45.10	0.000
I_d^3	0.08	0.783
Lack-of-fit	0.61	0.972
R2 =93.48%		

The value R^2 is a statistically measured fitting of the regression model to the experimental data. For the relative tool wear model, the value is 93.48% (Table 3-5). It means that the model is able to explain the entire volume of data with good reliability. The F-value of the regression is higher than the critical F-value (2.04- tabulated value) with the significance level of α=0.05, so the test is statistically significant. Also, the p-value of lack-of-fit is 0.972, which indicates the significance of the achieved results. It means that terms such as interactions and quadratic terms are included in the model.

Regression coefficients are present in Table 3-6 since all variables have their own units, the transformation of units is included in regression coefficients. SE coefficient stands for the standard error of the coefficient, and a t-value is the relative error difference in contrast to the null hypothesis.

Table 3-6: Regression coefficients for electrode wear E_W.

Source	Coefficient	SE Coefficient	T-value	p-value
T_{on}	6.85	0.01	6.79	0.000
I_d	-1.84	1.48	-1.24	0.214
T_{on}^2	-0.2728	0.0398	-6.85	0.000
I_d^2	0.0248	0.0785	0.32	0.752
$T_{on}\times I_d$	0.0048	0.0066	0.72	0.471
T_{on}^3	0.0033	0.0005	6.72	0.000
I_d^3	0.0004	0.0012	0.28	0.783

The regression model of electrode wear based on coefficients from Table 3-6 is calculated as

$$E_W = 6.85 \cdot T_{on} - 1.84 \cdot I_d - 0.2728 \cdot T_{on}^2 + 0.0248 \cdot I_d^2 + 0.0048 \cdot T_{on} \cdot I_d + 0.0033 \cdot T_{on}^2 + 0.0004 \cdot I_d^2 \qquad (3\text{-}7)$$

E_W [%]; T_{on} [µs]; I_d [A]

Pulse duration parameter T_{on} has a higher effect on the electrode wear than the discharge current parameter I_d. The electrode wear decreases with the increase of T_{on} and I_d parameters until T_{on} = 32 µs and I_d= 20A. For the discharge current the optimum value is 20 A, and for the pulse duration, the optimum value is 28 µs. Further increase of discharge current leads to an increase of electrode wear, whereas the increase of pulse duration does not have a significant effect. The lowest achieved value of relative electrode wear is 20 %. The response surface of electrode wear is in Fig. 3-16.

The regression analysis of MRR in Table 3-7 shows that the effect from all variables T_{on}, I_d, T_{on}^2, I_d^2 and $T_{on}\times I_d$ has a significant contribution to the relative tool wear regression model since p-values are less than 0.05

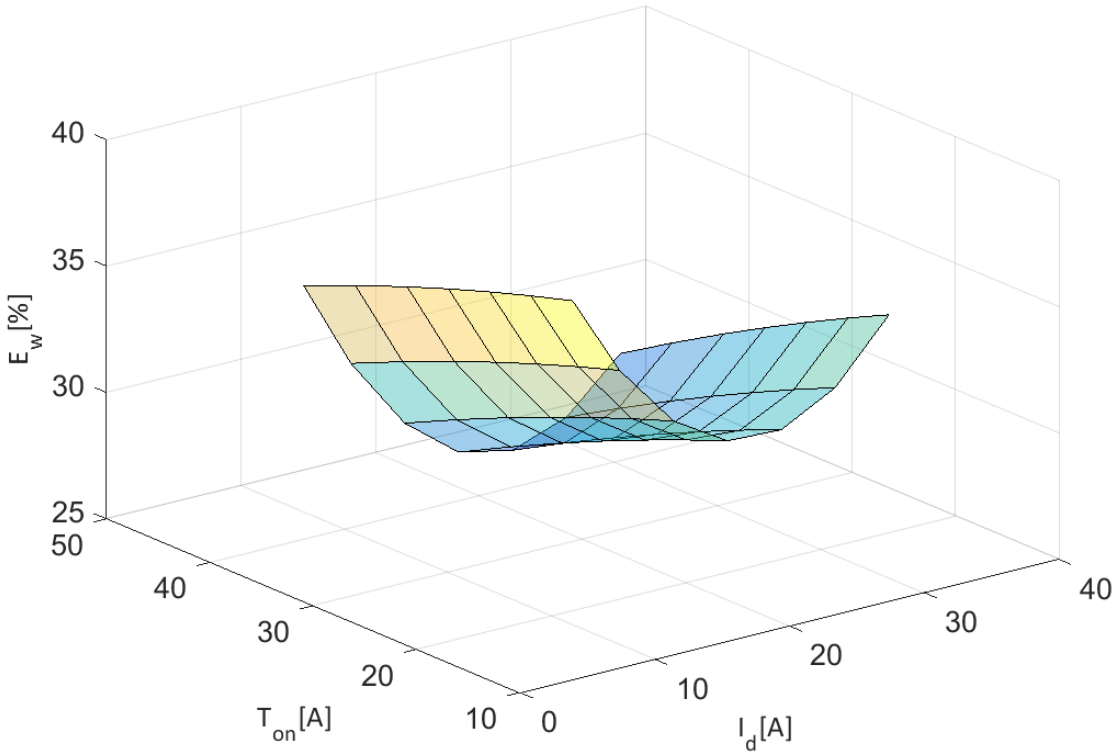

Fig. 3-16: The effect of the main input parameters on relative tool wear, during erosion of Inconel 718.

Table 3-7: Results from the analysis of variance for MRR.

Source	F-value	p-value
Regression	3499.62	0.000
T_{on}	15.80	0.000
I_d	65.07	0.000
T_{on}^2	14.23	0.000
I_d^2	13.20	0.000
$T_{on}\times I_d$	12.43	0.000
Lack-of-fit	0.49	0.997
R^2 =98.1%		

For the MRR model, the value is R^2=98.1% (Table 3-7). It means that the model is able to explain the entire volume of data with excellent reliability. The F-value of the regression is higher than the critical F-value (2.24- tabulated value) with a significant level of α=0.05. Also, the p-value of Lack-of-fit is 0.997, which indicates its insignificance.

Table 3-8: Regression coefficients for MRR.

Source	Coefficient	SE Coefficient	T-value	p-value
T_{on}	0.705	0.177	3.97	0.000
I_d	2.061	0.256	8.07	0.000
T_{on}^2	-0.015	0.004	-3.77	0.000
I_d^2	-0.023	0.006	-3.63	0.000
$T_{on}\times I_d$	0.016	0.005	3.53	0.000

The regression model of MMR based on coefficients from Table 3-8 is calculated as

$$\dot{V}_{MRR} = 0.705 \cdot T_{on} + 2.061 \cdot I_d - 0.015 \cdot T_{on}^{\ 2} - 0.023 \cdot I_d^{\ 2} + 0.016 \cdot T_{on} \cdot I_d \quad (3\text{-}8)$$

$\dot{V}_{MRR}$ [mm^3/min]; T_{on} [µs]; I_d [A]

The discharge current parameter has the highest effect on the MRR; its sensitivity is almost ten times higher than the one from the pulse duration. A discharge current of 32 A maximizes the MRR, which is the highest value achieved in the tests. The effect of pulse duration on MRR is similar to the effect on the electrode wear. The highest material removal rate achieved is 77 mm^3/min. The response surface of MRR is shown in Fig. 3-17.

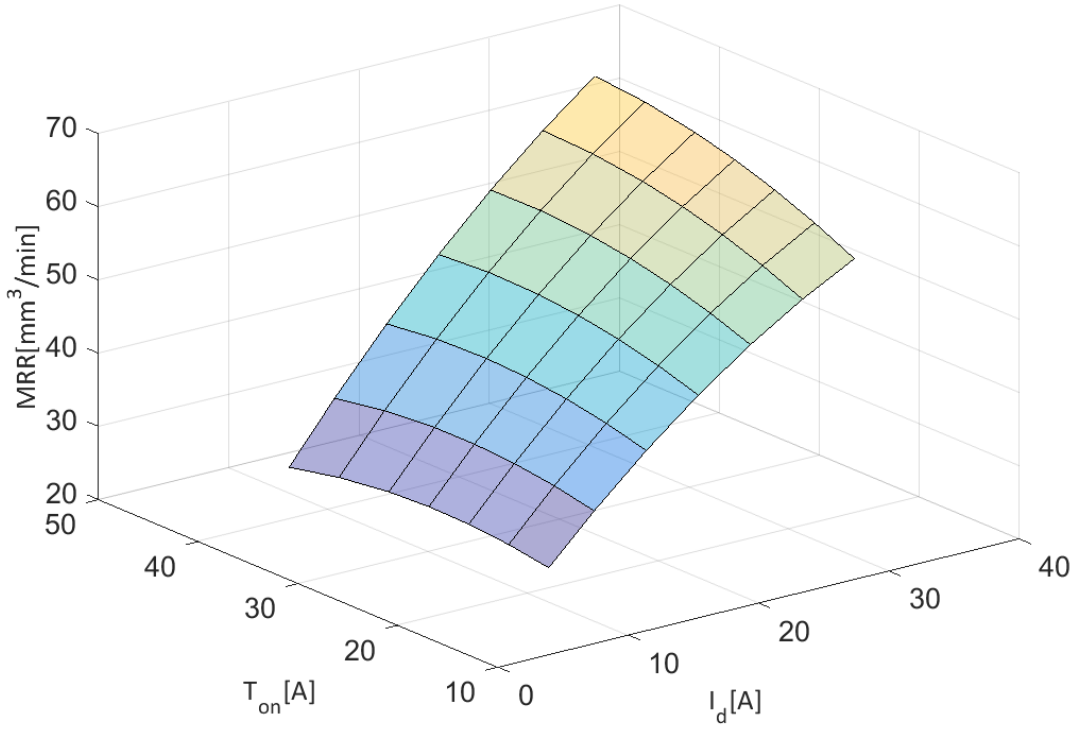

Fig. 3-17: The effect of the main input parameters on MRR, during erosion of Inconel 718.

The MRR is proportional to the energy per pulse. This happens because the diameter of the plasma channel grows simultaneously with the pulse duration and the same amount of power is spread into a growing area. After 32 µs the power per area becomes insufficient for maximum material vaporization, and the MRR decreases.

The results of the regression analysis for RLT in Table 3-9 shows that the effect from individual variables T_{on} and I_d as well as effect from higher order variables T_{on}^2 and I_d^2 has significant contribution to the relative tool wear regression model, since the p-values are less than 0.05, whereas interaction between T_{on} and I_d is insignificant.

Table 3-9: Results of the analysis of variance for RLT.

Source	F-Value	p-value
Regression	2979.84	0.000
T_{on}	104.03	0.000
I_d	25.99	0.000
T_{on}^2	48.18	0.000
I_d^2	24.32	0.000
$T_{on}\times I_d$	4.49	0.035
Lack-of-fit	0.74	0.889
R^2 =97.2%		

For the recast layer model, the value is R^2 =97.2% in Table 3-9. It means that the model is able to explain the entire volume of data with excellent probability. The F-value of the regression is higher than the critical F-value (2.24- tabulated value) with a significant level of α=0.05. Also, the p-value of Lack-of-fit is 0.889, which indicates its insignificance.

Table 3-10: Regression coefficients for RTL.

Source	Coefficient	SE Coefficient	T-value	p-value
T_{on}	0.5401	0.053	10.20	0.000
I_d	0.3878	0.076	5.10	0.000
T_{on}^2	-0.008	0.001	-6.94	0.000
I_d^2	-0.009	0.002	-4.93	0.000
$T_{on}\times I_d$	0.003	0.001	2.12	0.035

The regression model of the recast layer based on coefficients from Table 3-10 is calculated as

$$R_L = 0.54 \cdot T_{on} + 0.389 \cdot I_d - 0.008 \cdot T_{on}^{\ 2} - 0.009 \cdot I_d^{\ 2} + 0.003 \cdot T_{on} \cdot I_d \qquad (3\text{-}9)$$

R_L [µm]; T_{on} [µs]; I_d [A]

The lowest value of the RLT is achieved with the minimum values of the pulse duration T_{on} and discharge current I_d parameters. Minimum for discharge current is 8.5A and

minimum for time duration is 16 µm. The lowest average RLT achieved is 8 µm with 0.8 % standard deviation. The response surface of RLT is in Fig. 3-18.

Both independent variables have a significant effect on the dependent variables: MRR, electrodes wear E_W and RLT and interactions between pulse duration and discharge current are insignificant in all three analyses.

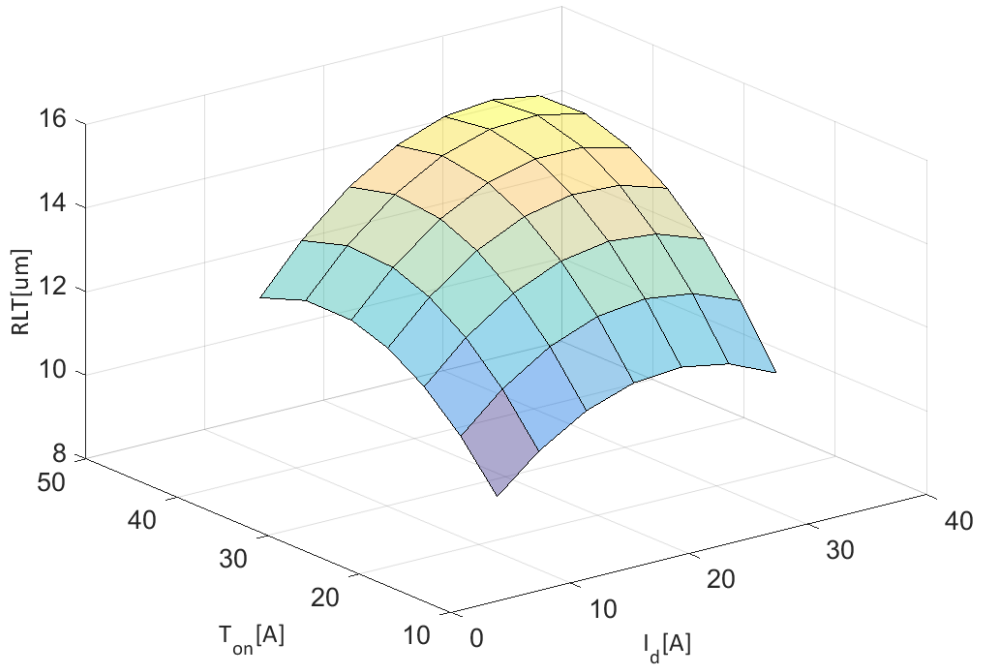

Fig. 3-18: Effect of main input parameters on RLT, during erosion of Inconel 718.

The recast layer is formed by molten material which is not vaporized or flushed away with the dielectric and then solidifies on the surface. The recast layer increases with the volume of molten material which depends on the amount of energy transferred to the surface. Therefore minimum RLT is reached with minimum T_{on} and minimum I_d

The maximum MRR meaning and minimal Electrode wear are achieved with the value of pulse duration parameter T_{on} = 32µs. For discharge current I_d optimization the maximum MRR is achieved under the maximum meaning of this parameter of I_d = 30A. The minimum meaning of electrode wear is achieved with parameter I_d = 18A. Minimum recast layer is reached with minimum T_{on} and minimum I_d.

3.4 Erosion of SiSiC ceramic

EDM of SiC is essential for analyses, since this widely used ceramic has relatively low electrical resistivity (from 100 Ω · cm) and a significant number of industrial applications. Also, the new generation CMC SiC/SiC materials are becoming the key material to replace superalloys in the hot section of the turbine engine.

The surface integrity measurements of all drilled holes are presented and discussed in this section. Specimen preparation including grinding and polishing is performed. Polishing is made with diamond abrasive with 5 µm average grain diameter.

The surface observation, as well as the measurement and imaging of holes, are made using Alicona infinite focus microscope.

All experiments are repeated three times, and standard deviation (SD) is an indication for the stability of the process and repeatability of the experiment.

3.4.1 Experimental Method and Procedure

A parameter study is performed in order to analyze the EDM-drilling of SiSiC. Main input parameters and EDM conditions are presented in Table 3-11 and Table 3-12 respectively. As well as in the previous section the experiments are carried out on Drill 300 GF Machining Solutions, Agie Charmilles SA, Switzerland.

The influence of pulse duration, ignition voltage and polarity on the material removal rate, electrode wear and hole quality is analyzed. Levels of parameters are presented in Table 3-11. Different pulse durations are studied with fixed ignition voltage and the influence of ignition voltage is studied with fixed pulse duration. The experiment is repeated with electrode positive and negative polarities. Table 3-12 presents the main process parameters which are not changed during the experiments.

Table 3-11: Table of input parameters.

Variable	Unit	Level				
		1	2	3	4	5
Pulse duration (T_{on})	µs	5	3	2	1	0.6
Ignition voltage (U_{open})	V	120	100	80	60	50
Polarity		+/-	+/-	+/-	+/-	+/-

Table 3-12: EDM conditions.

	EDM Condition
Workpiece material	SiSiC
Electrode material	Copper
Electrode diameter	0.5 mm
Dielectric	Deionized water
Holes type	Blind
Pause duration	10 µs
Feed of the electrode*	1.3 mm
Discharge current	8 A

* Feed of the electrode is set on EDM machine and wear is not compensated

3.4.2 Hole quality

Figures 1-4 represent the effect of different process parameters to the quality of drilled holes in SiSiC, namely to the hole diameter accuracy, roundness, and resolidified material around the hole. Heat affected layer (HAZ) is analysed in the next section. Fig. 3-19 and Fig. 3-20 show the reduction of diameter and the amount of resolidified material with a decrease

of pulse duration with negative and positive polarities. The effect of ignition voltage is shown in Fig. 3-21 and Fig. 3-22. In the case of negative electrode polarity, the increase of ignition voltage reduces the resolidified material area and radius of the hole, with positive polarity the increase of ignition voltage has the opposite effect.

Fig. 3-19: Drilling tests with a different pulse duration from left to right: 5 µs; 3 µs; 2 µs; 1 µs; 0.6 µs; U_{open}= 100 V and polarity is positive in all experiments. The red circles indicate the border of the holes.

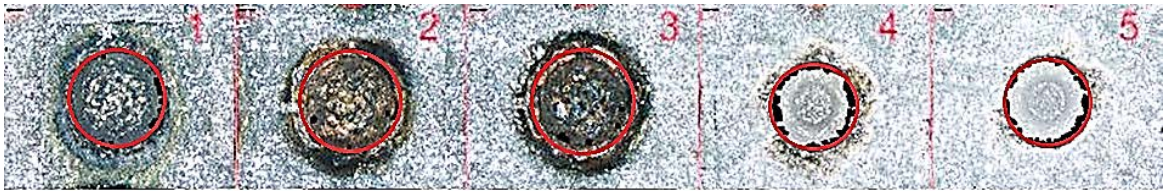

Fig. 3-20: Drilling tests with a different pulse duration from left to right: 5 µs; 3 µs; 2 µs; 1 µs; 0.6 µs; U_{open} = 100 V and polarity is negative in all experiments. The red circles indicate the border of the holes.

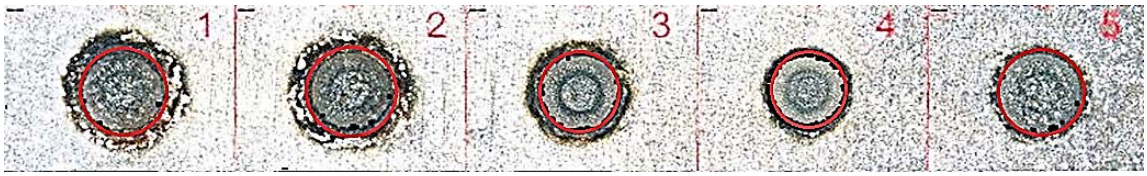

Fig. 3-21: Drilling tests with a different ignition voltage from left to right: 120 V; 100 V; 80 V; 60 V; 50V; T_{on}=1 µs and polarity is positive in all experiments. The red circles indicate the border of the holes.

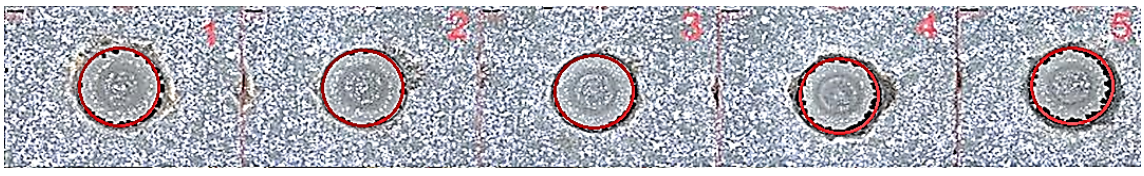

Fig. 3-22: Drilling tests with a different ignition voltage from left to right: 120 V; 100 V; 80 V; 60 V; 50 V; T_{on}=1 µs and polarity is negative in all experiments. The red circles indicate the border of the holes.

The best quality of the hole is achieved with negative electrode polarity, the lowest pulse duration and the highest ignition voltage. Pulse duration higher than 1 µs dramatically reduces the quality of the hole. The experimental results concerning hole diameter and depth are shown in Table 3-13.

Table 3-13: Experimental data of hole depth and diameter after SiSiC drilling.

Input parameter			Hole radius [µm]	Hole depth [mm]
T_{on} [µs]	U_{open} [V]	Electrode polarity		
0.6	100	negative	270	1.17
1	100	negative	272	1.06
2	100	negative	300	0.63
3	100	negative	288	0.61
5	100	negative	301	0.47
0.6	100	positive	271	0.70
1	100	positive	278	0.68
2	100	positive	276	0.53
3	100	positive	293	0.31
5	100	positive	320	0.14
1	50	negative	278	1.05
1	60	negative	275	1.09
1	80	negative	263	1.03
1	100	negative	265	1.01
1	120	negative	261	1.06
1	50	positive	274	0.56
1	60	positive	266	0.70
1	80	positive	268	0.68
1	100	positive	275	0.66
1	120	positive	285	0.66

3.4.3 Relative tool wear and material removal rate (MRR)

The influence of pulse duration and ignition voltage with negative and positive polarity to the relative tool wear is shown in Fig. 3-23 and Fig. 3-24 respectively.

The electrode wear measurement is performed after each erosion test and is calculated relative to the eroded workpiece volume.

The relative tool wear is always lower with negative polarity. The increase of pulse duration has a substantial effect on wear. The ignition voltage does not influence the tool wear significantly, except the value of 50 V, where wear is much higher especially for positive polarity. Low voltage influence can be explained by shortening of the gap and therefore worse material evacuation and at the same time the lower voltage increases a probability of the short circuit, which causes additional electrode wear.

The influence of pulse duration and ignition voltage with negative and positive polarities on MRR is shown in Fig. 3-25 and Fig. 3-26 respectively.

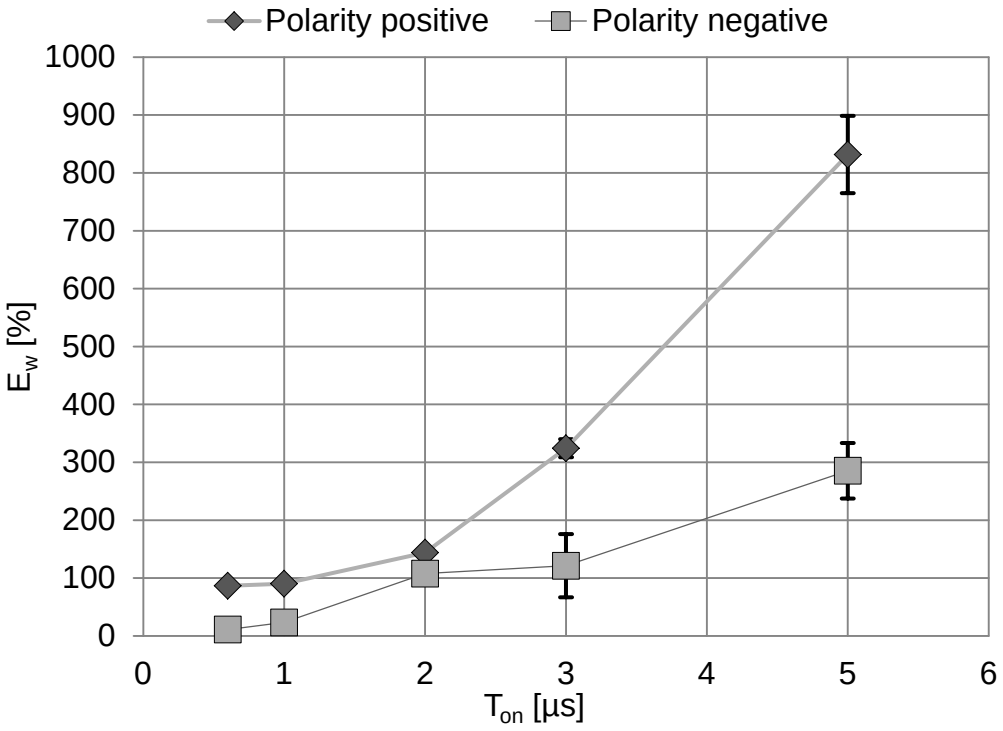

Fig. 3-23: The effect of pulse duration T_{on} on the relative tool wear of SiSiC material. Ignition voltage U_{open} is 100 V.

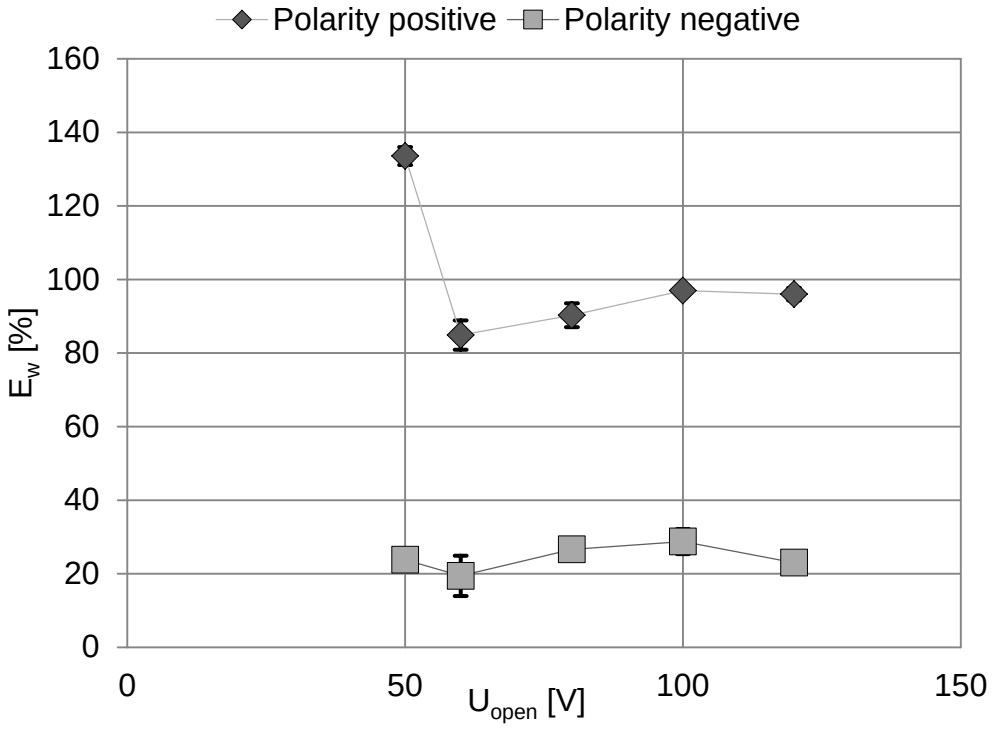

Fig. 3-24: The effect of ignition voltage U_{open} on the relative tool wear of SiSiC material. Pulse duration is 1 µs.

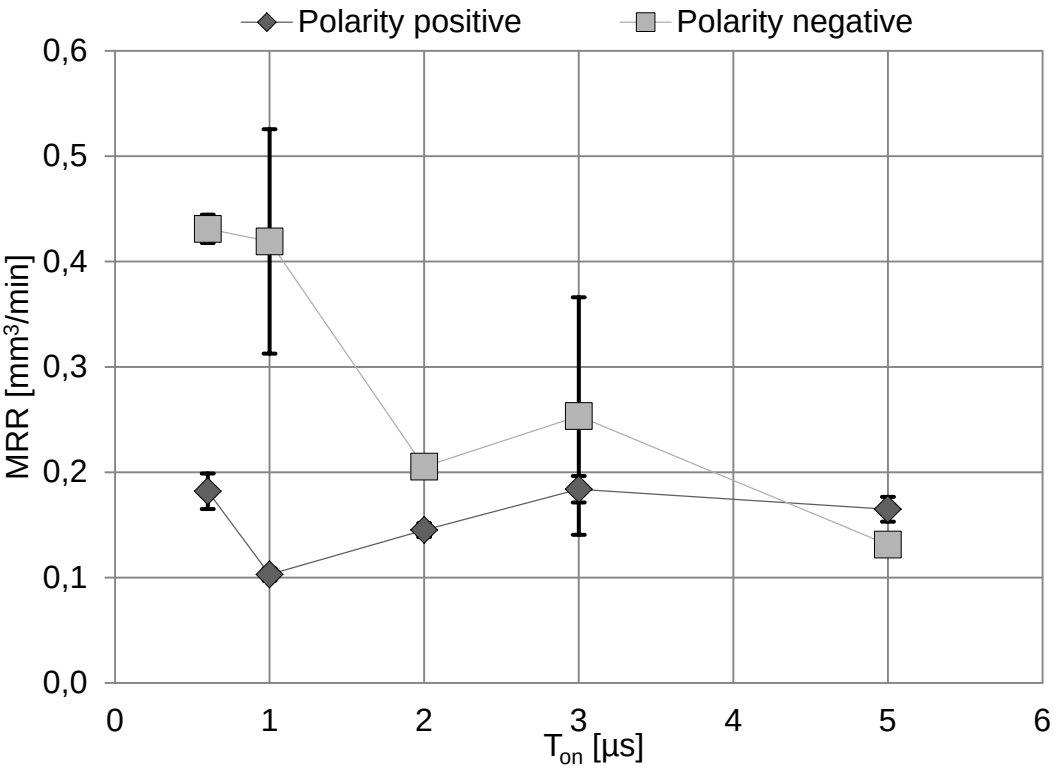

Fig. 3-25: The effect of pulse duration T_{on} on MRR of SiSiC material. Ignition voltage U_{open} is 100 V. The deviation of the MMR at the certain regions is caused by process instability.

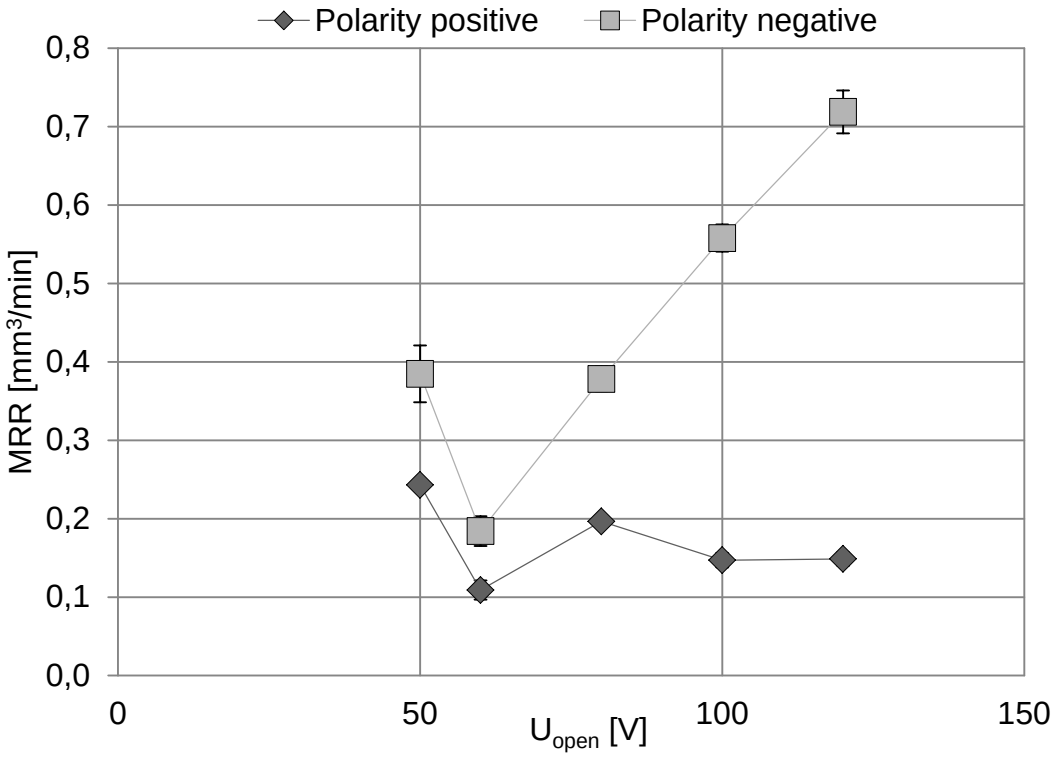

Fig. 3-26: The effect of ignition voltage U_{open} on MRR of SiSiC material. Pulse duration is 1 µs.

As opposed to the relative tool wear, the MRR is always higher with negative polarity. The variation of the process parameters has a similar effect on the process and its results for positive and negative polarity. The increase of pulse duration or an increase of ignition voltage reduces MRR.

Based on the analysis of the data presented in Fig. 3-23, Fig. 3-24, Fig. 3-25 and Fig. 3-26, the optimum technology (lowest electrode wear and highest MRR) in the researched process window for quality and speed erosion of SiSiC are with negative polarity in the range of high ignition voltage and low pulse duration.

3.4.4 Material removal mechanism

It is essential to examine the material removal mechanism in detail since the effect of short pulses is not analysed in EDM drilling and cannot be explained only by melting and evaporation mechanism of removal. Fig. 3-27 and Fig. 3-28 represent the surface of SiSiC after erosion.

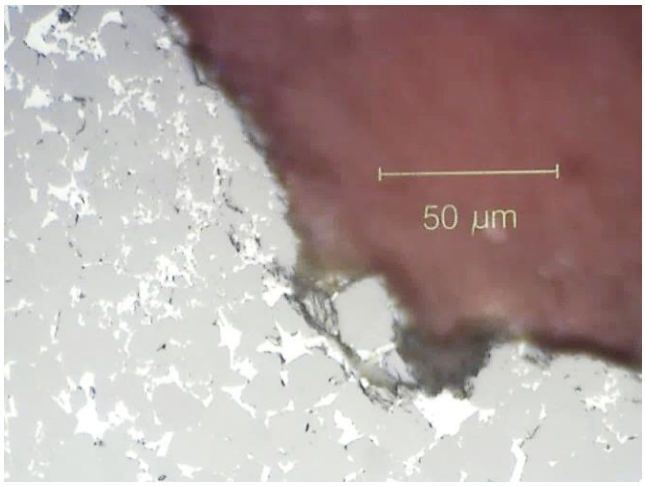

Fig. 3-27: Longitudinal section of a hole of SiSiC after EDM drilling showing spalling of SiSiC in the corner after discharge. In the microstructure of SiSiC material, Si is white, and SiC is grey

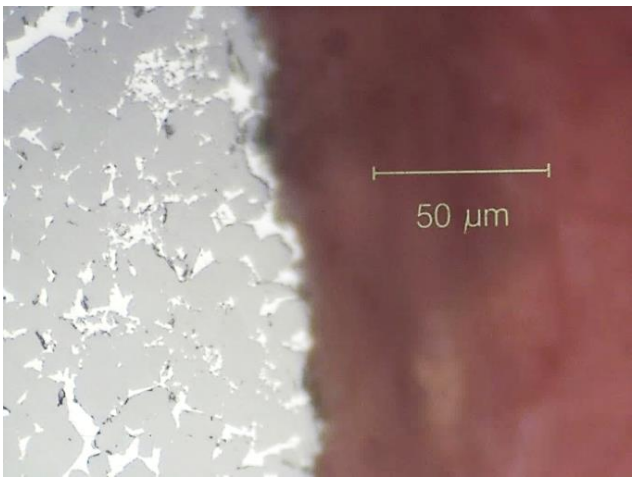

Fig. 3-28: Longitudinal section of a hole lateral part of SiSiC after EDM drilling, the material is removed on the border of SiC crystals. In the microstructure of SiSiC material, Si is white, and SiC is grey.

According to [26] the material removal mechanism of SiSiC is based not only on the melting and vaporization but also on cracking and spalling. Spalling is another main material removal mechanism for brittle, hard materials, which is not bound to phase changes but removes solid state material by crack development and propagation. According to [109] this effect is often related to the mechanism of micro-cracks generation since micro-cracks grows due to the temperature gradient and therefore due to tensile stresses. In Fig. 3-27and Fig. 3-28it is seen that the material is removed at the border of SiC crystals. The reason for even higher tensile stresses between the grains of SiC could be in thermal conductivity of Si, which is three times lower than the conductivity of the SiC. Therefore the temperature gradient is even higher in these areas. Higher thermal expansion in these areas is a source of micro-cracks generation and therefore promotes spalling.

3.5 Erosion of SiC ceramics

3.5.1 Experimental method and procedure

The influence of pulse duration, ignition voltage and discharge current to the material removal rate, electrode wear and hole quality are analysed. It must be mentioned that SiC specimens are coated with a silver layer to start the erosion, as it is shown in Fig. 3-29. The hole entrance is shown in Fig. 3-30 and Table 3-14 represents the main process conditions for SiC drilling test.

The experiments reveal that the increase of ignition voltage and discharge current enhances the roundness and hole radius, but the increase of time duration has an opposite effect. Notably, the increase of pulse duration T_{on} has a negative effect on the resolidified material around the hole, what reduces the quality similar to SiSiC processing. The reason for this is the additional material removal mechanism of spalling as well as for SiSiC.

Table 3-14: EDM conditions for SiC drilling

	EDM Condition
Workpiece material	Silicon Carbide (SiC)
Electrode material	Copper
Dielectric	Deionized water
Holes type	Blind
Pause duration	10 µs
Feed of the electrode*	5.3 mm
Tool electrode polarity	negative

* Feed of the electrode is set on EDM machine and wear is not compensated

Table 3-15 shows experimental results: hole diameter and depth.

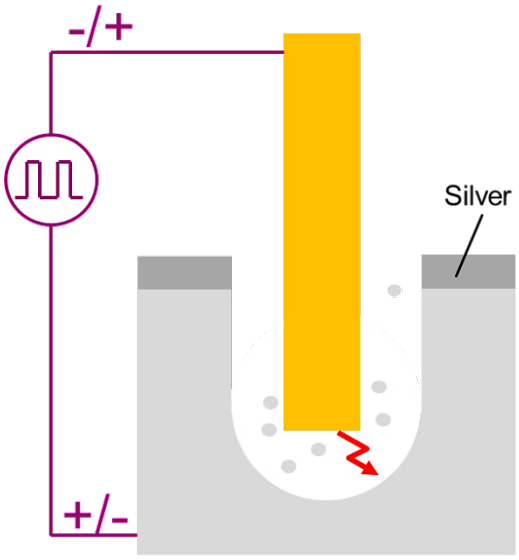

Fig. 3-29: SiC machining conditions. The workpiece electrode is coated with a silver layer in order to initiate the erosion process.

Table 3-15: Experimental results of hole depth and diameter of process parameters after SiC drilling.

Exp. no.	Parameter			Hole radius [µm]	Hole depth [mm]
	T_{on} [µs]	U_{open} [V]	I_d [A]		
1	8	200	16	341±4.5	1.87±0.01
2	8	250	16	293±1.6	2.41±0.02
3	8	200	24	285±0.8	2.81±0.02
4	16	200	16	312±22	1.22±0.06

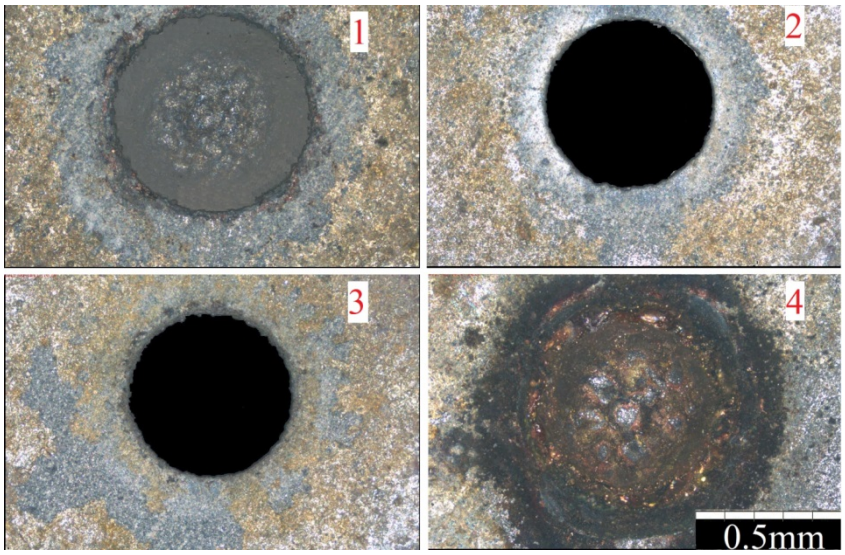

Fig. 3-30: Holes drilled in SiC, parameters are presented in Table 3-15. The diameter significantly varies depending on the process parameters, longer discharge duration increases the electrode wear, and its solidification can be seen at the 4th test. In experiments 2 and 3 the bottom of the hole is not visible due to the limit of the optical measurement.

The influence of the process parameters on MRR is shown in Fig. 3-31. The most significant positive effect on MRR has the ignition voltage U_i increase since it supports the discharge creation, which is spatially important during machining semiconductors. and the most significant negative effect on MRR has the pulse duration T_{on} increase. The highest MRR is found with 250 V ignition voltage and 8 µs pulse duration.

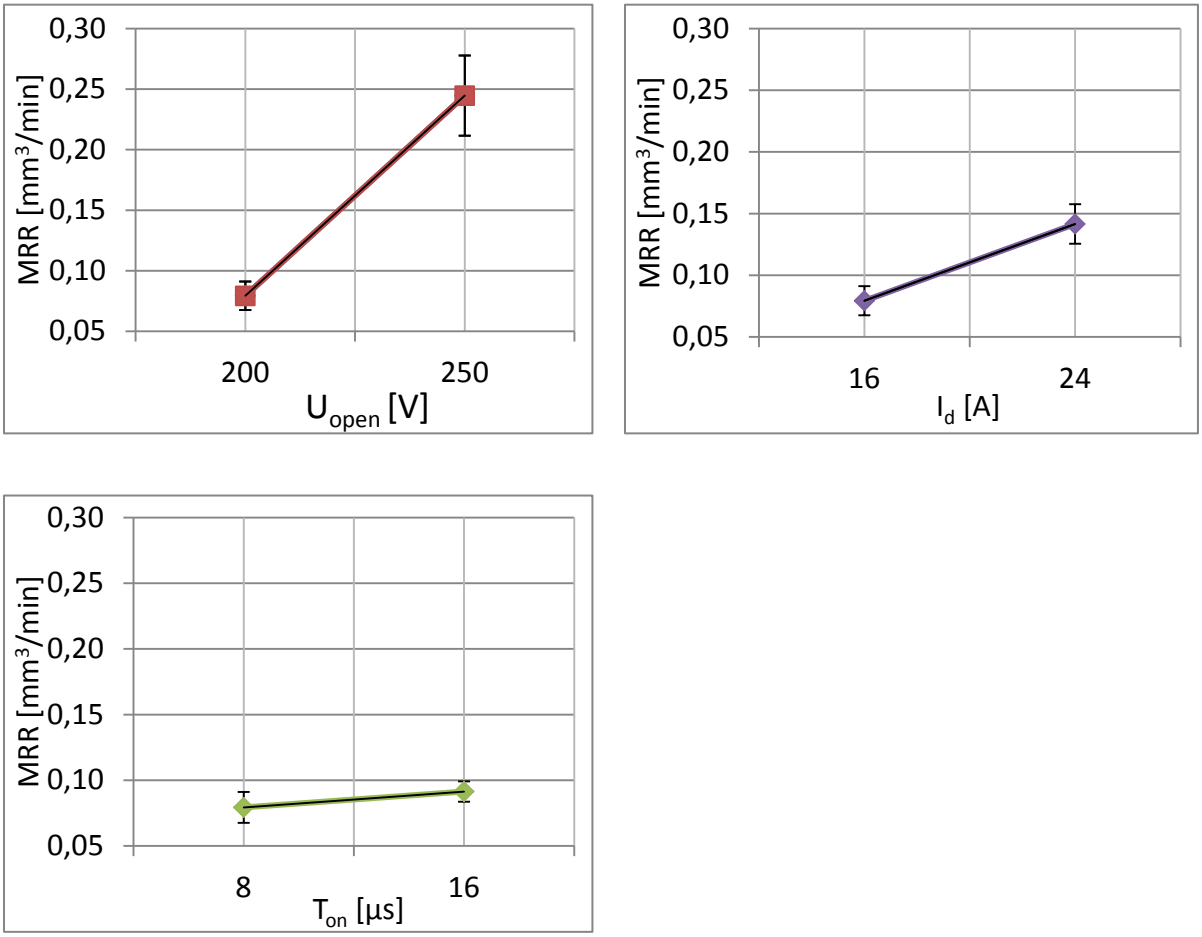

Fig. 3-31: Effect of increase of pulse duration, ignition voltage and discharge current on MRR for the erosion of SiC.

The influence of the process parameters on electrode wear is shown in Fig. 3-32. The most significant effect on wear reduction has the discharge voltage increase. The increases of time duration and current have the most significant negative effect on wear.

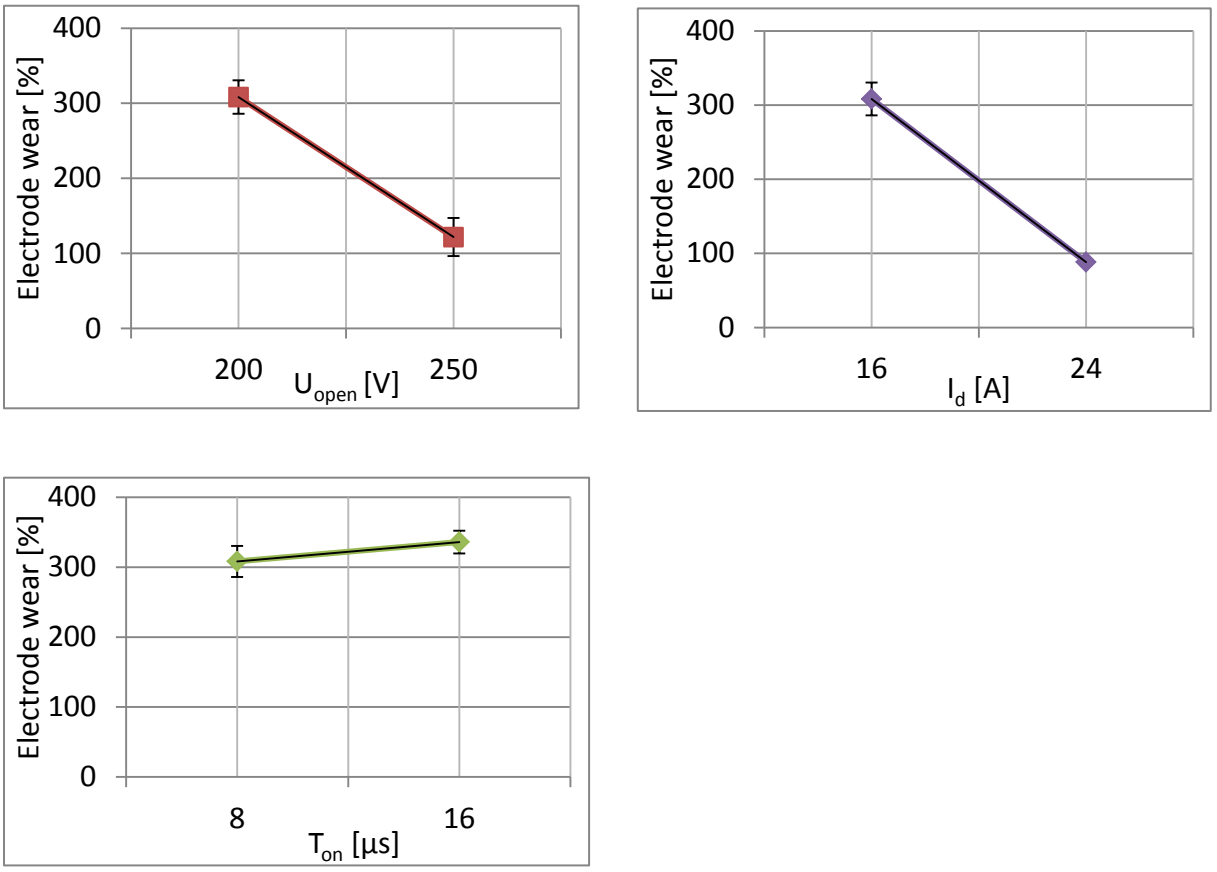

Fig. 3-32: Effect of increase of pulse duration, ignition voltage and discharge current on electrode wear for the erosion of SiC.

The longitudinal section of SiC after drilling is shown in Fig. 3-33 and Fig. 3-34. The material has a porous structure and solidified copper layer on the machined surface after erosion.

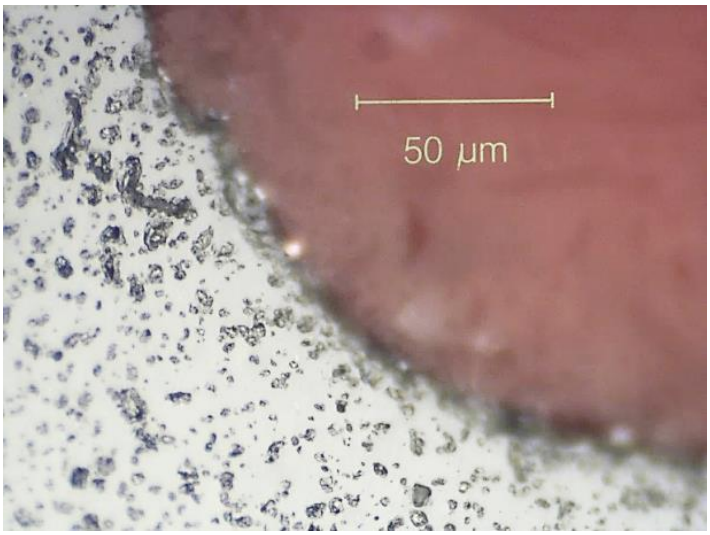

Fig. 3-33: Longitudinal section of an EDM drilled hole in SiC shows the corner after discharge, darker areas as it is shown in BSE image are precipitations of carbon. Erosion was made using the set of parameters N 3 of Table 3-15

Fig. 3-34: Longitudinal section of an EDM drilled hole in SiC, using deionized water as a dielectric, solidified copper (red areas) are found on the machined surface.

Before the erosion, the resistivity of the SiC was 100 Ω · cm which is considered by König [10] as a highest possible resistivity for EDM, after erosion of SiC material its specific resistivity was measured and the value is 50 Ω · cm. That effect can be caused by the influence of copper layer deposited on the eroded surface by erosion process. A similar effect is known from the sinking EMD. Electrical conductive compounds involving carbon from dielectric oil are generated on the surface of the ceramics. According to [37] it keeps electrical conductivity on the surface of the workpiece during the machining. The copper layer rapidly increases the electric conductivity by copper solidification on the machined surface and supports erosion stability. The increase of conductivity is particularly important for SiC, since the resistivity of this material is higher.

3.5.2 Erosion of semiconductors (SiC) in deionized water

By the assisting electrode method, blind holes in SiC are drilled using 1 mm diameter brass electrode in deionized water, as shown in Fig. 3-35. The process parameters are: t_{on} = 16 µs, t_{off} = 16 µs, I_d = 16 A, U_{op} = 200 V and polarity of the tool is negative.

The analysis of the eroded cavity surface revealed that the renewal of the conductive layer stems from the deposition of material from the tool anode, and the conductive copper layer was detected due to copper solidification on the workpiece. The conductivity of the renewed assisting layer was not caused by the temperature rise during the erosion process and was not changing with time. Further energy-dispersive X-ray spectroscopy (EDX) of SiC machined surfaces as shown in Fig. 3-35 reveal not only copper solidification on the workpiece, but also penetration of copper into the top layer of the material.

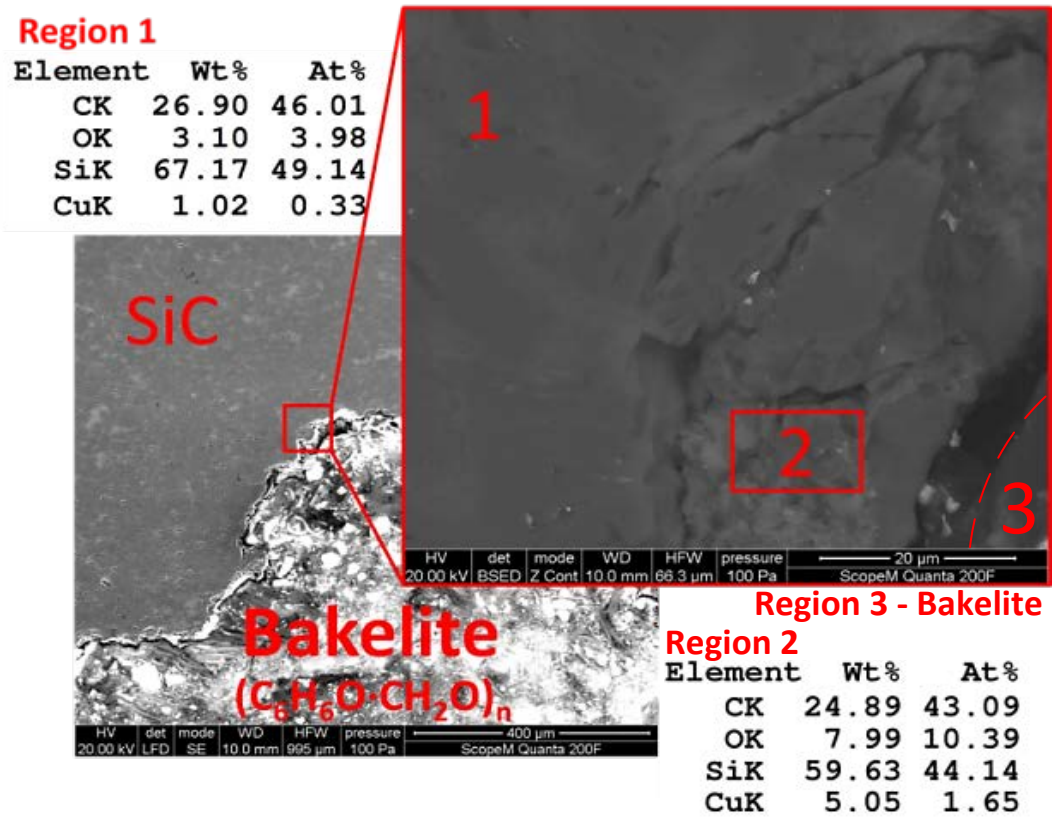

Fig. 3-35: Polished longitudinal section of the eroded surface to analyse the surface and sub-surface process effect on the SiC material. The zone 2 has about five times more copper concentration than in zone 1. The specimen is mounted in bakelite in order to be polished.

EDX analysis of the heat affected region 2 and the region 1 nearby from the bulk material revealed that the zone 2 has about five times more copper concentration than in the zone 1. Thus, electrical conductivity increases not only due to copper solidification on the workpiece but also by copper penetration into the material. Also, cracking due to the process heat is clearly visible in the region 2, which additionally supports that spalling is one of the main material removal mechanisms for such materials.

3.6 A new method of electrically non-conductive material erosion

Erosion of hard to cut, conductive materials is naturally the field where EDM has an advantage since the process depends more on thermal and electrical conductivities than on hardness and stiffness. EDM drilling of Inconel is well known and researched in the literature, but the state-of-art Inconel turbine blades have the thermo-isolative coating which is at the same time not electrically conductive. Erosion of such a layer is one of the limitations which EDM has to overcome in order to machine diffusors and film cooling channels in coated Inconel turbine blades.

EDM drilling experiments are carried out by Drill 300 GF Machining Solutions, Agie Charmilles SA, where deionized water is used a dielectric. EDX analysis is performed using SEM Quanta 200F FEI; optical microscopy is performed using Alicona Infinite Focus and Keyence VHX-5000. The experimental setup is based on the assisting electrode method,

where the conductive layer is applied to the surface of the electrically non-conductive workpiece, and discharges take place between the tool electrode and assisting electrode. The 20-40 µm silver layer (the specimen is coated with silver by a paintbrush and steel foil is placed on the top).

EDM of ZrO_2 in deionized water is nearly impossible with conventional assisting electrode method since the initial assisting layer cannot be renewed by a carbonaceous layer. Therefore, a new conductive layer is proposed to be deposited from the tool electrode, using the phenomenon observed while EDM of SiC. An erosion condition of electrically non-conducting materials in deionized water is shown schematically in Fig. 3-36. Here, a conductive silver layer is used as an assisting electrode to initiate the erosion process.

Stable erosion is empirically found with the set of parameters presented in Table 3-16. Process parameters for ceramics machining in deionized water are based on the electrode dressing strategy, as presented [88] and described in details in section 3.1.

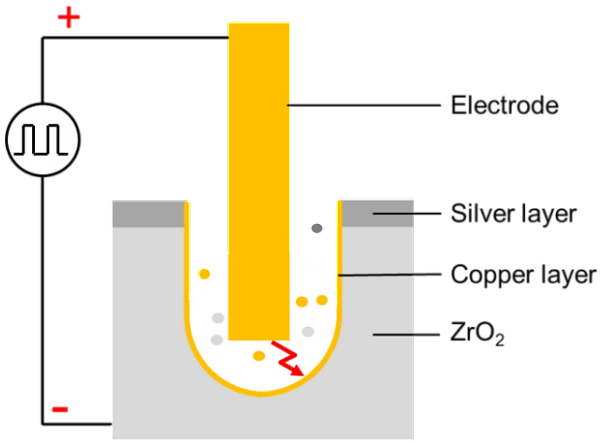

Fig. 3-36: Schematic representation of electrically non-conducting material erosion in deionized water. The electrical conductivity increases due to copper deposition from the electrode on the workpiece.

The dressing strategy is developed to rapidly remove the tool-electrode material to achieve similar to the original electrode front shape, as it is described in section 3.1. It is found that during the erosion using these parameters, the eroded material from the tool electrode re-solidifies on the workpiece surface, creating a thin layer. The thickness of such coating is further increased by lowering the open/ignition voltage since the gap between the electrodes decreases and molten copper in the plasma region has a higher tendency to re-solidify on the workpiece surface compared to being flushed away from the erosion region. The significant aspect of the described method is the balance between material removal and regeneration of assisting conductive layer.

Table 3-16: Main EDM process parameters used for Yttrium stabilized ZrO_2

Parameter	value
T_{on}	487 µs
T_{off}	50 µs
I_d	0.8 A
pol	+
U_{open}	40 V

A hole drilled in Zirconia using 1 mm diameter electrode with 1.5 mm depth is shown in Fig. 3-37. Several holes are machined using the described conditions and process parameters to ensure the repeatability and viability of the method. The machining time for each hole is about two hours. Drilling of even deeper holes is found to be challenging due to insufficient flushing in the experimental setup. The flushing through the internal electrode channels is off to support copper deposition.

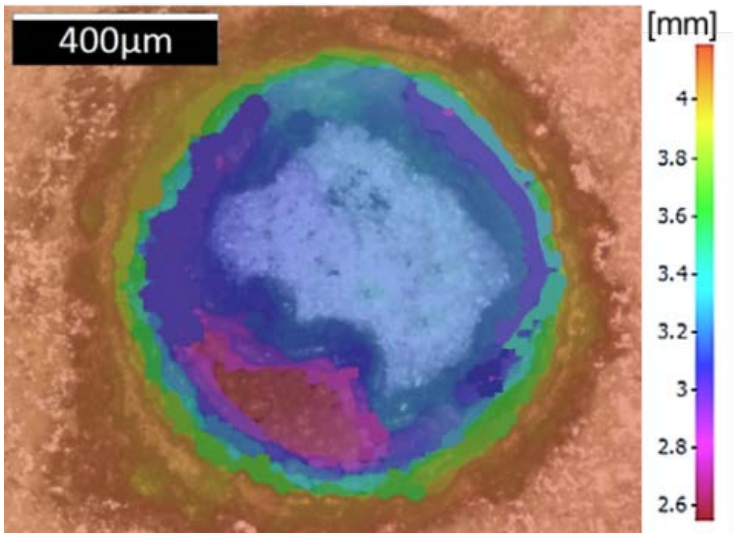

Fig. 3-37: Top view in height profile of a blind hole machine in ZrO_2, where the total hole depth is 1.5 mm.

The erosion of electrically non-conducting materials in deionized water combines two processes: EDM and electrical discharge coating (EDC). EDC was investigated by Suzuki [110], where the coating of the high-speed steel workpiece was performed by TiC from the tool electrode. It was found by Suzuki [110] that when the voltage signal remains constant, the TiC coating is localized in the crater area, whereas if the voltage drops during the discharge the amount of adhesion is higher. This reopening effect was explained by Suzuki as a reduction of the gap, this reduction could also cause short circuits at which the electrode material deposition on the workpiece is usually significant. A similar effect is found during machining in deionized water in the current work, from which the electrical signals are shown in Fig. 3-38.

Similar to EDC tests by Suzuki, the material deposition presumably occurs during voltage drops, when the plasma channel closes and opens again. Series of voltage drops are probably caused by short circuits. The decrease in the gap is aimed to enhance this reopening effect. It is also experimentally proven, that the increase of current is changing the balance from material removal to more deposition [110].

The machined surface of ZrO_2 is investigated with an optical microscope and with EDX. The results are shown in Fig. 3-39 and Fig. 3-40 respectively. After erosion in dielectric oil, the machined surfaces contain a significant amount of carbon. While after machining in deionised water, a layer of copper is found, it is also found that copper is not only deposited on the surface but also penetrates into the workpiece material within a heat affected zone similar to the erosion of SiC. Thus, the assisting electrode transforms during the erosion process into two conductive layers: in the top layer where copper dominates and in the layer where it is mixed with the bulk material.

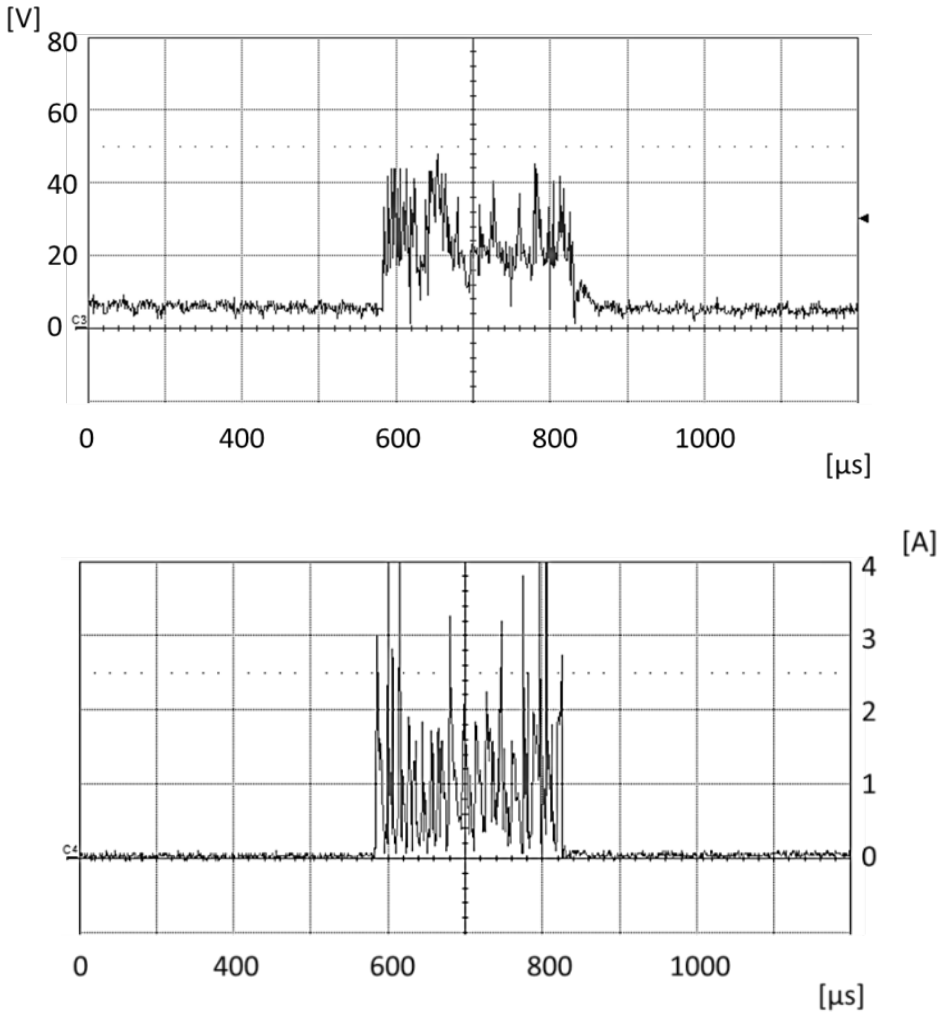

Fig. 3-38: Voltage (top) and current (bottom) signals during ZrO_2 ceramics erosion. The material deposition presumably happens during voltage drops, while series of voltage drops are caused by gap reduction. The gap reduction can be caused by electrode vibrations and servo-movements during the process.

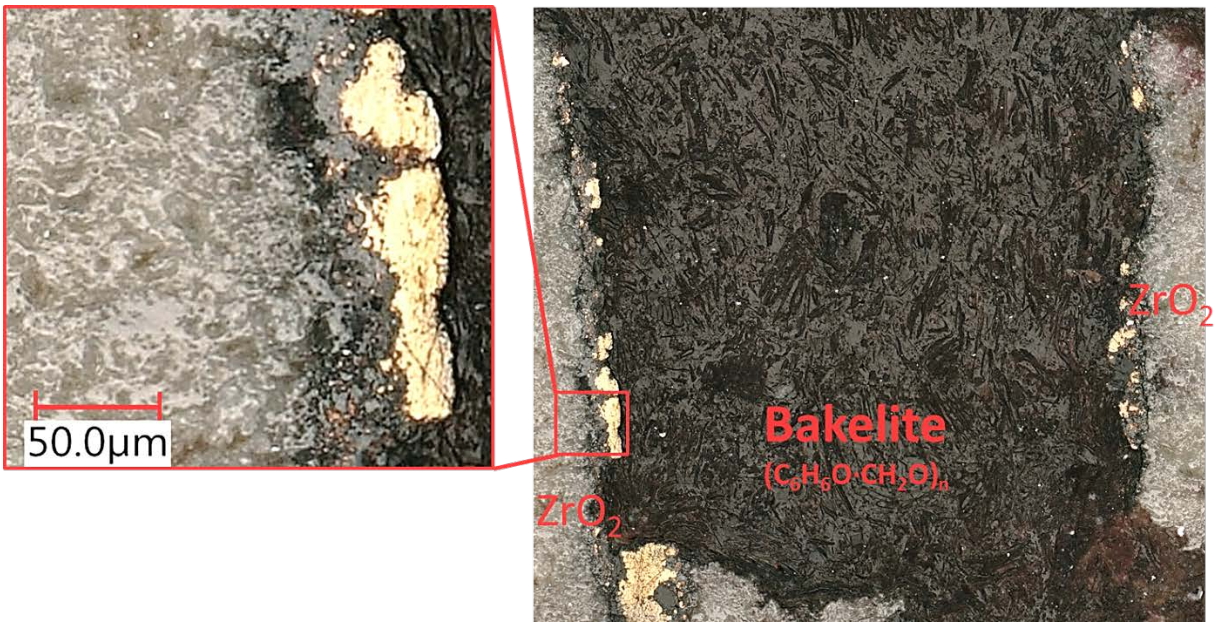

Fig. 3-39: Optical observation of copper layer on the longitudinal-section of the hole, drilled in zirconium dioxide. The specimen is mounted in bakelite in order to be polished.

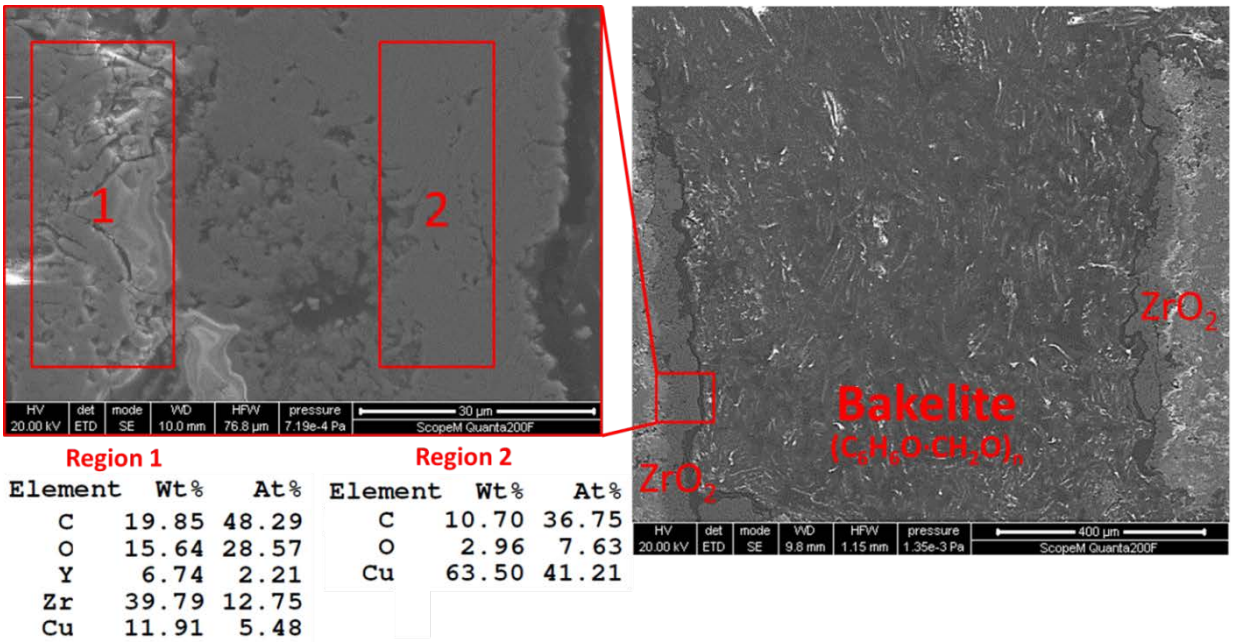

Region 1

Element	Wt%	At%
C	19.85	48.29
O	15.64	28.57
Y	6.74	2.21
Zr	39.79	12.75
Cu	11.91	5.48

Region 2

Element	Wt%	At%
C	10.70	36.75
O	2.96	7.63
Cu	63.50	41.21

Fig. 3-40: EDX investigation of the copper layer on the longitudinal-section of the hole drilled in ZrO_2. The assisting electrode layer consists of two conductive layers. Copper from the tool-electrode is not only deposited on the surface but also penetrates into the material in the heat affected zone. It is seen, that the conductive layer is presented on the entire lateral surface of the hole.

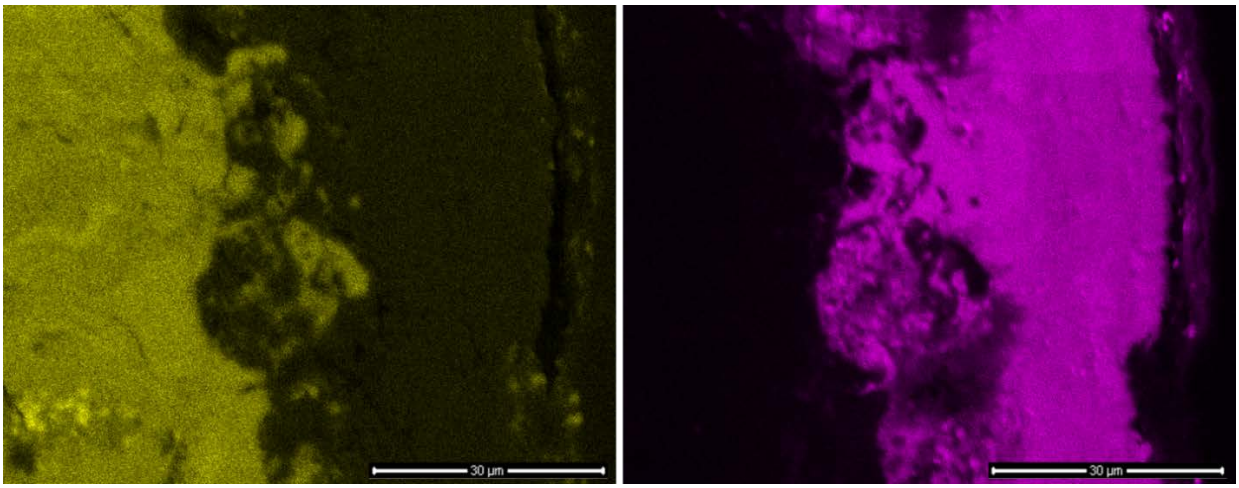

Fig. 3-41: EDX mapping of the selected zone on Fig. 3-40, which shows the distribution of elements, Zirconium is on the left and Copper is on the right.

After a series of investigations into the erosion of electrically non-conductive ceramics, the following conclusions can be drawn:

It is possible to machine 1.5 mm deep holes in electrically non-conducting materials in deionized water, using the assisting electrode method, with the renewal of the assisting electrode by deposition of material from the tool anode instead of hydrocarbon oil. Further removal is challenging due to the insufficient flushing conditions in the experimental setup.

The material deposition presumably occurs during the series of voltage drops, which are indicative of short circuit conditions. The discharge time is increased to 487 µs (limit of the generator) in order to further increase the deposition rate.

The material removal mechanism of ZrO_2 in deionized water is a combination of several phenomena consisting of melting, vaporization due to electrical discharges and thermal stresses which cause micro-cracks and spalling.

3.7 Spark location in EDM drilling

EDM is often used for drilling deep, high aspect ratio holes (depth of the hole is more than 10 times bigger than the diameter of the tool). The vibrations of the electrode in such a deep hole can be caused by lateral discharges during the drilling process. The reduction of the lateral discharges should increase the roundness of the hole and at the same time reduce electrode wear and recast layer of the hole. The method of lateral and corner spark detection was described by Maradia [111]. This method is based on voltage level measurements in meso-micro die-sinking EDM. As it was shown by Maradia, the sparks located on the corner of the electrode have a lower mean discharge voltage level, and the sparks located on the lateral side of the electrode have a higher mean discharge voltage level. The measurement window is shown in Fig. 3-42.

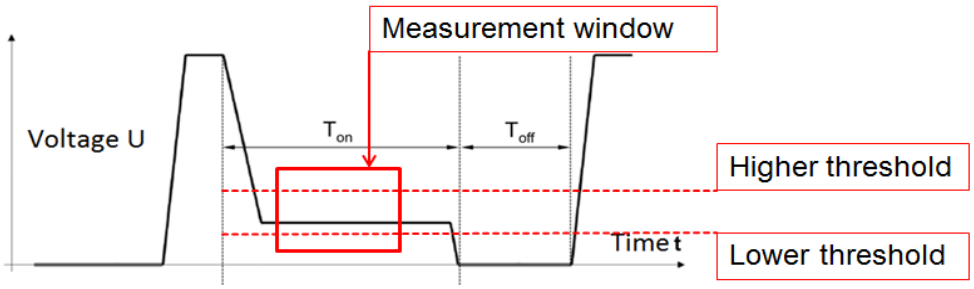

Fig. 3-42: The method of spark location characteristic based on lower and higher thresholds in the measurement window on the voltage signal. The sparks with the voltage under lower threshold have a higher probability to locate on the corner of the electrode and with the voltage upper higher threshold have a higher probability to locate on the lateral side of the electrode.

Voltage is measured with Teledyne Lecroy WaveRunner 640Zi oscilloscope, which has a resolution of 40 GigaSamples/s on 2 channels. The average voltage levels are compared during the EDM drilling process in order to analyse the distribution.

The voltage levels after 500 measured sparks are compared with the levels after 3000 sparks and further during the erosion process. The voltage between 12 V and 14 V is in the is moving to the next level between 14 V and 16 V and further to the region between 16 V and 18 V after 3000 sparks. The increase of the average voltage during the erosion process indirectly confirms the potential of higher threshold implementation.

For the further investigations in drilling tests, the voltage higher threshold levels are selected (namely 22.5 V, 20 V, 17.5 V). The experimental conditions are selected the same as in section 3.3. Experiment results are in Fig. 3-43. The comparison of two holes with the thresholds of 20 V, and 17.5 V are in Fig. 3-44:.

The reduction of higher voltage threshold shows a clear trend to reduce RLT and electrode wear. The most significant (more than 30%) reduction of RLT is found during voltage level change from 22.5V to 20V. The reduction of the recast layer correlates with the reduction of hole radius. Significant reductions in electrode wear and MRR are also detected.

On the one-hand experiments clearly show the trend to increase surface integrity, which is indicated by the reduction of RLT on the other hand MRR reduction shows that not only lateral sparks were prevented.

Summarising, the utilisation of the spark location algorithms is limited in EDM drilling since the achieved reduction of the recast layer and electrode wear is accompanied with the decrease of MRR. The same effect can be achieved by the reduction of the pulse energy. The desired quality of the hole decides on the achievable MRR.

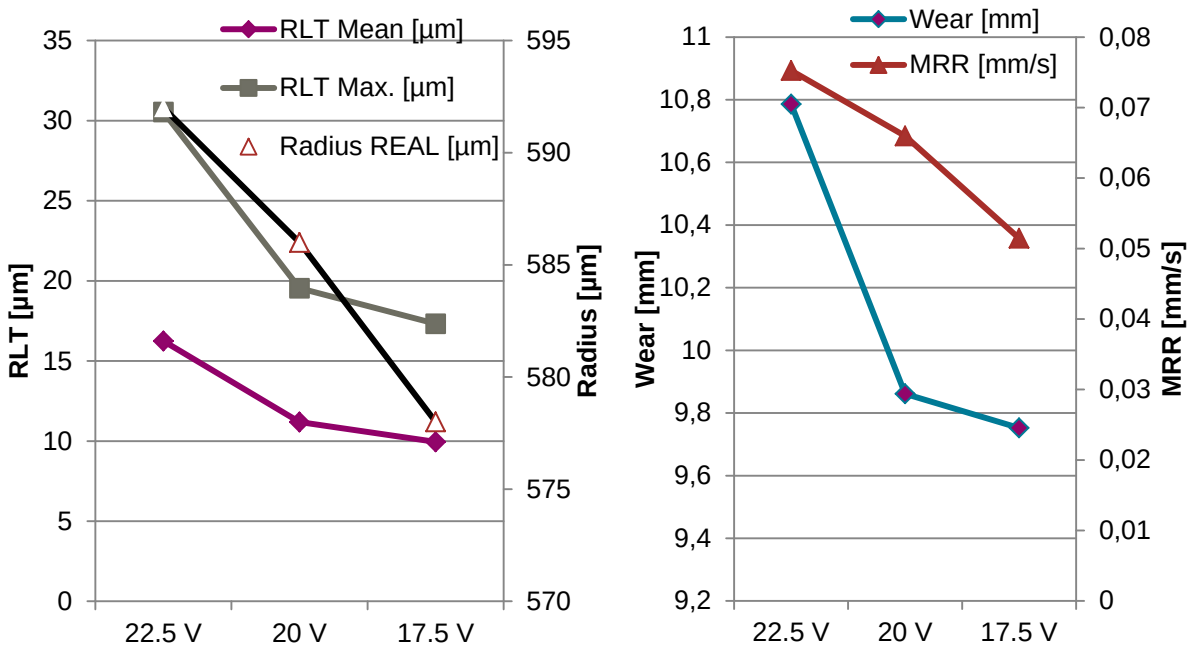

Fig. 3-43: Left: the dependence of recast layer thickness and radius of the drilled hole on the applied voltage threshold. Right: the dependence of MRR and electrode wear on the applied voltage threshold. Sparks above upper threshold are stopped as soon as detected.

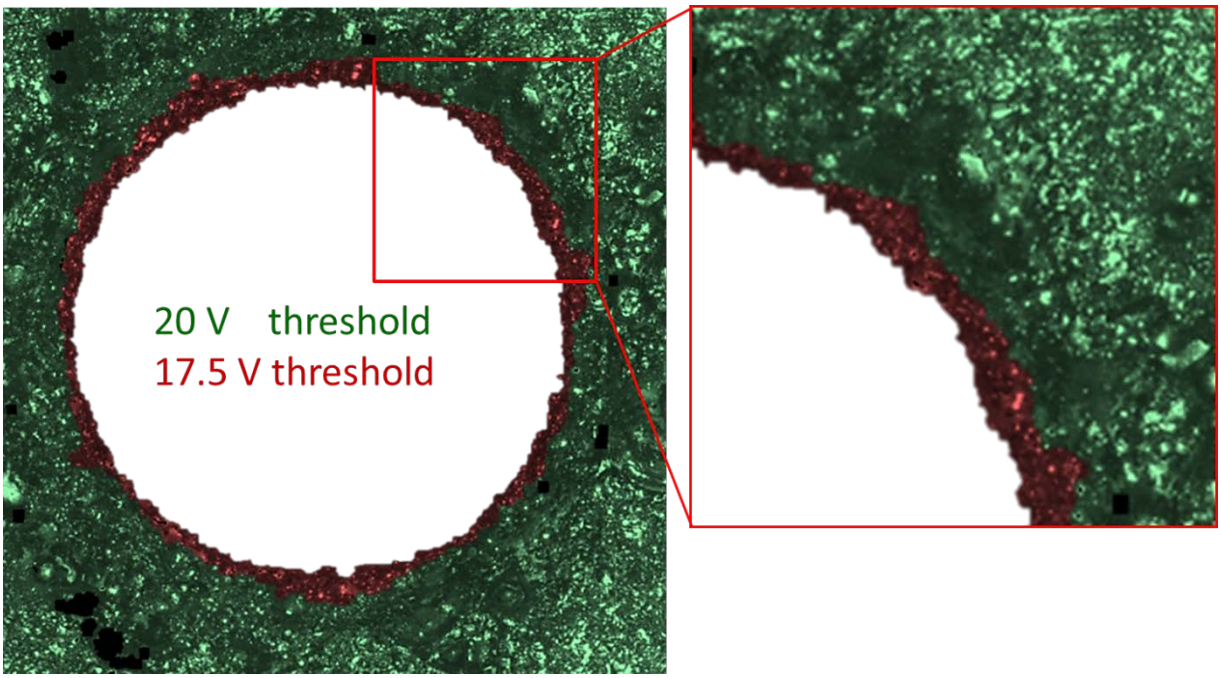

Fig. 3-44: The holes cross-sections drilled with 20 V threshold (green, R=625 µm, Rona=14.5 µm, Ronq=17.6 µm) and 17.5 V threshold (red, R=576 µm, Rona=4.1 µm, Ronq=5.7 µm). The diameter of the hole decreases with the reduction of the higher voltage threshold.

4. EDM milling

This chapter explores and extends the abilities of a commercial EDM drilling machine to be used in the milling and shaping applications, increases the performance to machine film cooling holes, diffusers and seal slots on the turbine blade. The layer-by-layer strategies to machine diffusors are investigated and combined with drilling experiments, which are previously described in chapter 3. A new strategy to machine seal slots for aeroengines is developed. Strategies described here allow machine film cooling holes and seal slots on one machine without reclamping.

Parts of this chapter have been published [48, 88, 112, 113].

4.1 EDM layer-by-layer milling of Inconel 718

One of the potential applications of the EDM drilling machine is in shaping diffusors, by combining shaping and drilling it is possible to machine film cooling of the turbine blade on one machine. This section investigates in machining strategies of Inconel 718, which is one of the most used materials of the turbine blades.

The uniform wear method introduced [49] as shown in Fig. 4-1 is applied for the shaping of Inconel 718. A standard electrode of cylindrical shape is used to produce a complex shape as layer-by-layer machining. The depth of layers influences the quality of the shape and the MRR of the machining process. Naturally, the best condition for the shape precision would be to keep the thickness of the layers near the gap width between electrode and workpiece. But then the MRR and productivity will be very low. The other extreme will be the maximization of the MRR, which is achieved when the thickness of the layer is in the range of the radius of the electrode. This limitation occurs because during the shaping process the top of the electrode becomes round and the roundness depends on the electrode size. If the thickness of the layer is higher than the electrode radius, then the electrode erosion will start to happen on the lateral part, and it will change the shape condition of the electrode unpredictably.

It has to be mentioned that electrode wear depends on the type of machining, as it is shown in Fig. 4-2, on machining parameters and on the volume of the removed material. Taking all mentioned above into consideration, an electrode dressing step has to be performed in order to verify the machined geometry.

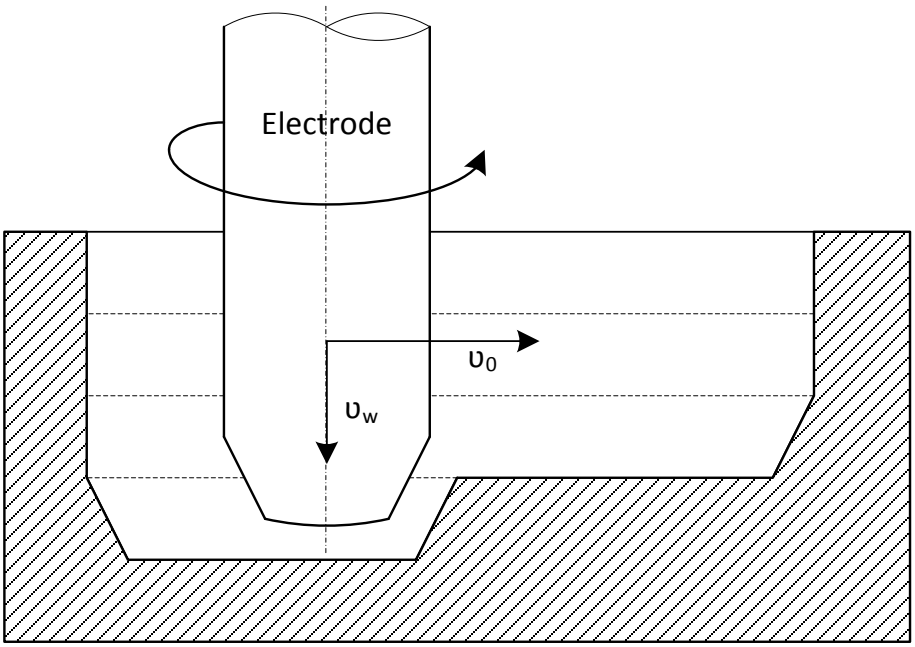

Fig. 4-1: Layer-by-layer machining. The electrode is rotating, the vector of wear compensation and the vector of feed rate in machining are shown.

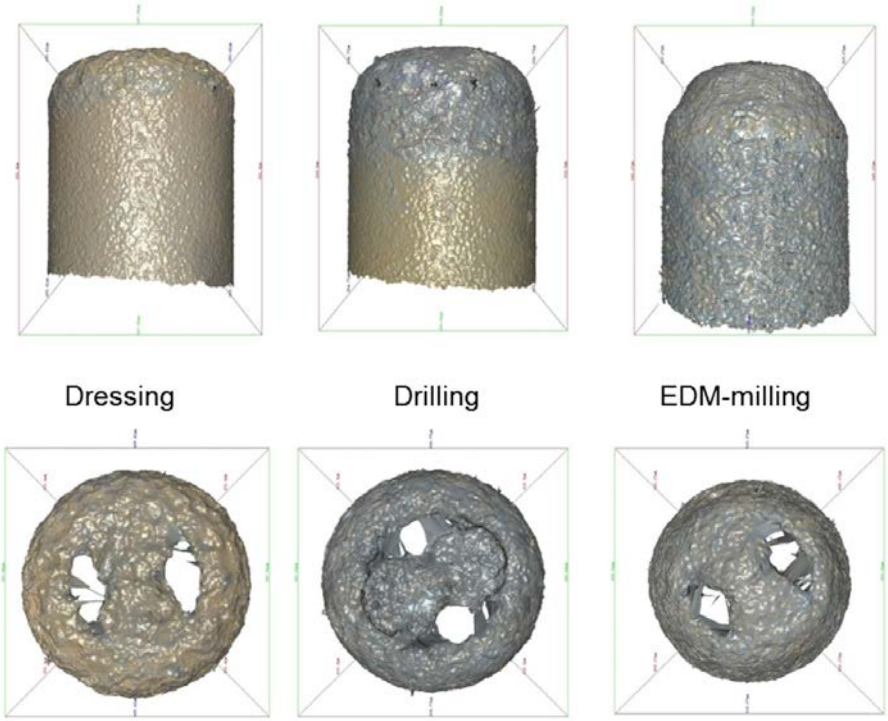

Fig. 4-2: Electrode wear pattern of 0.5 mm diameter multi-hole electrode. The tapered shape of the electrode tip can be clearly recognised after the EDM-milling, while after dressing and milling the electrode has a round shape. Graphical representation is given in Fig. 4-3

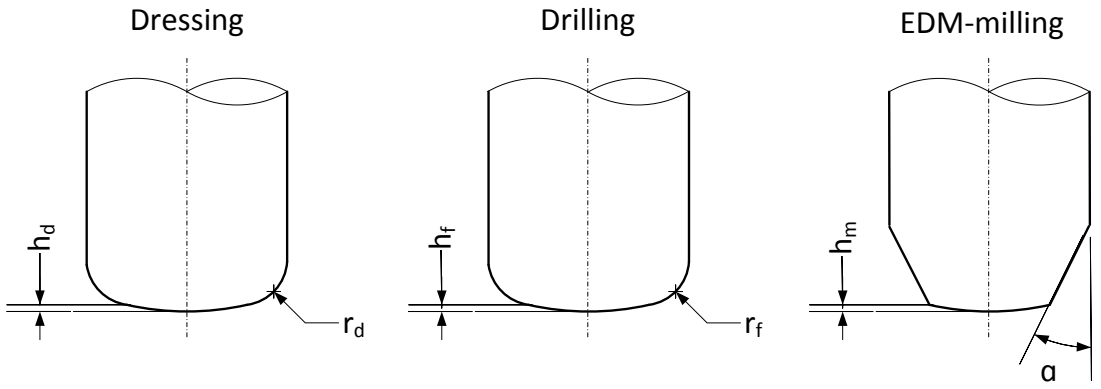

Fig. 4-3: Graphical representation of the electrode wear pattern, where h_d, h_f and h_m are all varies between 80 µm and 120 µm; α is 30±3˚.The electrode wear information is based on microscopic measurements.

A pocket made by EDM layer-by-layer shaping is shown in Fig. 4-4, the shape is selected in order to study the overlapping of machining passes. The total depth of erosion is 0.5 mm, and the shape is produced in three layers. The roughness S_a of the bottom surface is less than 1 µm. The electrode path is shown by solid lines, and the finishing path is shown by dashed lines. Finishing is performed to mitigate waviness. Machining parameters are selected based on the analysis in section 3.3.

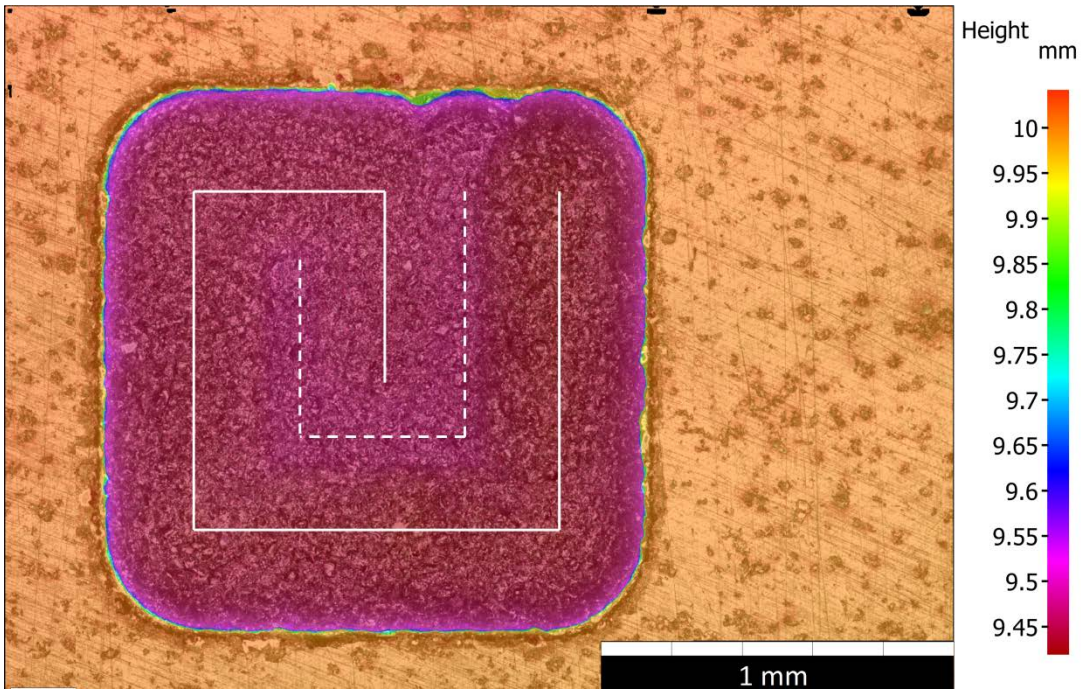

Fig. 4-4: EDM layer-by-layer shaped pocket in Inconel 718, dash-line shows a finishing pass to prevent waviness. Graphical representation is given in Fig. 4-5.

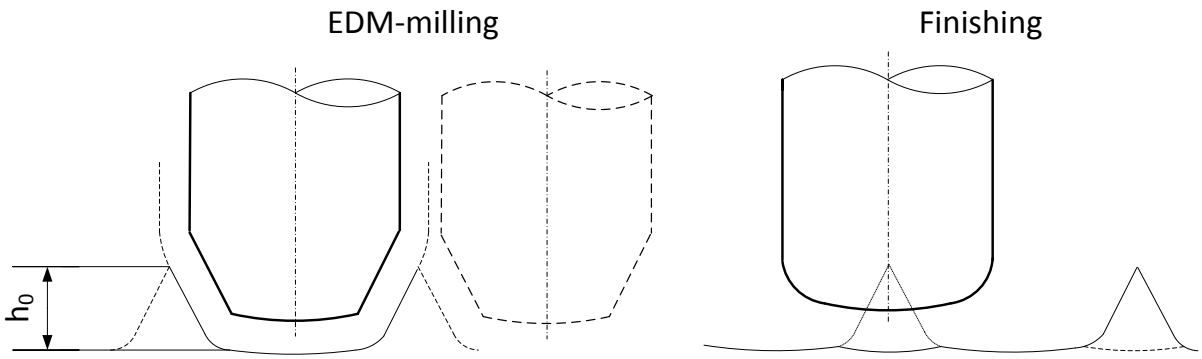

Fig. 4-5: Graphical representation EDM-milling is on the left and finishing is on the right. h_0 is equal to the layer thickness.

Another more complicated case is the diffusor, several diffusor shapes are in Fig. 4-7, Fig. 4-8, Fig. 4-9. It is made using the same layer-by-layer strategy as in the previous test, and the workpiece is tilted by 45°. The lateral part of the shape has a waviness from the chosen layer-by-layer strategy and can be improved by the reduction of step size between layers or using the same angle as the wear angle α, as it is shown in Fig. 4-10.

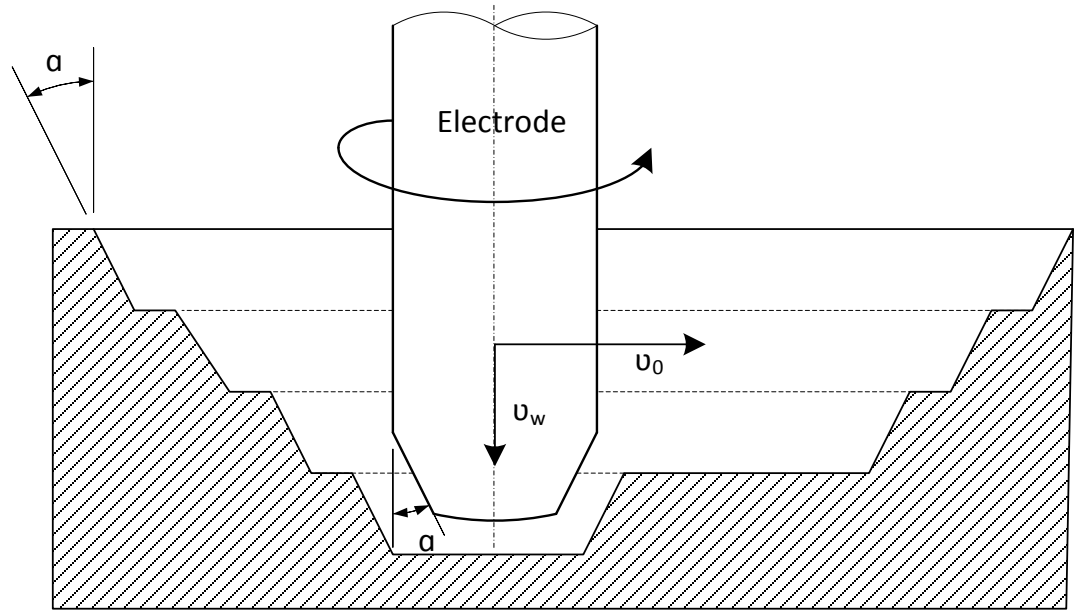

Fig. 4-6: Schematic representation of conical cavity machining under lateral cavity inclination angels above α.

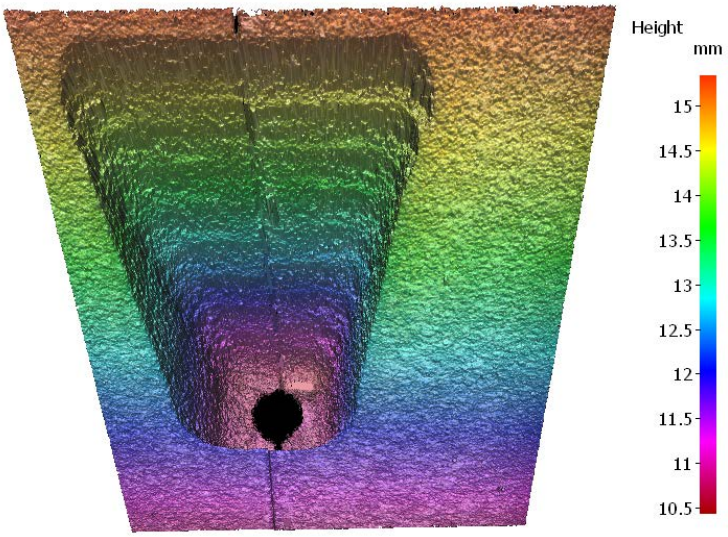

Fig. 4-7: EDM shaped diffusor in Inconel 718 under 20˚ inclination with the layer-by-layer strategy. The longitudinal-section is shown in Fig. 4-8.

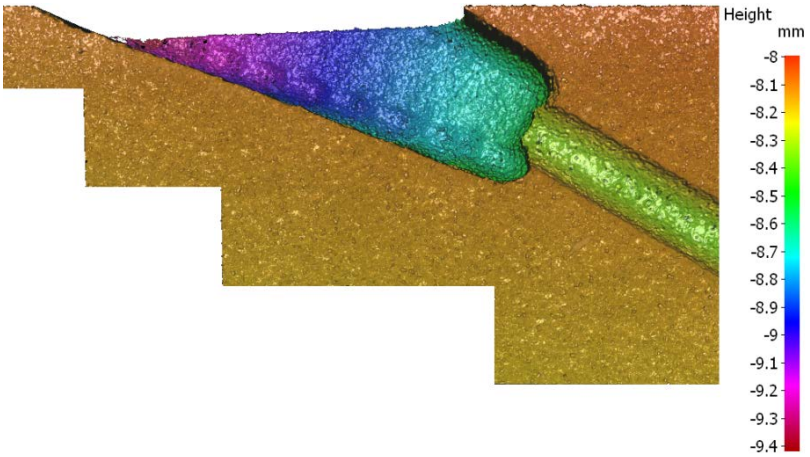

Fig. 4-8: Longitudinal-section of an EDM shaped diffusor in Inconel 718 under 20˚ inclination with the layer-by-layer strategy.

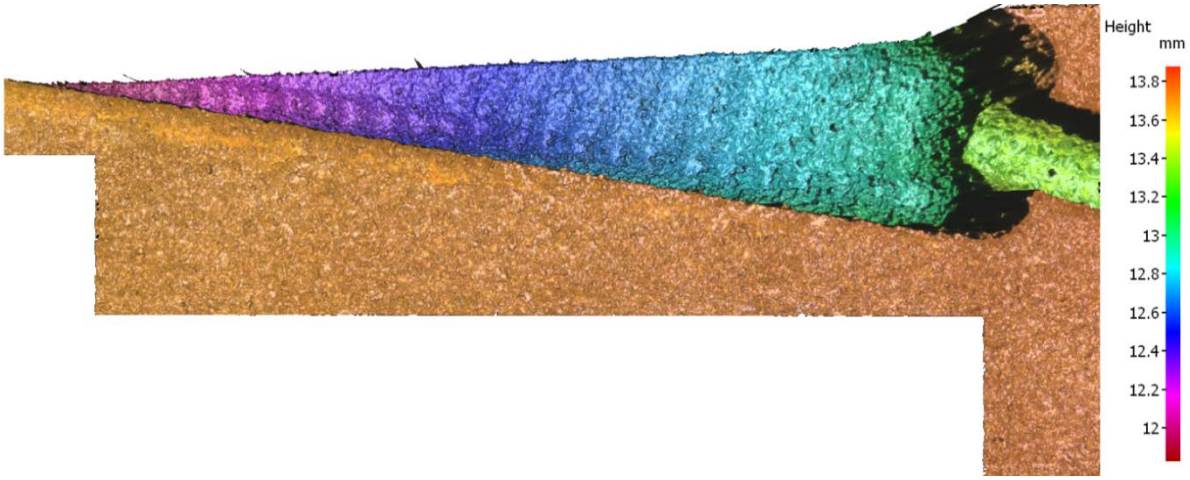

Fig. 4-9: Longitudinal-section of an EDM shaped diffusor in Inconel 718 under 10˚ inclination with the layer-by-layer strategy.

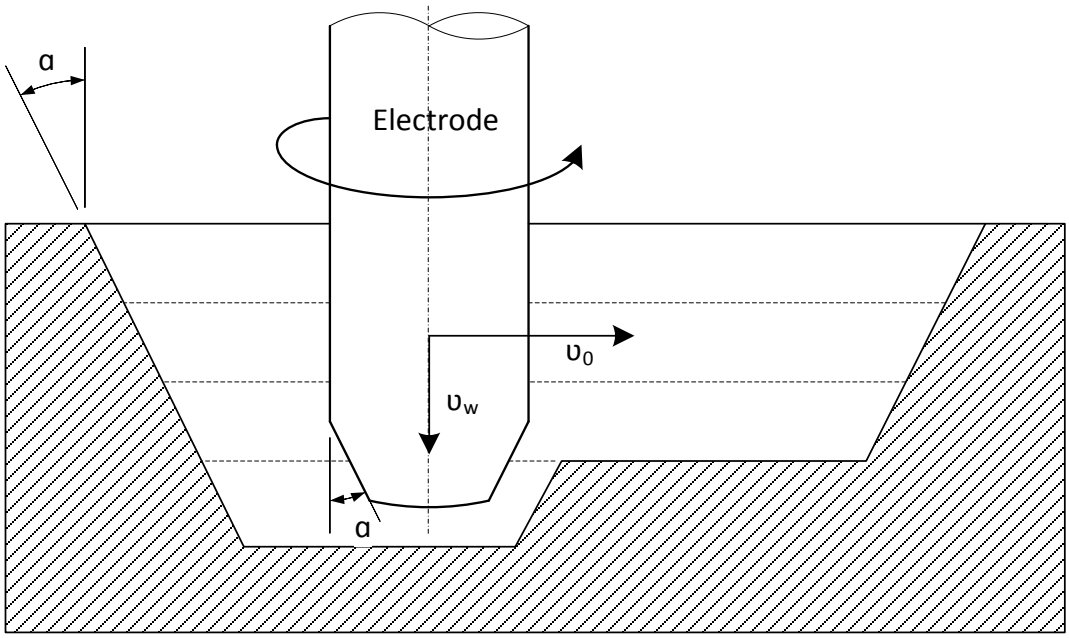

Fig. 4-10: Schematic representation of a conical cavity machining, where the waviness on the lateral side can be avoided.

In Fig. 4-11, the longitudinal-section of the diffusor is shown. The recast layer on the shaped part of the diffusor is even lower than in the drilled hole. For the drilling and milling parts, the strategy to minimise the recast layer is used based on the analysis in section 3.3 (T_{on} = 32µs, I_d = 18A).

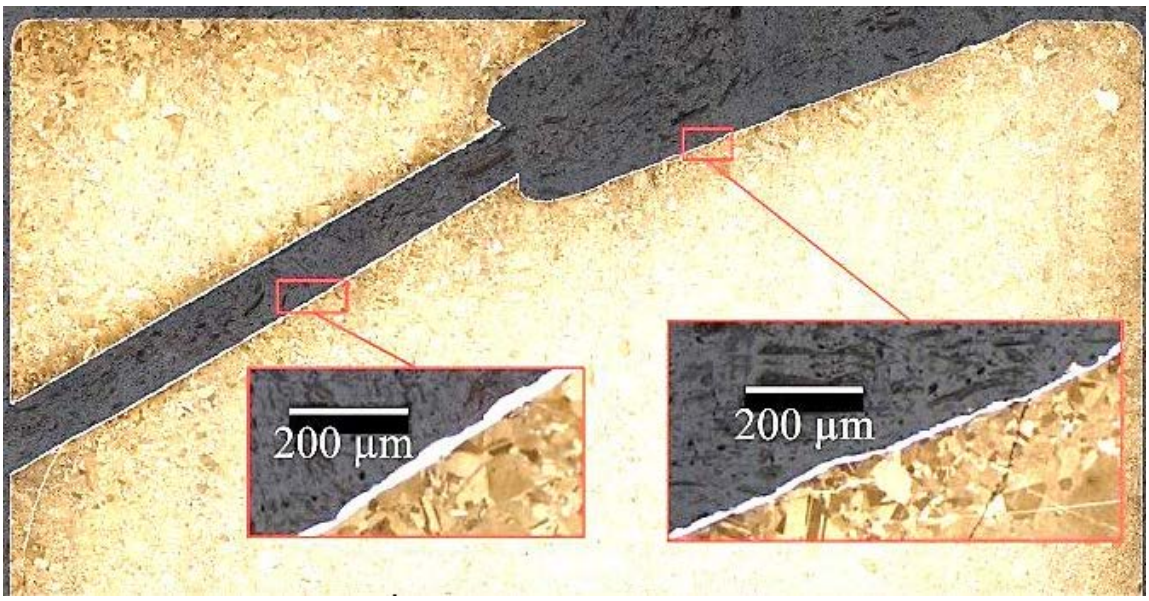

Fig. 4-11: Longitudinal-section of diffusor in Inconel 718 for recast layer analysis.

4.2 SiC and SiSiC shaping

Another essential material of the turbine blade is SiC since SiC/SiC CMCs are becoming the material of the new generation for the turbine blades. In order to investigate the

machining abilities of such materials by EDM, the shaping of SiSiC is investigated. The parameters for shaping are selected as ignition voltage 120V, pulse duration 2 µs and negative electrode polarity, based on drilling of SiSiC tests in section 3.3. The electrode diameter in this test is 0.5 mm, and the depth of the trace is 0.25 mm (the same as for Inconel 718).

The experiment showed a minimal difference between drilling and shaping of SiSiC and the suitability of using the same set of parameters. The result of the shaping test is shown in Fig. 4-12. The comparison of the diffusor machined in SiSiC and diffusor machined in Inconel 718 is shown in Fig. 4-12. This experiment shows that shaping of the diffusor in Inconel and in SiSiC is feasible.

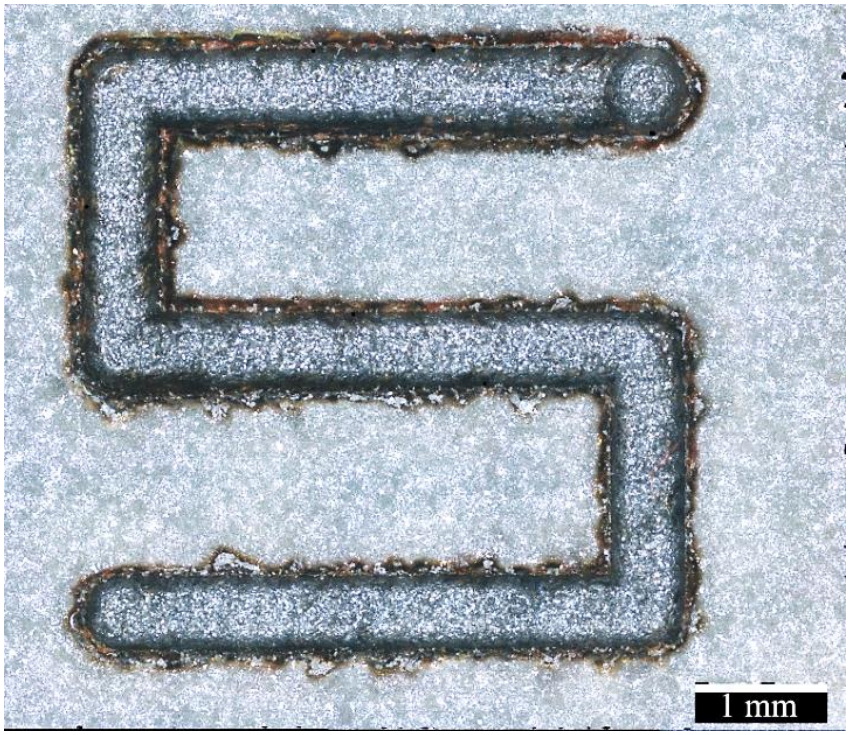

Fig. 4-12: Shaping of SiSiC. The shaping test showed a minimal difference between drilling and shaping parameters of SiC. Pulse parameters remain the same except of the pause duration which is doubled in order to increase process stability.

4.3 CMC layer-by-layer slot milling

Machining of CMC materials is analysed in this section in order to understand the main influences of the EDM process to the surface roughness and analyse the potential limitations. CMC materials provided by Schunk AG are used. SEM/EDX analysis is performed for two materials, and the results of CMC material analysis is found in Table 4-1, and EDX mapping is in Fig. 4-13, all fibres consist of 98% of Carbon and 2% of Oxygen, with the exception of CF226 where all the matrix is made out of SiC.

Table 4-1: Results of SEM/EDX analysis of Schunk AG materials.

Material identification number	Atomic fibre composition	Atomic matrix composition
CF 226/2 P77	98% C; 2% O	64% Si; 35% C; 1% O
CF 226 P75	98% C; 2% O	60% Si; 39% C; 1% O

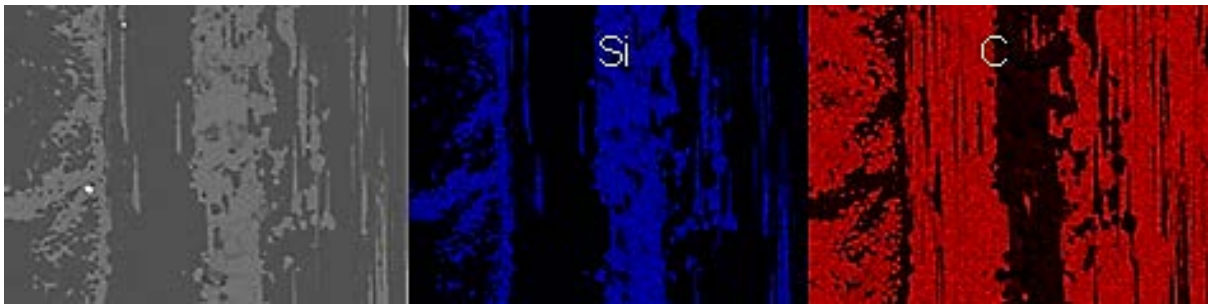

Fig. 4-13: EDX of CF226P75, CMC's fibres for 98% made out of carbon, and the matrix consists of silicon and carbon.

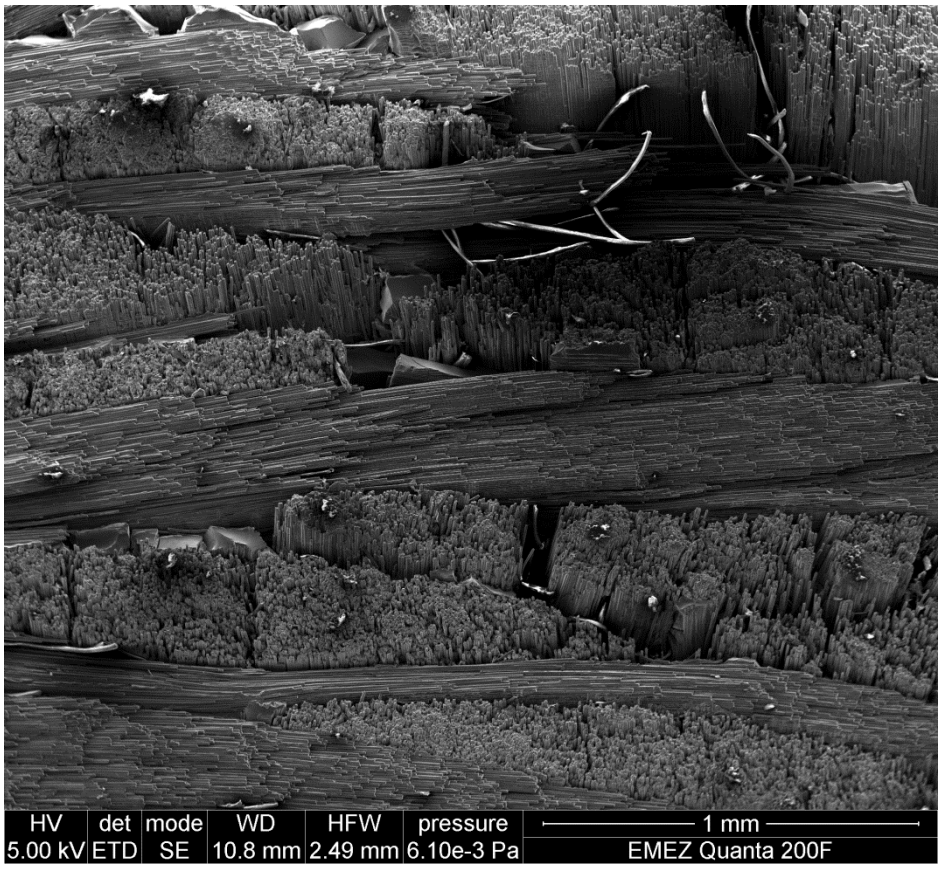

Fig. 4-14: Energy Dispersive X-Ray Analysis (EDX) of CF226P75 CMC material by secondary electrons (SE) detector.

Two analysed materials: CF226P75 and CF226/2P77 are further selected for layer-by-layer milling by 0.5 mm electrode. The CF226P75 material has internal cavities (probably due to the manufacturing process of the material), which have a significant influence on the

resulting slot and roughness measurements. The second type of CMC materials is analysed with the same parameter set and the same lengths of the slot. Slot in CF226P75 is shown in Fig. 4-15 and slot in CF226/2P77 CMC material is shown in Fig. 4-16. Process parameters T_{on} = 1.51 µs; I_d = 2 A are selected based on the information collected form SiC machining in section 3.5. The CF226/2P77 CMC material is selected for more detail analysis due to lower volume of internal cavities.

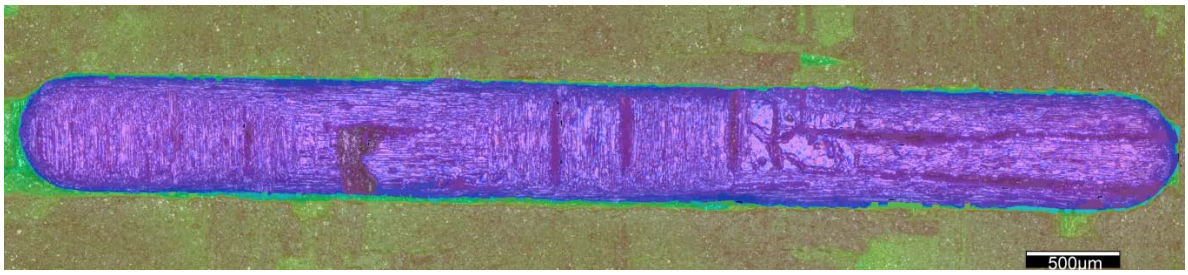

Fig. 4-15: Slot in CF226P75 CMC material, S_a= 9.5 µm, depth is 580 µm.

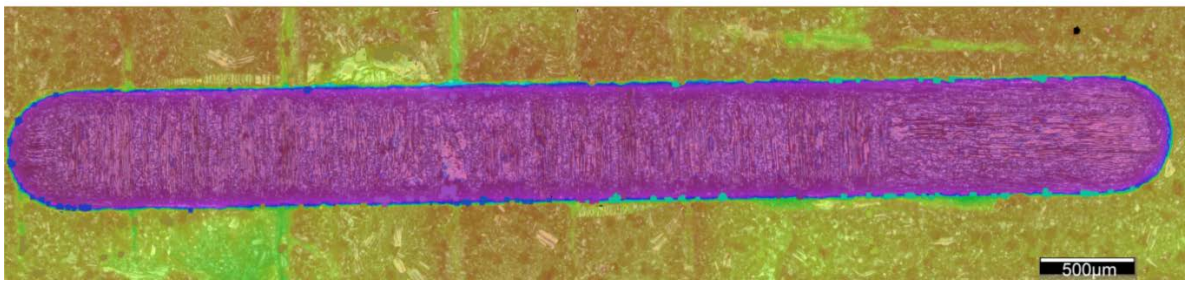

Fig. 4-16: Slot in CF226/2P77 CMC material, S_a= 3.1 µm, depth is 712 µm. Lower measured roughness is caused by a more homogeneous material structure.

The parameter study was performed for slot shaping analysis for CF226/2P77 CMC. The main process parameters and the results are in Table 4-2. The influence of discharge current is insignificant as it is shown in Fig. 4-17 and the influence of pulse duration is shown in Fig. 4-18.

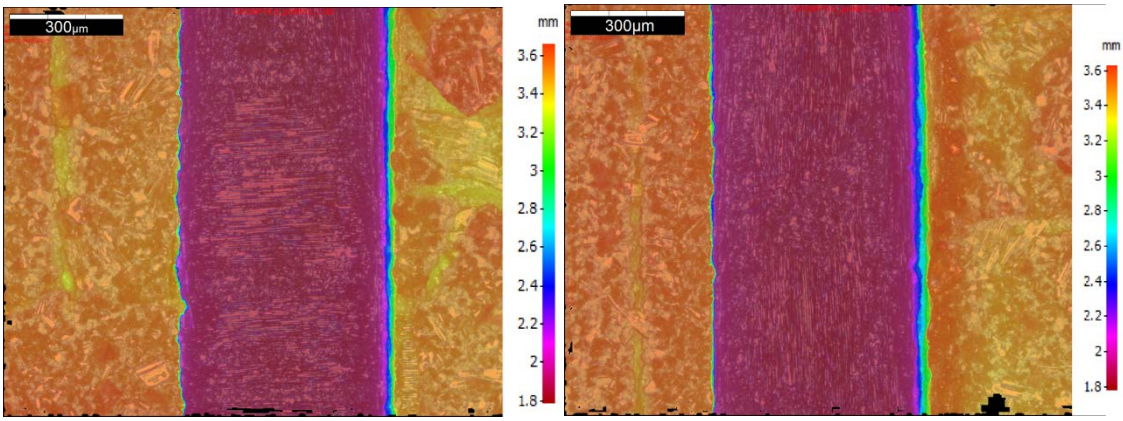

Fig. 4-17: Basic parameters are on the left, the effect of discharge current increase from 2A to 4A is on the right. No significant changes can be observed.

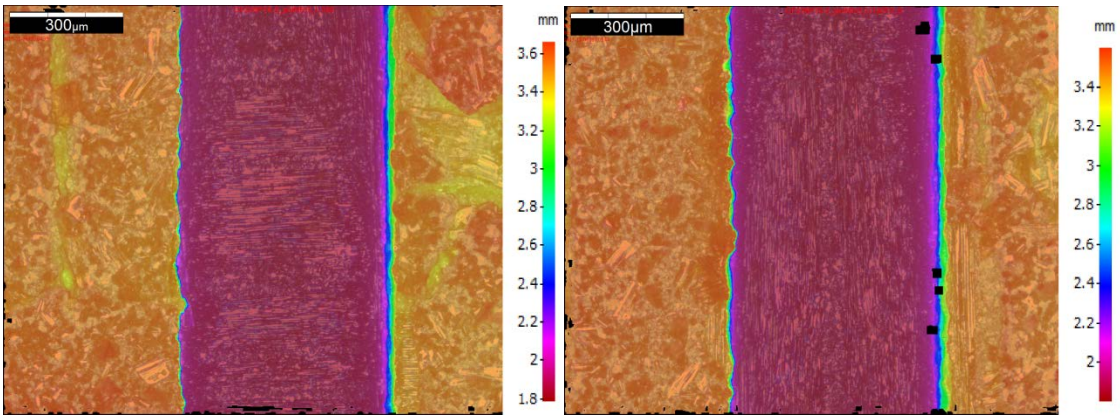

Fig. 4-18: The effect of the pulse duration increase from 1.51µs to 2.5µs is on the right. The rougher border can be seen with the increase of the pulse duration.

Table 4-2: Results of the parameter study.

T_{on}	I_d	Erosion time	H [mm]	W [µm]	MRR mm/min
1.51 µs	2 A	29min 34 sec	1.74	566	0.059
1.51 µs	4 A	28min 6 sec	1.76	556	0.063
2.5 µs	2 A	26min 44 sec	1.71	554	0.064

Where *h* is the slot depth and *w* is the slot width.

The tendency to increase MRR can be seen with the increase of pulse duration and discharge current, but machining time of a single slot remained above 26 minutes, which made this method not competitive to the die-sinking process. It is observed that the roughness of the machined surface is highly dependent on the porosity and internal cavities of the CMC material.

The interdependency between roughness and the porosity of the material (Fig. 4-15) or between roughness and the fibre diameter are observed and will remain independent from the type of CMC material.

4.4 The new method of slot machining

This section presents a new method to machine seal slots, which in comparison to the layer-by-layer method can compete to the die-sinking process for straight slots and can be much faster for complex slots taking into consideration the time of the electrode machining for a die-sinking EDM.

4.4.1 Experimental setup and methods

A 7-axis high-speed EDM drilling machine dedicated for aerospace applications (GF Machining Solutions, Agie Charmilles SA Drill 300) is used for experiments related to EDM drilling and milling. Deionised water is used as a dielectric. Commercially available brass tubes with dimensions ø0.5 x 300 mm (single hole) and ø1 x 400 mm (multi-hole) are used as tool electrodes. Inconel 718 is primarily used as workpiece material, and γ-TiAl (TNM®-B1), CMC (SiC-SiC) are used to demonstrate feasibility. Results from modern die-sinking EDM

machines (AgieCharmilles FORM series seal slot dedicated technology) are used for reference comparisons.

An optical microscope (Keyence VHX-5000 Series) with 100x magnification is used for imaging, whereas the Alicona Infinitefocus microscope is used for optical 3D measurements. Talysurf from Taylor Hobson is used for surface roughness measurements. Surface integrity is analysed by polishing and etching of eroded samples, where re-solidified layer thickness and surface crack propagation is observed using optical microscopy.

Computational fluid dynamics (CFD) simulations are carried out using the commercial solver ANSYS 18.1. To investigate the lowest flow speed due to the pressure drop, a 400 mm long electrode is used. The length of the simulation geometry of the ø1 mm single-hole electrode is set to 100 mm to save computational power by reducing the mesh size. The inlet condition is defined according to measured data on the used EDM-machine, which supplies 65 bar by the dielectric fluid pump. Referring to the 100 mm long tube geometry, a pressure of 25 bar is calculated concerning the pressure drop. The gap between the tool electrode and workpiece is set at 50 µm. Electrode wall and the wall of the workpiece hole are set to no-slip condition, whereas the wall of the workpiece is treated as a rough-wall with a sandstone roughness of Ra=5.36 µm according to surface measurement and employing the formula from [114]. The flow domain is limited by an opening boundary condition flush with the workpiece surface. The Reynolds number of the flow inside the 0.6 mm diameter cooling channel is calculated by $Re = (\rho\, d\, v)/\mu = 6700$ (slowest velocity of about v=10 m/s, dynamic viscosity μ=8.9.10-4 kg/(m·s) and density of water of ρ =997 kg/m^3). Thus, turbulent flow conditions can be assumed and taken care of by using the k-ε turbulence model. No thermal models are applied.

4.4.2 Comparison of different EDM strategies

Since productivity is of high importance for seal slot machining, a comparison between die-sinking EDM and layer-by-layer EDM milling strategy is performed for a straight slot in Inconel 718 with dimensions (W L H) 0.6 x 40 x 3 mm and final surface roughness Ra 3.2 µm. For the next strategy, the thickness of the layer is chosen as half of the electrode diameter of 0.5 mm. In terms of erosion time, die-sinking EDM takes between 6-10 min depending on the chosen strategy between the maximum material removal rate (MRR) to minimum wear. On the other hand, after optimisation of process parameters to achieve comparable geometric accuracy, EDM milling strategy results in total machining time of 45-50 min Since high geometric accuracy is not a priority for seal slots, in order to reduce machining time, an alternate milling strategy is analysed, termed here as EDM shaping. Here, tube electrode is first fed towards the workpiece until the required slot depth achieved, followed by machining in the lateral direction, i.e. electrode feed parallel to slot length. Using this strategy, by applying for electrode wear compensation, the defined slot is machined in about 30 minutes within required geometric accuracy, which is still considerably higher than the observed die-sinking EDM performance. While EDM milling has obvious advantages over die-

sinking EDM regarding electrode setup-cost and geometric flexibility, the machining time does not justify it as an alternative method for machining complex shaped seal slots.

In order to utilise the above-mentioned benefits of EDM milling, an alternative method is found [115], termed here as the Bridgestone method. Here, EDM drilling is performed for rough machining of a slot followed by EDM shaping for finishing to achieve desired geometric accuracy and surface quality. In this strategy during roughing, a hole is drilled into the workpiece, followed by consecutive holes with some pitch/overlap with the previous hole to make an opening, thus forming a groove, as depicted in Fig. 6(a). Using the proposed method, with 40% overlap between consecutive holes, rough machining time of the above-mentioned slot geometry is about 10 min. Subsequently, a finishing operation is performed using EDM shaping described above. The total machining time is about 16 minutes. Thus, using the mentioned strategy, a considerable reduction in machining time is achieved compared to the EDM milling or shaping while preserving the advantages of the use of simple tube electrodes and flexibility to machine different geometric shapes of a groove.

Despite machining time improvement by the Bridgestone method, it is still relatively slower than the die-sinking EDM. In the Bridgestone method, the first hole is machined in a normal condition, i.e. in full workpiece material, whereas the subsequent holes only partially remove the diametrical material in the workpiece. In order to further improve the efficiency of the roughing operation, a hypothesis is presented and analysed using experimental analysis and fluid simulations.

It is proposed that the EDM drilling efficiency is low for subsequent (overlapping) hole drilling, mainly due to the electrode vibration resulting from sparking on only one side of the electrode and decrease in flushing efficiency in an open groove, as depicted Fig. 4-19 (a), compared to drilling a hole in full workpiece material (termed odd-hole), as shown in Fig. 4-19 (b). An additional drilling condition is imagined, where a hole (termed even-hole) is drilled between two previously machined holes into full workpiece material. In such scenario, highest MRR is expected from drilling odd-holes, followed by even-holes and overlapping holes. Finally, drilling condition of a hole (termed middle-hole) for cusp removal is considered, where drilling is performed to remove triangular shaped area formed between adjacent odd- and even-holes.

EDM drilling of holes in Inconel 718 and γ-TiAl using ø1 mm and ø0.5 mm brass tubes is performed in the above-mentioned drilling conditions to analyse erosion efficiency, through MRR and relative wear rate. MRR is calculated by measuring the erosion time and projection area of the hole, while simplifying the eroded depth to a perfectly cylindrical shape, as opposed to slightly conical shape. As it is seen in

Fig. 4-20, MRR is more than double for odd-holes compared to the overlapping holes. In order to analyse underlying mechanisms in these observations, the drilling process is monitored in terms of good sparks, shorts and arcs, as shown in Fig. 4-21. Increasing short sparks indicate process instability, specifically electrode vibration, which is evident from the

analysed spark analysis during erosion in different drilling conditions. The ratio of good sparks and shorts correlates well with the measured MRR for different drilling conditions. Also, it is visible that for drilling by ø0.5 mm electrode, ratio of good sparks decreases considerably, while some arcs are observed as well compared to drilling by ø1 mm electrode, which can be partially explained by higher vibrations of thinner electrodes, as it is indicated in Fig. 4-22. Thus, electrode vibration is confirmed to considerably deteriorate erosion efficiency in the overlapping hole drilling conditions, whereas the higher occurrence of shorts and arcs may also adversely affect surface integrity. Electrode vibrations are also confirmed by high-speed imaging and are shown in Fig. 4-22. Electrode vibrations are detected during the Bridgestone method of slot machining. Side discharge causes up to 90 µm electrode displacement.

Vibrations during machining (Fig. 4-22) by the Bridgestone method are considered to be the main reason of shorts increase (Fig. 4-21) and therefore the reason of wear increase and MRR drop. Additionally to vibrations the flushing conditions are investigated.

In order to clarify the role of flushing in different hole drilling conditions, fluid dynamics simulation is performed. More details about fluid dynamics model and the applied simplifications are in the sections 6.1 and 6.2.

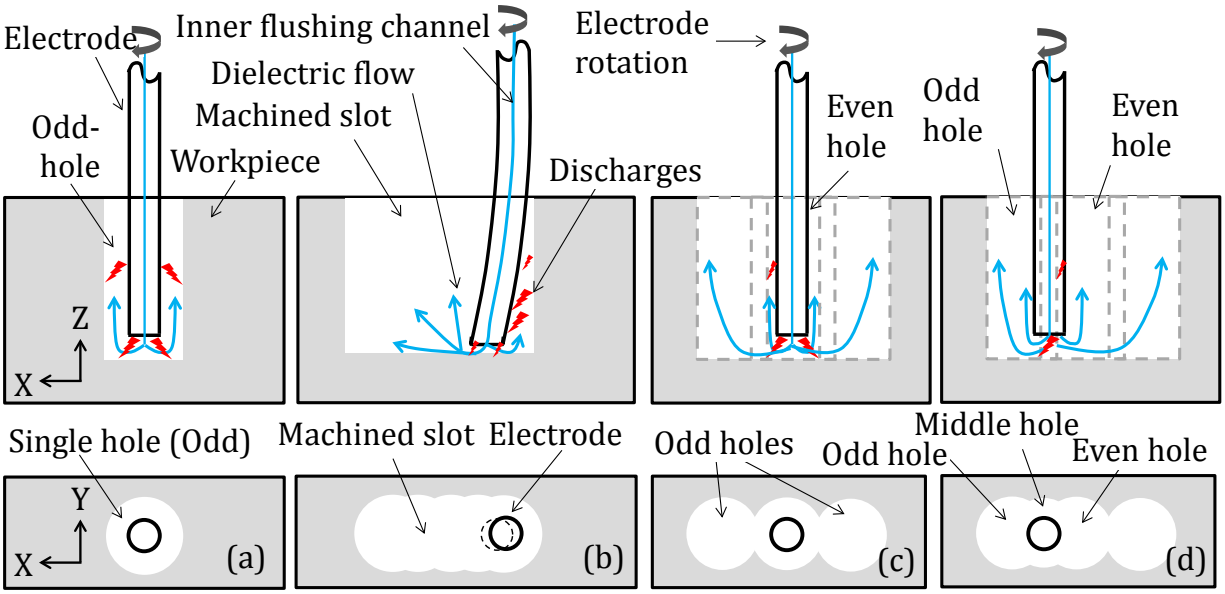

Fig. 4-19: Depiction of three distinct EDM drilling conditions. (a) Drilling condition in the Bridgestone method; (b) drilling condition for a single hole (odd-hole) and (c) Drilling condition between adjacent odd-holes.

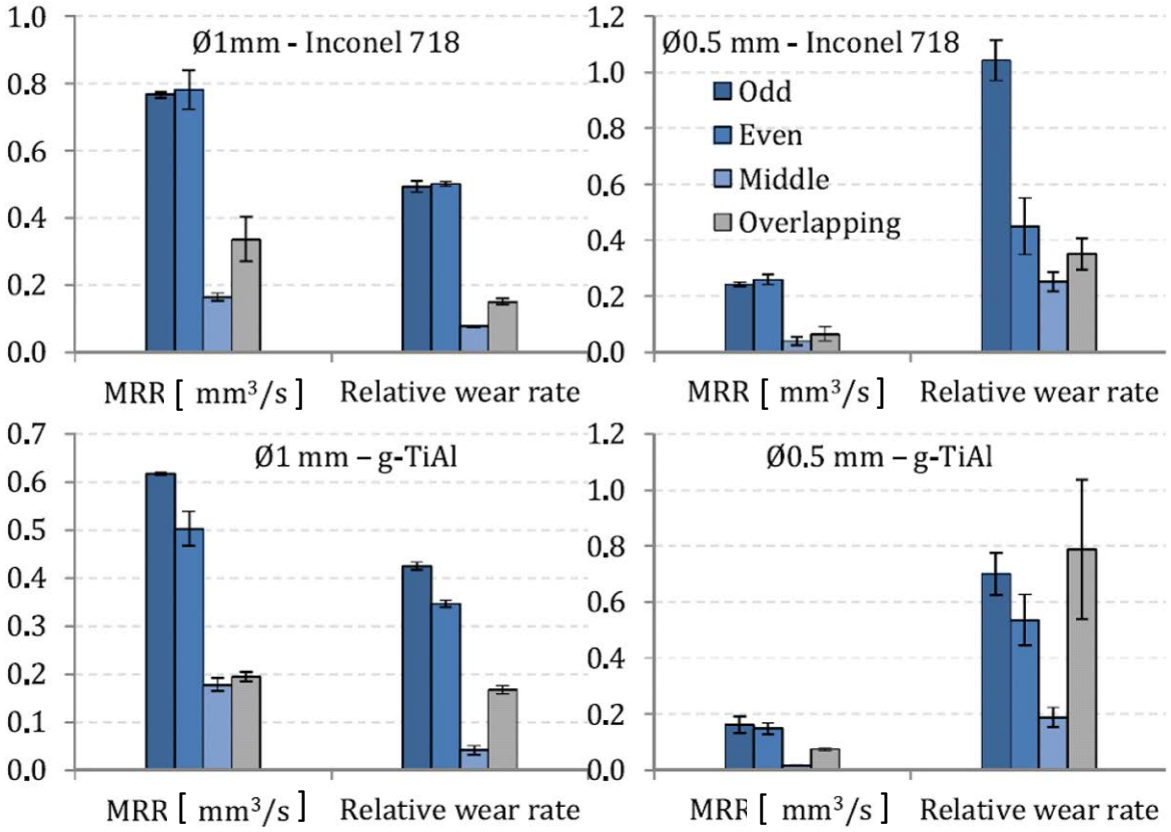

Fig. 4-20: Experimentally obtained material removal rate (MRR) and relative electrode wear for different hole drilling conditions in Inconel 718 and γ-TiAl using ø1 mm and ø0.5 mm brass tube electrodes.

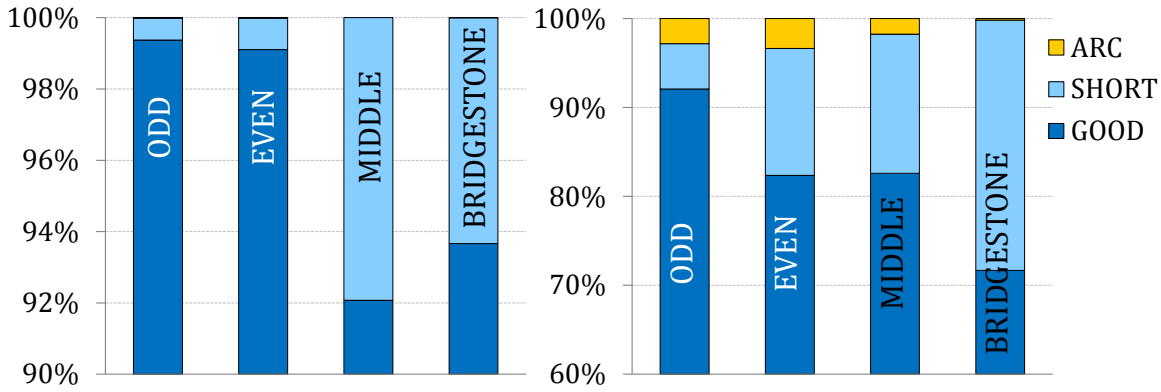

Fig. 4-21: Analysis of good sparks, shorts and arcs for different drilling conditions in Inconel 718 by ø1 mm (left) and ø0.5 mm (right) electrodes.

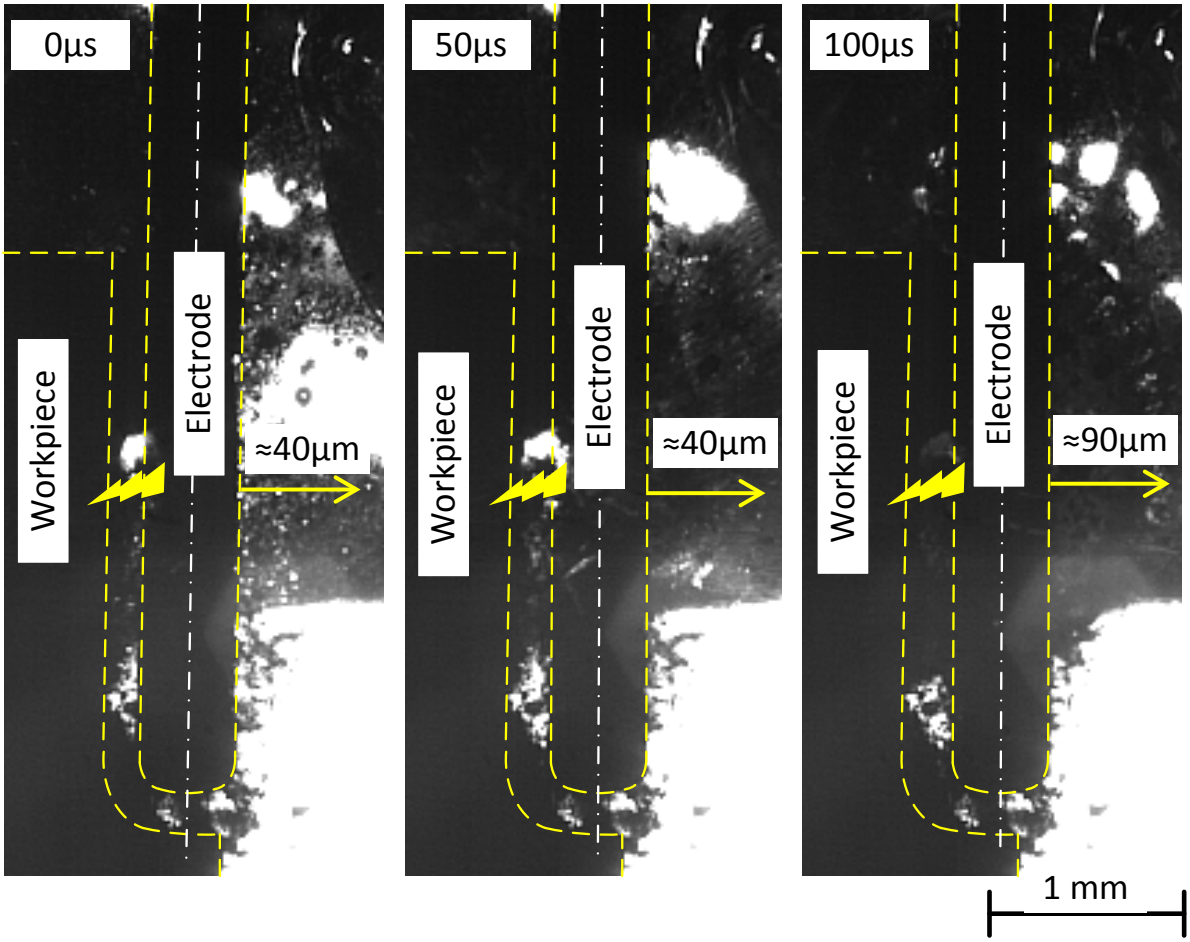

Fig. 4-22: High-speed imaging during slot machining by Bridgestone method, side discharge causes electrode vibrations with electrode displacement up to 90 µm. The sparks are indicated with the icons.

In Fig. 4-23 three drilling conditions are shown in the XZ/YZ planes as cross sections for the velocities of the fluid (deionised water). It is visible that due to the high-pressure drop, the velocities at the electrode outlet in odd-hole conditions are lower (about 17 m/s) compared to the other conditions (about 22 m/s), however the velocity profiles in the gap along the electrode towards the opening in erosion region is much smoother and higher. In fact, simulation results indicate that even-hole and overlapping hole conditions show high flow velocities only where the distance between the electrode and the workpiece surfaces are small (YZ). However, the flow velocities are much lower towards the side exposed to the bulk fluid (XZ). It can be argued that the flushing of the debris, which is mainly generated at the electrode front, is also lower on the sides of the electrode with no workpiece material (XZ). Thus, it is inferred that the flushing efficiency in even-hole and overlapping hole conditions is not homogeneous along all directions, further deteriorating erosion efficiency. Mode details regarding flow analysis are given in section 6.2.

4.4.3 ODEM strategy

Based on the analysis of EDM drilling process efficiency for rough machining of a slot, a strategy, named ODEM is proposed to further increase the productivity of slot machining. In

order to utilise the ideal machining conditions as in the case of odd-hole drilling, the strategy maximises material removal for a slot by odd-hole drilling. Thus odd-holes are drilled along the slot geometry with a defined separation. Subsequently, even-holes are drilled between adjacent odd-holes to make an opening, thus generating a groove. Additionally, middle holes can be drilled between two adjacent odd- and even-holes, to remove the cusp. The ODEM strategy is depicted in Fig. 4-24 (b).

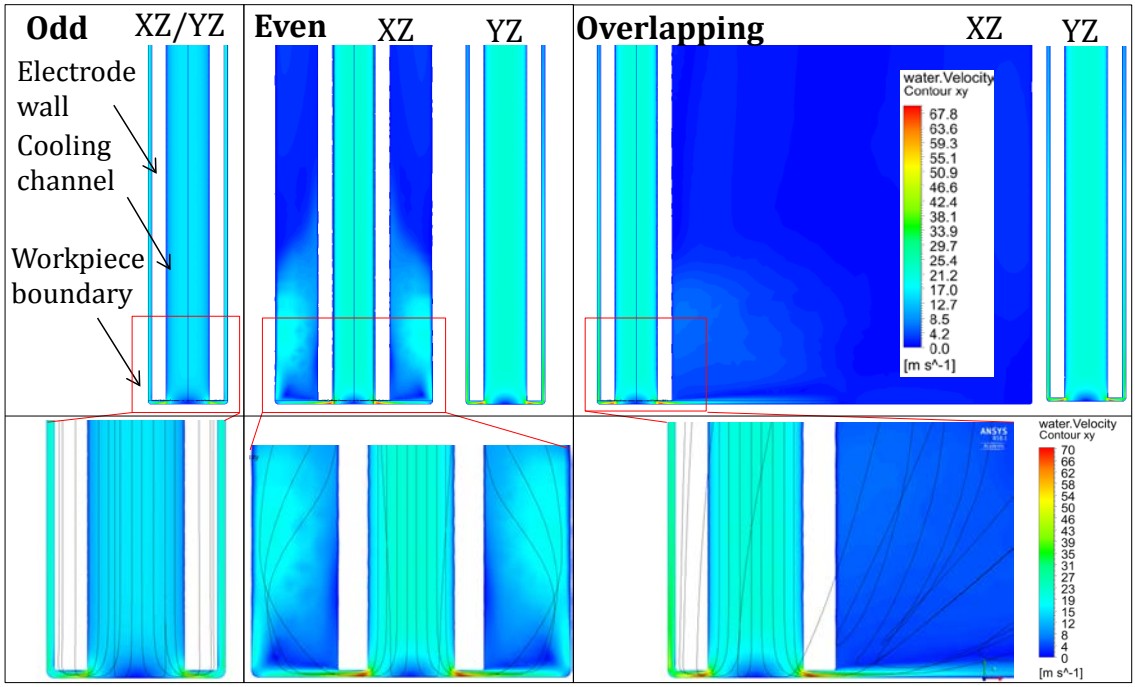

Fig. 4-23: Cross sections of the simulated velocities of the flushing fluid in different drilling conditions.

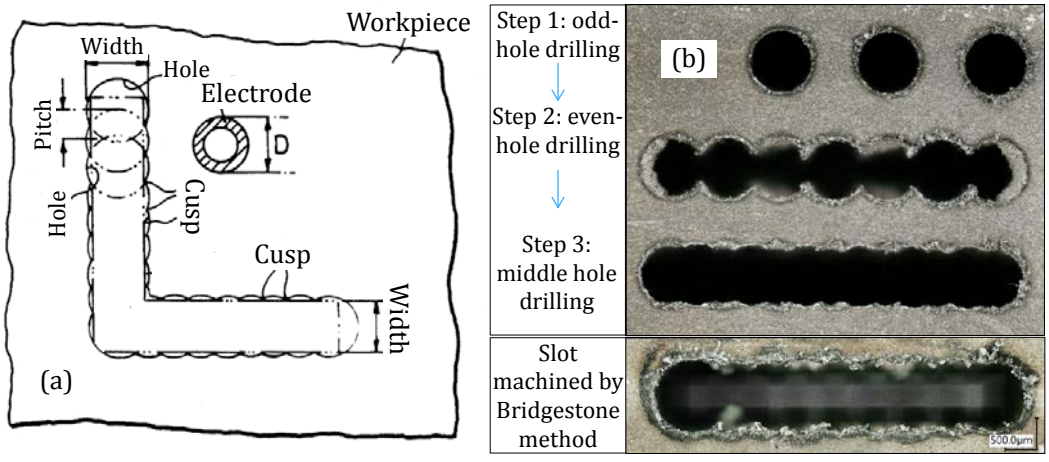

Fig. 4-24: (a) schematics of the Bridgestone method adapted from [115], where EDM drilling is performed using a tube-like electrode to machine overlapping holes with a pitch/overlap to form a groove. The resulting cusps between overlapping holes are removed during finishing using EDM shaping and (b) straight slots machined in Inconel 718 using ø1 mm brass electrode using ODEM strategy consisting three steps and comparison of resulting rough machined slots by ODEM and the Bridgestone method.

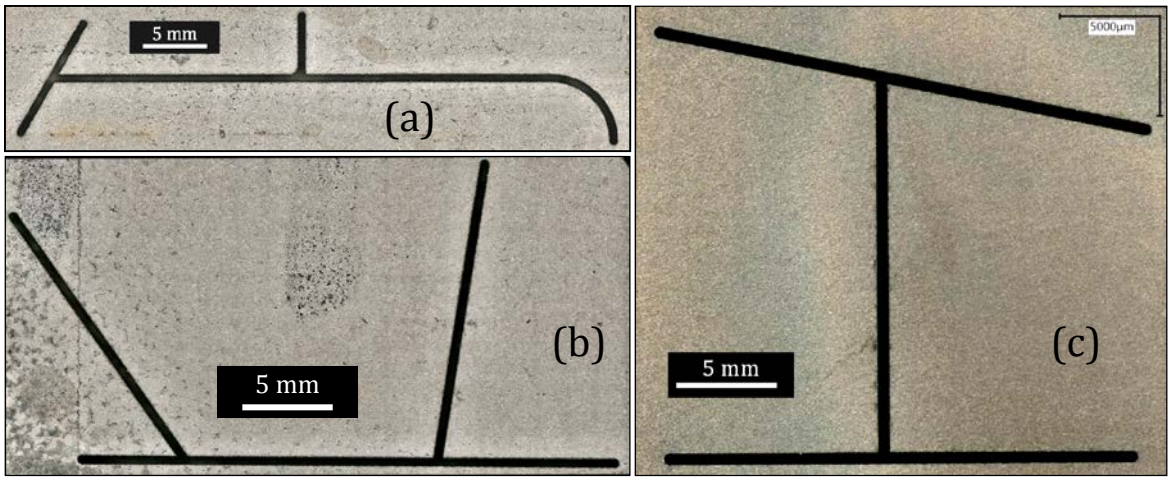

Fig. 4-25: Examples of complex shaped slots machined using ODEM roughing and EDM shaping finishing in Inconel 718 (a, b) and γ-TiAl (TNM-B1) (c).

A comparison between the proposed ODEM method and Bridgestone method is performed by rough machining slots. A slot with dimensions (W x L x H) 0.6 x 40 x 3 mm using a ø0.5 mm electrode takes 10 min for the Bridgestone method and 6 min for ODEM method and slot with dimensions 1.1 x 12 x 11 mm using a ø1 mm electrode takes 4.5 min using the Bridgestone method and 3 min for ODEM method. Thus, it can be confirmed that higher efficiency is reached using ODEM method by maximising rough machining using odd-holes.

To analyse slot quality after complete machining, rough machining using ODEM and finishing using EDM shaping is performed to machine complex shaped slots in Inconel 718 (Fig. 4-25 a,b) and in γ-TiAl (Fig. 4-25 c). The complete machining of the slot (Fig. 4-25 a) with total length 63 mm and 3.3 mm depth takes about 31 min (roughing 11 min; finishing 20 min). Total erosion time for a slot with 'H-shape' (Fig. 4-25 7c) machined in TiAl with total profile length about 61 mm and 3.3 mm depth is 25 min. Comparing machining times with die-sinking, a 'U-shape' slot as shown in Fig. 2-4 with profile length about 67 mm and 3.3 mm depth takes about 15-18 min by die-sinking EDM (Ra = 5.0 µm) and 24 min (roughing 10 min, finishing 14 min) using ODEM and EDM shaping (Ra = 3.2 µm). Machining of both 'H-shape' and 'U-shape' slots can be performed using one 0.5 mm x 300 mm brass tube each. Thus, it can be summarised that in terms of productivity, roughing using ODEM is faster than the Bridgestone method, and offers the advantage of lower setup time, tool costs and more environmentally-friendly dielectric over die-sinking EDM.

Since surface integrity is a high priority for turbine components, re-solidified layer and surface micro-cracks are analysed in slots machined in Inconel 718. For a straight slot machined by ø1 mm electrode (Fig. 4-26), the average re-solidified layer thickness is about 9.9 µm, and isolated maximum thickness is below 40 µm. Also, no visible micro-cracks propagating into bulk material are observed.

For 'H-shape' slot machined using a ø0.5 mm tool (Fig. 4-27), the average re-solidified layer thickness is 8.7 µm, with maximum isolated recast layer thickness below 25 µm. Since,

ODEM method exploits better erosion, shown by lower shorts, arc and flushing conditions during roughing, surface defects are limited to a thinner layer, reducing the required finishing layer thickness.

Ceramic matrix composites (CMC) can considerably contribute to increasing turbine efficiency due to their outstanding material properties [53]. However, their machinability is poor by conventional machining processes. Thus, a complex shaped slot is machined in SiC-SiC matrix composite using ODEM roughing (38 min) and EDM shaping finishing (25 min), as shown in Fig. 4-28.

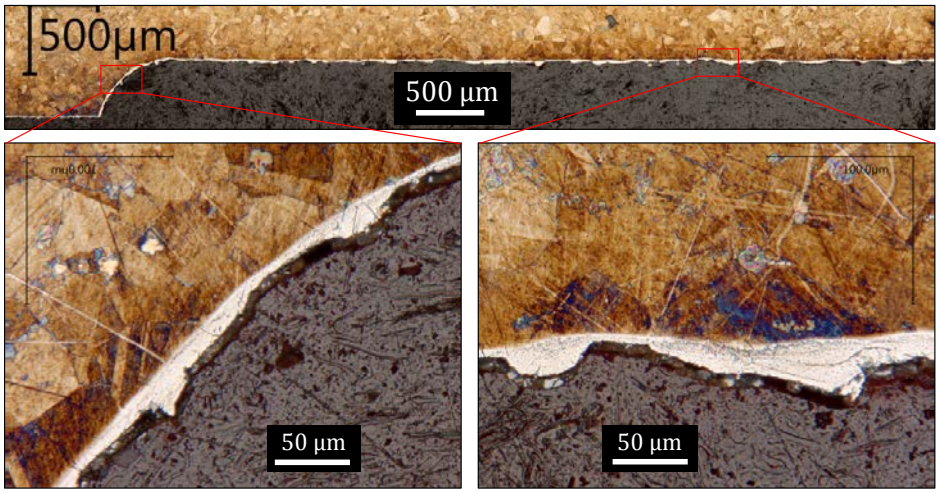

Fig. 4-26: Re-solidified layer analysis (in XY plane) of straight slot machined using ODEM+EDM shaping with ø1 mm tool in Inconel 718.

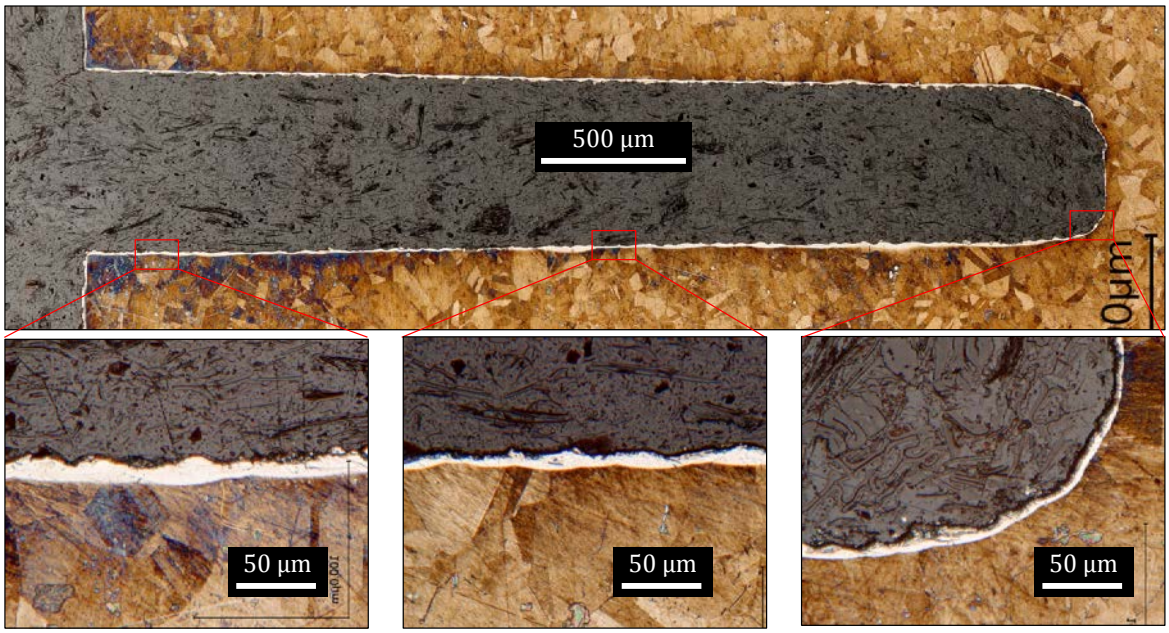

Fig. 4-27: Re-solidified layer analysis (in YZ plane) of 'H-shape' slot machined using ODEM+EDM shaping with ø0.5 mm tool in Inconel 718.

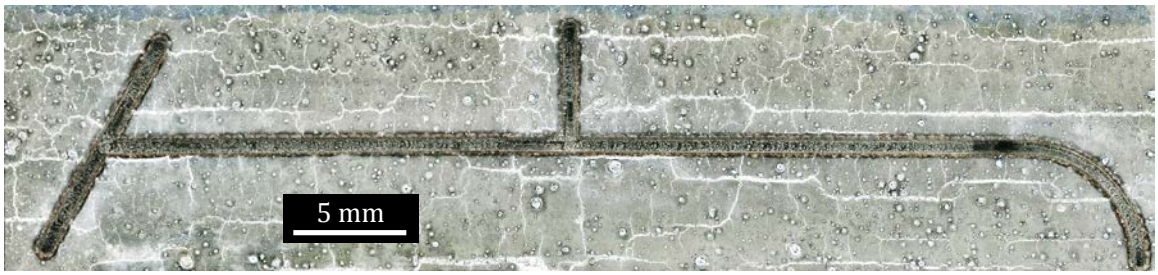

Fig. 4-28: A complex-shaped slot machined in SiC-SiC CMC using ODEM roughing and EDM shaping finishing using a ø0.5 mm brass tube. Cracks on the surface were present before machining and are not caused by erosion process.

5. Single crater simulation and measurements

Parts of this chapter have been published [116-118].

This chapter starts with a single crater model. The aim is to understand the influence of the pulse parameters from the individual discharge and compare them to the results of pulse parameters influence to the drilling process in chapter 3. Through this comparison, it is found that the most crucial process parameter responsible for the difference between the single and multiple discharges is flushing.

A single spark with melting and fluid flow is simulated as an axisymmetric problem with COMSOL Multiphysics® 5.2 software. The geometry is discretized with 3-nodes triangular elements and linear shape functions. More details about the geometry discretization and the boundary conditions are given in the next subsections 5.1, 5.2 and 5.3. The main assumptions are summarized in the following:

- Vaporization is negligible
- PFE is 100%, and the recast layer is generated in the mushy zone
- The workpiece material is isotropic and homogeneous
- The fluid in the molten pool is incompressible, and the flow is laminar
- The surface of the molten pool is flat

5.1 Model inputs

Current and voltage are measured with Teledyne Lecroy WaveRunner 640Zi oscilloscope, which has a resolution of 40 GigaSamples/s on 2 channels for a single discharge. The change of 5 A in discharge current is used as a trigger. The simulation is considering only the spark-on-time, from the moment of the breakdown. Therefore, the amount of discharge energy W_e per single discharge in the EDM process is given by:

$$W = \int_o^t U_d(t) \cdot I_d(t) \cdot dt \tag{5-1}$$

While the heat flux $Q_a(t)$ supplied to the workpiece (anode) is given by

$$Q_a(t) = F_a U(t) I(t) / A_w \tag{5-2}$$

Q_a is used as the heat source for the erosion model, where A_w is the surface of the workpiece affected by the plasma, F_a is the fraction of energy flux going into the workpiece, that is, in the specific case, the anode. In the observed literature, there are no investigations about how the F_a value changes within the discharge and it is therefore considered constant.

In the present simulations, F_a is also considered constant, but the time-dependence of the equations (5-1) and (5-2) is studied by the variation of the discharge time duration. F_a cannot be measured directly and its approximation has a great impact on the results of the simulations, therefore in the present work the optimization algorithm is used for fitting the crater dimensions of the experiments in order to get the value of F_a. As a simplification, the discharge voltage U_d is considered constant during discharge, as well as the discharge current I_d. Input model parameters are Id, t_{ON} and U_{open}, since this parameters have the main influence on the total amount of energy equations (5-1) and (5-2).

The work of Revaz et al. [119] shows that the plasma is growing rapidly in the first stage of the discharge, but it slows down at a later stage; therefore the heat surce radius r_p can be calculated as:

$$r_p = V_p\, t^{0.2} + r_0 \tag{5-3}$$

where V_p is the velocity of plasma, t is time and r_0 is initial plasma radius. The value of V_p and r_0 is fit through the same optimization algorithm as for F_a. The parameters define the heat flux dimensions and intensity (energy fraction from the total calculated amount of energy). Furthermore, the flux of energy is considered as Gaussian, distributed over the radius, in order to reproduce the higher temperature and pressure in the middle of the plasma compared to the border as it was measured during experiments by Perez [120].

A Gaussian distribution is considered for the heat flux according to [73]. The aim is to approximate the total energy flux. It is then necessary that the following equation holds:

$$2\pi \int_{-\infty}^{+\infty} q_a(r,t)dr = Q_a \tag{5-4}$$

where q_a is a heat flux by conduction. The area below the Gaussian curve is calculated as:

$$Q_a = \int_{-\infty}^{+\infty} a \exp\left(-\frac{r^2}{2c^2}\right) dr = ac\sqrt{2\pi} \tag{5-5}$$

where a and c are the two parameters, that define a Gaussian function as

$$f(r) = a\, e^{-\frac{r^2}{2c^2}} \tag{5-6}$$

The radius of plasma is considered to be equal to three times the standard deviation, in order to fit the width of the Gaussian distributed heat source with the radius of the plasma, therefore:

$$c = \sigma = \frac{r_p}{3} \tag{5-7}$$

Finally, the value of a is found as:

$$a = \frac{Q_a}{c\sqrt{(2\pi)}} = \frac{3Q_a}{r_p\sqrt{(2\pi)}} \tag{5-8}$$

5.2 Material properties

All the material properties used in the simulation need to be temperature dependent. Furthermore, material properties can dramatically change during the phase transition, which increases the complexity for FEA dramatically. Even the most recent works in the field as [85] and [83] do not take into account the temperature dependence of material properties. However, Weingaertner [82] proved the significance of their impact, therefore in the current work temperature dependent parameters are considered whenever possible.

Data for solid Inconel 718 are implemented up to the melting temperature. Above melting temperature, no data about Inconel 718 are found in the literature, but there are data for liquid Inconel 713C. However, the values for the specific heat capacity C_p and temperature-dependent surface tension are estimated by the results of the experiments conducted [121], considering that:

$$C_p = \left(\frac{\partial H}{\partial T}\right)_p \tag{5-9}$$

The phase change temperature and the value of latent heat are set according to values from Zla, et al. [122] of respectively $1336\ K$ and $165\ J/g$. Temperature-dependent surface tension is estimated by taking the one for a nickel based alloy with 10% Chromium. The material is modelled as a liquid and a viscosity of 400 $Pa \cdot s$ in the solid phase (0.01 $Pa \cdot s$ is chosen for the liquid phase) is chosen as a value high enough such that no significant displacements are calculated in the solid part of the workpiece. On the other hand, an extremely high value of viscosity would be detrimental for the simulation since it would lead to ill-conditioning of the system of equations.

In order to simulate the change of phase a Mushy zone of 100 K is considered. The mushy zone represents a heat affected zone, and it is selected based on the crater measurements. The mushy zone can be also simulated based on Ni-Cr phase diagram, but since Inconel 718 is 55% Ni and 20% Cr for this particular type of Inconel simulation the Mushy zone is too narrow (about 10K) for the simulation convergence. In this zone heat capacity assumes a suitable value in order to be equivalent to the total heat of melting. In the specific case, latent heat of melting is $165\ kJ/kg$ [122] (Inconel 918).

The values and expressions for material properties are given in Table 5-1.

Table 5-1 Temperature dependent material properties.

Material property	Value for solid phase	Value for liquid phase
Thermal conductivity k, $[\frac{W}{m \cdot K}]$	$3.4959 + 0.026733\,T - 1.118\,10^{-0}\,T^2 + 3.6068\,10^{-0}\,T^3 + 8.2355\,10^{-0.}\,T^4$ [123]	$-12.3\ \ 0.03T$ [124]
Density ρ, $[\frac{kg}{m^3}]$	$8288.965 - 0.05548692\,T^1 - 7.190094\,10^{-0}\,T^2 + 7.974854\,10^{-0}\,T^3 - 3.478001\,10^{-04}\,T^4$ [125]	$8519.8 - 0.85788\,T^1$ [126]
Viscosity μ, [Pa·s]	400 *	$0.01112618 + 1.798841\,10^{-0}\,T^1 - 2.924501\,10^{-0}\,T^2$ [124]
Specific heat capacity C_p, [J/(kg·K)]	$361.3373 + 0.2378248\,T^1 + 7.560689\,10^{-0}\,T^2$ [127]	$(69/220) * T + (2888/11)$ [121]
Surface tension σ, $[\frac{mN}{m \cdot K}]$	-	$1816 - 0.417 * (T - 1717)$ [128]

* value high enough to avoid significant displacement, as it mentioned above. T is given in [K].

5.3 Simulation approach, thermal analysis and fluid flow analysis

The simulation consists in a transient analysis, which calculates the temperature profile of the workpiece and therefore the profile of the molten part which will be then ejected during the plasma collapse, assuming a PFE of 100%.

The basic partial differential equations used are the heat transfer equation and the Navier-Stokes equations, to which the Marangoni effect as surface tension are added.

The equations used for modelling the heat transfer and conduction during the discharge are given below:

$$\rho C_p \frac{\partial T}{\partial t} + \nabla \cdot \underline{q} \ + \ \rho C_p \underline{u}\ \nabla T = Q_a \tag{5-10}$$

$$\underline{q} = -k \nabla T \tag{5-11}$$

$$Q_a = \frac{F_a U(t) I(t)}{A_p} \quad at\ the\ specified\ boundary\ (r < r_p) \tag{5-12}$$

where $r_p(t)$ the radius of the plasma is defined by (5-3).

CFD is performed in order to take into account the Marangoni effect, also called thermo-capillarity, which generated forces on the surface of the melt pool towards the opposite of the temperature gradient direction. It is generated by the temperature dependent surface tension. The increase in diameter and decrease in depth due to the Marangoni effect can be useful to explain the discrepancy between measurements and simulations, which is found in most of the works in literature, where the crater depth was always overestimated.

In the Navier-Stokes

$$\rho \frac{\partial \underline{u}}{\partial t} + \rho \left(\underline{u} \cdot \nabla \right) \underline{u} = \nabla \cdot \left[-p \underline{\underline{I}} + \underline{\underline{\tau}} \right] \tag{5-13}$$

where $\underline{u}$ is the velocity field, $\underline{\underline{I}}$ is the identity matrix and $\underline{\tau}$ is the viscous stress. The molten material is assumed to be a Newtonian fluid (according to [129]). Therefore the following holds:

$$\underline{\underline{\tau}} = 2\mu \underline{\underline{S}} - \frac{2}{3}\mu \left(\nabla \cdot \underline{u} \right) \underline{\underline{I}} \tag{5-14}$$

where $\underline{\underline{S}}$ is the strain rate tensor. The second term of the strain rate tensor is zero because for an incompressible fluid $\nabla \cdot \underline{u}$ is equal to zero**.**

In the continuity equation

$$\frac{d\rho}{dt} + \nabla \cdot \left(\rho \underline{u} \right) = 0 \tag{5-15}$$

the first term is 0 since the density is constant due to incompressibility.

In order to keep into account the Marangoni effect, the surface tension must be added:

$$\left[-p \underline{\underline{I}} + \mu \left(\nabla \underline{u} + \left(\nabla \underline{u} \right) T \right) \right] \underline{n} = \gamma \otimes \nabla_t T \tag{5-16}$$

where γ is the temperature derivative of the surface tension (*N/(K·m)*), which is derived by the expression in Table 5-1. $\nabla_t T$ is the tangential temperature gradient. The Navier-Stokes equations are solved using the incremental pressure-correction schemes based on [130]. More details about Marangoni effect implementation and Navier-Stokes equations can be found [131].

The boundary conditions are shown in Fig. 5-1. Initially, no velocity is considered, and the temperature is considered as room temperature. Linear shape functions with 3-nodes triangular elements are used for discretizing the geometry. Since there is not any geometrical nonlinearity in this FE simulation, the problem of selecting the element shape is solved by considering a triangular element which can represent any crater shape and then checking the mesh convergence, element formulation and number of integration points, more details [130]. As an example in Fig. 5-1, the region with the finer mesh, where the melt pool is expected, is not rectangular and can be represented by the triangular element. The gradients of temperature and velocity are expected to be higher in these areas, where the crater will be formed. Therefore, in order to reduce the size of the computation, only finer

elements are used near the centre and on the top surface of the workpiece, where the crater is expected. The mesh is generated on the basis of the measured crater size. The dependencies of the results to the mesh type, size and element formulations are performed. For different simulations, the number of elements varies between ≈4000 and ≈17000 (for the experiments number 1 and 5, respectively, according to Table 5-3), because the size of the crater also varied considerably (see Table 5-3).

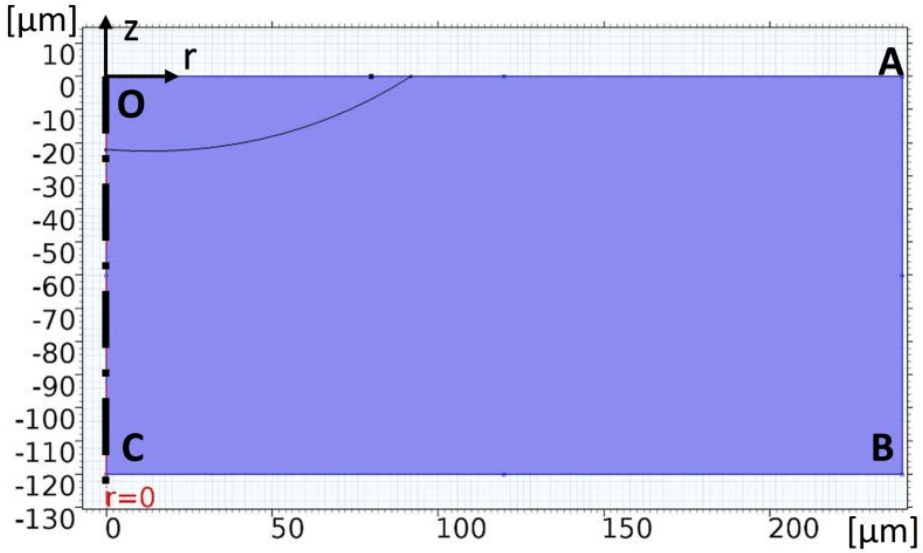

Fig. 5-1: Boundary conditions: OA: heat flow Q according to the eq. (5-2), (5-3) and (5-6), AB: adiabatic, BC: adiabatic, OC: symmetry axis

The value of crater diameter and depth are calculated and compared to the experimental results. The Nelder-Mead algorithm [132] is used to perform new simulations with the objective of fit the values of the plasma velocity V_p, the plasma radius r_0 and the fraction of energy going into the workpiece f_a. The reason why these 3 parameters are fit by the algorithm is that they are difficult or impossible to be measured. The initial values for them are an average of estimations in the literature. The algorithm is, therefore, able to identify which values of plasma velocity, plasma radius and fraction of energy in the model gives the best fit with the experimental results. The method is an algorithm for multidimensional unconstrained optimization without derivatives. The objective function is the difference between the calculated diameter (as a result of the simulation) and experimentally measured one. Due to the high number of iterations needed by the optimization solver and the high number of expected experiments, the computations are performed by ETHZ-supercomputer. The time stepping method is the Backward Differentiation Formula (BDF) [133], and the initial step is 0.001 µs.

According to [85] the Marangoni effect imposes the speed of molten material in the crater up to $130\,m/s$. Weingaertner [82] shows that, taking into account temperature dependent material properties and latent heat, the resultant material removal rate could even be less than a half of the otherwise calculated value. In this work, the influences of

these effects (Marangoni, latent heat and temperature dependent material properties) are analysed individually.

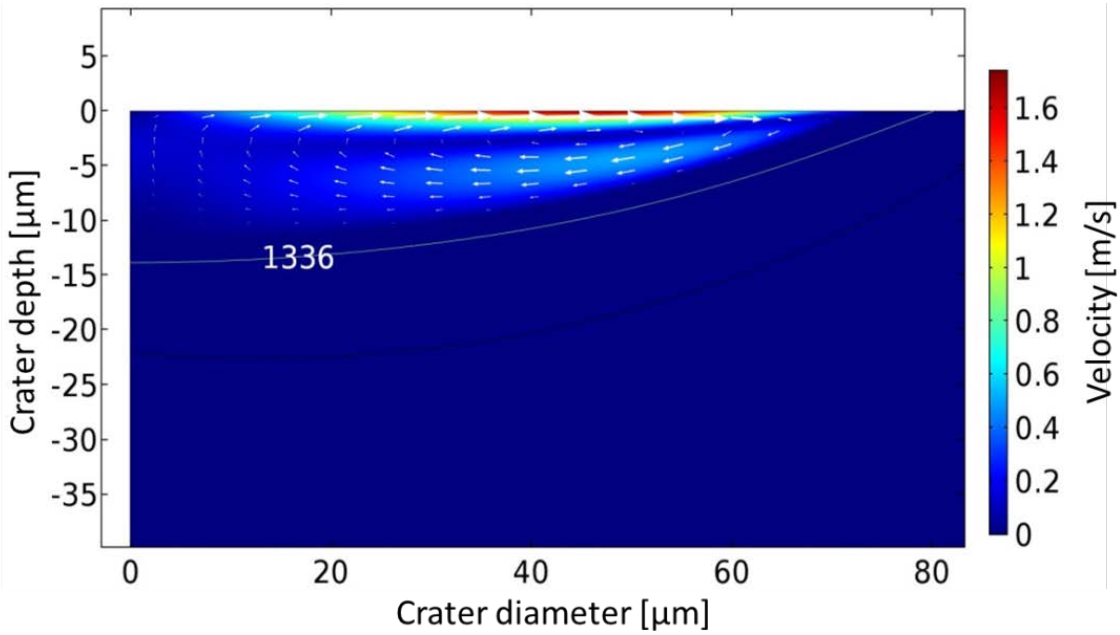

Fig. 5-2: Velocity field induced by the Marangoni effect in the EDM melt pool simulation, the velocity field is shown by the arrow field representing the local flow speed.

Marangoni effect influences the movement of hot fluid towards the colder area of the melt pool in the area close to the surface, as it is shown in Fig. 5-2. Therefore it is able to change the temperature distribution, which means, that also the estimated value of F_a is influenced. Fig. 5-3 shows the influence of the Marangoni effect on the crater shape, as well as the effects of temperature dependent material properties and latent heat on the crater shape. The reduction in depth and at the same time the increase of diameter due to the Marangoni effect partially explains the difference in the experiment and simulated results in most of the previously observed works, including [83].

In the current work, the case in which Marangoni effect shows to impose the highest velocity on the melt pool is the experiment number 3 (according to Table 5-2), which is also the one that has the largest depth. In this case, the velocity in the melt pool is growing up to 1.74 m/s, which is about 2 orders of magnitude less than the results of Mujumdar [85]. The influence on the crater depth is estimated to be only 2-3% ($0.3 - 0.4\ \mu m$). The reasons for the difference between [85] and the current work cannot be only explained by the different machining parameters and the different material, but also by differences of the simulation model.

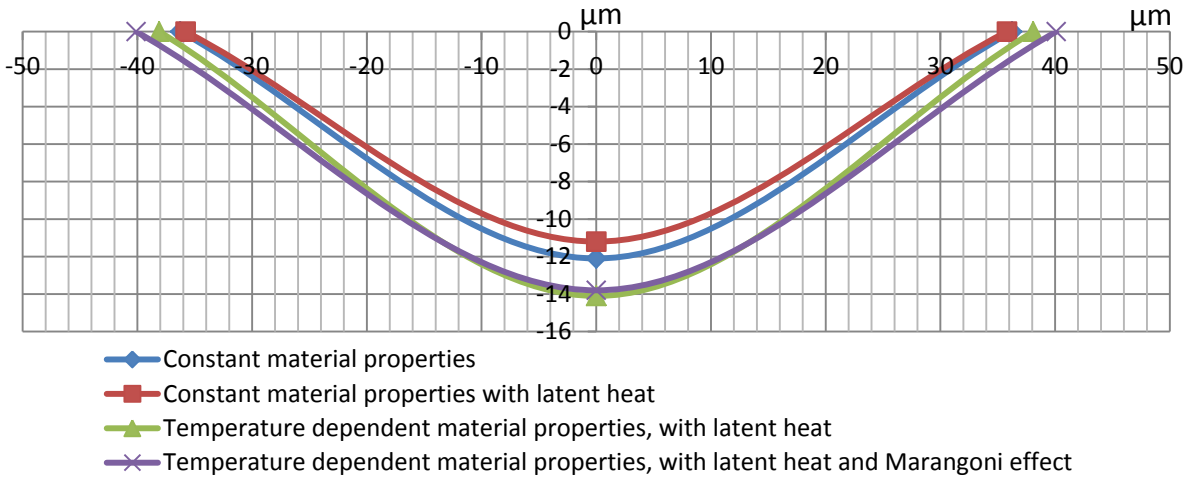

Fig. 5-3: Craters simulated with constant material properties, temperature dependent material properties, latent heat and Marangoni effect.

The comparison in Fig. 5-3 is based on the results of experiment number 5 (according to Table 5-2). The results show that temperature dependent material properties have the most significant effect, which is up to 24% on crater depth estimation. The results of the investigation depending on the value of the constant material parameter chosen. In this comparison, the averages between the value of temperature dependent material properties between 300K and 2000K are considered, since this assumption is often used in the literature [77, 83, 85].

5.4 Experiment and validation

The experiments are made on a commercial EDM drilling machine Drill 300 from GF Machining Solutions, Agie Charmilles SA, Switzerland, equipped with single discharge function. Deionized water is used as a dielectric. Oscilloscope (Teledyne Lecroy WaveRunner 640Zi) measurements are made in order to confirm the discharge and disregard open pulses, short circuits and arcs. Measurements are performed for monitoring current and voltage during the discharges, and microscope measurements in the micrometre scale are made for evaluating the crater shape. Leica DCM 3D confocal microscope is used for 3D measurements of the craters. Several particular properties of the craters are found during the measurements: most craters are strongly non-axisymmetric and the variability between discharges with the same input parameters is high. Therefore, each crater was measured in two perpendicular directions, and each experiment is conducted 3 times. The average standard deviation is 16% for the diameter and 41% on the depth.

The Taguchi method is used in the design of experiments (DOE) due to the complexity of the setup and in order to reduce the number of experiments. This method allows reducing of the experiments number from $3^3 = 27$ (used in full factorial design) to 9, using three levels for each of the three input parameters. Table 5-2 summarizes the DOE. The confidence interval for ANOVA is 0.15.

Table 5-2: Design of experiments following Taguchi methods

Experiment number	Crater number	$I_d(A)$	t_{ON} (µs)	U_{open} (V)
1	1-3	10	20	100
2	4-6	20	30	150
3	7-9	30	40	200
4	10-12	10	30	200
5	13-15	20	40	100
6	16-18	30	20	150
7	19-21	10	40	150
8	22-24	20	20	200
9	25-27	30	30	100

Crater measurements are shown in Fig. 5-4. Crater is measured as the mean value between inscribed circle radius r_{in} and circumcircled radius r_{cr}.

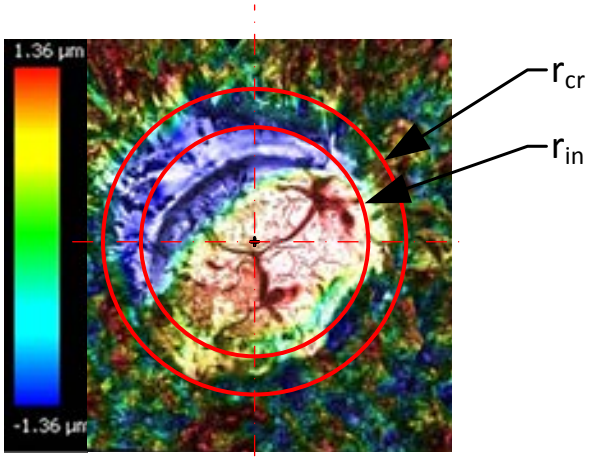

Fig. 5-4: Crater measurements, crater radius is measured as the mean value between inscribed circle radius r_{in} and circumcircled radius r_{cr}.

An agreement between experiments and simulation is achieved with the use of the Nelder-Mead algorithm for fitting the crater. The values of the calculated diameter and depth in the simulation are in the range of $\pm 5\ \mu m$ (diameter) and $\pm 1\ \mu m$ (depth) of the measured values respectively. The comparison between simulated and measured crater shapes is shown in Fig. 5-5. The variability between discharges obtained using the same input parameters is shown in Fig. 7.

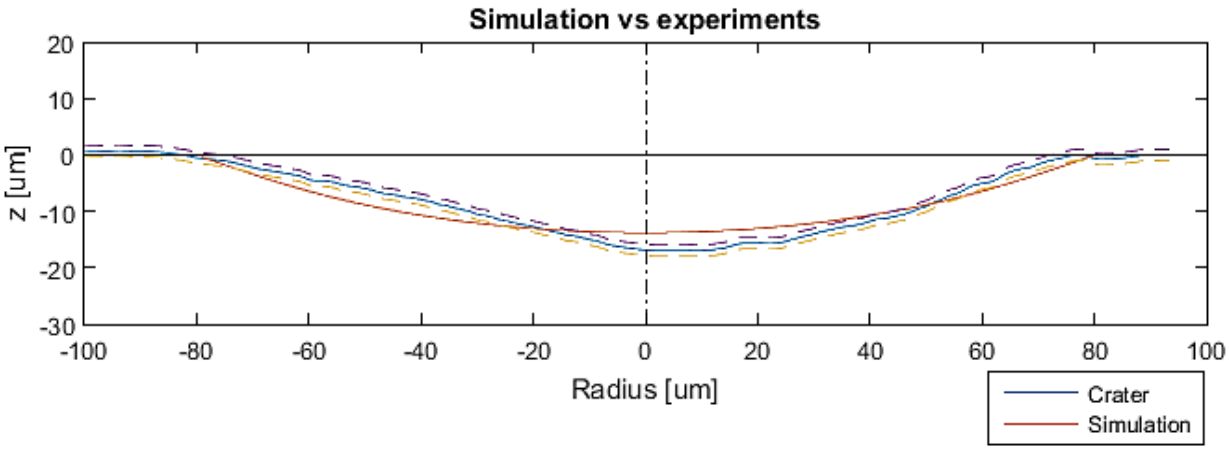

Fig. 5-5: An example of simulated and measured crater shape comparison. The error bars of the measurement are shown by dotted lines, representing the standard deviation out of 5 measurements of the same crater. The average of three repetitions is used of diameter and radius simulation.

It must be noted that infinite solutions are possible varying the control inputs of the optimization algorithm (the algorithm is fitting the crater dimensions for identification of output parameters), that are the fraction F_a of energy going into the anode, velocity V_p, of plasma, and initial radius, r_0 and the achieved results may change if the starting point of the optimization algorithm is varied.

Table 5-3: Results of simulation , more details about crater diameter and depth are shown in Fig. 5-6

	Machining conditions				Fitted crater dimensions		Output of optimization		
Exp. no.	$I_d(A)$	t_{ON} (µs)	$U_{open}\ (V)$	$U_d\ (V)^*$	Diameter (µm)	Depth (µm)	F_a	Velocity of plasma $(V_p, m/s)$	Initial radius (r_0, m)
1	10	20	100	37	84,4	3,9	0,217	38,729	8,69E-05
2	20	30	150	40	128	6,6	0,156	50	1,00E-04
3	30	40	200	30	160,4	13,8	0,157	36,343	1,00E-04
4	10	30	200	40	134,2	4,3	0,450	71,91	1,40E-04
5	20	40	100	37.5	162,4	11,95	0,192	25	1,40E-04
6	30	20	150	38.3	125	5,2	0,196	57,856	1,00E-04
7	10	40	150	21.7	146,8	6,7	0,646	27,9	2,00E-04
8	20	20	200	40	136	9,5	0,234	102,92	1,85E-05
9	30	30	100	31.7	168	7,4	0,163	47,834	1,63E-04

* U_d is a mean value of discharge voltage measured by an oscilloscope.

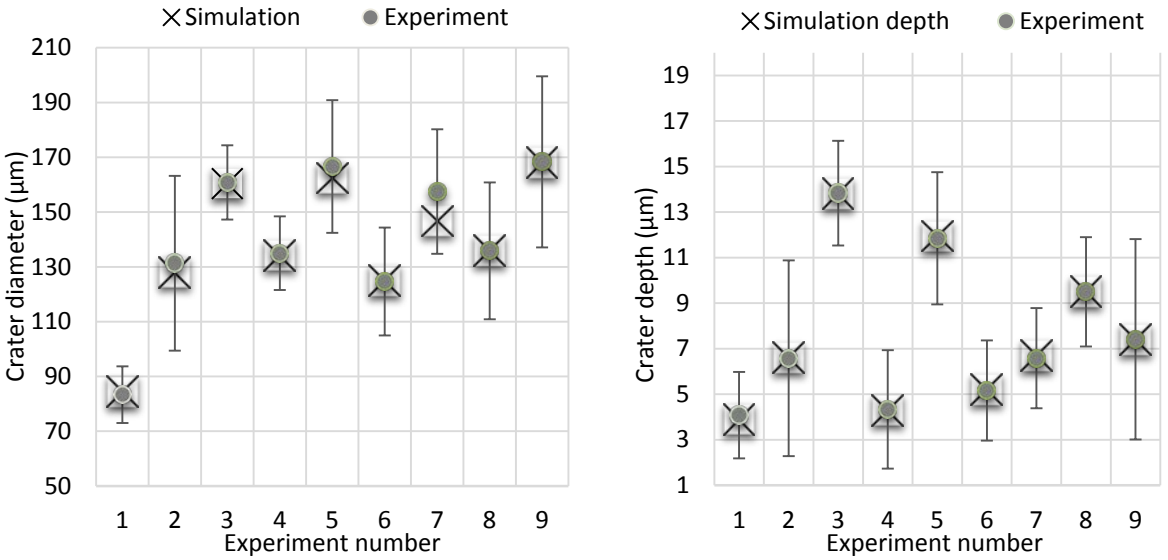

Fig. 5-6: The measurement results with respect to the simulation results, from left to right crater diameter and crater depth.

Recast layer around the crater is measured according to the procedure explained [134]. The workpieces are embedded in Bakelite ground and polished until the eroded crater becomes visible. Etching by V2A (H_2O, Hydrochloric acid, Nitric acid, Vogel's pickling inhibitor) performed to make the recast layer visible.

Fig. 5-8 (right) shows the recast layer of the crater. The ejection of the molten material is incomplete, which is seen from the recast layer. The depth of the recast layer, which is molten, but not ejected material, is approximately $11\ \mu m$. Because of this phenomenon, the measurements of the crater depth is difficult and subject to great scatter, as mentioned also later in this section.

Fig. 5-8 (left) shows a case in which material is mostly ejected. However, also, in this case, a recast layer between 2 and $3\ \mu m$ is still present. This value is not negligible since the average crater depth in all the experiments performed is $8.2\ \mu m$. However, the recast layer in this case it is not only due to a lower PFE (which means not all the molten material is ejected), but it is also generated in the mushy zone.

Recast layer thickness, therefore, should be taken into account for a proper estimation of the fraction of energy that heats up the workpiece (F_a), since the real melt pool can be considerably larger than the final crater shape as often assumed in the literature (for instance [85]). The PFE is lower than 100%, the energy lost for melting the material that will form the recast layer should be taken into account as energy that flowed into the anode. The minimum recast layer thickness of 2 µm is included in the crater measurements and consider it in the simulation as a mushy zone.

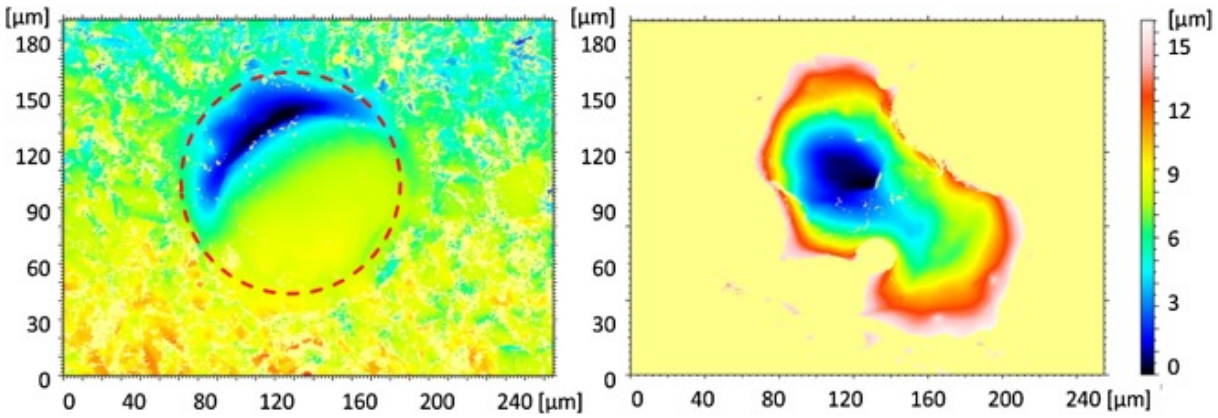

Fig. 5-7: Microscopic observations of the craters made with the same process parameter set.

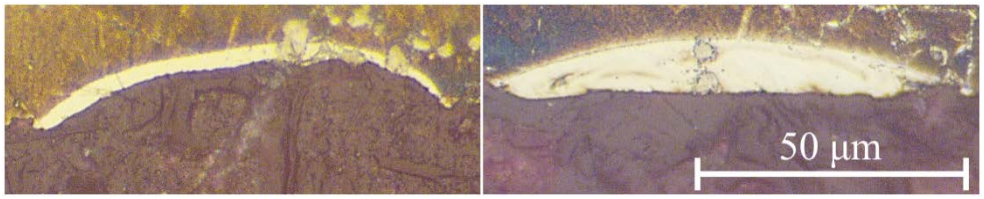

Fig. 5-8: Recast layer measurements, the craters are performed with the same set of parameters, but the material in the left picture is almost entirely ejected and not ejected in the right picture.

Fig. 5-9 shows the influence of the discharge current (I_d), the discharge duration (t_{ON}) and the open voltage U_{open} on the fraction of energy that is going into the anode (workpiece).

Longer discharge duration is shown to be beneficial for increasing the fraction of energy going into the anode and thus the efficiency of the process, while the opposite trend is shown for the discharge current. Open voltage has no clear trend, and this is confirmed by the high p-value obtained through the analysis of variance (0.372 for open voltage U_{open}).

Discharge current shows the major impact on efficiency (f_a) of the process, which is confirmed also by the relatively low values of their p-value of 0.140 for the intensity of the discharge). Longer discharge duration is increasing the efficiency (f_a), but it would also considerably increase the crater size. The p-value of the discharge duration is 0.259 which is relatively high, however the influence of t_{ON} was shown to be significant [88]. The high p-value could be due to the high variability in the crater shape and size, which may be greater than the influence of a longer or shorter discharge duration.

The increase of discharge current increases the electrons and ions flow through the gap between the electrodes. The increase of their density supports the collisions of the elements in the gap. Therefore less energy is carried by them to the workpiece. The increase of plasma density with the increase of discharge current was shown [135].

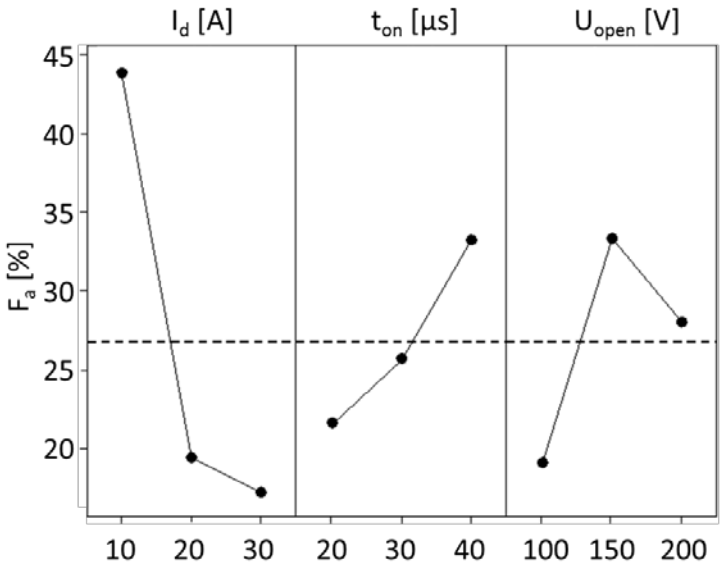

Fig. 5-9: Effect of different machining parameters on the fraction of energy going into the workpiece (anode). The solid lines show the trend of F_a change. Discharge current and duration of discharge show respectively a negative and a positive correlation with F_a, while the correlation between the open voltage and the fraction F_a due to the analysis of variance is not statistically significant.

Fig. 5-10 and Fig. 5-11 show the effect of the machining parameters on the crater diameter and depth. The first figure shows, that there is presumably a direct proportion between discharge currents and time length of the discharge on the final diameter, while the voltage seems to have a not significant influence on the final shape. The observation is confirmed by the analysis of variance: p-value for the discharge voltage is 0.555 while for the other three parameters are always less than 0.002. The open voltage does not have a high influence: this may be explained by the fact that the energy, which is flowing into the workpiece during the discharge, is determined by the discharge current and discharge voltage and not by the open voltage. Open voltage influences the gap between the tool electrode and the workpiece, as it was shown by Kunieda [136], therefore a variation of open voltage can change the plasma channel resistivity and accordingly it can have an influence to the discharge voltage and the total amount of energy.

The results of the depth measurements are less reliable due to the complexity of the crater measurements and low repeatability, which is caused by different PFE. Linear regression analysis gives a R^2 of only 39.80%, showing that the parameters taken into account are not relevant or not sufficient for determining the depth. The discharge current and the discharge duration have a stronger impact on the crater depth, however, considering the problems in the depth estimation due to the difficulties with the recast layer estimation and due to the non-axisymmetric shape of the crater, the crater measurements are only relevant if they are measured considering the recast layer from micrographs of the cross-sections.

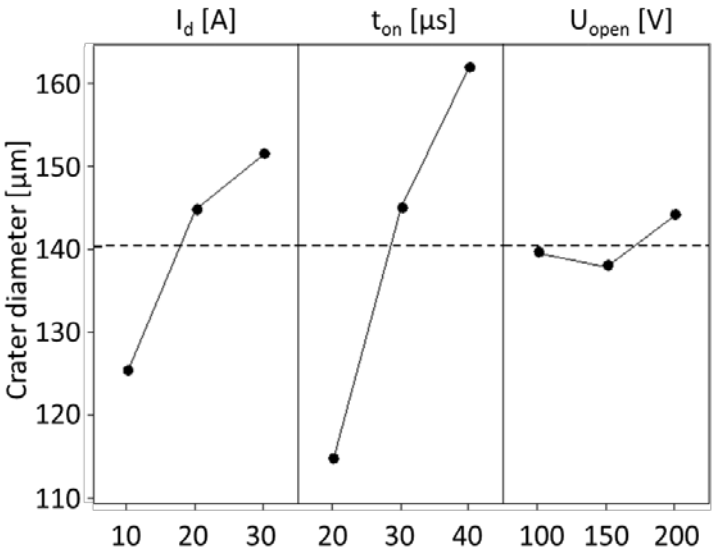

Fig. 5-10: Effect of different machining parameters on the diameter of the crater.

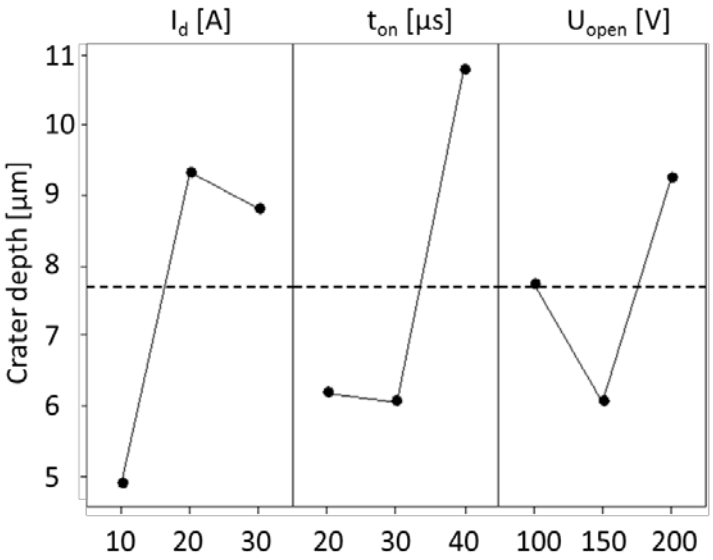

Fig. 5-11: Effect of different machining parameters on the depth of the crater.

5.5 Correlation between a single discharge and multiple discharges in EDM process.

After the estimation of the pulse parameters influence to the EDM drilling process through the full factorial experiment in chapter 3, it can be summarised that the MRR is almost linearly increasing with the increase of discharge current for Inconel 718. Discharge duration is interdependent to discharge current in a way that higher discharge current requires longer pulse duration. Therefore lower discharge current requires shorter pulse duration to achieve higher MRR. This effect can be explained by the density of the discharge energy which is distributed through the growing plasma channel. The growth rate of this channel is described in eq. (5-3), the plasma radius is increasing rapidly at the very beginning of the discharge, and its velocity slows down with the time. For the maximization of the

material removal, the energy density of the discharge has to be big enough to melt the material, but not much higher in order to not overheat it.

The influence to the fraction of energy going to the workpiece is opposite to the MRR calculation of Inconel 718 erosion in chapter 3, as is seen in the single discharge model results in the subsection 5.4, while the fraction of energy is interdependent to the MRR. The fraction of energy is decreasing with the increase of the discharge current parameter, but at the same time, the material volume removed per single discharge is increasing. This indicates another limitation of the process, where the increase of the discharge current has a saturation, after which the material removal per discharge and therefore in EDM drilling process will not increase any more.

Another important effect is the influence of the duty factor, which is estimated as a ratio between pulse duration and pause duration. The influence of the duty factor to the MRR is interdependent with a discharge current of the spark since more powerful sparks are removing more material. Therefore by keeping discharges short, the lower material volume removed by single discharge will be at the same time compensated by the increase of the number of discharges.

As it was reported [3], several microseconds are required for the deionisation of the gap between the electrodes in the EDM process. The next discharge should happen after the deionisation of the discharge channel. Otherwise, the location of the next discharge will be influenced by the previous one, which causes unwanted discharge concentration at the certain area. The deionisation effect is highly influenced by flushing, in a way that the better flushing – the faster the deionisation. In order to increase the duty factor and therefore the productivity, flushing has to be analysed, which is done in the following sections.

5.6 Graphene coating for the electrode

The electrode protective coatings for the needs of EDM drilling are barely investigated. This section gives an overview of the potential utilisation of graphene-based coating in EDM drilling; single craters are analysed and compared with simulation. Graphene is also often used to enhance the ceramics properties [137-139], it is also used as a coating of wire-EDM electrodes [140], but its influence on the EDM drilling process is not investigated in the literature.

5.6.1 Graphene fabrication and the properties of samples

The graphene growths on the copper foil by chemical vapour deposition synthesis (CVD), as it is schematically indicated in Fig. 5-12. This growth process involves high/low-temperature decomposition of a hydrocarbon source on a heated substrate (in this case copper). For the experiments, the graphene-coated copper foils from Graphenea S.A. are used. The foils have single layer graphene grown on a copper foil substrate. The properties and dimensions of the copper foils and the graphene film are provided by Graphenea S.A. and indicated in Table 5-4.

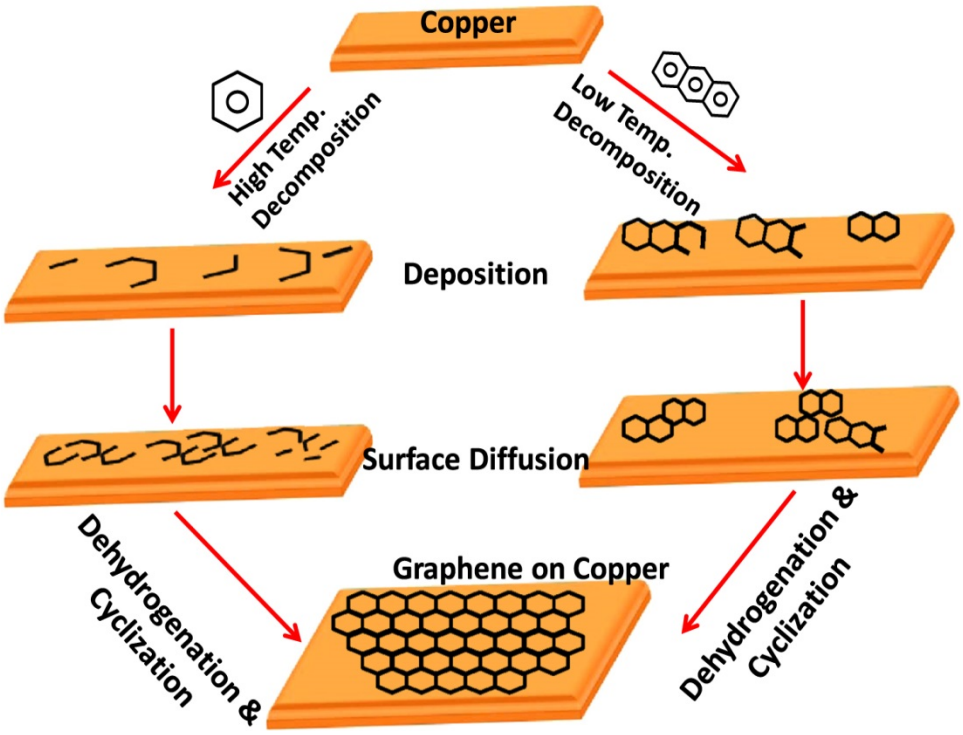

Fig. 5-12: Proposed mechanism for the growth of graphene on copper in an RF-CVD synthesis. A higher proportion of smaller radicles (left), due to ring opening at higher temperatures (1000 °C) and predominantly aromatic radicles (right) at lower temperatures (800 °C) [141].

Table 5-4: Copper foil properties and film properties of graphene.

graphene Film	
graphene film thickness (theoretical)	0.345nm
growth method	CVD synthesis
appearance (colour)	transparent
transparency	> 97%
coverage	> 98%
number of graphene layers	1
grain size	up to 20 µm
Substrate Cu Foil	
length and width	10 x 10 mm
foil thickness	18 µm
roughness	around 80nm

5.6.2 A preliminary study of graphene coating layers

This section investigates the potential utilisation of the graphene coating layers for all types of EDM machines, capacitor and transistor pulses are investigated in deionised water and oil dielectrics.

Experiments are performed on Drill 300 and Form 1000 machines from GF Machining Solutions, Agie Charmilles SA, Switzerland. EDM process parameters and erosion conditions

for both machines are presented in Table 2-2. Craters measurements are made with Alicona infinite focus microscope.

Table 5-5: EDM pulse parameters

Impulse type	Type 1	Type 2	Type 3	Type 4
Pulse duration	0.6 µs	4.9 µs	12.5 µs	205 µs
Discharge current	32 A	44 A	84 A	20 A
Ignition voltage	210 V	200 V	200 V	100 V
Dielectric	Oil	Deionized water	Deionized water	Oil
Workpiece material	Copper	Copper	Copper	Copper
Electrode material 1	Graphene-coated Cu foil	Graphene-coated Cu foil	Graphene-coated Cu foil	Graphene-coated Cu foil
Electrode material 2	Cu foil	Cu foil	Cu foil	Cu foil
EDM machine	Form 1000	Drill 300	Drill 300	Form 1000
Workpiece polarity	positive	positive	positive	negative

Crater diameter and shape are analysed on graphene coated foils in respect to uncoated foils. Crater diameter and shape are compared for craters on graphene coated foil and uncoated foil. For short duration pulses, foils have negative polarity, and for long duration (Type 4) pulse, foils have positive polarity. Polarity is chosen in accordance with typical polarities of the tool electrode and workpiece polarities for wire or drilling EDM and die-sinking EDM. Capacitor type pulses with high peak current and short duration are typically used in wire-EDM, EDM drilling and finishing in die-sinking EDM.

Crater measurement comparison is shown in Table 5-6. The diameter of the crater is shown as the average between the maximum (inscribed circle) and minimum (circumscribed circle) measured diameters. The maximum crater depth is measured as the deepest measured point with respect to the not-eroded surface.

Table 5-6: The results of craters measurements

N	Impulse type	Electrode material	Average crater diameter* [µm]		Maximum crater depth [µm]	
			tool	workpiece	tool	workpiece
1	Type 1	Graphene coated copper foil	32	40	2.3	2.5
2	Type 1	Copper	37	30	4.5	3
3	Type 2	Graphene coated copper foil	49	36	6	3.5
4	Type 2	Copper	35	35	7.6	3.8
5	Type 3	Graphene coated copper foil	77	69	-	5.2
6	Type 3	Copper	41	50	4.5	5.2
7	Type 4	Graphene coated copper foil	-	372	-	-2
8	Type 4	Copper	-	400	-	0

* standard deviation Ϭ is less than 10 %

The comparison between coated and uncoated tools with the impulse Type 1 is shown in Fig. 5-13. For the coated tool, the crater diameter on the copper workpiece is 40±4 µm, and on the graphene-coated tool , it is 32±3 µm. On the uncoated foil the crater diameter on the workpiece is 30±3 µm and on the tool is 37±4 µm. The crater diameter on the coated tool is bigger than on the uncoated tool but, as it is explained in section 5.4, crater diameter can significantly vary during from one discharge to another (with standard deviation ϭ is less than 10 % from the measured value).

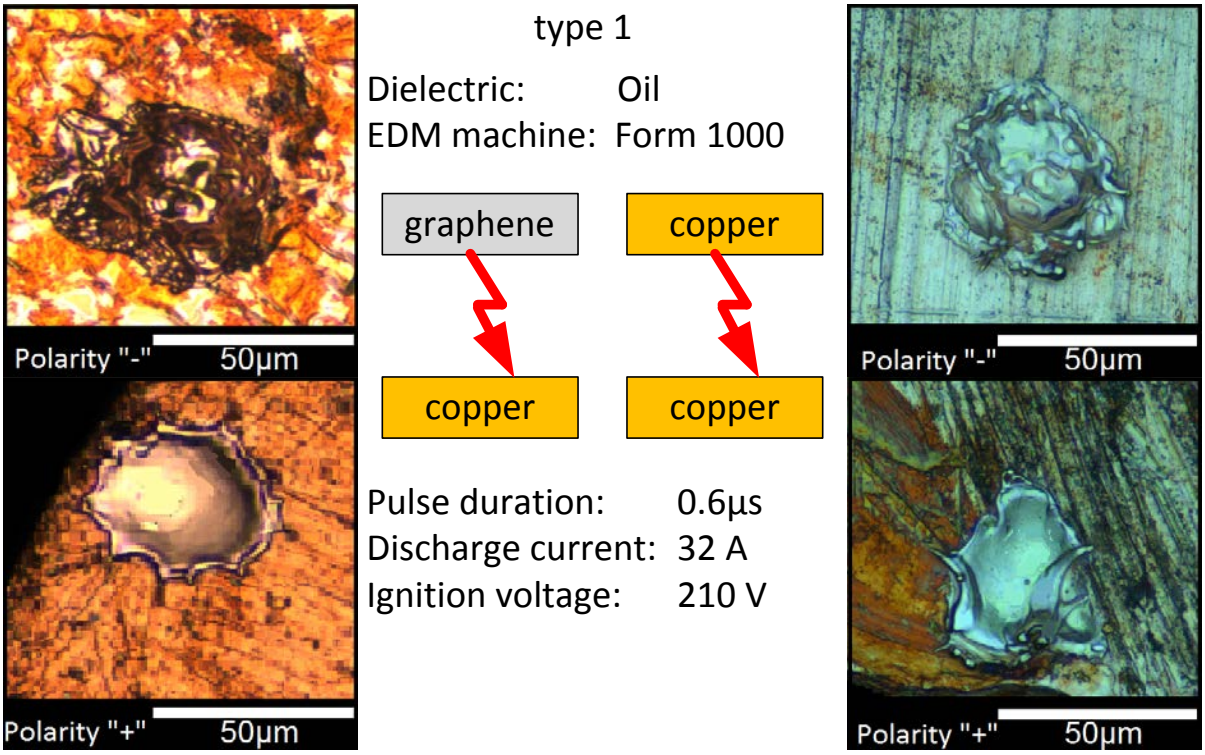

Fig. 5-13: Comparison of the craters generated by type 1 pulse. Left is a tool coated with graphene and right is an uncoated copper tool, craters on the workpieces are below the craters on tools.

Pulse type 2 and type 3 are generated using Drill 300. The experimented result with the coated and uncoated tool is shown in Fig. 5-14. Crater diameter on graphene coated foil is 49±5 µm and on the workpiece is 36±4 µm. The crater on the workpiece is not clearly visible due to copper oxidation in water dielectric. The diameter of the crater on the uncoated tool and the crater on workpiece have same 35±4 µm diameters, while on the coated tool the crater is significantly bigger.

Craters generated by impulse type 3 are shown Fig. 5-15. The diameter of the crater on the coated tool is 77±8 µm, and the crater on the workpiece is 69 ±7 µm. Craters in the experiment with the uncoated copper tool are both significantly smaller. The diameter of the crater on the uncoated tool is 41±4 µm and on the workpiece is 50±5 µm. The diameter comparison of craters on the coated tool is difficult, since the craters made on the graphene coated tool are in a burnt out region, and it could be the reason for the diameter increases.

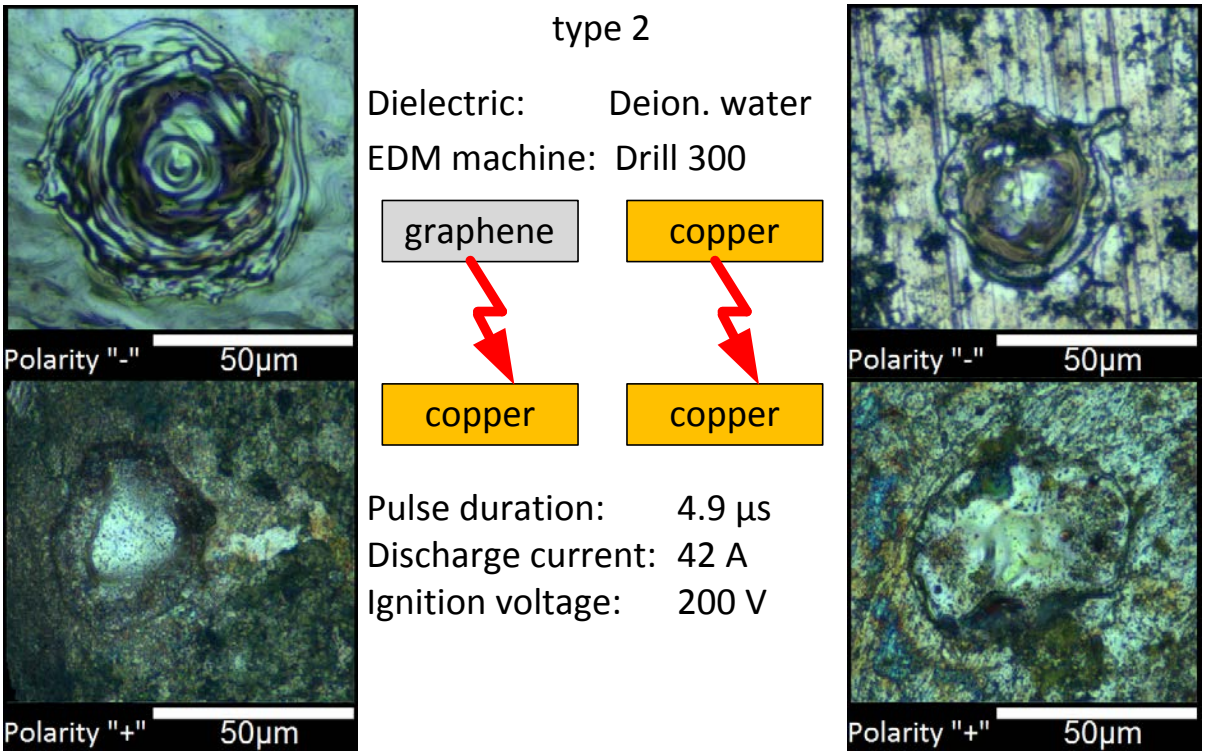

Fig. 5-14: Comparison of the craters generated by a type 2 pulse. Left is a tool coated with graphene and right is an uncoated copper tool, craters on the workpieces are below the craters on tools.

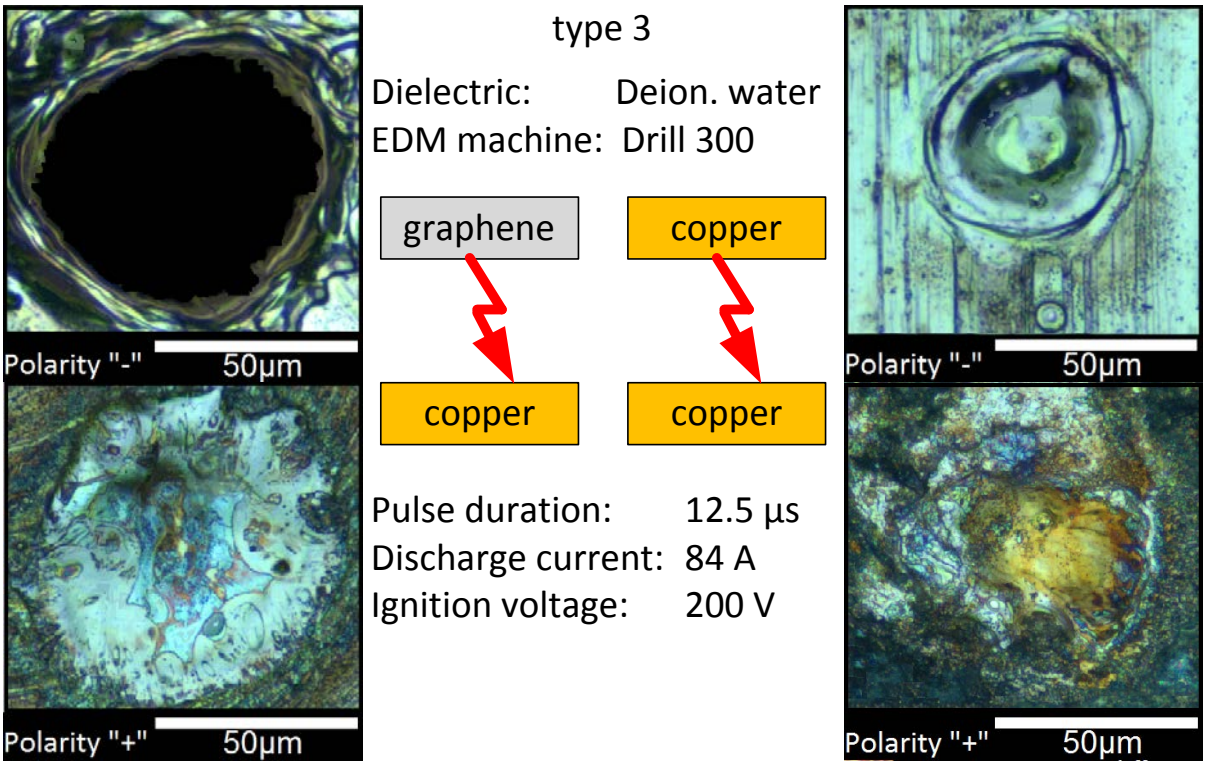

Fig. 5-15: Comparison of the craters generated by type 3 pulse. Left is a tool coated with graphene and right is an uncoated copper tool, craters on the workpieces are below the craters on tools.

The selected capacitor pulses show the growing trend of the crater size at graphene coated tool with the increase of the pulse energy in comparison to the crater on the workpiece, while on the uncoated tool the crater remained similar on the tool and on the workpiece. This trend is opposite to what was expected and analysed in more details in section 5.4.

Transistor discharges are tested in order to understand the potential of graphene layer utilisation for the needs of die-sinking EDM. Transistor pulse Type 4 is used (Table 5-6). On graphene coated copper tool it is possible to observe the burnout region of foil as well as it is observed with capacitor impulse Type 3.

Craters made using transistor pulses are shown in Fig. 5-16. The average diameter of the crater on workpiece made by the uncoated tool electrode is around 400±40 µm, and the crater made by the coated tool electrode is around 350±35 µm. Carbonisation of the workpiece is visible as a black zone in the centre of the crater when a coated tool copper electrode is used.

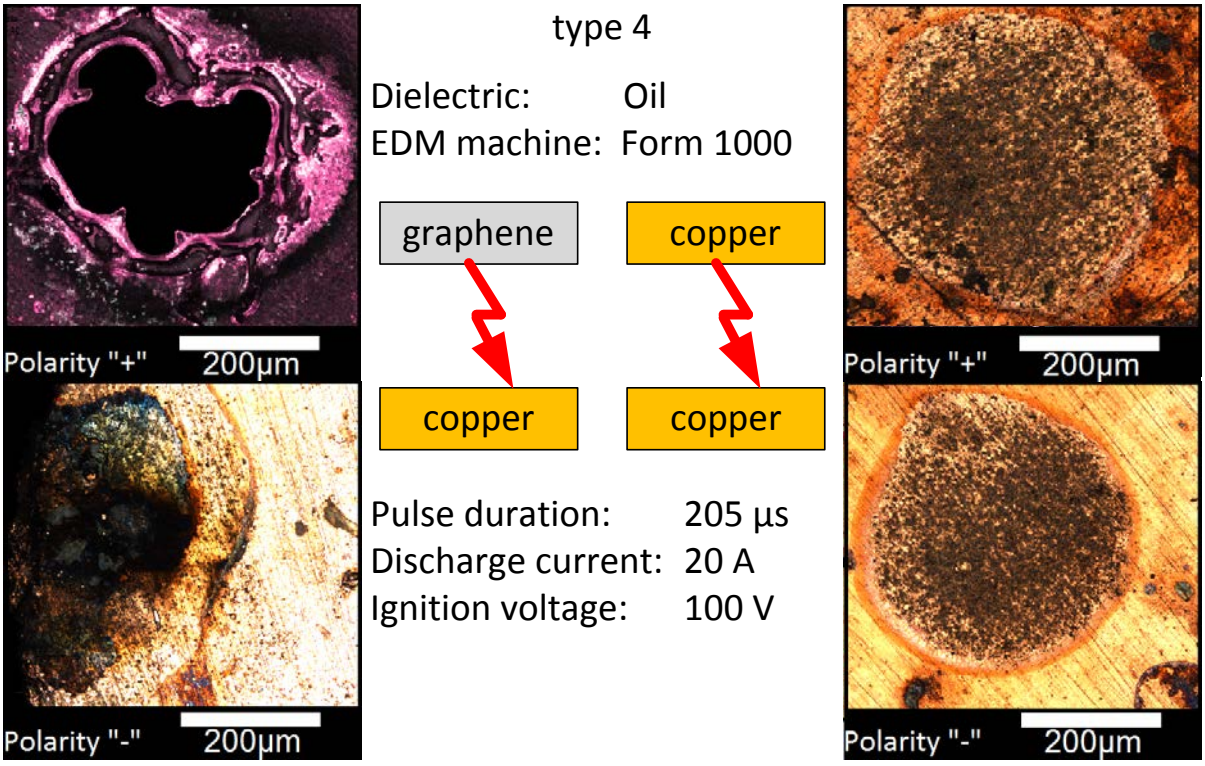

Fig. 5-16: Comparison of the craters generated by Type 4 pulse. Left is a tool coated with graphene and right is an uncoated copper tool, craters on the workpieces are below the craters on tools.

Machining with transistor types of discharge is difficult to analyse due to the destruction of the 18 µm thickness foil. Furthermore, with higher energy, the thin graphene layer is evaporated at the beginning of the discharge and will not have a significant effect on the erosion process.

The experiments with short duration pulses Type 1 (0.6 µs) show lower diameter on the graphene-coated foil. According to [142, 143], the high evaporation temperature of the coating materials is the most critical parameter, for low net power loss at the cathode surface is directly related with the high erosive yield on the anode surface. The energy balance phenomenon for zinc-coated electrodes is explained in detail [143] . Experimental results with higher energy pulses Type 2 and Type 3 shows a trend of the crater growth on the graphene-coated tool. Next section 5.7 analyses the effect of the short, low energy pulses, since there the thin coating of graphene in this process should be more significant to the erosion process.

Transistor type discharge (Type 4) does not have a positive effect on the crater diameter and crater depth on WP. Effect of the electrode wear could not be detected because of foil burnout region.

5.7 Potential utilisation of graphene coating layers for electrode protection and increase of MMR.

The analysis of the single crater discharges to the graphene-coated foil is shown, the influence of short capacitor discharges is analysed. Finally, the experiment results are compared with the simulation of the single discharge.

Experiments are performed with Form 1000 machine from GF Machining Solutions, Switzerland. The graphene coated foil is hold by the clamping device, as it is shown in Fig. 5-17. Pulse parameters are selected based on the previous research and are shown in Fig. 5-9. The coated foil is used as a tool electrode and 1 mm copper cylindrical electrode is used as a workpiece.

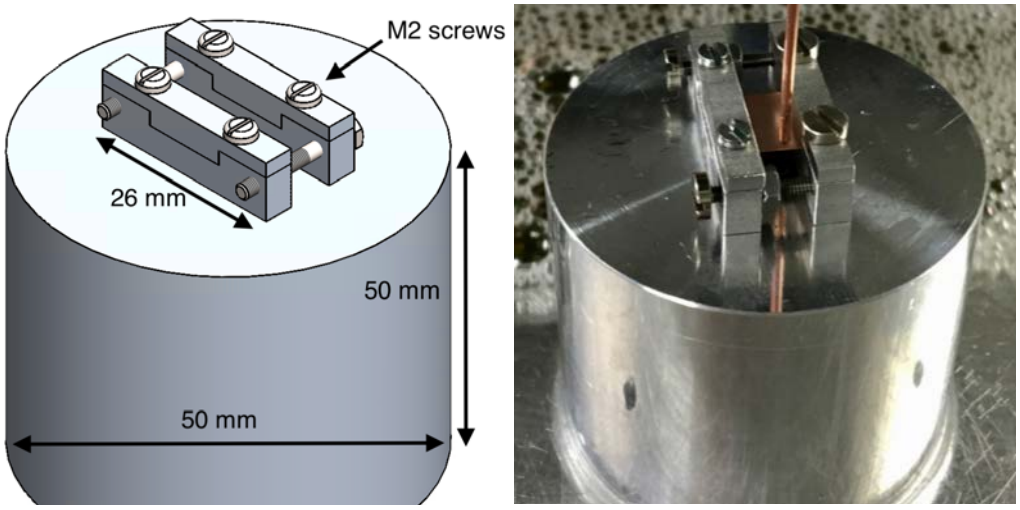

Fig. 5-17: The foil clamping device is designed to hold 20 mm width and 20 mm length graphene coated copper foil. The drawing of the holder is on the left and the holder during experiments is on the right.

Table 5-7: EDM pulse parameters.

Impulse type	Type 1	Type 2	Type 3	Type 4
Pulse duration	0.6 µs	0.3 µs	0.2 µs	0.2 µs
Discharge current	32 A	11 A	5 A	2.5 A
Ignition voltage	210 V	200 V	200 V	110 V
Dielectric	oil	oil	oil	oil

The craters measured on the graphene-coated foil are shown in Fig. 5-18and the measurement results are in Table 5-8. The energy of the pulses is selected in the way that each next crater is about two times smaller than the previous one; the pulse Type 4 is the limit of the current EDM machine. The diameter of the smallest crater is about 5 µm.

The results of the measurements showed that the difference between craters on coated and uncoated foils is increasing with the reduction of the pulse energy. With the smallest possible pulse energy, the crater on the graphene-coated foil is more than 15% bigger. This difference is statistically significant as it is indicated in Table 5-8. and can be only explained by the influence of the graphene layer. A possible explanation of this phenomenon is given after the simulation of the graphene foil in the heat transfer model in section 5.8; the experiment results are shown in Table 5-8.

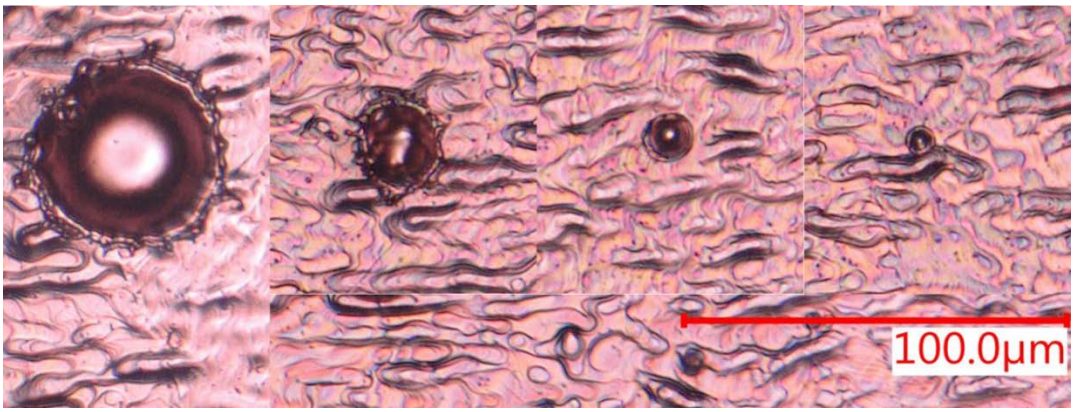

Fig. 5-18: Craters on the graphene-coated foil with pulse parameters from left to right types from 1 to 4. Each next crater is about twice smaller than the previous one.

Table 5-8: The measurements of the crater diameter.

Crater Diameter	Type 1 [µm]	Type 2 [µm]	Type 3 [µm]	Type 4 [µm]
uncoated foil				
average	41.9	19.4	10	3.6
σ (standard deviation)	2.8	0.9	0.7	0.5
graphene coated foil				
average	44.9	21	11	4.2
σ.2standard deviation)	2.5	0.8	0.8	0.4

Difference	7.4%	8.2%	10.1%	15.5%

5.8 Simulation results of graphene and discussion

The single crater based model, similar to the model described in section 5.3, is used to simulate the influence of the graphene coating to the heat distribution. The thermally thin approximation (approximation of a thin uniform structure) is used in the model to simulate the properties of the graphene-coated layer. The temperature difference between the top of the layer and the bottom of the layer is neglected. More details regarding thermally thin approximation can be found [144].

The craters on the foil without the coating layer are compared with the craters on the foil with the coating layer. The results are shown in Table 5-9. The average difference is less than 0.5 %, which is significantly lower in comparison to the experimental results.

Table 5-9: Difference between the crater simulated on the graphene coated foil and on uncoated foil.

Pulse Type	Crater radius deviation [%]	Crater depth Deviation [%]
Difference between uncoated and graphene coted foils	0.45 %	1.27 %

The difference between simulation and experiment is significant and indicates imperfection of the heat transfer model to describe the influence of the graphene coating. Difference shows that the influence of graphene layer is more than the just the heat transfer trough the increase of thermal conductivity, but graphene is changing the fraction of energy distribution towards the coated electrode. The influence of the layer becomes higher with the reduction of the pulse energy which can be explained by the destruction of the layer at the beginning of the discharge. The lowest energy craters have the diameter of below 5 µm, which increase the probability that the crater is inside one grain of Graphene (as it is indicated in Table 5-4, the Graphene grain size is up to 20 µm). Overall the graphene coating is influencing the EDM process, but utilisation of such coating becomes problematic due to the destruction of the layer at the beginning of the discharge.

6. CFD simulations of flushing aspects and models verification

The flushing during EDM drilling processes is analysed in this section, the influence of the electrode length and flushing channel configuration is shown. Flushing during slot machining is investigated. Finally, flushing the conditions during the drilling process are investigated experimentally by particle tracking velocimetry. For the computational flow simulations, the commercial software ANSYS CFX 18.1 is used in order to compute the main flow directions and velocity distribution at the electrode outlet.

6.1 Flow analysis in electrode flushing channel

In order to calculate the flow conditions, the flow regime has to be estimated by using the Reynolds number *Re*:

$$\mathrm{Re} = \frac{\rho \cdot v \cdot L}{\mu} \tag{6-1}$$

, where ρ is the density of the fluid, v is the velocity of the fluid with respect to the object, L is characteristic length and μ is dynamic viscosity of the fluid. In a cylindrical tube flow, the transition from laminar to turbulent flow is considered at a Reynolds number of about 2300. The characteristic length as it shown by Sigloch [145] is defined for tube flows as

$$L = \frac{4 \cdot A_c}{P_c} \tag{6-2}$$

where P_c is the perimeter of the flushing channel and A_c is the area of the flushing channel. Water data at 25 °C is used and has a density ρ=997 kg/m^3 and dynamic viscosity μ=8.9·10^{-4} kg/(m·s), while the velocity depends on the electrode length for the given input pressure of p=6.5 MPa. Table 2-2 shows the expected flow conditions for the investigated electrodes depending on the chosen electrode as well as their length.

Table 6-1: Reynolds numbers estimation.

Electrode type	characteristic length L [mm]	Reynolds number, l=100 mm	Reynolds number, l=400 mm
Multi-channel 1.0 mm	0.19	4874	2365
Multi-channel 0.5 mm	0.085	1450	744
Single-channel 0.5 mm	0.2	992	744

While the 0.5 mm outer-diameter electrodes show Reynolds numbers below 2300, the calculated Reynolds number for the 1.0 mm multi-channel electrode is above 2300 and even

for the longer electrode, which usually shows lower velocities due to the higher pressure drop. Thus the flow can be simulated assuming laminar flow conditions for the 0.5 mm electrodes while for the 1.0 mm electrode turbulence models are applied.

Considering laminar flow conditions in a circular tube, the Hagen-Poiseuille law, which is showed in Eq. (6-3), can be used to estimate analytically the mean flow rate or flow velocity in the electrodes based on the provided pressure from the machine.

$$V_f = \frac{\pi \cdot \Delta p \cdot r^4}{8 \cdot \mu \cdot l} \tag{6-3}$$

where V_f is the volumetric flow rate, Δp is the pressure difference, r is the radius of the flow channel and l is the linear dimension. The flow rate is in inverse proportion to the length of the electrode but proportional to the radius to the power of four. An electrode which is worn down to half of its length will provide doubled flow rate. On the other hand, the cross section of the electrode influences the flow rate. To investigate the conditions of multi-hole configurations fluid flow simulations are conducted. The performance of the process depends strongly on the removal of the debris, which is highly influenced by the flushing and thus the flow rate of the dielectric out of the electrode.

As the 1.0mm multi-hole configuration electrode needs to be simulated by employing turbulence models the wall roughness needs to be estimated. Besides the no-slip condition, which means flow velocity of zero at the walls, the roughness is used to calculate the wall flow profile close to the wall. To include the roughness inside electrode chambers and the drilled hole in the simulation the relation between ten-point mean roughness Ra and sand-grain roughness is used. The relation was empirically found by Adams [114] and shown in Eq.(6-4).

$$\varepsilon = 5.863\mathrm{Ra} \tag{6-4}$$

where ε is the sand-grain roughness. Measured Ra roughness and calculated sand-grain roughness are shown in Table 6-2.

Table 6-2 Ra roughness and sand-grain roughness.

Roughness	Inside of electrodes channel	Outer electrode surface	The surface of the hole
Ra [µm]	1	6.4	6.4
ε [µm]	5.86	37.52	37.52

Talysurf from Taylor Hobson is used for tactile measurements of the roughness inside the flushing channel of pre-cut piece of the electrode. For CFD simulations ANSYS 18.1 is used, while the geometry files are made with SolidWorks 2016 in analogy to the experimental set-

up. The cross-section of the multi-hole electrode was determined by an Alicona measurement with a slightly simplified inner geometry at the corners to mesh the model. The standard k-ε-model for turbulence is applied. Due to the small geometry features of the multi-hole electrode a rather fine mesh consisting of 200'000-1'000'000 elements, depending on the size and length of the electrode, is used to resolve the flow profile over the cross-section. Electrode rotation is neglected, since it is relatively low in comparison to the flushing flow, for instance about 200 mm^3 of dielectric flow is pumped during 1 rotation, therefore all liquid in the gap between electrode and workpiece is replaced multiple times during one rotation.

The single-channel electrode flow can be treated as the well-known flow through a cylindrical tube. From experience and analytical investigation, a circular cross-section offers the best geometry for lower pressure drop. The flow profile of the fully developed laminar flow can be assumed to be parabolic. Tietjens [146] proposed for the entry length l_e for a stable laminar flow the following relation:

$$l_e = 0.06 \cdot \mathrm{Re} \cdot \mathrm{L} \tag{6-5}$$

Thus for the short single hole electrode, an entry length of about 12 mm for a fully developed flow is estimated.

In order to study the flow in the multi-channel electrode, the computational simulations are used. Fig. 6-1 shows on the left side the velocity distribution of the 1.0mm multi-hole electrode, while due to the turbulent flow conditions high-velocity gradients towards the wall occur. On the right side, the turbulent kinetic energy distribution is shown, which reaches the maxima close to the centre walls.By turbulence kinetic energy in fluid dynamics is considered the value of mean kinetic energy correlated in turbulent flow with eddies. The volume flow rate is about factor eight times smaller compared to the single hole electrode due to cross-section and velocity profile.

Fig. 6-2 is showing the cross-section at the lower part of the multi-hole configuration electrode in a workpiece for the turbulent kinetic energy distribution (YZ-plane). It can be observed, that the highest turbulence kinetic energy of the flow occurs in the corner of the gap, where the flow changes its direction. Due to the pressure drop lower flow rates are measured, where shorter electrodes have a much higher influence compared to longer ones (25% to almost zero) due to the lower flow speed.

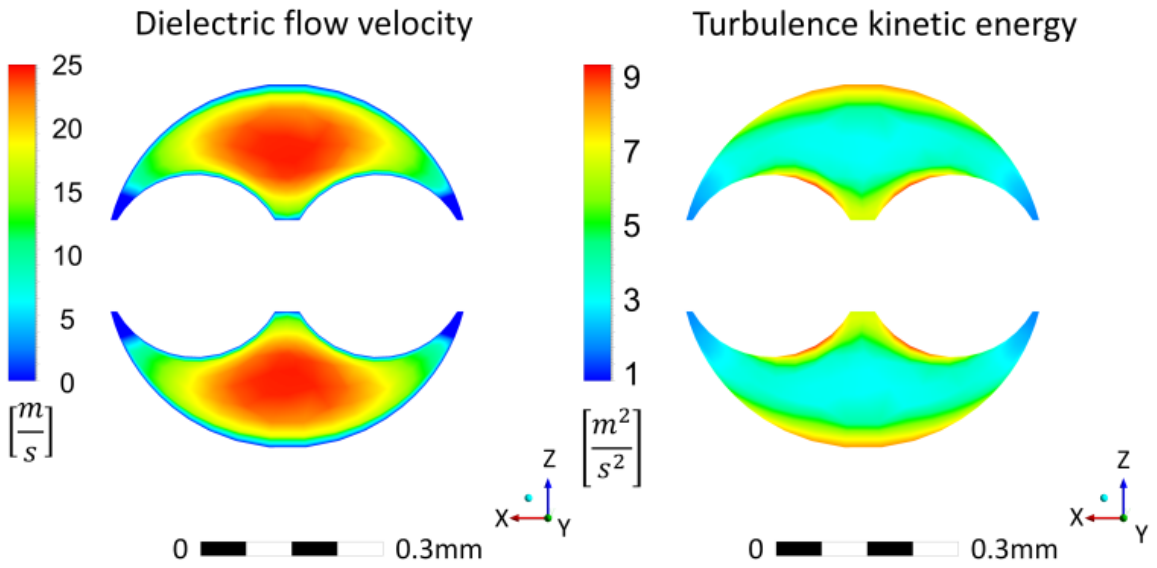

Fig. 6-1: Axial flow velocity distribution at the outlet (left) and turbulence kinetic energy at the outlet (right) of type 1 (Fig. 2-6), 1.0 mm outer diameter multi-hole electrode, where turbulent flow conditions are considered

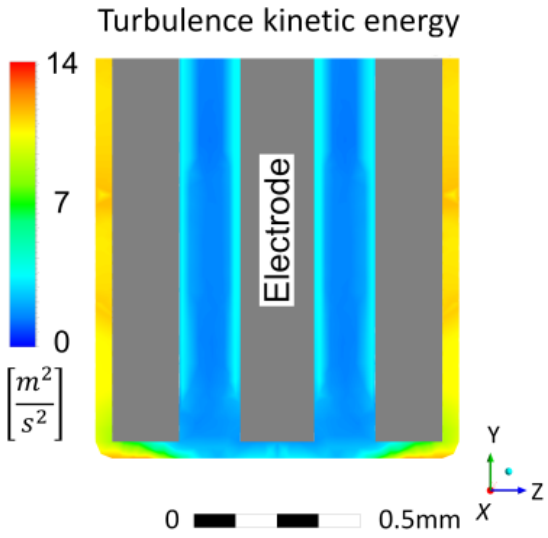

Fig. 6-2: Turbulence kinetic energy plot in longitudinal-section of YZ-plane of the lower part of the multi-hole electrode insertion into the eroded hole in the workpiece.

6.1.1 Results and verification

In order to investigate flow dynamics and influence of electrical discharge on the flow, a high-speed camera Phantom v12.1 from Vision Research is used. The image recording frame rate is set to 30000 fps. The experiments are performed on Drill 300 from GF Machining Solutions, Agie Charmilles SA. The experimental setup is shown in Fig. 6-3.

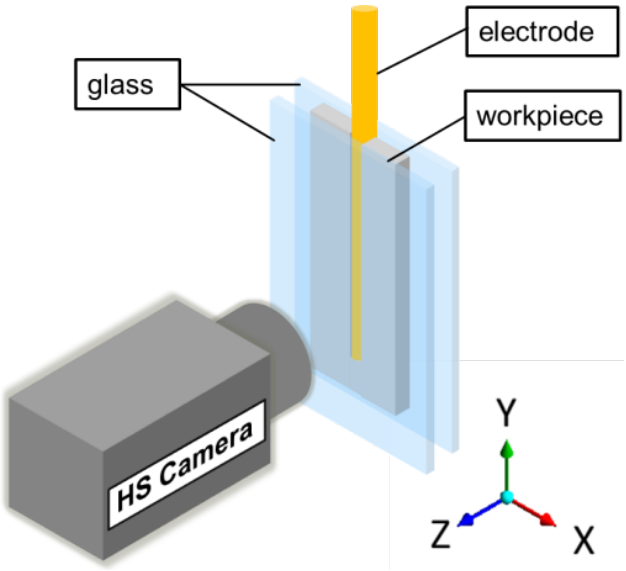

Fig. 6-3: High-speed camera setup, the workpiece is mounted between two pieces of glass

The workpiece is clamped between pieces of glass in order to be observed by the camera. Light sources are used from the front and from the backsides. An electrode is placed in the cuboidal 12 mm long slot, which is machined in Inconel 718. Observations are made with 0.5 mm multi-channel and single-channel electrodes.

The velocity of the flow is analysed based by tracking of the bubble movement. Of course, the movement of bubbles is not equal to the flow velocity. However, the flow velocity influences the velocity of the bubble. Fig. 6-4 and Fig. 6-5 show the bubble movement with single-channel and multi-channel electrodes. The analysis of the flow in the gap between the electrode and the workpiece by PTV is in the section 6.3.

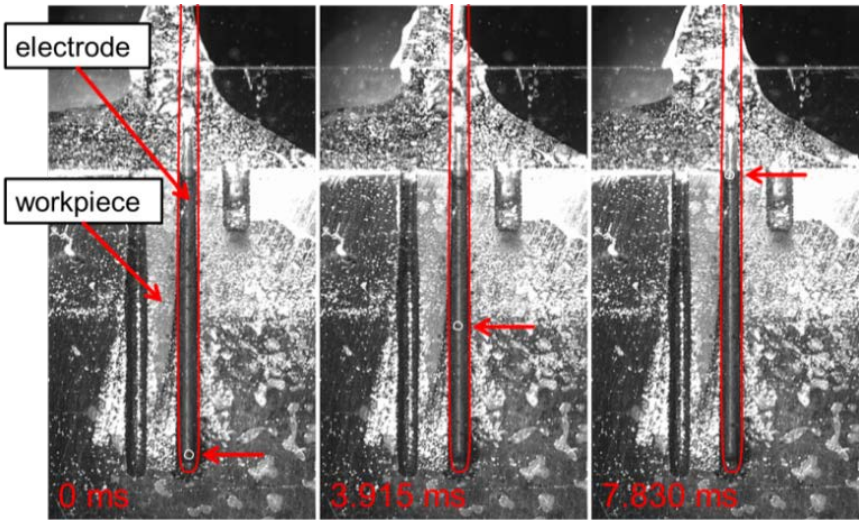

Fig. 6-4: The high-speed tracking of the bubble movement with 0.5 mm single-channel electrode, the time indicator for each frame is at the bottom. The stream of water is visible above the hole. The two other slots inside the workpiece are used for a different experiment

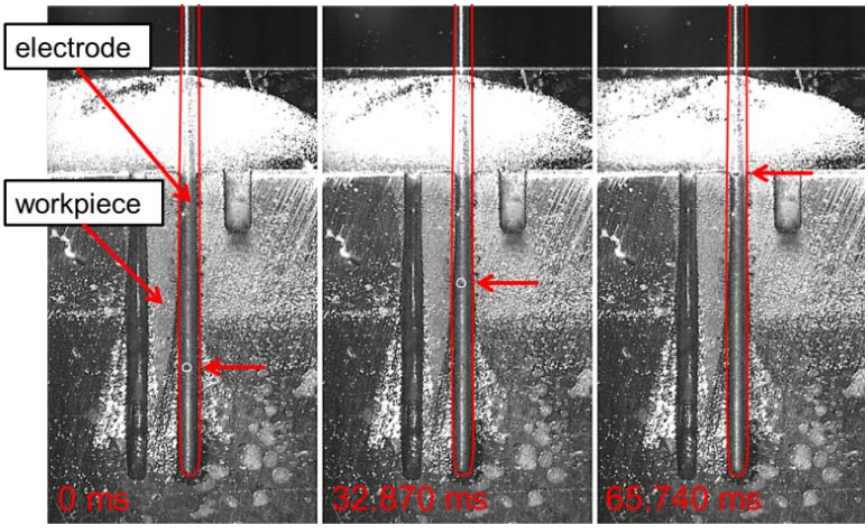

Fig. 6-5: The high-speed tracking of the bubble movement with 0.5 mm multi-channel electrode, the time indicator for each frame is at the bottom.

The bubble tracing shows that the flow velocity with the multi-channel electrode is significantly lower in comparison to the single-channel electrode. The experiment was repeated with and without erosion. Discharges do not have a significant influence on the bubble movement; however, the movement of the single-bubble is no longer possible to track since far more bubbles are created. Nevertheless, the discharge should have an influence on the flushing conditions, and this influence is analysed in the section 6.3.

6.1.2 Volume flow rate, MRR, recast layer and electrode wear measurements

The flow rate of a 1 mm multi-channel electrode Type 1 (see Fig. 2-6) is measured and simulated in- and outside of a workpiece, whereas the results are shown in Fig. 6-6. Generally, the flow through the electrode inside the workpiece is slower due to the higher pressure drop, which is induced at the walls of the workpiece and due to the change of flow direction and cross-section. The difference between the flow when the electrode inside or outside the workpiece is higher when the flow rate is higher than 1 ml/sec, where it can be caused by a higher pressure drop due to turbulence, considering a non-linear problem. The influence of the electrode length on the flow rate is significant. Considering Hagen-Poiseuille law, a 100 mm electrode has four times higher flow rate as a 400 mm long electrode.

The experimental flow rate is usually higher than the simulated one due to the unknown pressure drop through the variation in the cross section of the small electrodes and from the measurement at the pump to the electrode. The pressure drop from the pump to the electrode is neglected considering Hagen-Poiseuille law, as the flow rate is very low and the diameter of the ducts from the pump is larger compared to the electrode channels. Finally, the properties of the fluid are supposed to be the ones of clean water without particles.

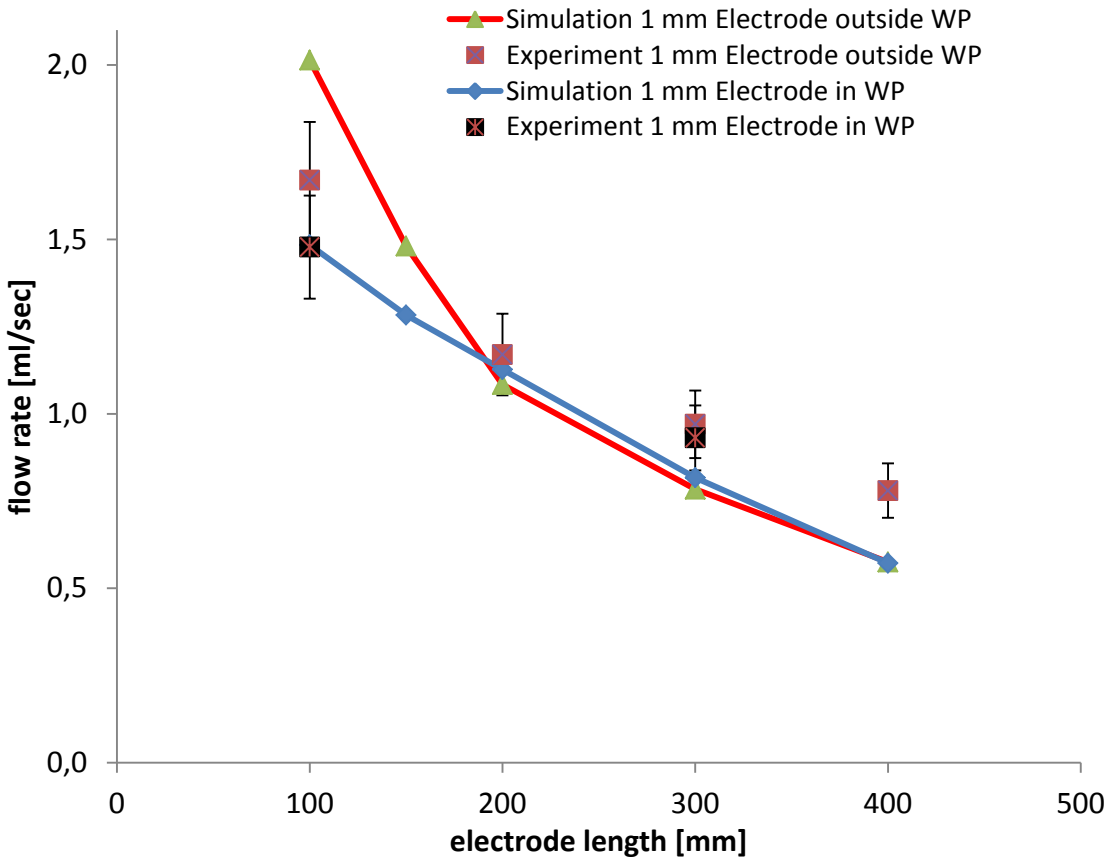

Fig. 6-6: Flow rate through the 1 mm diameter multi-channel electrode 10 mm inside the workpiece (WP) and outside the workpiece, simulation and experiment.

Table 6-3: Flow rate measurements and simulation for 1 mm multi-channel, 0.5 mm single/multi-channel electrodes outside workpiece.

	Experiment				Simulation				
Electrode length [mm]	100	200	300	400	100	150	200	300	400
1 mm electrode outside work-piece [ml/sec]	1.67	1.17	0.97	0.78	2.01	1.48	1.08	0.78	0.58
1 mm electrode inside work-piece [ml/sec]	1.48		0.93		1.48	1.28	1.13	0.82	0.57
0.5 mm multi-channel electrode [ml/sec]	0.2	0.069	0.045		0.131	0.131	0.96	0.069	0.052
0.5 mm electrode single -channel [ml/sec]	0.78	0.56	0.41		0.81	0.60	0.49	0.35	0.25

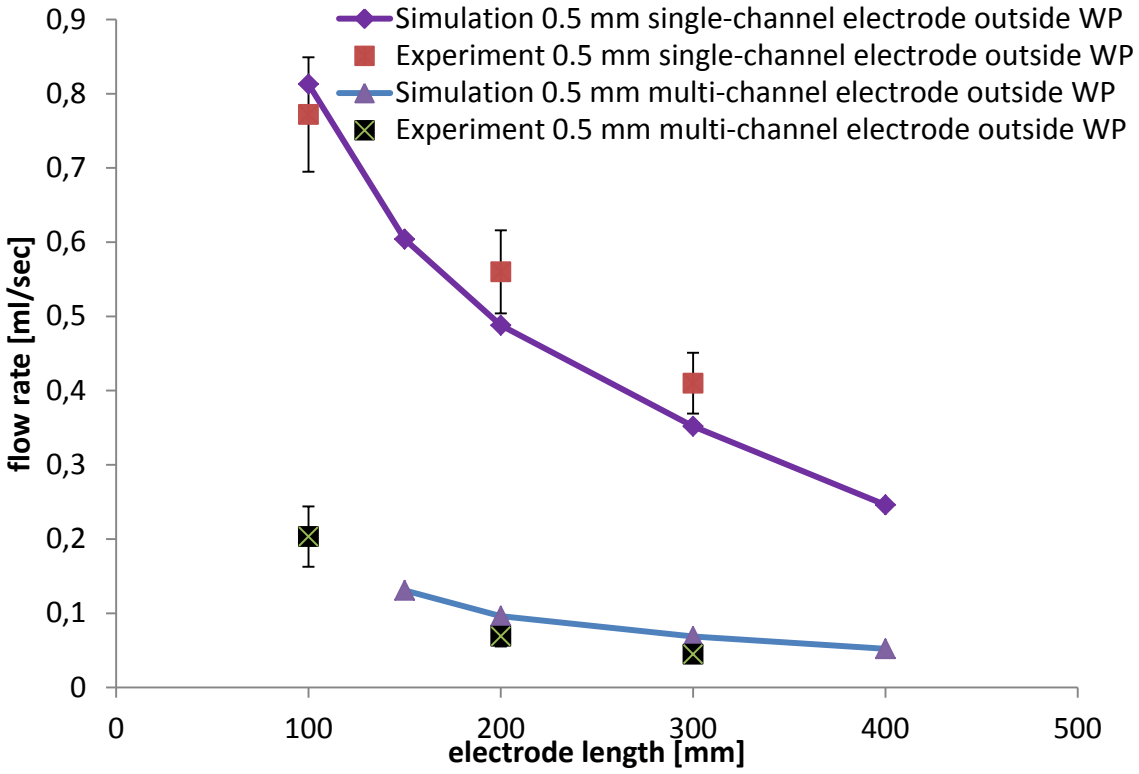

Fig. 6-7: Flow rate through the 0.5 mm diameter single-channel electrode for 10 mm inside the workpiece (WP), simulation and experiment

In order to see the effect of flushing on MRR and relative electrode wear (E_W), drilling tests are performed. The measurement of electrode wear E_{Wt} is performed after every erosion, and it is considered as a reduction of the length of the electrode. From those measurements, the relative tool wear as wear related to the eroded workpiece volume is calculated.

Experimental data regarding MRR and electrode wear are shown in Table 6-4, experimental conditions and erosion parameters in Table 6-5.

Table 6-4: MRR measurements.

Electrode diameter	Electrode length [mm]	E_w [%]	MRR [mm^3/s]
1 mm multi-channel	200	34.2	2.83
	400	33.96	2.76
0.5 mm multi-channel	200	37.0	0.33
	400	95.2	0.15
0.5 mm single-channel	200	125.4	0.76
	400	155.0	0.70

For 0.5 mm multi-channel electrode, the discharge current is significantly reduced, due to electrode destruction through melting. Thereby it was recognized that internal flushing has also electrode cooling function, which is essential for thin electrodes, where electrical resistivity is high.

Experiments showed that MRR is not significantly influenced by the fluid flow reduction for 1 mm multi-channel and 0.5 mm single-channel electrodes. However, with the shorter electrode, a slight increase of MRR is seen.

The electrode wears significantly reduces along with the electrode length reduction for the 0.5 mm single-channel electrode and even more for the 0.5 mm multi-channel electrode. The influence of electrode length to MRR is insignificant with the 1 mm electrode.

As it is previously shown, the 0.5 mm multi-channel electrode has the most significant drop of flushing flow with the length. This fact leads to an almost linear increase of MRR along with the electrode length reduction. The electrode wear with long 0.5 mm diameter multi-channel electrodes is almost three times higher than with short electrodes. If flushing efficiency is insufficient to remove the eroded material from the hole, it will lead to ineffective discharges. The increase of pause duration helps to evacuate the eroded material, which will not increase the MRR but will help to decrease E_w and enhance the process stability.

Table 6-5: EDM conditions.

	EDM Condition
Workpiece material	Inconel 718
Electrode material	Copper
Dielectric	Deionized water
Holes type	Blind
Pause duration	15 µs
Ignition voltage	120 V
Pulse duration	32 µs
Discharge current	28 A, 14 A*
H	10 mm
Dielectric pressure	6.5 MPa
Electrode polarity	negative

* Lower discharge current is applied for 0.5 mm multi-channel electrode

The recast layer thickness (RLT) measurements are presented in Table 6-6. The flushing conditions have an influence on the RLT with both 1mm multi-channel and 0.5 mm single-channel electrodes. However, the difference is much higher with smaller electrodes. A higher RLT in case of 0.5 mm electrodes can be caused by a smaller electrode-workpiece gap and not by internal electrode flushing. The method and preparations for recast layer measurements are shown [88].

Summarising, insufficient flushing efficiency is the crucial limiting factor in deep hole drilling. In this case, a simple cylindrical flushing channel provides the best performance of the flow. Furthermore better flushing is not only enhancing the abilities of deep hole drilling and increasing MRR, but it is also reducing the recast layer thickness.

Table 6-6: Recast layer measurements.

Electrode length [mm]	Measuring site of the drilled hole	RLT 1 mm electrode [µm]	RLT 0.5 mm electrode [µm]
200	entrance	18.9	12.7
200	exit	18.9	17.8
400	entrance	19.2	15.3
400	exit	20.5	24.6

RLT is the most significant output, influenced by the flow rate reduction.

6.2 Fluid dynamics simulations during slot machining

This section explains in more details the fluid simulations during slot machining, as it is mentioned in subsection 4.4.3. It gives more explanation to the influence of the flushing condition to the machining process during odd, even and overlapping holes drilling in the ODEM strategy, which is described in details in subsection 4.4.2.

Flow conditions during slot machining process are shown in Fig. 6-8, it is indicated that having the same inlet pressure in all three conditions during slot machining, on the one hand, the inlet dielectric velocity during odd hole drilling is the lowest, but on the other hand, the outlet velocity is the highest.

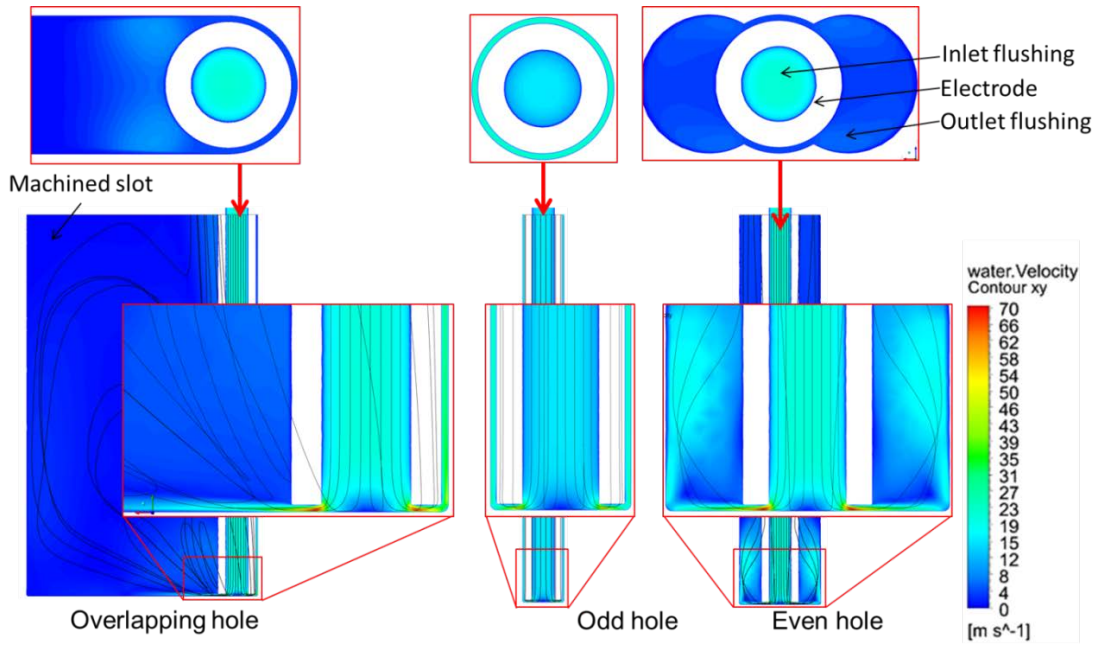

Fig. 6-8: Fluid flow in different drilling conditions. Overlapping hole machining has a region with low velocities in the opposite corner to machining area. The highest outlet velocity of the fluid is in odd holes; it is an indicator of better particle evacuation condition. During even hole machining eroded particles are colliding the wall of neighbouring hole far from the erosion process, as it is indicated in Fig. 6-9.

Low outlet velocity can lead to non-evacuated material in the machining area. The concentration of non-evacuated material in the erosion zone can cause a significant reduction of MRR and increase of wear as it was mentioned in section 5.5.

The comparison of three types of hole drilled during the slot machining process is given in Fig. 6-9. The agglomeration of unremoved material deposited on the lateral side of the neighbouring hole is visible after even hole drilling.

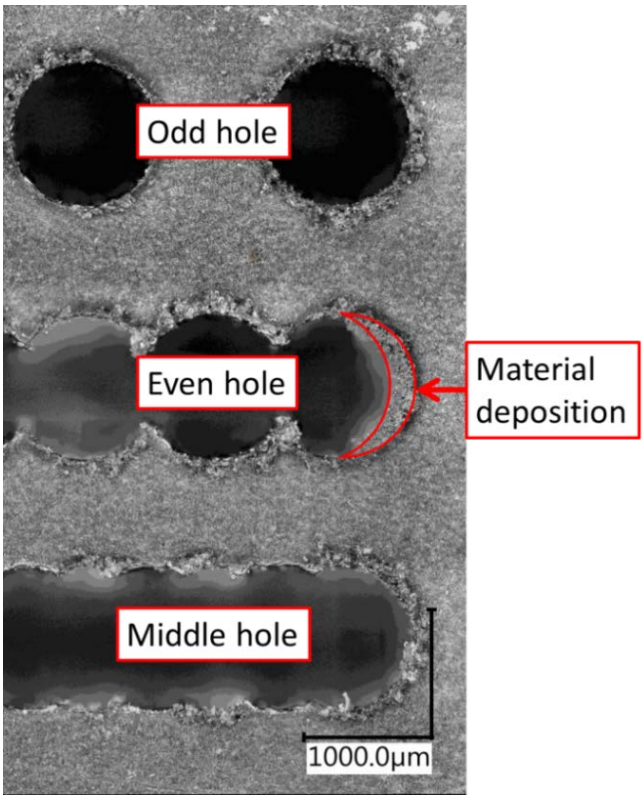

Fig. 6-9: Comparison of hole entrances after odd, even and middle hole drilling in the ODEM strategy, which is described in details in subsection 4.4.2. The material deposition is visible on the lateral side of the hole after even hole drilling. This deposition is completely or partially removed during machining of the middle hole and not more visible.

The analysis of material deposition after even hole machining is done considering Stokes number (S_{tk}) calculation in the next section 6.2.1. It is indicated that the velocity of the flow is too high for the eroded particles are detaching the flow.

During the machining of overlapping holes, the particles can agglomerate in the bottom slots corner on the other side of the machining process, this agglomeration can be explained by gravity forces as it is shown in the section 6.2.2.

6.2.1 Stokes number calculation

During machining of even holes, the machining is located in between on two drilled holes (after odd holes machining) as it is shown in Fig. 6-9, at the same figure the agglomeration of the particles is seen on the lateral side of the slot. The dielectric flow is changing its direction as it is shown by the streamlines in Fig. 6-10.

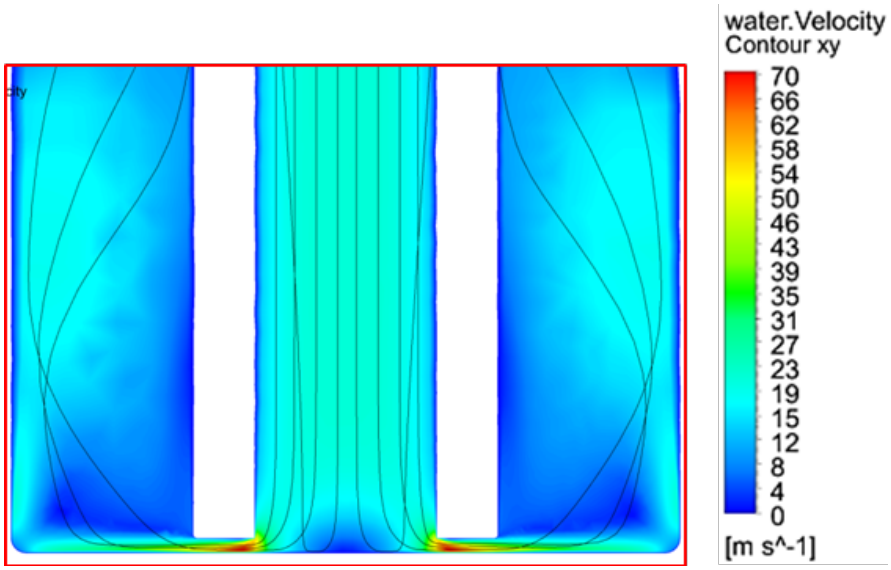

Fig. 6-10: Flow velocity during even hole machining. The flow is changing its direction as it is indicated by the streamlines, the measured velocity is above 20 m/s.

The Stokes number (Stk) is an indicator of particles behaviour in the fluid flow if Stk ≤ 0.1 the accuracy of tracing error is below 1%, but if Stk ≥ 1 particles detach the flow. The Stokes number can be calculated as

$$S_{tk} = \frac{(\rho_p - \rho_d) \cdot d_p^{\,2} \cdot \upsilon_d}{18 \cdot \mu_d \cdot l_o} \tag{6-6}$$

where υ_d is the velocity of the flow, ρ_p is a particle density, ρ_d is a density of dielectric media, μ_d is a dynamic viscosity of dielectric medium, d_p is a diameter of the particle, which is based on knowledge from section 6.3.3 considered 10 µm and l_o is a dimension of the obstacle, considered here as a radius of the hole. Therefore the Stokes number is calculated as

$$S_{tk} = 0.08 \cdot \upsilon_d \tag{6-7}$$

Thus the particles of eroded material are not capable of following 20m/s flow and getting attached to the wall of the hole.

6.2.2 Terminal velocity of eroded particle sinking in a fluid

The situation during overlapping hole drilling is different to the even hole drilling, as it is indicated in Fig. 6-11. Starting from the electrodes outlet hole, the flow is losing velocity and Y-direction component of the fluid velocity falls below zero at the right half of the figure.

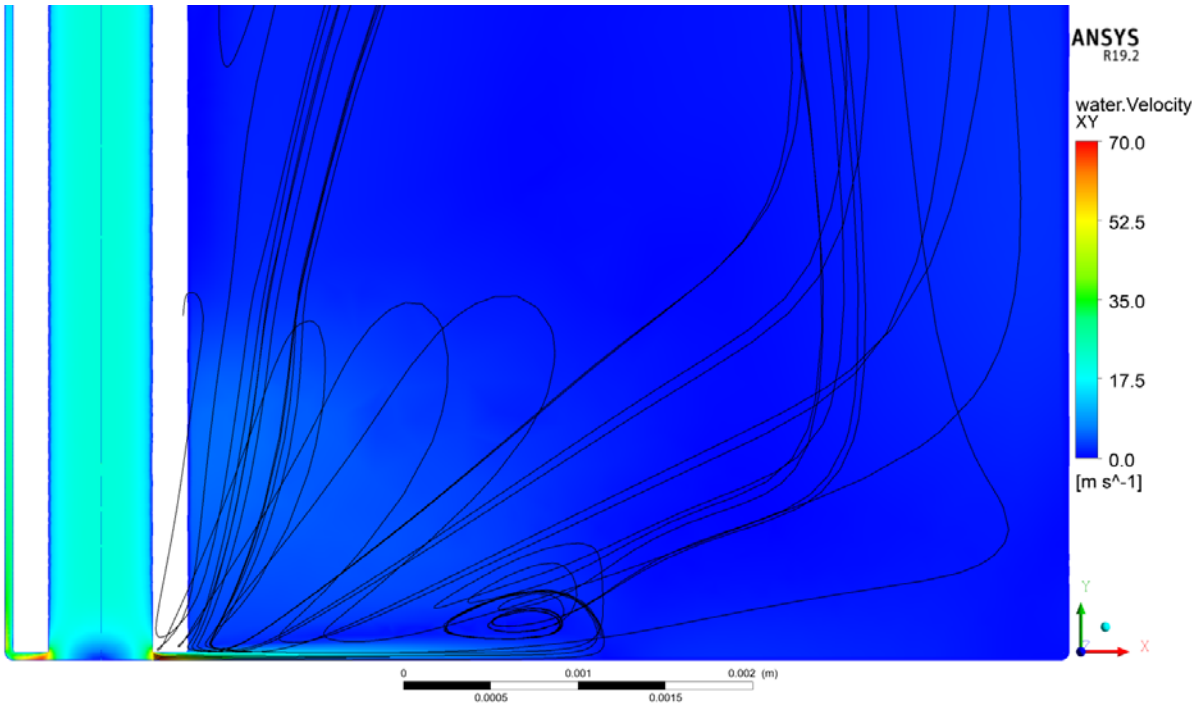

Fig. 6-11: Flow velocity during overlapping hole machining. At the right bottom corner, the flow velocity is almost zero, thus eroded particles are agglomerated in the corner and therefore more particles are concentrated in the slot.

In order to not sinking in the dielectric, the spherical particle of eroded material has to be carried by the flow with a certain velocity, in this case, the gravity force is

$$F_g = 4/3 \cdot (\rho_p - \rho_d) \cdot g \cdot \pi \cdot r_p^3 \tag{6-8}$$

where g is the gravitational acceleration, r_p is the radius of the particle. The balance force carried by the flow should be equal to it then the minimum velocity required to evacuate particle can be shown as

$$\upsilon_g = \frac{2 \cdot (\rho_p - \rho_d) \cdot g \cdot r_p^2}{9 \mu_d} \tag{6-9}$$

where υ_g is the minimum required velocity, which in this case is υ_g = 1.56 mm/s, if the flow velocity is lower than this value, the particle will sink to the bottom of the slot. The flow is also significantly influenced by the discharge, this influence is investigated by particle image velocimetry (PIV) in the next section.

6.3 Particle tracking velocimetry (PTV) and particle image velocimetry (PIV)

This section shows the innovative experiment setup in which the particles are tracked in the 50 µm gap between electrode and workpiece.

6.3.1 Flushing flow observation and analysis

The proposed high-speed camera observation setup is shown in Fig. 6-12. The analysis of the erosion process is performed within two conditions: first, the initial contact of the

electrode with the material surface and second, erosion inside a predrilled hole. The optics are protected by a glass pane, for the second condition two glasses are used. The observed images are shown in Fig. 6-13.

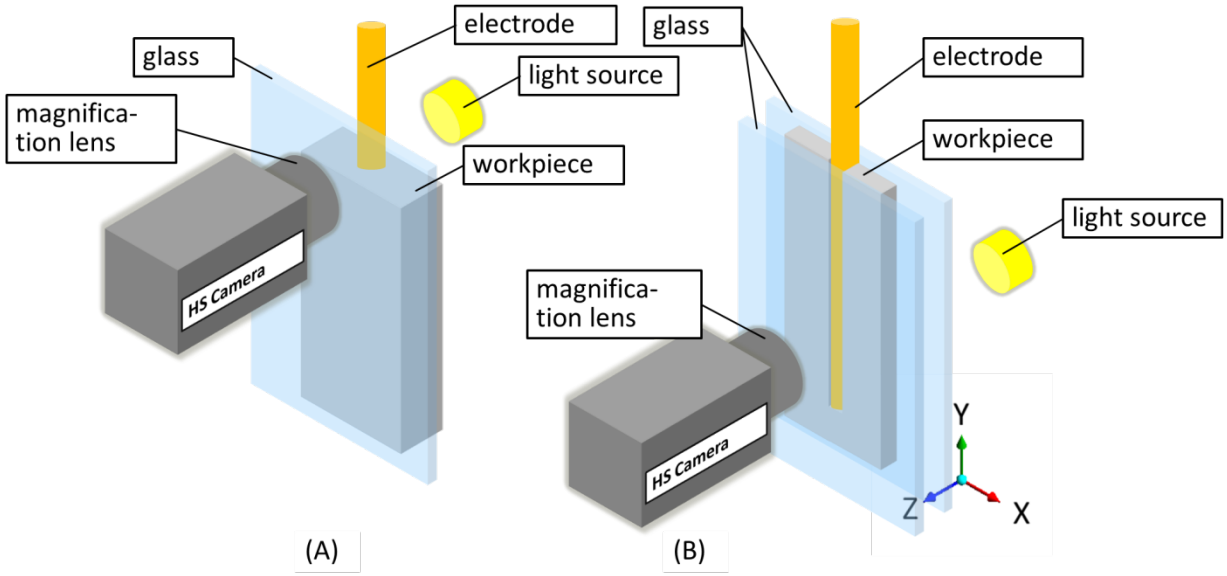

Fig. 6-12: High-speed camera observation setup, A is the condition, when the drilling electrode is outside the workpiece and B is the condition when the electrode is inside the workpiece.

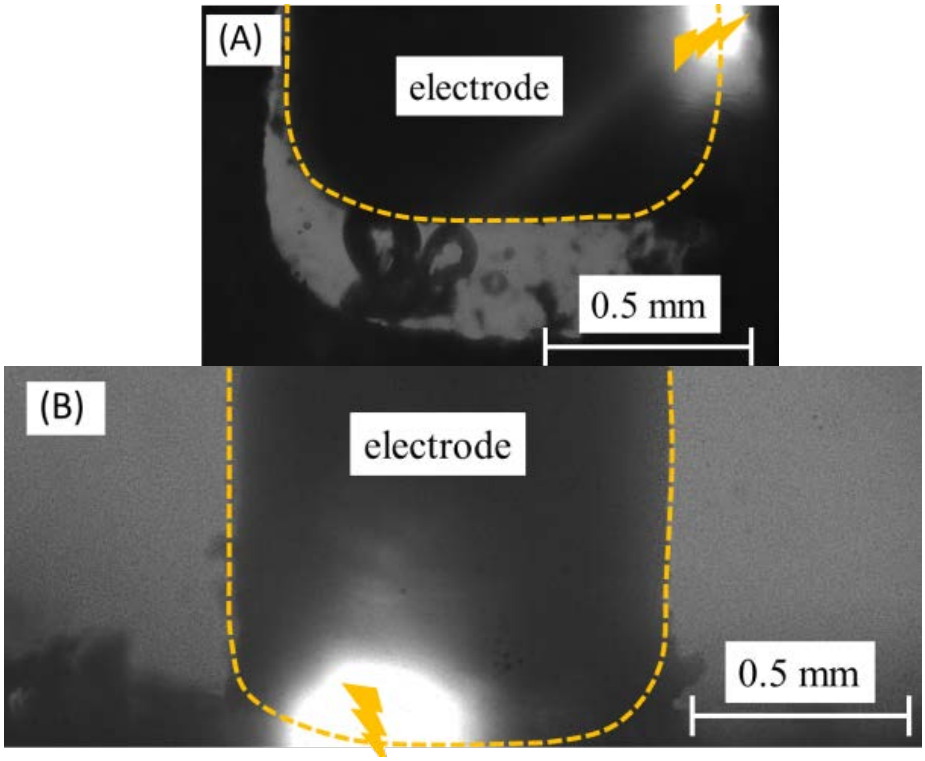

Fig. 6-13: High-speed camera images during discharge, A: erosion inside a predrilled hole, B: the beginning of hole erosion. The sparks are indicated with the icons.

The experiments are made on a commercial EDM drilling machine Drill 300 from GF Machining Solutions, Agie Charmilles SA. A high-speed camera Phantom v12.1 from Vision Research is used to track particles during erosion. The experimental conditions are indicated in Table 6-7. All observations are taken during EDM drilling process.

Table 6-7: EDM conditions

	EDM Condition
Workpiece material	Inconel 718
Electrode material	Copper
Dielectric	Deionized water
Pause duration	15 µs
Ignition voltage	120 V
Pulse duration	32 µs
Discharge current	28 A
Electrode rotation	300 rpm
Dielectric pressure	6.5 MPa
Electrode polarity	Negative

In past research high-speed imaging was often limited from low magnifications and insufficient external light sources. However, the novelty in the presented setup is in the advanced modification of the imagining equipment. The combination of Keyence optics from Digital Microscope VHX-5000 Series and the high-speed camera delivers high-resolution images in micrometre scale with a magnification up to 1000x. The external light sources are supported by an internal confocal light, which allows sufficient illumination in the area of interest. In this setup, the optics have a fixed focus distance. Therefore only particle movements in XY-plane are taken into account.

6.3.2 Particle tracking velocimetry and flushing flow simulation

The open source software PTVlab is used to calculate the velocities of bubbles and particles during the EDM drilling process. The software work is described by Thielicke and Stamhuis [147]. Software detects particles and compares two images to track the difference therefore the particle velocity (as it is shown in Fig. 6-14) is calculated based on particle movement from one image to another.

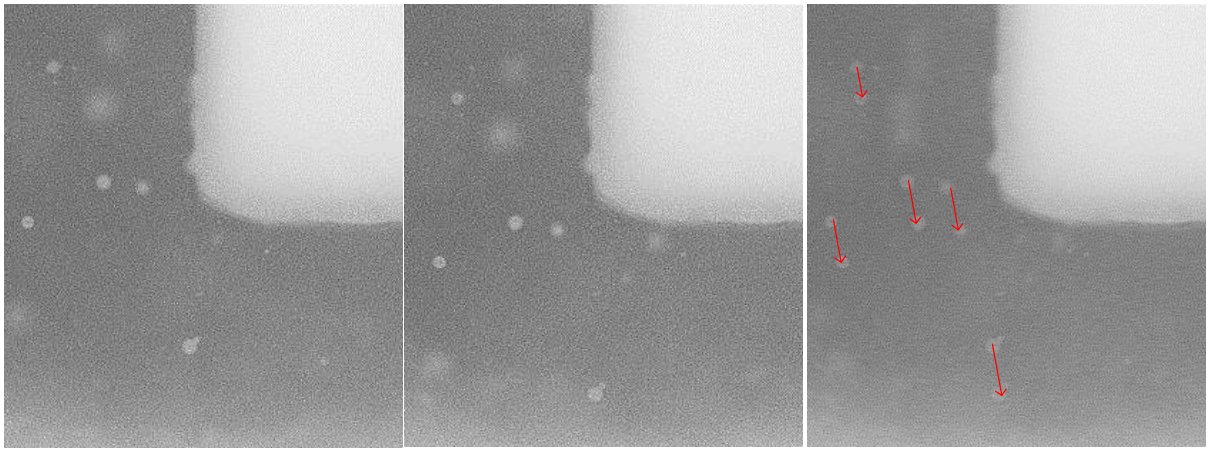

Fig. 6-14: Particle tracking velocimetry is based on frames comparison, from left to right: the first frame, second frame and comparison of two frames, particles movement is indicated.

PTV is performed in two conditions, in the condition of the initial contact of the electrode with the workpiece material the average calculated speed in the outlet area of the electrode is 0.9 m/s at the outlet of the electrode. For the second condition, when the electrode is inside the eroded cavity, an average value in the gap of $v = 0.75$ m/s is determined.

It is observed, that the direction of the flow on the electrode is changing when the electrode is inside the hole since the dielectric flow is influenced by the eroded cavity. Observations at the discharge moment are difficult due to the experimental setup and intense light emission of the spark, more dilate are given in the next subsection 6.3.3.

According to the experiments and PTV observations, two different geometries are investigated. A multi-hole configuration electrode of 1 mm diameter is used, where the cross-section is shown in Fig. 6-15 on the left side. An unworn 400 mm long electrode is assumed to investigate the lowest possible flow speeds by the highest pressure drop due to the length of the electrode. To reduce the computational time in the simulation, the geometry is set to 100 mm electrode length (as shown in Fig. 6-15 right) and inlet conditions adapted according to the pressure drop in the electrode from 400 mm to 100 mm length. The set pressure of 65 MPa drops to 25 MPa at the height of 100 mm, which is calculated by CFD simulations. The outlet is also set to static pressure difference 0 MPa to the reference pressure of 0.101325 MPa (atmospheric pressure). A single phase water flow is simulated employing a standard k-epsilon turbulence model without heat model.

The two investigated geometries are shown in Fig. 6-16. First an electrode in a 10 mm deep workpiece hole with a working gap size of 50 µm and a frontal gap of 200 µm (Fig. 6-16 left) and secondly an electrode in a distance of 1200 µm to the workpiece to investigate the bulk flow (Fig. 6-16 right). Comparison of these two conditions is aimed to analyze the change of the dielectric flow during the drilling process.

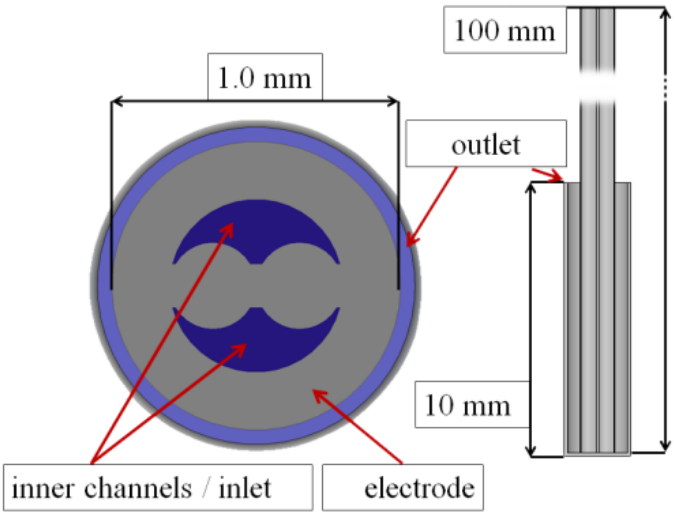

Fig. 6-15: Geometry of the electrodes, left horizontal cross-section of used multi-hole configuration electrode, right the vertical cross-section of the electrode in workpiece set-up.

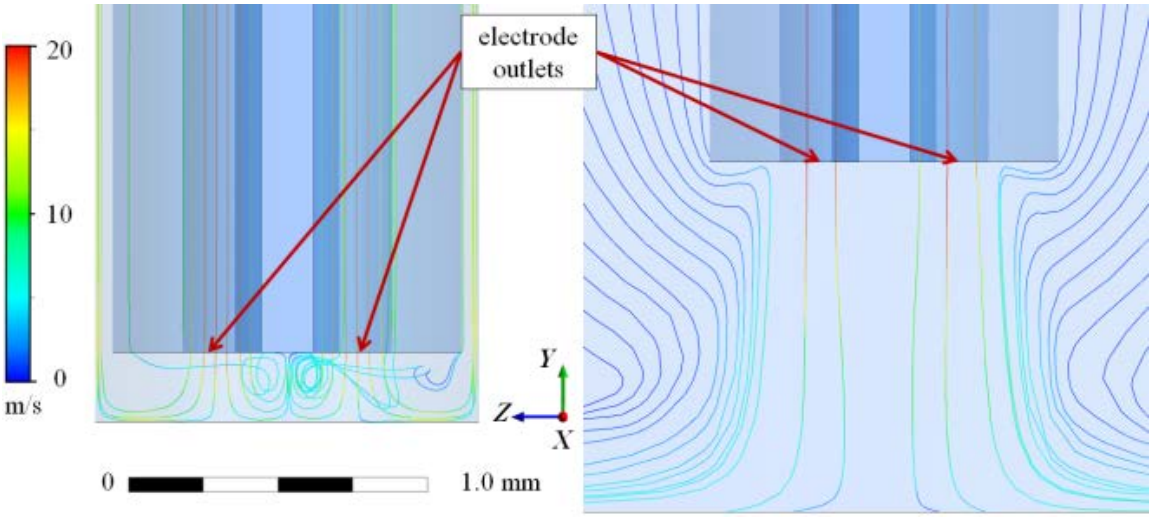

Fig. 6-16: Streamlines coloured to indicate the velocity of the two simulated geometries. On the left the electrode in the gap with 200 µm distance to bottom, on the right picture the bulk flow with a distance of 1200 µm to the bottom, the right case has an open boundary outlet condition (Ansys: opening).

The geometry data of the electrode channels are gathered by a magnified picture from the electrode cross-section and is simplified to decrease computational time. Electrode rotation is neglected as it is mentioned in section 6.1. The number of elements of the tetrahedral mesh varies from 7.8 million to 6.4 million elements in the workpiece hole respectively bulk flow geometry due to small geometry features inside the electrode as well as small flow channels for the first geometry.

6.3.3 Simulation results and verification

Employing CFD simulations the flow of the bulk media is investigated to evaluate the general flow conditions which control the particles and bubbles and thus the flushing flow from the electrode. In Fig. 4 the streamlines of the flow starting in the electrode channel in

the YZ-plane are shown for both cases, coloured to indicate the velocity. On the one hand, the fluid is swirling in the centre of the gap towards the workpiece bottom. On the other hand in the second geometry, it can be seen, that due to the outflowing dielectric fluid, bulk fluid from the sides is sucked into the centre, as it is shown in Fig. 4 right, and accelerated. In both cases, the speeds of the outflowing medium are much lower compared to the speed in the channels and below 5 m/s. The speed in the channels is defined by the volume flow in the electrode and the cross-section. After leaving the electrode the cross-section of the flow increases and according to the continuity equation the flow speed reduces.

The particle tracing, when the electrode is inside the eroded cavity, is shown in Fig. 6-17. The velocities along the gap remain equally distributed in the simulation and in the measurement. The resulting picture for the electrode outside the workpiece is shown in Fig. 6-18. Coloured lines indicate the trajectories of tracked particles. In the lateral region around the electrode, the particles are sucked into the main stream from electrode flushing channels as pointed out in the simulation.

Comparison between CFD simulations and PTV tracking shows similar behaviour for the bulk flow of the dielectric medium. In both cases, the velocities outside the electrode are much lower, and the outflow is influencing the bulk media around the electrode. These flow conditions are influencing the particle and bubble flow and thus the flushing of the EDM process.

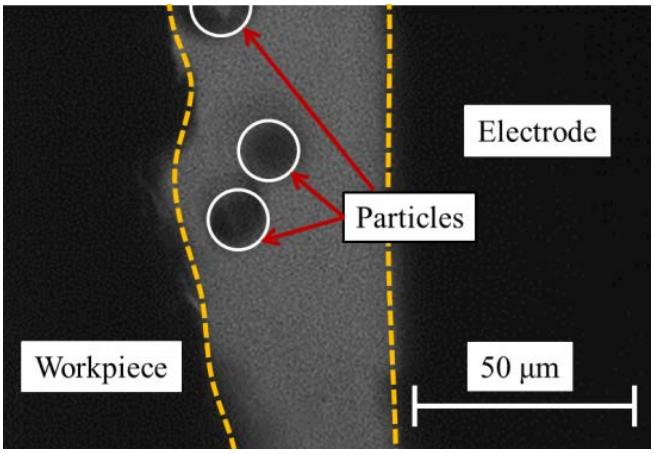

Fig. 6-17: The particle tracing in the gap between the electrode and the workpiece. The average value of the velocity of the particles is approximately 0.75 m/s.

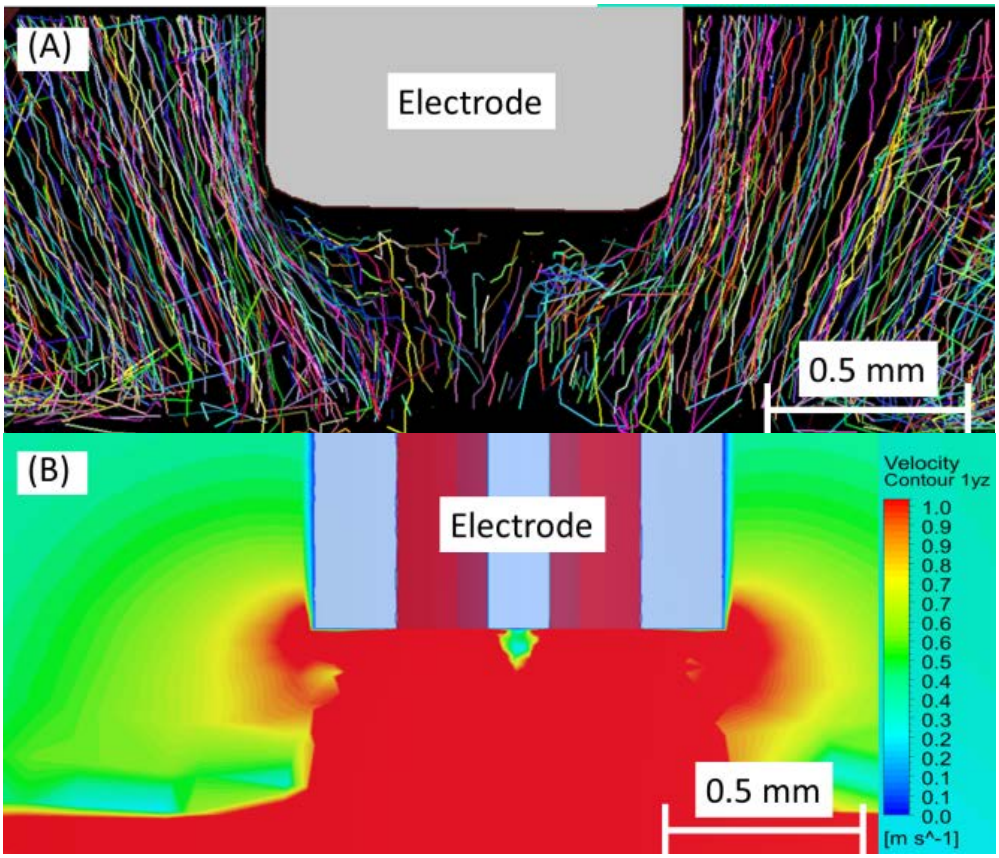

Fig. 6-18: Result of particle tracking velocimetry at the beginning of EDM drilling, the electrode is approaching the workpiece, at this case an open boundary outlet condition is used. Coloured lines in A indicate the trajectories; a number of trajectories in the middle part is lower since the number of particles to track from the electrode is low. Simulated flow is shown in B.

This section described a setup for high-speed imaging in micrometre scale of EDM drilling process within two conditions: first, the initial contact of the electrode with the material surface and second, erosion inside a predrilled hole. For the condition, when the electrode is approaching the workpiece the average calculated speed in the outlet area of the electrode is v = 0.9 m/s. For the second condition, when the electrode is inside the eroded cavity, the average value of velocity in the gap is v = 0.75 m/s. The challenges of flushing velocity measurement in EDM are discussed, and a novel image recording setup is presented. Due to the tracking of bubbles and particles the trajectories and thus the velocities were analyzed and calculated. It is seen, that the movement behaviour strongly depends on the machining conditions, whereas the electrode erodes a planar surface or a large aspect ratio hole. Due to impeded flushing behaviour in machining deep holes debris remains in the area of erosion and is delivered to the environment with delay. However, machining of planar surfaces leads to more efficient flushing.

6.3.4 Particle image velocimetry (PIV) and the discharge influence to the flushing flow

PIV is an optical and thus non-intrusive measurement technique that gives instantaneous 2D velocity data for a whole plane in a 3D flow field [148]. To study the influence of the single discharge to the flushing flow conditions in EDM Drilling OpenPIV software [149] is

used. The result of the image HS camera image analysis is shown in Fig. 6-19. The flow of the dielectric out of the eroded hole is significantly increasing at the moment of the discharge. This phenomenon can be explained by gas bubble creation in the region of the electrical discharge. The bubble pushes away the liquid dielectric media during its growth phase. After the end of the discharge the bubble is collapsing and dielectric flows back to the hole.

The discharge has an influence to the dialectic flow and additional volume created after the bubble collapse can slightly enhance the flushing efficiency. More important outcome of this flow disturbance is a destruction of eroded particle agglomeration in the regions with low velocities, since at the moment of the discharge the velocities of the dielectric medium in this region increases significantly.

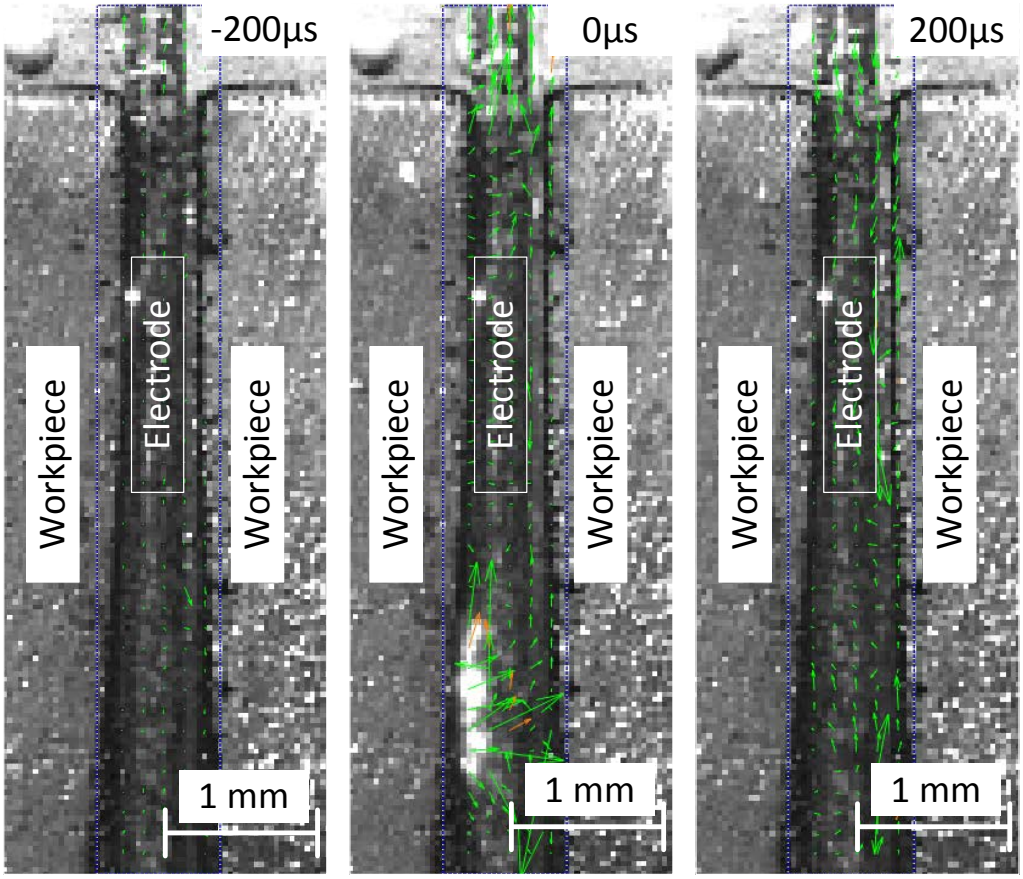

Fig. 6-19: Particle Image Velocimetry (PIV) from left to right 200 µs before discharge, during discharge and 200µs after discharge. The dielectric medium is displaced from the discharge region and therefore from the eroded cavity at the moment of the discharge (middle). After bubble collapse (right), dielectric flows back to the eroded cavity.

7. Conclusion and outlook

This thesis primarily investigates new EDM-milling and EDM-drilling strategies of the materials which are widely used by the aerospace industry. The restrictions of the EDM process utilisation for such applications are analysed, several new methods and machining strategies are proposed to expand the abilities of EDM and in order to increase productivity and precision of the existing methods.

EDM drilling can be used for machining Inconel 718 faster than state-of-art methods and fulfilling high requirements of the aerospace industry. The study experimentally proved that the average recast layer thickness can be reduced to 8 µm keeping high MRR. Moreover, the significant drawbacks of die-sinking EDM in hole drilling process which are relatively low MRR and expensive tool manufacturing are overcome by using standard cylindrical electrodes.

Concerning EDM drilling the erosion speed of 1.6 mm/sec is achieved through process parameter optimization by means of nonlinear regression and response surfaces. The results reached with 1 mm diameter electrode are as follows: An MRR of 77 mm^3/min is reached, the relative tool wear is reduced down to 20 %, and the average RLT is reduced to 8 µm (more details are section 3.3).

A new method to machine non-conducting materials is presented. Applying this method, it is possible to machine 1.5 mm deep hole in non-conducting ZrO_2 ceramic in deionized water, using the assisting electrode method, with the renewal of the assisting electrode by deposition of material from the tool anode instead of hydrocarbon oil decomposition. Further removal is challenging due to the insufficient flushing conditions in the experimental setup.

It is shown that the material removal mechanism of ZrO_2 in deionized water is a combination of several phenomena consisting of melting, vaporization due to electrical discharges and thermal stresses which cause micro-cracks and spalling. This process needs be further developed in order to be industrialized, for instance minimum thickness copper sacrificial layer has to be defined in order to increase productivity.

The capability of EDM drilling cooling holes and shaping diffusor geometries in Inconel 718 and SiSiC is proven. The combination of EDM drilling and shaping processes demonstrates the possibility to produce cooling holes with diffusors without electrode change. After diffusor shaping, the roughness of the internal surface is less than S_a = 1 µm. Particular attention is given to the RLT. It is found that the thickness after shaping is even lower than after drilling and significantly lower in comparison with laser drilling.

Additionally, a method for complex shaped slot machining is proposed by combining EDM drilling and shaping, thus offering high geometric flexibility for different shapes using standard tube electrodes. A strategy, named ODEM is a combination of odd even and middle

holes made in sequence in order to utilise the optimum machining conditions and reduce vibrations. Optimal erosion conditions from single hole drilling are used for maximal material removal for a slot, resulting in high productivity and surface integrity. This strategy is faster than any other known drilling strategy of slots machining. Also, since electrode position is known during each machining phase, through process monitoring the possible defects can be identified and corrected easily. As a next step, process parameter optimisation can further increase the suitability of the method for industrial implementation and other applications such as rib machining and pocket roughing.

Simulations are employed to understand the results of machining experiments. This work showed analysis of the fraction of energy in EDM process optimization, which can be used in the development of the new generation of EDM machines since the energy fraction can be maximised on the workpiece side. The novelty of this work is an analysis of the process parameters influence of an industrial EDM machine on the energy fraction f_a. Furthermore, the influence of temperature-dependent material properties and the inverse FEA are considered, which is a new approach in the field. The present work proved that the energy fraction going into the workpiece in EDM can vary substantially depending on different process conditions, such as discharge current and discharge duration. This is important because the fraction of energy is directly linked to maximization of removal rate and minimization of tool wear.

These results are achieved with a CFD simulation, which takes into account measured energy input, temperature-dependent material properties and Marangoni effect. The simulation is used for fitting (through the Nelder-Mead algorithm) the value of energy fraction going into the anode, having the crater dimensions as inputs. Therefore an inverse FEA is performed with the results of single crater measurements in order to analyze the influence of open voltage, discharge current and discharge duration on the energy fraction f_a, crater diameter and depth.

It is proven that temperature dependent material properties and latent heat have an essential influence on the accuracy of the simulation (up to 24% on the crater depth), while the Marangoni effect accounts for only 2-3% difference in crater depth. However, the Marangoni effect increases the crater diameter and lowers the depth, which influences the balance between energy fraction and heat source expansion.

By the single crater simulation, it is shown that the fraction of energy depends on machining conditions and in particular on the discharge current. It is proven that a longer discharge time and lower discharge current, increase the fraction of energy going to the workpiece (anode) and also increase the crater diameter. On the other hand, the open voltage does not have a significant influence on the flow of energy.

This work can be continued in further analysis of the PFE and modelling the discharge pressure influence to the crater shape and to the material properties. The great scatter of the crater depth can be explained by fluctuation of PFE, which depends on the discharge

pressure. Recast layer measurements showed that in some cases most of the molten material is re-solidified on the crater surface.The CFD simulation of the dielectric flow concludes in the following: the internal flushing channel diameter and configuration have a significant effect on the flushing speed and efficiency of debris particle removal. The effect is particularly significant for small diameter electrodes and complex multi-channel electrodes. For such electrodes, flushing can be insufficient to evacuate eroded material, which will lead to ineffective discharges, where MRR is low, and E_w is high.

It is clearly seen, that the flow velocity is influenced by the high aspect ratio between hole diameter and hole depth. Flow simulations have been used to compare the flow rates of the different electrodes, where the relation between length and flow rate is confirmed, and also complex cross-sections of multi-hole electrodes are investigated.

As it is shown in subsection 6.1.2, insufficient flushing has a tendency to increase the recast layer thickness; the effect is significant for high aspect ratios between hole diameter and hole depth. The effect needs to be taken into account since RLT is the crucial limiting factor of EDM drilling application in aerospace.

High-speed observations showed that the bubbles, created during the discharge in water, are very different from the bubbles in the oil. In water, instead of one big bubble, numerous small bubbles are created. Small bubbles do not significantly interfere with the erosion process.

The flushing behaviour is observed with particle tracking velocimetry (PTV), which is confirming the simulation. The simulation shows similar behaviour for the bulk flow of the dielectric medium. The precision of the fluid flow simulation can be further enhanced by simulating gas bubble growth and collapse and the influence of eroded material particles of both electrodes to the flow.

This thesis shows that drilling of film cooling holes, shaping of diffusers and machining of seal slots can be performed on one EDM machine without the workpiece re-clamping. Average recast layer thickness after machining of Inconel 718 is reduced to 8 µm. It is shown that EDM drilling is applicable for the new, perspective generations of the SiC-SiC CMC materials. Electrically non-conducting zirconia dioxide, which is often used as a TBC, can now be eroded in the deionised water, which was not possible before. The influence of the electrical discharge pulse parameters and flushing conditions are analysed by simulations and the simulation results are confirmed by experiments.

References

[1] Stavitskii B. Glimpses of the history of electrospark machining of materials. Surface engineering and applied electrochemistry;46. 2010:178-191.

[2] Nikolaeva J. Academicianul Boris Lazarenko Biobibliografie. Biblioteca Ştiinţifică Centrală „Andrei Lupan" a Academiei de Ştiinţe a Moldovei. 2011.

[3] Schumacher BM. After 60 years of EDM the discharge process remains still disputed. Journal of Materials Processing Technology;149. 2004:376-381.

[4] Bhuyan R, Routara B. Optimization the machining parameters by using VIKOR and Entropy Weight method during EDM process of Al–18% SiCp Metal matrix composite. Decision Science Letters;5. 2016:269-282.

[5] Ho KH, Newman ST. State of the art electrical discharge machining (EDM). International Journal of Machine Tools and Manufacture;43. 2003:1287-1300.

[6] Boeing. 777 Propulsion Design Review GE90 Strut Structure and Fairings. 1991.

[7] Reed RC. The Superalloys: Fundamentals and Applications: Cambrige universety press; 2006.

[8] Administration FA. Airplane Flying Handbook 2nd Edition: FAA-H-8083-3A: Skyhorse Publishing Inc.; 2011.

[9] Cherrared D. Numerical simulation of film cooling a turbine blade through a row of holes. Journal of Thermal Engineering;3. 2017:1110-1120.

[10] König W, Dauw DF, Levy G, Panten U. EDM-Future Steps towards the Machining of Ceramics. CIRP Annals - Manufacturing Technology;37. 1988:623-631.

[11] Lauwers B, Kruth JP, Liu W, Eeraerts W, Schacht B, Bleys P. Investigation of material removal mechanisms in EDM of composite ceramic materials. Journal of Materials Processing Technology;149. 2004:347-352.

[12] Zhao Y, Kunieda M, Abe K. Study of EDM cutting of single crystal silicon carbide. Precision Engineering;38. 2014:92-99.

[13] Padture NP, Gell M, Jordan EH. Thermal barrier coatings for gas-turbine engine applications. Science;296. 2002:280-284.

[14] Aksit MF, Chupp RE, Dinc OS, Demiroglu M. Advanced Seals for Industrial Turbine Applications: Design Approach and Static Seal Development. Journal of Propulsion and Power;18. 2002:1254-1259.

[15] Boeke MA, Rajchel K, Salzillo RM, DeGray JJ, Mainelli A. Gas turbine engine component having variable width feather seal slot. Google Patents; 2016.

[16] Chae J, Park SS, Freiheit T. Investigation of micro-cutting operations. International Journal of Machine Tools and Manufacture;46. 2006:313-332.

[17] Naeem M. Advancement in laser drilling for aerospace gas turbines. Proceedings of the 3rd Pacific International Conference on Application of Lasers and Optics 2008 2008.

[18] Okasha MM, Mativenga PT, Driver N, Li L. Sequential laser and mechanical micro-drilling of Ni superalloy for aerospace application. CIRP Annals - Manufacturing Technology;59. 2010:199-202.

[19] Kuppan P, Rajadurai A, Narayanan S. Influence of EDM process parameters in deep hole drilling of Inconel 718. Int J Adv Manuf Technol;38. 2008:74-84.

[20] Hasçalık A, Ay M. CO2 laser cut quality of Inconel 718 nickel – based superalloy. Optics & Laser Technology;48. 2013:554-564.

[21] Sharma S, Jain VK, Shekhar R. Electrochemical Drilling of Inconel Superalloy with Acidified Sodium Chloride Electrolyte. Int J Adv Manuf Technol;19. 2002:492-500.

[22] Yilmaz O, Okka MA. Effect of single and multi-channel electrodes application on EDM fast hole drilling performance. The International Journal of Advanced Manufacturing Technology;51. 2010:185-194.
[23] Sánchez H, Estrems M, Faura F. Development of an inversion model for establishing EDM input parameters to satisfy material removal rate, electrode wear ratio and surface roughness. Int J Adv Manuf Technol;57. 2011:189-201.
[24] Cusanelli G, Hessler-Wyser A, Bobard F, Demellayer R, Perez R, Flükiger R. Microstructure at submicron scale of the white layer produced by EDM technique. Journal of Materials Processing Technology;149. 2004:289-295.
[25] Lee HT, Tai TY. Relationship between EDM parameters and surface crack formation. Journal of Materials Processing Technology;142. 2003:676-683.
[26] Clijsters S, Liu K, Reynaerts D, Lauwers B. EDM technology and strategy development for the manufacturing of complex parts in SiSiC. Journal of Materials Processing Technology;210. 2010:631-641.
[27] Zhao Y, Kunieda M, Abe K. Experimental Investigations into EDM Behaviors of Single Crystal Silicon Carbide. Procedia CIRP;6. 2013:135-139.
[28] Zhu D. Aerospace Ceramic Materials: Thermal, Environmental Barrier Coatings and SiC/SiC Ceramic Matrix Composites for Turbine Engine Applications. 2018.
[29] Spitsberg I, Steibel J. Thermal and environmental barrier coatings for SiC/SiC CMCs in aircraft engine applications. International Journal of Applied Ceramic Technology;1. 2004:291-301.
[30] Padture NP. Advanced structural ceramics in aerospace propulsion. Nature materials;15. 2016:804.
[31] Zhu D, Miller R, Fox D. Thermal and environmental barrier coating development for advanced propulsion engine systems. 48th AIAA/ASME/ASCE/AHS/ASC Structures, Structural Dynamics, and Materials Conference2008. p. 2130.
[32] Feagin RC. Casting of reactive metals into ceramic molds. US Patent 4,787,439; 1988.
[33] Hung C-C, Hou G-L, Tsai C-C, Huang C-C. Pure titanium casting into zirconia-modified magnesia-based investment molds. Dental Materials;20. 2004:846-851.
[34] Miller RA. Thermal barrier coatings for aircraft engines: history and directions. Journal of Thermal Spray Technology;6. 1997:35.
[35] Denry I, Kelly JR. State of the art of zirconia for dental applications. Dental Materials;24. 2008:299-307.
[36] Tamarin Y. Protective coatings for turbine blades: ASM international; 2002.
[37] Mohri N, Fukuzawa Y, Tani T, Saito N, Furutani K. Assisting Electrode Method for Machining Insulating Ceramics. CIRP Annals - Manufacturing Technology;45. 1996:201-204.
[38] Schubert A, Zeidler H, Hahn M, Hackert-Oschätzchen M, Schneider J. Micro-EDM Milling of Electrically Nonconducting Zirconia Ceramics. Procedia CIRP;6. 2013:297-302.
[39] Schubert A, Zeidler H, Wolf N, Hackert M. Micro electro discharge machining of electrically nonconductive ceramics. AIP Conference Proceedings: AIP; 2011. p. 1303-1308.
[40] Gotoh H, Tani T, Mohri N. EDM of Insulating Ceramics by Electrical Conductive Surface Layer Control. Procedia CIRP;42. 2016:201-205.
[41] Guo YF, Bai JC, Deng GQ, Lu ZS. High speed wire electrical discharge machining (HS-WEDM) phenomena of insulating Si3N4 ceramics with assisting electrode. Key Engineering Materials: Trans Tech Publ; 2007. p. 281-285.

[42] Sabur A, Ali MY, Maleque MA, Khan AA. Investigation of Material Removal Characteristics in EDM of Nonconductive ZrO2 Ceramic. Procedia Engineering;56. 2013:696-701.
[43] Chen Y, Lin Y, Lin Y, Chen S, Hsu L. Optimization of electrodischarge machining parameters on ZrO2 ceramic using the Taguchi method. Proceedings of the Institution of Mechanical Engineers, Part B: Journal of Engineering Manufacture;224. 2010:195-205.
[44] Ojha N, Hösel T, Zeller F, Müller C, Reinecke H. Major parameters affecting the electric discharge machining of non-conductive SiC. Proceedings of the 10th International Conference on Multi-Material Micro Manufacture, S Azcárate and S Dimov, eds, Research Publishing2013. p. 978-981.
[45] Ferraris E, Reynaerts D, Lauwers B. Micro-EDM process investigation and comparison performance of Al3O2 and ZrO2 based ceramic composites. CIRP Annals - Manufacturing Technology;60. 2011:235-238.
[46] Melk L, Antti M-L, Anglada M. Material removal mechanisms by EDM of zirconia reinforced MWCNT nanocomposites. Ceramics International;42. 2016:5792-5801.
[47] Wüthrich R, Fascio V. Machining of non-conducting materials using electrochemical discharge phenomenon—an overview. International Journal of Machine Tools and Manufacture;45. 2005:1095-1108.
[48] Kliuev M, Maradia U, Boccadoro M, Perez R, Stirnimann J, Wegener K. Experimental Study of EDM-Drilling and Shaping of SiSiC and SiC. Procedia CIRP;42. 2016:191-196.
[49] Yu ZY, Masuzawa T, Fujino M. Micro-EDM for Three-Dimensional Cavities - Development of Uniform Wear Method. CIRP Annals - Manufacturing Technology;47. 1998:169-172.
[50] Bleys P, Kruth J-P, Lauwers B. Sensing and compensation of tool wear in milling EDM. Journal of Materials Processing Technology;149. 2004:139-146.
[51] Kunleda M, Miyoshi Y, Takaya T, Nakajima N, ZhanBo Y, Yoshida M. High speed 3D milling by dry EDM. CIRP Annals-Manufacturing Technology;52. 2003:147-150.
[52] Solutions GM. GF Machining Solutions' eTracking and new Seal Slot Technology represent breakthroughs in die-sinking EDM for aerospace manufacturing. http://www.gfms.com/com/en/about-gf-machining-solutions/press-room/press-releases/2017/gfms-etracking-and-new-seal-slot-technology.html2017.
[53] Klocke F, Klink A, Veselovac D, Aspinwall DK, Soo SL, Schmidt M, Schilp J, Levy G, Kruth J-P. Turbomachinery component manufacture by application of electrochemical, electro-physical and photonic processes. CIRP Annals;63. 2014:703-726.
[54] Hasçalık A, Çaydaş U. Electrical discharge machining of titanium alloy (Ti–6Al–4V). Applied Surface Science;253. 2007:9007-9016.
[55] Ayesta I, Izquierdo B, Sánchez JA, Ramos JM, Plaza S, Pombo I, Ortega N, Bravo H, Fradejas R, Zamakona I. Influence of EDM Parameters on Slot Machining in C1023 Aeronautical Alloy. Procedia CIRP;6. 2013:129-134.
[56] Klocke F, Holsten M, Hensgen L, Klink A. Experimental Investigations on Sinking-EDM of Seal Slots in Gamma-TiAl. Procedia CIRP;24. 2014:92-96.
[57] Uhlmann E, Domingos DC. Investigations on Vibration-Assisted EDM-Machining of Seal Slots in High-Temperature Resistant Materials for Turbine Components. Procedia CIRP;6. 2013:71-76.

[58] Flaño O, Ayesta I, Izquierdo B, Sánchez JA, Zhao Y, Kunieda M. Improvement of EDM performance in high-aspect ratio slot machining using multi-holed electrodes. Precision Engineering;51. 2018:223-231.
[59] Aas KL. Performance of two graphite electrode qualities in EDM of seal slots in a jet engine turbine vane. Journal of Materials Processing Technology;149. 2004:152-156.
[60] Uhlmann E, Domingos DC. Dressing of Graphite Electrodes for EDM of Seal Slots in Nickel-base Alloy MAR-M247. Procedia CIRP;42. 2016:328-333.
[61] Yuangang W, Fuling Z, Jin W. Wear-resist Electrodes for Micro-EDM. Chinese Journal of Aeronautics;22. 2009:339-342.
[62] Uhlmann E, Rosiwal S, Bayerlein K, Röhner M. Influence of grain size on the wear behavior of CVD diamond coatings in micro-EDM. Int J Adv Manuf Technol;47. 2010:919-922.
[63] Suzuki K, Sharma A, Sano S, Iwai M, Uematsu T. A New Application of PCD as a Very Low Wear Electrode Material for EDM Key Engineering Materials. 2005:549-554.
[64] Fuente JdL. Graphene - What Is It? Graphenea: Graphenea; 2013.
[65] Van Dijck FAS, R. Investigation of electro discharge machining operations by means of thermo-mathematical model (secondary source). CIRP Annals - Manufacturing Technology;20. 1971:35–37.
[66] Van Dijck FAS, R. Plasma channel diameter growth affects stock removal in EDM (secondary source). CIRP Annals - Manufacturing Technology;21. 1972:39-40.
[67] Dijck FSv, Dutré WL. Heat conduction model for the calculation of the volume of molten metal in electric discharges. Journal of Physics D: Applied Physics;7. 1974:899.
[68] Singh A, Ghosh A. A thermo-electric model of material removal during electric discharge machining. International Journal of Machine Tools and Manufacture;39. 1999:669-682.
[69] Kliuev M, Maradia U, Boccadoro M, Perez R, Stirnimann J, Wegener K. 18th CIRP Conference on Electro Physical and Chemical Machining (ISEM XVIII)Experimental Study of EDM-Drilling and Shaping of SiSiC and SiC. Procedia CIRP;42. 2016:191-196.
[70] Tariq Jilani S, Pandey PC. Analysis and modelling of edm parameters. Precision Engineering;4. 1982:215-221.
[71] Tariq Jilani S, Pandey PC. An analysis of surface erosion in electrical discharge machining. Wear;84. 1983:275-284.
[72] Pandey PC, Jilani ST. Plasma channel growth and the resolidified layer in edm. Precision Engineering;8. 1986:104-110.
[73] DiBitonto DD, Eubank PT, Patel MR, Barrufet MA. Theoretical models of the electrical discharge machining process. I. A simple cathode erosion model. Journal of Applied Physics;66. 1989:4095-4103.
[74] Patel MR, Barrufet MA, Eubank PT, DiBitonto DD. Theoretical models of the electrical discharge machining process. II. The anode erosion model. Journal of Applied Physics;66. 1989:4104-4111.
[75] Eubank PT, Patel MR, Barrufet MA, Bozkurt B. Theoretical models of the electrical discharge machining process. III. The variable mass, cylindrical plasma model. Journal of Applied Physics;73. 1993:7900-7909.
[76] Yeo SH, Kurnia W, Tan PC. Critical assessment and numerical comparison of electro-thermal models in EDM. Journal of Materials Processing Technology;203. 2008:241-251.

[77] Yeo SH, Kurnia W, Tan PC. Electro-thermal modelling of anode and cathode in micro-EDM. Journal of Physics D: Applied Physics;40. 2007:2513–2521.
[78] Rajendran R, Vendan SP. Single Discharge Finite Element Simulation of EDM Process. Journal of Advanced Manufacturing Systems;14. 2015:75-89.
[79] Kunieda M, Lauwers B, Rajurkar KP, Schumacher BM. Advancing EDM through Fundamental Insight into the Process. CIRP Annals - Manufacturing Technology;54. 2005:64-87.
[80] Xia HH, H.; Kunieda, M.; Nishiwaki, N. Measurement of energy distribution in continuous EDM process (secondary source). Journal of the Japan Society for Precision Engineering (in Japanese);269. 1996:1141-1145.
[81] Das S, Klotz M, Klocke F. EDM simulation: finite element-based calculation of deformation, microstructure and residual stresses. Journal of Materials;142. 2003:434–451.
[82] Weingaertner E, Kuster F, Wegener K. Modeling and simulation of electrical discharge machining. Procedia CIRP;2. 2012:74-78.
[83] Tao JJ, Ni J, Shih JA. Modeling of the anode crater formation in electrical discharge machining. Journal of Manufacturing Science and Engineering;134. 2012:11002.
[84] Mujumdar SS, Curreli D, Kapoor SG, Ruzic D. A Model of Micro Electro-Discharge Machining Plasma Discharge in Deionized Water. Journal of Manufacturing Science and Engineering;136. 2014:031011-031011.
[85] Mujumdar SS, Curreli D, Kapoor SG, Ruzic D. Modeling of melt-pool formation and material removal in micro-electrodischarge machining. Journal of Manufacturing Science and Engineering;137. 2015:031007.
[86] Weingärtner E. On-machine wire electrical discharge dressing of metal bonded grinding wheels: ETH Zurich; 2013.
[87] Bozdana AT, Ulutas T. The Effectiveness of Multichannel Electrodes on Drilling Blind Holes on Inconel 718 by EDM Process. Materials and Manufacturing Processes;31. 2016:504-513.
[88] Kliuev M, Boccadoro M, Perez R, Dal Bó W, Stirnimann J, Kuster F, Wegener K. EDM Drilling and Shaping of Cooling Holes in Inconel 718 Turbine Blades. Procedia CIRP;42. 2016:322-327.
[89] Plaza S, Sanchez JA, Perez E, Gil R, Izquierdo B, Ortega N, Pombo I. Experimental study on micro EDM-drilling of Ti6Al4V using helical electrode. Precision Engineering;38. 2014:821-827.
[90] Pontelandolfo P, Haas P, Perez R. Particle Hydrodynamics of the Electrical Discharge Machining Process. Part 2: Die Sinking Process. Procedia CIRP;6. 2013:47-52.
[91] Wang J, Han F, Cheng G, Zhao F. Debris and bubble movements during electrical discharge machining. International Journal of Machine Tools and Manufacture;58. 2012:11-18.
[92] Maradia U, Wegener K, Stirnimann J, Knaak R, Boccadoro M. Investigation of the Scaling Effects in Meso-Micro EDM. 2013:V02BT02A038.
[93] Y.Q. Wang MRC, Sheng Qiang Yang, Wen Hui Li. Numerical Simulation of Liquid-Solid Two-Phase Flow Field in Discharge Gap of High-Speed Small Hole EDM Drilling. Advanced Materials Research;Vols. 53-54. 2008:pp. 409-414.
[94] Haas P, Pontelandolfo P, Perez R. Particle Hydrodynamics of the Electrical Discharge Machining Process. Part 1: Physical Considerations and Wire EDM Process Improvement. Procedia CIRP;6. 2013:41-46.

[95] Okada A, Uno Y, Onoda S, Habib S. Computational fluid dynamics analysis of working fluid flow and debris movement in wire EDMed kerf. CIRP Annals;58. 2009:209-212.
[96] Mohd Abbas N, Solomon DG, Fuad Bahari M. A review on current research trends in electrical discharge machining (EDM). International Journal of Machine Tools and Manufacture;47. 2007:1214-1228.
[97] Luthra KL, Corman GS. Melt infiltrated (MI) SiC/SiC composites for gas turbine applications. DER Peer Review for Microturbine and Industrial Gas Turbines Programs, Fairfax, VA, Mar. 2002:12-14.
[98] Lee C-P, Johnson RA, Abuaf N. Modification and repair of film cooling holes in gas turbine engine components. Google Patents; 2001.
[99] Juan Dai H, Gebelin J-C, Newell M, Reed RC, D'Souza N, Brown PD, Dong HB. Grain Selection During Solidification in Spiral Grain Selector2008.
[100] Kliuev M, Maradia U, Wegener K. EDM Drilling of Non-Conducting Materials in Deionised Water. Procedia CIRP;68. 2018:11-16.
[101] Munz D, Fett T. Physical properties. Ceramics: Springer; 1999. p. 9-17.
[102] Levy D. Ceramic matrix composites take flight in LEAP jet engine. Oak Ridge National Laboratory. 2017.
[103] Chawla KK. Ceramic matrix composites. Composite Materials: Springer; 1998. p. 212-251.
[104] Bansal NP. SiC fiber-reinforced celsian composites. Handbook of Ceramic Composites: Springer; 2005. p. 227-249.
[105] Droillard C, Lamon J. Fracture Toughness of 2-D Woven SiC/SiC CVI-Composites with Multilayered Interphases. Journal of the American Ceramic Society;79. 1996:849-858.
[106] Naslain R. Fibre-matrix interphases and interfaces in ceramic matrix composites processed by CVI. Composite Interfaces;1. 1993:253-286.
[107] Rebillat F, Lamon J, Guette A. The concept of a strong interface applied to SiC/SiC composites with a BN interphase. Acta materialia;48. 2000:4609-4618.
[108] Dean A. Design and analysis of experiments: New York [etc.] : Springer; 1999.
[109] Garg RK, Singh KK, Sachdeva A, Sharma V, Ojha K, Singh S. Review of research work in sinking EDM and WEDM on metal matrix composite materials. Int J Adv Manuf Technol;50. 2010:611-624.
[110] Suzuki T, Kobayashi S. Mechanisms of TiC layer formation on high speed steel by a single pulse in electrical discharge machining. Electrochimica Acta;114. 2013:844-850.
[111] Maradia U, Knaak R, Dal Busco W, Boccadoro M, Stirnimann J, Wegener K. Spark location adaptive process control in meso-micro EDM. The International journal of advanced manufacturing technology;81. 2015:1577-1589.
[112] Maradia U, Kliuev M, Baumgart C. Efficient machining of complex-shaped seal slots for turbomachinery. CIRP Annals;67. 2018:209-212.
[113] Akbari M, Kliuev M, Boos J, Wegener K. Temperature and force measurements in single diamond scratch tests. The International Journal of Advanced Manufacturing Technology. 2018:1-13.
[114] Adams T, Grant C, Watson H. A simple algorithm to relate measured surface roughness to equivalent sand-grain roughness. Journal ISSN;2929. 2012:2724.
[115] Yoshida H, Kigawa T, Oota K. Groove forming method by discharge machining. In: EP, editor.: Bridgestone Corp.; 1994.

[116] Kliuev M, Baumgart C, Wegener K. Fluid Dynamics in Electrode Flushing Channel and Electrode-Workpiece Gap During EDM Drilling. Procedia CIRP;68. 2018:254-259.
[117] Kliuev M, Baumgart C, Büttner H, Wegener K. Flushing Velocity Observations and Analysis during EDM Drilling. Procedia CIRP;77. 2018:590-593.
[118] Kliuev M, Florio K, Akbari M, Wegener K. Influence of Energy Fraction in EDM Drilling of Inconel 718 by Statistical Analysis and Finite Element Crater-Modelling. Journal of Manufacturing Processes. 2018.
[119] Revaz B, Witz G, Flükiger R. Properties of the plasma channel in liquid discharges inferred from cathode local temperature measurements. Journal of Applied Physics;98. 2005:113305.
[120] Pérez R, Carron J, Rappaz M, Wälder G, Revaz B, Flükiger R. Measurement and metallurgical modelling of the thermal impact of EDM discharges on steel. Proceedings of the 15th International Symposium on Electromachining, ISEM XV2007. p. 17-22.
[121] Pottlacher G, Hosaeus H, Kaschnitz E, Seifter A. Thermophysical properties of solid and liquidInconel 718 Alloy. Scandinavian Journal of Metallurgy;31. 2002:161-168.
[122] Zlá S, Smetana B, Žaludová M, Dobrovská J, Kalup A, Vodárek V, Konečná K. Determination of thermophysical and structural properties of nickel super-alloy. Metalurgija;54. 2015:639-642.
[123] Tye R, Hayden R, Spinney S. The thermal conductivity of a number of alloys at elevated temperatures. High Temperatures-High Pressures;4. 1972:503-511.
[124] Overfelt R, Bakhtiyarov S, Wang D, Taylor R. ENGINEERING, Div. 1-Thermophysical Properties of 319 Aluminum, Compacted Graphitic Iron and Inconel 713. Transactions of the American Foundry Society;109. 2001:141-150.
[125] Defense USDo. Military Standardization Handbook: Metallic Materials and Elements for Aerospace Vehicle Structures: Department of Defense; 1987.
[126] Mukai K, Li Z, Mills KC. Prediction of the densities of liquid Ni-based superalloys. Metallurgical and Materials Transactions B;36. 2005:255-262.
[127] Rozner AG, Buehler WJ. High strength nickel-base alloys. Google Patents; 1967.
[128] Xiao F, Liu L-x, Yang R-h, Zhao H-k, Fang L, Zhang C. Surface tension of molten Ni-(Cr, Co, W) alloys and segregation of elements. Transactions of Nonferrous Metals Society of China;18. 2008:1184-1188.
[129] Szekely J. Fluid flow phenomena in metals processing: Elsevier; 2012.
[130] Pepper DW, Heinrich JC. The Finite Element Method: Basic Concepts and Applications with MATLAB, MAPLE, and COMSOL: CRC Press; 2017.
[131] Mitra SK, Chakraborty S. Microfluidics and nanofluidics handbook: fabrication, implementation, and applications: CRC Press; 2011.
[132] Nelder JA, Mead R. A Simplex Method for Function Minimization. The Computer Journal;7. 1965:308-313.
[133] Gear B. Backward differentiation formulas. Scholarpedia;2. 2007:3162.
[134] Isler Y. Recast layer analysis of EDM drilled nickel based alloy: ETH Zurich; 2015.
[135] Macedo F, Wiessner M, Bernardelli G, Kuster F, Wegener K. Fundamental Investigation of EDM Plasmas, Part II: Parametric Analysis of Electric Discharges in Gaseous Dielectric Medium. Procedia CIRP;68. 2018:336-341.
[136] Kunieda M, Muto H. Development of multi-spark EDM. CIRP Annals;49. 2000:119-122.

[137] Nieto A, Bisht A, Lahiri D, Zhang C, Agarwal A. Graphene reinforced metal and ceramic matrix composites: a review. International Materials Reviews;62. 2017:241-302.
[138] Miranzo P, Ocal C, Osendi MI, Belmonte M, Ramirez C, Roman-Manso B, Gutierrez HR, Terrones M. Process for production of graphene/silicon carbide ceramic composites. Google Patents; 2018.
[139] Porwal H, Grasso S, Reece M. Review of graphene–ceramic matrix composites. Advances in Applied Ceramics;112. 2013:443-454.
[140] Perez R, Lyet D. Graphene electrode. Google Patents; 2016.
[141] Shanmugam R, Rangarajan M, Devanathan S, Sathe VG, Senthilkumar R, Kothurkar NK. A design of experiments investigation of the effects of synthesis conditions on the quality of CVD graphene. Materials Research Express;3. 2016:125601.
[142] Perez R, Chiriotti N, Demellayer R, Flükiger R, Zryd A. Investigations of physical processes in wire-EDM by means of single and multiple discharge measurements and analysis. Proc ISEM XIII;1. 2001:473–484.
[143] Perez R, Rojas H, Walder G, Flükiger R. Theoretical modeling of energy balance in electroerosion. Journal of Materials Processing Technology;149. 2004:198-203.
[144] Pryor RW. Multiphysics modeling using COMSOL: a first principles approach: Jones & Bartlett Publishers; 2009.
[145] Sigloch H. Strömungen ohne Dichteänderung. Technische Fluidmechanik: Springer; 2017. p. 131-354.
[146] Sigloch H. Technische fluidmechanik. s.l. : Springer-Vieweg: Springer; 2014.
[147] Thielicke W, Stamhuis E. PIVlab–towards user-friendly, affordable and accurate digital particle image velocimetry in MATLAB. Journal of Open Research Software;2. 2014.
[148] Deen NG, Westerweel J, Delnoij E. Two-Phase PIV in Bubbly Flows: Status and Trends. Chemical engineering & technology;25. 2002:97-101.
[149] Taylor ZJ, Gurka R, Kopp GA, Liberzon A. Long-duration time-resolved PIV to study unsteady aerodynamics. IEEE Transactions on Instrumentation and Measurement;59. 2010:3262-3269.

List of publications

1. Kliuev, M., Boccadoro, M., Perez, R., Dal Bó, W., Stirnimann, J., Kuster, F. and Wegener, K., 2016. EDM Drilling and Shaping of Cooling Holes in Inconel 718 Turbine Blades. *Procedia Cirp*, *42*, pp.322-327.
2. Kliuev, M., Maradia, U., Boccadoro, M., Perez, R., Stirnimann, J. and Wegener, K., 2016. Experimental Study of EDM-Drilling and Shaping of SiSiC and SiC. *Procedia CIRP*, *42*, pp.191-196.
3. Maradia, U., Benavoli, A., Boccadoro, M., Bonesana, C., Klyuev, M., Zaffalon, M., Gambardella, L. and Wegener, K., 2018. EDM Drilling Optimisation Using Stochastic Techniques. *Procedia CIRP*, *67*(1), pp.350-355.
4. Kliuev, M., Baumgart, C. and Wegener, K., 2018. Fluid Dynamics in Electrode Flushing Channel and Electrode-Workpiece Gap During EDM Drilling. *Procedia CIRP*, *68*, pp.254-259.
5. Kliuev, M., Maradia, U. and Wegener, K., 2018. EDM Drilling of Non-Conducting Materials in Deionised Water. *Procedia CIRP*, *68*, pp.11-16.
6. Akbari, M., Kliuev, M., Boos, J. and Wegener, K., 2018. Temperature and force measurements in single diamond scratch tests. *The International Journal of Advanced Manufacturing Technology*, pp.1-13.
7. Kliuev, M., Baumgart, C., Buettner H. and Wegener, K., 2018. Flushing Velocity Observations and Analysis during EDM Drilling, 8th CIRP Conference on High Performance Cutting (HPC 2018). Procedia CIRP (2018) 77 590-593
8. Maradia, U., Kliuev, M. and Baumgart, C., 2018. Efficient machining of complex shaped seal slots for turbomachinery, CIRP Annals Manufacturing Technology. CIRP Annals (2018) 67(1)
9. Kliuev, M., Florio, K., Akbari, M. and Wegener, K., 2019. Influence of energy fraction in EDM drilling of Inconel 718 by statistical analysis and finite element crater-modelling. Journal of Manufacturing Processes, 40, pp.84-93.

Patents:

1. U. Maradia, M Kliuev, 2017. Method and device for machining shapes using electrical machining. European Patent Office Application no. 17202531.4-1019.